

**Studying the Microstructure of Electrodes for Low-temperature
Solid Oxide Fuel Cell and Electrolysis Applications**

by

Sajad Vafaenezhad

A thesis submitted in partial fulfillment of the requirements for the degree of

Doctor of Philosophy

in

Materials Engineering

Department of Chemical and Materials Engineering

University of Alberta

Abstract

Solid oxide fuel cells (SOFCs) is an important developing technology for energy conversion. This research was mainly focused on improving the fuel or air electrode of SOFCs in order to reduce the degradation rates and operation temperature. In chapters 3 and 4, a highly conductive Ni-yttria-stabilized zirconia (YSZ) anode was developed and tested in proton conductor and oxygen ion conductor SOFCs with improved stability and performance. In chapter 5, the composition and stability of an infiltrated praseodymium nickelate air electrode was studied. The infiltrated cathode was proven to be stable for over 250 h of a stability test in SOFC mode with no degradation.

SOFCs – with proper modification - can also operate in electrolysis mode. Hydrogen is becoming an increasingly important medium for storage and transport of energy. It is possible to produce low-cost hydrogen using renewable energy and help balance the intermittent nature of renewable sources such as wind or solar. Solid oxide electrolysis cells (SOECs) have the highest conversion efficiencies compared to other alternatives such as alkaline or proton exchange membrane (PEM) electrolyzers. However, high steam content during high temperature electrolysis can degrade the Ni-YSZ fuel electrode. In addition, the air electrode can degrade due to anodic overpotentials. In chapter 6, the stability of the cell optimized for SOFC condition was studied in electrolysis mode. It was found out that the Ni-YSZ electrode suffered from Ni migration towards electrolyte and left behind large pores 100 μm away from the electrolyte. In addition, the distribution of relaxation time data showed an increase of the total polarization resistance of the cell due to degradation of the praseodymium nickelate air electrode in an anodic environment. The results of this study show further modifications of the SOFC electrodes are required to withstand electrolysis conditions.

Keywords: SOFC, SOEC, electrolyte, Ni-YSZ, microstructure, PNO, NNO

Preface

The present dissertation was organized in a paper-based format. Author contributions for different chapters of the thesis are as follows:

Dr. Thomas Etsell, in addition to his academic supervision, provided the financial means necessary for all the chapters mentioned below to be completed successfully.

Chapter 1. Introduction

Writing the content, organizing different sections of the chapter, 3D modeling of the cell, 2D schematics of the cell setup and fabrication process was done by Sajad Vafaenezhad.

Chapter 2. Microstructure and Long-term Stability of Ni-YSZ Anode Supported Fuel Cells: A Review

Writing all sections of the review paper (except two) including the addition of references, interpretation of researchers' results, organizing different sections of the paper was done by Sajad Vafaenezhad. Dr. Amir Hanifi contributed in writing section 2.4. Dr. Miguel Laguna-Bercero contributed in writing section 2.3.6. Drs. Partha Sarkar and Thomas Etsell added constructive suggestions and comments to different sections of the paper.

Chapter 3. Development of Proton Conducting Fuel Cells Using Nickel Metal Support

Writing the entire paper, organizing the contents, analysis of the results including analysis and interpretation of the TEM and SEM images, pore content, shrinkage analysis of the performance of the cells including IV curve and Nyquist plot analysis, DRT graph generation and interpretations, drawing all graphs in OriginPro software was done by Sajad Vafaenezhad. Navjot Kaur Sandhu performed the test and acquired SEM images without any contribution to the rest of

the paper. Dr. Amir Hanifi contributed to the discussions and interpretation of the results. Dr. Partha Sarkar and Dr. Thomas Etsell provided constructive comments and suggestions during the work. The content of this chapter was published in a peer reviewed journal as follows:

Development of Proton Conducting Fuel Cells Using Nickel Metal Support (*S. Vafaenezhad, N.K. Sandhu, A.R. Hanifi, T.H. Etsell, P. Sarkar, J. Power Sources* **2019**, 435, 226763)

Chapter 4. Tailoring the SOFC Anode-support Composition and Microstructure for Low-temperature Applications

Writing the entire paper, drawing 2D illustrations of the setup, interpretation of the results including analysis of the SEM images, different phase fraction ratios and interpretations of them, interpretation of the IV curves, Nyquist plots, DRT graphs and redox cycling data was done by Sajad Vafaenezhad. In addition, fabrication of the cells as well as testing them was done by Sajad Vafaenezhad. Dr. Amir Hanifi contributed to the design of the experiments as well as commenting on analysis of the results, Drs. Mark Cuglietta, Partha Sarkar and Thomas Etsell added constructive comments and suggestions to different sections of the experiment. Dr. Mohtada Sadrzadeh provided laboratory equipment and consultation which were necessary to understand the rheology of Ni-YSZ pastes as well as thin film coating properties.

Chapter 5. Performance and Stability of Infiltrated Praseodymium Nickelate Cathodes for Low-temperature Fuel Cell Applications

Experimental work including fabrication of the cells was performed by Sajad Vafaenezhad and Miguel A. Morales-Zapata. Part of the experimental section (related to testing the cells with a PrO cathode and Figure 5-5) was solely performed by Sajad Vafaenezhad. SEM analysis, interpretation of the performance data (IV, Nyquist and DRT data) as well as writing the entire

paper was carried out by Sajad Vafaenezhad. Miguel A. Morales-Zapata collaborated in writing the introduction section and the sections related to the XRD data analysis (5.3.1 and 5.3.5). Critical comments and suggestions were provided by Drs. Amir Hanifi, Miguel Laguna-Bercero, Partha Sarkar and Thomas Etsell during the experimental work and writing of the paper.

Chapter 6. Degradation of Solid Oxide Electrolysis Cells with Infiltrated Praseodymium Nickelate Cathodes

Sajad Vafaenezhad contributed to the fabrication (electrolysis test setup and fabrication of the cells), measurements and analysis of the results (SEM, DRT, IV, Nyquist, potentiostatic test). Miguel A. Morales-Zapata as well as Drs. Amir Hanifi, Miguel Laguna-Bercero, Partha Sarkar and Thomas Etsell provided guidance and critical comments for the experiments.

Chapter 7. Planar SOFC Performance and Stability

Sajad Vafaenezhad contributed to the fabrication of the cells including tape casting the anode supports and optimizing tape cast parameters as well as measurements and analysis (SEM, EDS, DRT, IV, Nyquist, potentiostatic test) of the results and creating a 3D model of the setup (Figure 7.1). Drs. Amir Hanifi, Miguel Laguna-Bercero, Partha Sarkar and Thomas Etsell provided guidance and critical comments for the experiments.

Dedicated to my wife,

Farimah

And my parents,

Nezam and Nafiseh

For their endless love and support

Acknowledgements

I use this opportunity to express my gratitude to my supervisor, Dr. Thomas H. Etsell for his intellectual and financial supports throughout the period of this work. Without his support, none of my academic achievements would have been possible. I was fortunate to have good friends and colleagues during my study. Special thanks to Dr. Amir Hanifi as my academic and experimental consultant during my study. Hereby, I appreciate Dr. Partha Sarkar for his technical and academic support. I am very grateful to Dr. Mark Cuglietta for his helpful suggestions. It was a privilege to work with Taghi Amiri as my colleague in the lab and I'm thankful for his assistance. I appreciate Dr. Miguel Laguna Bercero and Jorge Silva for teaching me the fundamentals of tape casting and planar cell testing and their great hospitality during my stay at the University of Zaragoza, Spain. I also appreciate my friend, Miguel Morales Zapata for his assistance and consultant during his stay at the University of Alberta, Canada.

I would also acknowledge Dr. Mohtada Sadrzadeh for granting me access to the Advanced Water Research Laboratory which was essential for fabrication of tape cast SOFC supports. I also appreciate my friends Pouria Karami and Sadegh Aghapour Aktij for their assistance in the Advanced Water Research Laboratory.

I am thankful to Nathan Gerein for training me on the scanning electron microscopy (SEM) instrument in the University of Alberta's earth science department. I appreciate all my teachers at the University of Alberta including Drs. Hao Zhang, Stojan Djokic, Douglas G. Ivey and Hyo-Jick Choi for their valuable contribution to my knowledge in my field of study. I also appreciate Dr. Marc Secanell and the Future Energy Research Initiative for providing financial support for this study.

Contents

Chapter 1: Introduction	1
1.1 Research objectives	1
1.2 Thesis structure.....	2
1.3 Tubular cell.....	4
1.3.1 Solid oxide fuel cell and electrolysis setup	4
1.3.2 Tubular cell design	5
1.3.3 Experimental procedures for tubular cells	8
1.4 Reduction process.....	15
1.5 Electrochemical testing and characterization methods	15
Chapter 2: Microstructure and Long-term Stability of Ni-YSZ Anode Supported Fuel Cells: A Review	18
2.1 Introduction	19
2.2 SOFC components and reaction mechanisms inside the anode.....	21
2.3 Microstructural features which impact the electrochemical performance of Ni-YSZ anodes	25
2.3.1 Size and ratio of Ni to YSZ	26
2.3.2 Microstructural porosity	29
2.3.3 Impact of the characteristic pathway diameter	31
2.3.4 Tortuosity factor	32
2.3.5 Reduction process.....	33
2.3.6 Interfacial designs	35
2.4 Development of novel Ni-YSZ anodes by infiltration of porous YSZ.....	36
2.4.1 Calcination and milling of YSZ	36
2.4.2 Effect of pore-former on the microstructure of porous YSZ	38
2.4.3 Infiltration of porous YSZ to form electrodes	40
2.5 Application of Ni-YSZ in fabrication of proton conducting fuel cells	46
2.6 Degradation of Ni-YSZ supported SOFCs	47
2.6.1 Degradation of the Ni-YSZ electrode	48
2.6.2 Long-term degradation due to interconnects	56
2.6.3 Long-term degradation due to the test design parameters	67
2.7 Strategies to improve the electrochemical performance and durability of SOFCs	69
Chapter 3: Development of Proton Conducting Fuel Cells Using Nickel Metal Support	75
3.1 Introduction	76
3.2 Experimental procedures.....	80
3.2.1 Fabrication of the anode support	80

3.2.2 Synthesis of BZCYYb powder.....	80
3.2.3 Coating of the anode functional layer and the electrolyte.....	81
3.2.4 Coating of the cathode layer.....	81
3.2.5 Fuel cell setup and electrochemical testing.....	82
3.3 Results and discussion	83
3.3.1 Initial characterization of the support	83
3.3.2 Post-mortem SEM analysis of the cells	87
3.4 Conclusions	99
Chapter 4: Tailoring the SOFC Anode-support Composition and Microstructure for Low-temperature Applications	101
4.1 Introduction	102
4.2 Experimental procedures.....	106
4.2.1 Fabrication of the anode support	107
4.2.2 Coating of the anode buffer layer and functional layer.....	107
4.2.3 Coating of the electrolyte layer	108
4.2.4 Coating of the YSZ scaffold and cathode infiltration	108
4.2.5 Fuel cell setup and electrochemical testing.....	109
4.3 Results and discussion	110
4.3.1 Post-mortem SEM analysis of the cells	110
4.3.2 Electrochemical performance of the cell	117
4.3.3 Redox cycles	122
4.4 Conclusions	124
Chapter 5: Performance and Stability of Infiltrated Praseodymium Nickelate Cathodes for Low-temperature Fuel Cell Applications	126
5.1 Introduction	127
5.2 Experimental procedures.....	130
5.2.1 Fabrication of the anode support	130
5.2.2 Coating of the AFL	131
5.2.3 Coating of the electrolyte layer	131
5.2.4 Coating of the GDC scaffold and cathode infiltration	132
5.2.5 Preparation of scaffolds for X-ray diffraction (XRD) analysis.....	133
5.2.6 Fuel cell setup and electrochemical testing.....	133
5.3 Results and discussion	134
5.3.1 PNO reactivity with YSZ and GDC scaffolds	134

5.3.2 Post-mortem SEM analysis of the cells	137
5.3.3 Electrochemical performance of the cells	140
5.3.4 Stability test	148
5.3.5 Post-mortem XRD phase analysis	152
5.4 Conclusions	153
Chapter 6: Degradation of Solid Oxide Electrolysis Cells with Infiltrated Praseodymium Nickelate Cathodes	155
6.1 Abstract.....	155
6.2 Introduction	155
6.3 Experimental procedures and electrochemical testing	158
6.3.1 Electrochemical testing.....	158
6.3.2 Electrolysis cell configuration	159
6.4 Results and discussion	159
6.4.1 Electrochemical performance of the cells	159
6.4.2 Stability test	160
6.5 Conclusions	166
Chapter 7: Planar SOFC Performance and Stability	168
7.1 Abstract.....	168
7.2 Planar cell design	168
7.3 Experimental procedures.....	171
7.3.1 Fabrication of the support	171
7.3.2 Coating of the anode functional layer, buffer layer and the electrolyte	172
7.3.3 Coating of the scaffold and cathode infiltration	173
7.4 Results and discussion	175
7.5 Conclusions	179
Chapter 8: Conclusions and Future Directions	180
8.1 Conclusions	180
8.2 Future directions.....	182
8.3 Journal papers.....	182
References	183
Appendix A.....	197
Appendix B.....	198
Appendix C.....	201

List of Figures

Figure 1-1 Schematic of solid oxide fuel cell and electrolysis cell setup used in this research. In case of electrolysis, a heating tape was wrapped around the fuel inlet line.	5
Figure 1-2 Schematic of the tubular cell fabricated for this research.	7
Figure 1-3 Schematic of plaster mold fabrication (a) addition of water and gypsum to the two-part mold. (b) and (c) insertion of mandrel into the mold. (d) removing the mandrel and two-part mold after 30 minutes.	9
Figure 1-4 Slip cast process for fabrication of the anode supports. (a) filling the plaster mold cavity with the Ni-YSZ suspension (b) removing the excess suspension (c) shrinkage of the slip cast tube and separation from the plaster mold (d) removing the tube support from the plaster mold.	11
Figure 1-5 Dip coat process of the thin porous scaffold layer. (a) dipping the masked tube into the suspension (b) dwelling for 11 seconds (c) removing the tube from the suspension and peeling off the mask (d) heat treatment inside the furnace at 1200-1300 °C.	13
Figure 1-6 Schematic of the cathode infiltration process. (a) dipping the masked cell inside the precursors suspension and leaving under high vacuum (b) removing the cell from the suspension and removing the masking tape (c) initial nitrate decomposition at 350-450 °C in furnace (d) cleaning the excess decomposed infiltrates (e) final heat treatment of the cathode at 600-1000 °C.	14
Figure 1-7 The relationship between different variables in measured electrochemical parameters.	17
Figure 2-1. Schematic of (a) an oxygen ion conducting and (b) proton conducting SOFC.	23
Figure 2-2. (a) SEM image taken by a low acceleration voltage (1kV) secondary electron detector. Bright, grey and dark colors are Ni, YSZ and epoxy, respectively [19]. (b) schematic of TPB region inside a typical Ni-YSZ anode functional layer [23].	24

Figure 2-3. (a) Reconstructed 3D anode microstructures (Ni: yellow, 8YSZ: blue, pore: transparent), (b) the corresponding Ni phase of each sample illustrates that Ni grains are not percolated in samples A1 and A2 while they are almost totally percolated in sample A3 [37]..... 28

Figure 2-4. Schematic of the characteristic pathway diameter concept. (Red arrows highlight the characteristic pathway for the Ni phase, and percolating TPB between Ni (red), YSZ (gray) and pore (transparent) are circled in green) [49]. 32

Figure 2-5. Cross-sections SEM images of (a)(b)(c) pure Ni anodes reduced at 500°C, (d)(e) 800°C and (f)(g) 1000°C, (a) right after reduction, (b)(d)(f) before operation and (c)(e)(g) after operation and kept at 800°C under humidified hydrogen for 100 h [61]..... 35

Figure 2-6. TEM images of YSZ powders after 72 h milling. (a) as-received Tosoh YSZ (b) calcined at 1300, milled for 72 h (c) calcined at 1400, milled for 72 h and (d) calcined at 1500, milled for 72 h [75]..... 37

Figure 2-7. (a) YSZ zeta potential curve as a function of pH and (b) amount of acid or base per unit of YSZ surface consumed for pH adjustment [72]. 38

Figure 2-8. SEM images of the YSZ substrate sintered at 1350°C. (a) Tosoh YSZ + 20 vol.% graphite, (b) Tosoh YSZ + 20 vol.% PMMA, (c) calcined 1500°C-milled YSZ + 20 vol.% graphite and (d) calcined 1500°C-milled YSZ + 20 vol.% PMMA [75]. 40

Figure 2-9. (a) Ni-YSZ coverage by SDC near the interface of the fuel electrode and electrolyte, (b) YSZ coverage by LSM near the interface of the cathode and electrolyte [95]..... 42

Figure 2-10. (a) Electrochemical performance of the Ni-SDC infiltrated cell at different temperatures, (b) open circuit voltage curve during a redox cycling test at 650°C [105]. 44

Figure 2-11. SEM images showing the microstructure of infiltrated porous YSZ support structures (a) Within the Ni-SDC infiltrated porous YSZ anode and (b) Within the middle of a typical Ni infiltrated porous YSZ support [13]..... 44

Figure 2-12. SEM images of the cross-section of the anode after running under humidified hydrogen for 150 h. (a) substrate with fine YSZ grains and pores (b) substrate with large pores [106]. 45

Figure 2-13. SEM images of the cell following testing. (a) interfaces between cathode, electrolyte, and part of the cell anode, (b) interface between Ni-YSZ support and Ni-BZCYb anode functional layer [110]. 47

Figure 2-14. Location of the samples taken from the inlet, middle and the outlet of the cell [125]. 50

Figure 2-15. Quantified microstructure parameters conducted for the reference sample and the sample after 3700 h of long-term SOFC operation for (a) TPB length density (b) average grain size (c) tortuosity factor and (d) volume fraction. Samples were taken at different locations of the cell in the vicinity of the anode/electrolyte interface [125]. 51

Figure 2-16. Stability test for a stack operating at 700°C with 0.5 A·cm⁻². The fluctuations of the voltage for cell 6 are due to a contact wire issue and not degradation [125]..... 53

Figure 2-17. Visualization of skeletonized phase networks in the anode sample after redox cycling for Ni (top left), YSZ (top right), pores (bottom left) and all three skeletons superimposed [135]..... 55

Figure 2-18. The F1004-08 four-cell stack with LSM/YSZ cathode fabricated at Julich operated at 800°C for 19,000 h. The composition of the single cells can be found in Table 2-2 [138]..... 58

Figure 2-19. Stability tests of stacks developed at Julich with different interconnect protective coating, cathode contact material and interconnect materials (Crofer 22 APU vs. ITM) [113]..... 64

Figure 2-20. Stability test of the stack F1004-21 fabricated at Julich [141]. Details of the test condition are described in Table 2-2..... 65

Figure 2-21. Stability of different stacks developed at Julich with WPS-MnOx protective coating onto the interconnect at 700°C and 800°C. As can be seen, changing the interconnect material did not affect the degradation rate [113]..... 66

Figure 2-22. The effect of fuel type and fuel utilization on the stability of two stacks at 700°C developed at Julich. The composition of the single cells is described in Table 2-2. Stack 2018-07 undergoes a change of fuel utilization from 40% to 80% and type of fuel from hydrogen to liquified natural gas [113]. 67

Figure 3-1 TEM images of fine (a) BZCYYb (b) NiO and (c) YSZ powder..... 83

Figure 3-2 SEM micrographs of Ni-YSZ slip cast pellets with different weight ratios of NiO:YSZ for (a, b) Ni100 (c, d) Ni90 (e, f) Ni85 (g, h) Ni75 (i, j) Ni65. Pellets are described in Table 3-1. 86

Figure 3-3 Post-mortem SEM micrographs of the cells after SOFC testing for (a, b and c) Ni100 cell and (d, e) Ni90 cell. The red oval in (c) shows the crack formed inside the electrolyte..... 89

Figure 3-4 (a) Current density-voltage-power curves of (a) cell Ni100 and (b) cell Ni90 at different temperatures. The flow rate of the fuel (3 vol.% humidified hydrogen) was 10 mL · min⁻¹. (c) Nyquist plot of the cell Ni100 and (d) cell Ni90. (e) Peak power densities of the cells. (f) Area specific resistance of the cells Ni100 and Ni90 as temperature varied..... 92

Figure 3-5 Distribution of relaxation times (DRT) for (a) cell Ni100 and (b) cell Ni90 at different temperatures. 95

Figure 3-6 Power densities of the two cells Ni90 and Ni65 at 600 and 700°C. The fuel (3 vol.% humidified hydrogen) flow rate for cell Ni90 was 25 mL·min⁻¹ and the fuel flow rate for cell Ni65 was 50 mL·min⁻¹. 97

Figure 3-7 SEM micrograph of (a) Ni100 cell (b) half-cell with 100 wt% Ni metal support, Ni-BZCYYb AFL and BZCYYb electrolyte. The initial NiO powder used to fabricate this cell is NiO Baker. (c) Ni90 cell. All cells were sintered at 1450°C and reduced by hydrogen 98

Figure 3-8 (a) Potentiostatic operation of the cell Ni90 for 67 hours at 0.7 V and 700°C in SOFC mode. The flow rate of the fuel (3 vol.% humidified hydrogen) was 10 mL·min⁻¹. (b) Nyquist plot of the cell Ni90 before (pre-potentiostat) and after (post-potentiostat) the potentiostatic test at 600, 650, 700 and 750°C..... 99

Figure 4-1. Schematic of the tubular SOFC test setup used for these experiments..... 110

Figure 4-2. Post mortem SEM micrographs of (a, c, e, g) Ni82 cell and (b, d, f, h) Ni50 cell.	112
Figure 4-3. Post mortem SEM micrographs of the support in (a) Ni82 and (b) Ni50 cell and their corresponding EDS maps for (c) Ni82 and (d) Ni50 cell.	113
Figure 4-4. Volume fraction of Ni, YSZ and pores inside different layers of Ni82 and Ni50 cells. SL: support layer, BL: buffer layer, FL: functional layer.	115
Figure 4-5. Distribution of Ni, YSZ and pore sizes inside different layers of the Ni82 anode: (a) support layer (b) buffer layer (c) AFL. (d) Comparison of average phase sizes in different layers of the Ni82 anode.	117
Figure 4-6. Current density-voltage-power density plot of (a) Ni50 and (b) Ni82 cell at different temperatures (c) comparison of peak power density of Ni82 and Ni50 cells at different temperatures.	118
Figure 4-7. EIS comparison of Ni82 and Ni50 cells at (a) 600 °C (b) 550 °C and (c) 500 °C. The inset is the zoomed view of the same graph. Square and circle points show the fitting on experimental EIS using the DRT method. Corresponding DRT data for each temperature are shown in d, e and f.	121
Figure 4-8. (a) OCV graph of the Ni82 cell redox cycles at 550 °C. (b) IV curves and (c) Nyquist plots before and after each redox cycle. Hydrogen was cut off for 1 h and introduced again for 15 min during each cycle.	124
Figure 5-1. XRD diffractograms of (a) PNO-infiltrated YSZ and (b) PNO-infiltrated GDC scaffolds in samples annealed between 700 and 1000 °C for five hours using one infiltration.	136
Figure 5-2. Post-mortem 1 kV secondary electron in-lens SEM images of epoxy-embedded polished specimens from cell A (a, c and e) and cell B (b, d, f). Contrast shows different phases in AFL and support. Ni, YSZ and pores are bright, dark grey and light grey, respectively. 4 kV secondary electron in-lens SEM images of fractured specimens from the reference cell are shown in g and h.	139

Figure 5-3. Current density-voltage-power density graphs of (a) cell A and (b) cell B at different temperatures with 50 SCCM H₂ (3 vol.% humidified) on the anode side and 100 SCCM air on cathode side; (c) comparison of peak power densities of cell A and B at different temperatures. 141

Figure 5-4. EIS comparison of cells A and B at (a) 750 °C (b) 700 °C (c) 650 °C. Blue circles and green squares show the fittings on experimental EIS data using the DRT method. Corresponding DRT data for each temperature are plotted in d, e and f. 143

Figure 5-5. Comparison of DRT results of cell A and B with PNO and PO (Pr₆O₁₁) cathodes exposed to different cathode atmospheres. (a, b and c) cell A. (d, e and f) cell B. Humidified hydrogen with 50 SCCM was used as fuel on the anode side for both cells. 147

Figure 5-6. Potentiostatic test of cell A and B at 650 °C and 0.7 V. Fuel and air were provided on anode and cathode sides with 50 and 100 SCCM, respectively. 148

Figure 5-7. I-V-P, Nyquist plots and corresponding DRT graphs for cell A (a, b and c) and cell B (d, e and f). The solid line in (b) and (e) are experimental Nyquist data while the points on the curve show the accuracy of corresponding DRT fitting. Inset in (e) shows the zoomed Nyquist data. 151

Figure 5-8. Background-subtracted XRD in the 32 to 39° range of A (91 h test) and B (260 test) samples heat-treated at 1000 °C and operated at 650 °C in comparison with the reference cells (0 hours of operation) for the same heat treatment. 153

Figure 6-1 (a) I-V-P graph in fuel cell mode tested at different temperatures. (b) EIS graph measured at OCV. The fuel and air flow rates were 50 and 100 SCCM, respectively. 159

Figure 6-2 (a) Performance of the cell in fuel cell and electrolysis mode. (b) EIS data at OCV. Fuel composition was 50:50 mol ratio of H₂:H₂O. 160

Figure 6-3 Stability test in electrolysis mode at 1.3 V. The stability test was stopped at 28h for 9h (OCV was measured during this period), then continued from 37h up to 61h. Fuel composition was 50:50 mole ratio of H₂:H₂O. 161

Figure 6-4 Tracking the OCV of the cell (a) in the middle of the stability test from 28 – 37 h and (b) at the end of the stability test from 61-84 h. Fuel composition was 50:50 mole ratio of H ₂ :H ₂ O. Note the OCV is plotted on an expanded scale.....	162
Figure 6-5 (a) I-V and (b) EIS measurement of the cell at different intervals during the stability test. (c) DRT graph corresponding to EIS data in (b).....	163
Figure 6-6 Post-mortem SEM images of the cell after the stability test (a) backscattered image showing the pore distribution from bottom to the top of the support (b) secondary image of support close to the electrolyte and (c) away from the electrolyte.	164
Figure 6-7 (a) Post-mortem SEM image of cell B in chapter 5 after 260 of stability test in SOFC mode. (b) Post-mortem SEM image of the cell in chapter 6 after the stability test in SOEC mode. The lines in the images show the length of the pores inside the support.	165
Figure 7-1 Schematic of the planar cell's test setup used in the thesis.....	170
Figure 7-2 SEM micrograph of (a) dip coated and (b) spray coated electrolyte onto the presintered Ni-YSZ tape. Both electrolytes were sintered at 1400 °C for 3h.	173
Figure 7-3 (a), (b) and (c) Tape cast process and coating of Ni-YSZ film onto the Mylar sheet (d) multilayered Ni-YSZ tape after drying in room temperature (e) one inch planar cell following sintering (f) presintered Ni-YSZ tape (g) 7.5x7.5 cm electrolyte coated Ni-YSZ support following sintering (h) button cells following coating the cathode and heat treatment (i) planar test setup with silver and (j) gold current collector.	174
Figure 7-4 Stability test of the planar SOFC at 800 °C and 0.7 V.	175
Figure 7-5 (a) I-V-P and (b) EIS measurements of the cell prior and after the stability test (c) DRT data collected from EIS measurement prior and after the stability tests.	176
Figure 7-6 Post-mortem SEM micrographs of planar SOFC following 70 h of stability test at 850 °C. (a) 295 μm thick support (b) different components of the anode (c) thickness of the electrolyte and cathode	

(d) infiltrated cathode microstructure and (e) EDS map of the AFL, buffer and support layers in fuel electrode..... 178

Figure A 1 XRD pattern of NiO-BZCYYb functional layer following sintering at 1450°C for 3 h..... 197

Figure B 1 SEM images of polished samples for (a) Ni82 functional layer and buffer layer (b) Ni50 functional layer and support (c) Ni82 support (d) Ni50 support. Color contrast shows different phases; YSZ: dark gray, Ni: white, pores: light gray. 198

Figure B 2 Contribution of different resistances in the original DRT data extracted from EIS (experiment) at different temperatures for (a, b, c) Ni82 and (d, e, f) Ni50 cell. The values in the legends show the fraction of surface area under each peak to the total surface area under the DRT curves. 199

Figure B 3 (a) Nyquist plot of the Ni50 cell at 600 °C with two different fuel flow rates. (b) DRT data corresponding to the Nyquist plots. 200

Figure C 1 Comparison of the shape and size of cell A and B used for the SOFC test. 201

Figure C 2 DRT graphs for cell B with Pr₆O₁₁ (PO) cathode at 650 °C for different cathode and anode gas compositions and varying flow rates. 201

List of Tables

Table 1-1. Precision of different experimental parameters.	16
Table 2-1 Summary of the long-term stack and single cell tests mentioned in the text. SP, FL, TC, CD, FU, OU, WPS and T stand for screen print, functional layer thermal cycling, current density, fuel utilization, oxygen utilization, wet powder spray and temperature, correspondingly.	59
Table 2-2 Components for different stacks developed at Julich. SP, WPS and IC stand for screen print, wet powder spray and interconnect. All cells are composed of Ni-YSZ anode and YSZ electrolyte.	61
Table 3-1 Shrinkage and open porosity of different slip casted pellets, sintered at 1450°C and reduced by hydrogen gas. The NiO-YSZ pellets contained 30 vol.% graphite as pore former.	84
Table 3-2 The values of area specific resistance components for cells Ni90 and Ni100 fitted with the equivalent circuit of the Nyquist plots in Figure 3-4c and d.	95
Table 4-1 The value of different resistance and capacitance corresponding to the peaks in Figure 4-7 for Ni82 and Ni50 cells.....	119
Table 5-1 Composition and thickness of different layers in cells A and B.	130

Chapter 1: Introduction

1.1 Research objectives

The main objectives of this study were partly related to the existing challenges in performance and durability of tubular solid oxide fuel cells based on Ni-YSZ fuel electrode and infiltrated air electrodes. Preferably, long term stability of such cells was of interest due to limited published articles based on infiltrated air electrodes. Another challenge related to tubular cells was the current collection pathway which is longer compared to planar cells. As a result, the tubular cell was more prone to loss of contact and increase of ohmic resistance. Ceria-based proton conductors, despite their high proton conduction at lower temperature, face stability issues due to cerium mobility and reactivity inside the fuel electrode. A substitute support layer with higher stability was intended to be designed and implemented with a proton conductor electrolyte. Fabrication and testing planar cells with similar composition to tubular cells were of interest due to higher volumetric power density of planar cells. Finally, it was intended to study the challenges and possibility of operating the fabricated tubular cells in electrolysis mode. Thus, the objectives of this research were as follows:

- (i) Optimizing the microstructure of the Ni-YSZ support layer in tubular SOFCs to increase the electronic conductivity of the support without degrading the mechanical stability of the cell.
- (ii) Studying the possibility of using an oxygen ion conductor support with good stability for proton conductor SOFCs.
- (iii) Optimizing the microstructure of infiltrated Ruddlesden-Popper cathodes and studying their stability and reactivity in SOFC mode.

(iv) Studying the performance and stability of tubular SOFCs with a Ni-YSZ anode and infiltrated cathode in SOEC mode, finding the challenges and suggesting possible solutions to them.

(v) Developing a planar SOFC based on improved anode support structure for SOFC application.

1.2 Thesis structure

Chapter 1 of the thesis informs the reader about the objectives of this research. In addition, the setup used for testing the cells as well as electrochemical characterization methods and experimental procedures are described.

Chapters 2, 3, 4 and 5 were written based on submitted/published articles.

Chapter 2 is a literature review focusing on the degradation mechanisms and solutions for increasing the stability of SOFCs with a Ni-YSZ support. Initially, different components and reaction mechanisms of oxygen ion conducting and proton conducting SOFCs are described. The effect of different microstructural features of the Ni-YSZ electrode on the performance of the cell is described. Different methods for fabrication of the porous YSZ scaffold and the importance of infiltration methods in stability and performance of SOFCs are mentioned. The degradation mechanisms in the Ni-YSZ anode as well as cathode side degradation due to interconnects are discussed. At the end, strategies to improve the electrochemical performance of the cell are suggested.

In chapter 3, the possibility of utilizing the high chemical and mechanical stability of a Ni-YSZ support for proton conducting SOFCs was studied. Different compositions of the Ni-YSZ support with varying Ni and YSZ contents were studied. The performance and microstructure of an optimized composition (NiO:YSZ = 90:10 wt% prior to reduction) was compared to the

conventional Ni-YSZ support (NiO:YSZ = 65:35 wt% before reduction) and purely electronic conductor (100% NiO before reduction). According to the results, addition of just 10 wt% YSZ to the support inhibits Ni grain growth and crack formation inside the support as well as reduces the total polarization resistance of the cell. In addition to higher performance of the newly developed cell, no degradation in performance was detected during 67 h of a stability test at 700 °C.

In chapter 4, the highly conductive anode support developed in chapter 3 was improved (changing the particle size) and applied to an oxygen ion conductor SOFC with YSZ electrolyte. A buffer layer with intermediate electronic and ionic conduction was designed and placed in between the anode support and anode functional layer (AFL) to reduce the thermal expansion coefficient (TEC) between the support and AFL. An 87% boost in performance of the SOFC was detected at low operation temperature (550 °C) due to the optimized microstructure. In addition, the newly developed cell was tolerant of four redox cycles at 550 °C without any degradation.

In chapter 5, the performance and stability of an infiltrated PNO ($\text{Pr}_2\text{NiO}_{4+\delta}$) cathode into the GDC scaffold was studied in SOFC mode. The cathode was applied onto two different anode supports (with different composition and geometry) to study the repeatability and reliability of the experiment. According to the results, both cells were stable for 91 h and 260 h of a stability test at 650 °C and 0.7 V. An initial improvement in performance of the cells was detected and attributed to PNO's partial phase transformation into the $\text{Pr}_4\text{Ni}_3\text{O}_{10}$ phase with higher electronic conductivity and thermal stability. According to this study, PNO can be considered a promising cathode for SOFC applications.

In chapter 6, the performance and stability of a tubular cell with similar composition to cell B (PNO-infiltrated cathode and microtubular support) in chapter 5 is studied in SOEC mode. The

challenges as well as possible future directions to overcome the challenges faced are addressed at the end.

In chapter 7, the result of fabrication and testing a planar SOFC with a Ni-YSZ fuel electrode and infiltrated PNO cathode is described. According to the results, a planar cell with optimized microstructure was stable for 70 h of a stability test at 800 °C without any degradation.

Chapter 8 summarizes the major findings of this research. Moreover, it addresses future directions of this research.

1.3 Tubular cell

1.3.1 Solid oxide fuel cell and electrolysis setup

Figure 1-1 shows a schematic of the setup used for testing the cells in either SOFC or SOEC modes. Hydrogen gas enters the water and is saturated with 3 vol.% steam. Nitrogen is added during the initial reduction process of the Ni-YSZ electrode. Flow rates of the gases are precisely controlled by Alicat digital flowmeters. A custom-made water impinger (erlenmeyer flask with modified cap) is placed on top of an electric heater to increase the water temperature and increase the steam content in the fuel for electrolysis purpose. Fuel is fed to the cell through a thin stainless steel tube (about 1 mm inner diameter). The tip of the stainless steel tube enters the internal volume of the cell. Unreacted hydrogen exits the cell and enter the main alumina chamber and the fuel outlet tube through a hole provided at the cap of the alumina tube. A heating tape is wrapped around the fuel inlet line (stainless steel) to avoid water vapor condensation in electrolysis mode. The fuel outlet is fed into another water container. Bubbling of the water inside the outlet water container implies good sealing by the Ceramabond as well as no major gas leakage through the electrolyte. It was generally safe to proceed to the reduction process when the fuel outlet was bubbling inside the

casting process. Typical cell dimension was about 5.8 mm top diameter, 4.6 mm bottom diameter and 50 mm length. Fuel is fed inside the anode chamber through a stainless steel tube. A copper mesh is wrapped into a tubular shape and pushed inside the anode support as the current collector. A small alumina tube is inserted in between the copper mesh and the fuel inlet as a constraint to prevent the wrapped copper mesh from expanding into itself and loosening contact with the anode support during operation of the cell. A thin electrolyte layer is coated onto the surface of the anode support and sealed the outer surface of the cell and prevented mixing of fuel and air gases. About 1 cm length of the Ni-YSZ anode support at the beginning of the inlet was not coated by the electrolyte so it could be used for a second anode current corrector. A silver paste (Fuel Cell Materials) is coated onto the uncoated section and silver wires were firmly wrapped and twisted around it. Fuel electrode Ag wires were connected to the copper mesh for efficient current collection of the fuel electrode. The cathode was coated onto the electrolyte with 1.5-2 cm² active area. Silver paste is coated onto the cathode and dried on top of a hot plate. A silver mesh is cut and placed onto the silver paste and silver wires are firmly wrapped and twisted around it as the cathode current collector. The cell is sealed using Ceramabond 552 paste.

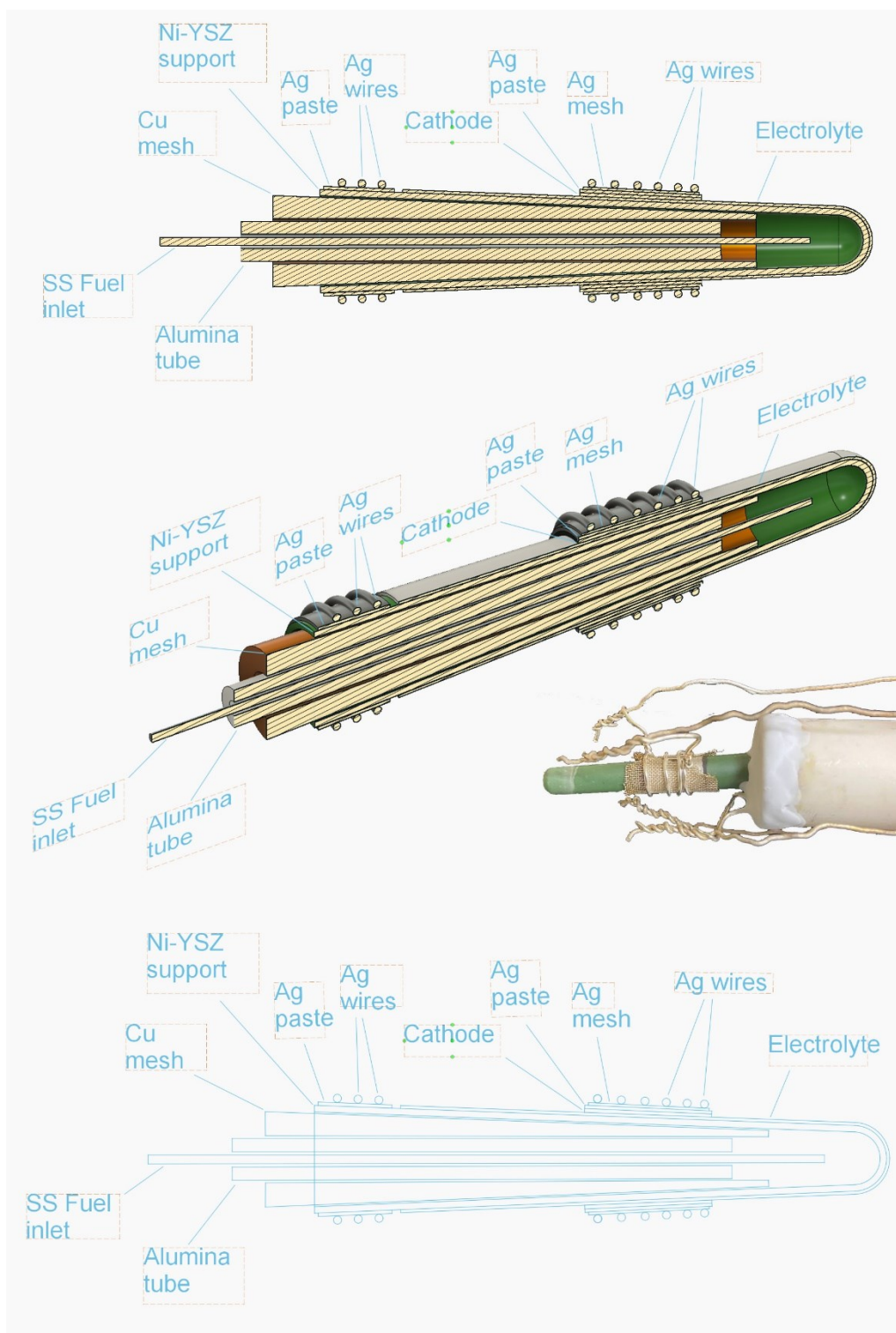


Figure 1-2 Schematic of the tubular cell fabricated for this research.

1.3.3 Experimental procedures for tubular cells

Fabrication method of the tubular cell components are described in detail in the experimental sections of chapters 3, 4 and 5. Even though, graphical demonstration of the important steps as well as additional experimental information of the method are included in the following sections.

1.3.3.1 Plaster mold fabrication

Anode supports are fabricated by the slip casting method. The steps for fabrication of the plaster mold are depicted in Figure 1-3. Water (133 g) is gently mixed with gypsum (200 g, dental grade) and vibrated using a vibrator (to remove entrapped air). The mixture is poured into a two-part mold (polyethylene tube) and a mandrel is inserted into the mixture. After 30 minutes, the mandrel is removed and the plaster mold is separated from the two-part mold. The plaster mold has to be fully dry before starting the slip casting process. By weighing the plaster mold after 1-2 days, one can ensure water is evaporated from the mold.

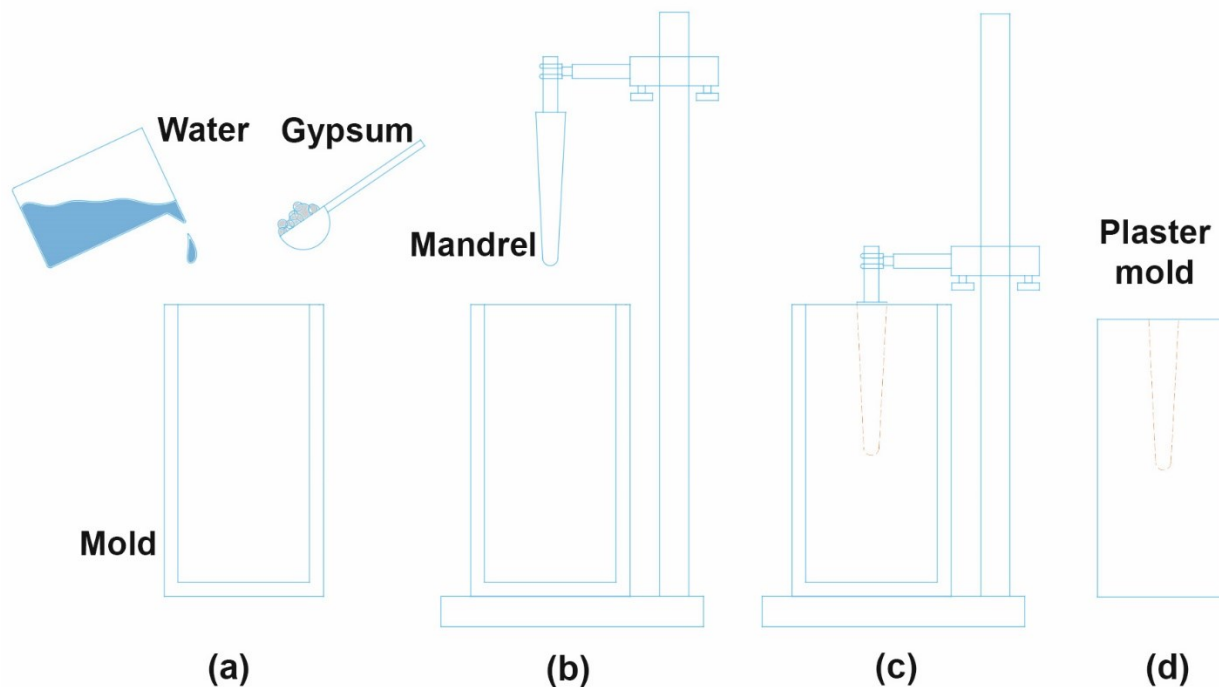


Figure 1-3 Schematic of plaster mold fabrication (a) addition of water and gypsum to the two-part mold. (b) and (c) insertion of mandrel into the mold. (d) removing the mandrel and two-part mold after 30 minutes.

1.3.3.2 Slip casting process

Slip casting is used for fabrication of the tubular anode supports. Initially, NiO powder (Fuel Cell Materials, average particle size of 1 μm or J.T. Baker with average particle size of 250 nm) was milled using a ball mill at 70 rpm for 24 h. Milled NiO was mixed with YSZ (Tosoh TZ8Y, 8 mol% Y_2O_3) with proper ratio (65:35 or 90:10 NiO:YSZ weight ratio). Powders were added to water (1:1 weight ratio) and zirconia balls. The pH of the slip was set to 4 using hydrochloric acid to gain a stable slip. The mixture was milled for 2 h using a ball mill at 70 rpm. Next, graphite (30-40 vol.% with 4.5 μm average particle size) was added to the suspension and milled

again for another 15 minutes. The slip was sonicated using an ultrasound bath for three minutes and cast into plaster molds.

The slip casting process is depicted in Figure 1-4. Initially, the Ni-YSZ suspension is poured into the plaster mold (Figure 1-4a). Then it was dwelled for a period of time for the particles to attach to the plaster mold due to suction as a result of capillary force through the plaster mold. Dwelling time can be adjusted from 45 seconds to 3 minutes to achieve different thicknesses. Then, the excess suspension is poured out and the coated film is let dry. The drying process (1-5 h, depending on the humidity) at room temperature results in shrinkage of the film and separation from the plaster mold (Figure 1-4c). A humidifier was used to adjust the humidity inside the lab. The shape of the tube is tapered to facilitate their removal from the plaster mold. Raw Ni-YSZ

supports were dried at room temperature and pre-sintered at 850-1100 °C for 3 h.

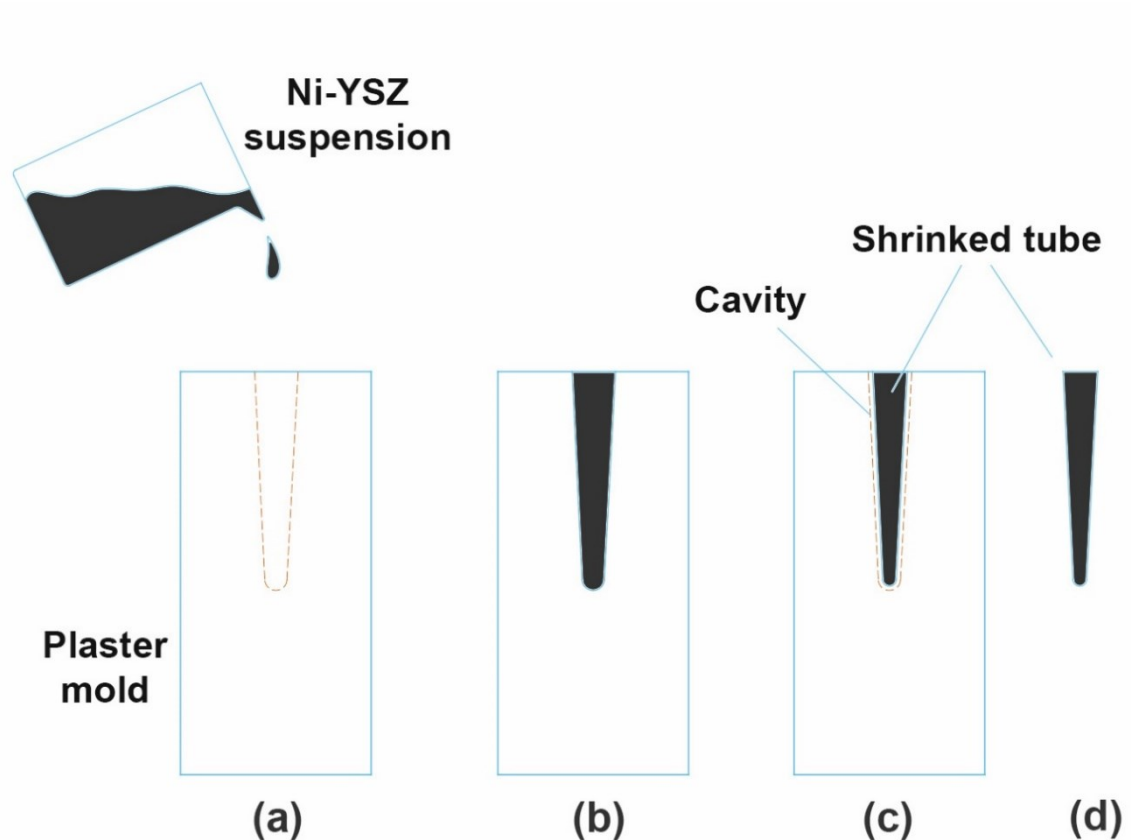


Figure 1-4 Slip cast process for fabrication of the anode supports. (a) filling the plaster mold cavity with the Ni-YSZ suspension (b) removing the excess suspension (c) shrinkage of the slip cast tube and separation from the plaster mold (d) removing the tube support from the plaster mold.

1.3.3.3 Dip coat process

Dip coating is used for deposition of very thin layers such as an anode functional layer (AFL) or electrolyte onto the support layer. AFL slurry was prepared by mixing NiO (J. T. Baker, average particle size of 250 nm):YSZ powders (65:35 weight ratio), ethanol (1:4 powder:ethanol weight ratio) and binder (6 wt% ethyl cellulose in terpineol (27 wt.% of solid powder)) using zirconia balls in a planetary mill for 2 h. The slurry was homogenized and de-gassed in an ultrasound bath for one minute before the dip coat.

For preparing the electrolyte suspension, YSZ and ethanol (1:7 weight ratio) and binder (6 wt% ethyl cellulose in terpineol) were milled using zirconia balls in a planetary mill at 300 rpm for 1 h. Afterward, the suspension was sonicated for three minutes using an ultrasound bath. The suspension was transferred to a vial and the tubular support was dipped (with the speed of $1.1 \text{ cm}\cdot\text{s}^{-1}$) into the suspension, dwelled for 11 seconds and removed from the suspension. This process might be repeated one to three times depending on the desired thickness of the layer. At least five minutes are used for drying the layers between dip coats. Moreover, sonication was repeated before any subsequent dip coats. Finally, the tubes were pre-sintered at 850-1100 °C for 3 h in case of the AFL coating and fully sintered at 1400 °C for 3 h in case of the electrolyte coating.

1.3.3.4 Fabrication of the thin scaffold layer

Cathode fabrication was composed of two steps: (i) coating a porous scaffold with sufficient ionic conductivity and open porosity and (ii) infiltration of active cathode catalysts with high catalytic activity for the oxygen reduction reaction (ORR).

The scaffold layer must be porous enough for easy infiltration of the catalyst as well as making good contact with the electrolyte. In the case of the YSZ scaffold, initially YSZ powder (8-YSZ, Tosoh) was calcined at 1500 °C for 3 h and then milled using a ball mill for 48 h. Dip coat suspension was prepared by mixing calcined and milled YSZ powder (12.2 g) with ethanol (7 g), dispersant (Menhaden fish oil in azeotropic solvent, 4.88 g) and binder (6 wt% ethyl cellulose in terpineol, 9 g). In the case of GDC (gadolinium-doped ceria $\text{Ce}_{0.9}\text{Gd}_{0.1}\text{O}_{1.95}$) as the scaffold, it was not calcined and milled; instead 30 vol.% PMMA (poly methyl methacrylate, 1.5 μm average particle size) microbeads were added to the suspension. The dip coating process of the scaffold is depicted in Figure 1-5. Active area of the cathode surface is measured (1.5-2 cm^2) and marked on the cell. The rest of the cell area is masked using Teflon tape and dipped into the suspension and

dwelled for 11 seconds. Then, the cell is removed from the suspension and masking tape is peeled off. Finally, the cell is heat treated at 1200-1300 °C for 3 h with two stops at 100 and 250 °C for full drying and binder removal process, respectively.

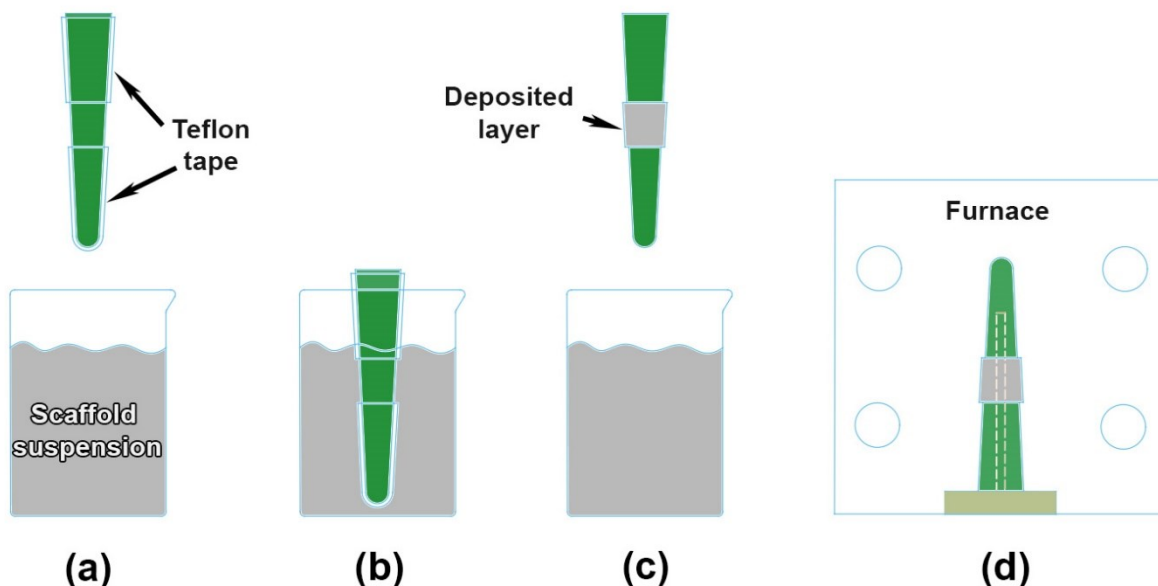


Figure 1-5 Dip coat process of the thin porous scaffold layer. (a) dipping the masked tube into the suspension (b) dwelling for 11 seconds (c) removing the tube from the suspension and peeling off the mask (d) heat treatment inside the furnace at 1200-1300 °C.

1.3.3.5 Infiltration process

Infiltration method was used to deposit cathode catalyst nanoparticles into the ionic conductor scaffold (YSZ or GDC) of the cathode. PNO (praseodymium nickelate, $\text{Pr}_2\text{NiO}_{4+\delta}$) and NNO (neodymium nickelate, $\text{Nd}_2\text{NiO}_{4+\delta}$) cathode catalysts with Ruddlesden-Popper structures were two choices of the cathodes in this study due to their high mixed ionic and electronic conduction. To prepare the infiltration suspension, nitrate constituents of Pr, Nd and Ni with stoichiometric ratios of the cathode composition were mixed with water (7 molar) and surfactant (Triton-X100, Union Carbide Chemicals and Plastics Co. Inc.) on a magnetic stirrer. Then the solution was infiltrated

into the scaffold. Infiltration process is depicted in Figure 1-6. Initially, masking tape was used to mask the cell except the scaffold area. The cell was dipped into the infiltration suspension and placed inside a vacuum chamber for five minutes. Vacuum process removes the entrapped air inside the scaffold and ensures a proper infiltration. Afterwards, the cell was removed from the vacuum and masking tape is peeled off (Figure 1-6b). Next, infiltrated nitrate decomposition took place at 350 °C for 15 minutes inside the furnace. The cell was removed and excess infiltrate was removed using a tissue. This process was repeated 2-3 times until the infiltrate solid loading reached to ~ 30 wt% of the scaffold. Final heat treatment was done at 600-1000 °C for single phase formation of the cathode catalyst.

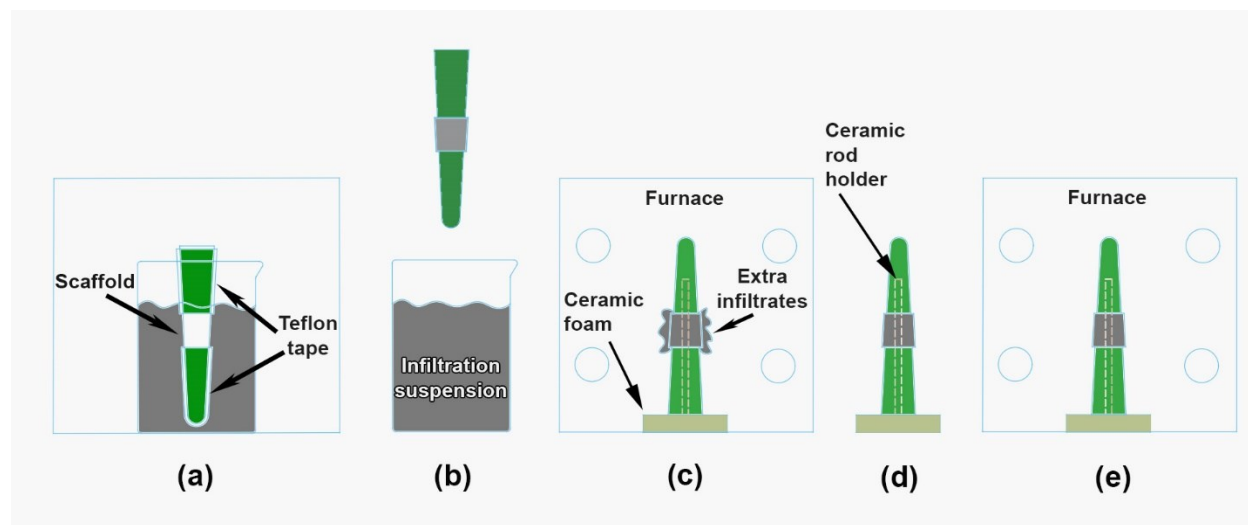


Figure 1-6 Schematic of the cathode infiltration process. (a) dipping the masked cell inside the precursors suspension and leaving under high vacuum (b) removing the cell from the suspension and removing the masking tape (c) initial nitrate decomposition at 350-450 °C in furnace (d) cleaning the excess decomposed infiltrates (e) final heat treatment of the cathode at 600-1000 °C.

1.4 Reduction process

Following assembling the cell into the testing setup, cell must be reduced by hydrogen gas for NiO to Ni transformation and increasing the electrical conductivity of the support. This process is accompanied by a volume shrinkage which affects the mechanical properties of the cell. In this study, the cells are reduced with 5-7 SCCM of hydrogen and 45-43 SCCM of nitrogen overnight. The temperature of the furnace is increased to 650-750 °C with a ramp of 2 °C·min⁻¹ and dwells at 90 and 260 °C for 1 h to cure the sealing cement. After reaching to the desired temperature and dwelling for at least 10 hours, the ratio of H₂ to N₂ is gradually changed to 50 SCCM of H₂ and 0 SCCM of N₂.

1.5 Electrochemical testing and characterization methods

Electrochemical impedance spectroscopy (EIS), IV and OCV measurements were performed mainly using a two-channel Metrohm Autolab potentiostat with 10A booster and FRA32M module for impedance measurements in four probe configurations. EIS measurement was performed with 20 mv voltage perturbation at OCV with varying frequency between 1 MHz - 0.1 Hz. IV measurement was performed by changing voltage with 3 mv·s⁻¹ and recording the current. One channel was allocated to short-term tests and the second channel was used when potentiostatic measurement was of interest. A Solartron 1255 frequency response analyzer in combination with a Solartron 1287 electrochemical interface was also available in case the Autolab device was in use. Microstructural analysis was carried out using a Zeiss Sigma 300 VP-FESEM scanning electron microscope. For image analysis purposes, low-KV SEM imaging with 0.6-1 KV accelerating voltage was used. Transmission electron microscopy (TEM) was used for estimation of the initial particle size and morphology using a Philips Morgagni 268 TEM at 80 kV (Philips,

Eindhoven, The Netherlands). X-ray diffraction (XRD) analysis was carried out using a Rigaku diffractometer RU-200B equipped with a rotating Cu anode (40 kV, 110 mA) and a graphite monochromator. Archimedes method was used to estimate the open porosity of the anode supports. Image J software was used to analyze the SEM images of the polished sample. Matlab optimization toolbox with a combination of DRT tools was used to extract distribution of relaxation time (DRT) data from EIS graphs based on Tikhonov regularization with continuous function discretization. Table 1-1 shows the precision of the different experimental parameters.

Table 1-1. Precision of different experimental parameters.

<i>Parameter</i>	<i>Tolerance</i>
<i>Temperature (°C)</i>	± 0.5
<i>I (A)</i>	± 0.001
<i>V (V)</i>	±0.001
<i>Resistance (Ω)</i>	± 0.01
<i>Cathode thickness (μm)</i>	± 1
<i>Electrolyte thickness (μm)</i>	± 0.5
<i>Anode functional layer thickness (μm)</i>	± 2
<i>Anode support thickness (μm)</i>	± 5
<i>Weighing scale (gr)</i>	± 0.0001
<i>Flow rates (SCCM)</i>	± 0.1
<i>Porosity (%)</i>	± 1

Figure 1-7 shows the relationship between different variables in measured electrochemical parameters.

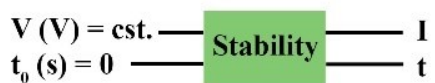


Figure 1-7 The relationship between different variables in measured electrochemical parameters.

Chapter 2: Microstructure and Long-term Stability of Ni-YSZ Anode Supported Fuel Cells: A Review

Sajad Vafaeenezhad¹, Amir Reza Hanifi¹, Miguel A. Laguna-Bercero^{2*}, Thomas H. Etsell¹ and Partha Sarkar¹

¹Department of Chemical & Materials Engineering, University of Alberta, Edmonton, Alberta T6G 1H9, Canada

²Instituto de Ciencia de Materiales de Aragón (ICMA), CSIC- Universidad de Zaragoza, C/ Pedro Cerbuna 12, E-50009, Zaragoza, Spain

Abstract

Nickel-yttria stabilized zirconia (Ni-YSZ) cermet is the most commonly used anode in solid oxide fuel cells (SOFCs). The current article provides an insight into parameters which affect cell performance and stability by reviewing and discussing the related publications in this field. Understanding the parameters which affect the microstructure of Ni-YSZ such as grain size and ratio of Ni to YSZ, volume fraction of porosity, pore size and its distribution, tortuosity factor, characteristic pathway diameter and density of triple phase boundaries (TPBs) is the key to design a fuel cell which shows high electrochemical performance. Lack of stability has been the main barrier to commercialization of SOFC technology. Parameters influencing the degradation of Ni-YSZ supported SOFCs such as Ni migration inside the anode during prolonged operation are discussed. The longest Ni-supported SOFC tests reported so far are examined and the crucial role of chromium poisoning due to interconnects (ICs), stack design and operating conditions in degradation of SOFCs is highlighted. The importance of calcination and milling of YSZ on development of porous structures suitable for Ni infiltration is explained and several methods to

improve the electrochemical performance and stability of Ni-YSZ anode supported SOFCs are suggested.

2.1 Introduction

Global energy demand is annually increasing by 1.2% until 2035 due to an increase of the world population [1]. Development of green sources of energy with high electrical efficiency is critical to reduce the share of fossil fuels on earth. SOFCs have attracted attention from the energy sector as a reliable and clean yet long term source of energy [2]. SOFCs are electrochemical devices that convert the chemical energy of a fuel such as hydrogen or hydrocarbons such as CH₄ directly into electricity [3] with efficiencies up to 60% [1,2] which is twice that of internal combustion engines [4]. Fuel cells are categorized based on the type of the electrolyte and the operation temperature.

SOFCs contain dense ionic conductors such as yttria stabilized zirconia (YSZ) which operate at medium to high temperatures with the electrolyte conducting oxygen ions. During their operation SOFCs produce high grade heat due to the occurrence of exothermic entropy reactions whereby the released heat can be used in combined heat and power (CHP) systems, increasing the overall efficiency to more than 70% [4].

Operating at higher temperatures has the advantage of higher catalytic activity (allow using non-precious material as catalysts) to reform the common abundant hydrocarbon fuels such as methane and generate electricity in a stable and silent condition [4]. The low emissions byproducts can be stored, managed and reused properly to minimize environmental impacts. Fuel cells running with hydrocarbon fuel are more suitable for commercialization compared with cells running under hydrogen due to lower price of the fuel as well as availability and easier storage of hydrocarbons [5]. Cost (fabrication and balance of plant) and long-term stability are the main challenges of

SOFCs for commercialization purposes. Although most of the cost is related to balance of plant (~75%), cell specific properties such as the operation temperature determine the plant design and its cost [6]. Operating at high temperatures limits the choice of electrode materials as well [7]. Lowering the operation temperature is a critical goal which can lead to reduction of degradation rates by decreasing Ni agglomeration and Cr volatilization from stainless steel or Cr alloy interconnects [6,7].

Efforts have been made to reduce the operation temperature of SOFCs [1]. There are advantages in operating at lower temperatures such as increasing the stability, reducing the price by using lower-cost components, reducing the start-up and shutdown duration [4,8,9], reducing the thermal insulation requirements or heat exchanger size, and improving the cell tolerance for thermal cycling [6]. It also expands the application of SOFCs to portable applications. However, most of the SOFC applications are still focused on stationary applications [6].

Actual SOFC applications require stacking of single cells into a high output unit using interconnects and sealing materials. The degradation mechanisms of the Ni-YSZ supported SOFC stack components are thoroughly described in the long-term section of the paper. In the following sections of the review, parameters which affect the microstructure of the Ni-YSZ anode and, therefore, cell performance, different degradation mechanisms of Ni-YSZ supported cells, and possible solutions to improve the electrochemical performance and reduce the degradation rate are discussed. Recent long-term SOFC stack results using mainly Ni-YSZ supports and YSZ electrolytes are described. Reviewing the stability results revealed that parameters such as stack design variables, interconnect preparation conditions and sealing materials which significantly affect the long-term stability of Ni-YSZ supported cells have been underestimated. This review will focus on hydrogen as a fuel for the anode. However, many of the degradation causes and

remedies discussed in this paper are also applicable and important when considering alternative SOFC fuels such as hydrocarbons. It is worth mentioning while numerical analysis is considered a greatly useful tool for understanding the degradation rate of SOFCs, the focus of the current review is on experimental results and discussions in the literature.

2.2 SOFC components and reaction mechanisms inside the anode

SOFCs are composed of three main parts: porous anode, dense electrolyte and porous cathode layer. The focus of this review paper is on SOFCs which use oxygen-ion conducting electrolytes such as YSZ and Ni-YSZ cermet as the anode layer. SOFCs are manufactured in two main designs: planar and tubular. Planar cells reach higher power densities while tubular cells have less sealing complications and are more resistant to thermal stresses [10]. There are also designs with a combination of planar and tubular cells capitalizing on the benefits of both. Considerable research and development has confirmed that Ni-YSZ is the most promising anode in terms of stability and from the commercialization point of view. In addition, the catalytic activity of nickel metal at high temperature is adequate without the need to use precious metals such as platinum. The anode is composed of a ceramic-metal (cermet) matrix of nickel and YSZ. Doping the zirconium lattice with larger ions of yttrium stabilizes the cubic polymorph of zirconia at room temperature up to elevated temperatures and increases the ionic conductivity. A composition providing mixed electronic and ionic conduction is required in fuel cell electrodes. High operation temperature (above 700°C) can change the grain size and shape, cause reaction between cathode and electrolyte, or lead to poisoning and crack formation in the cell [11,12]. Ni grain growth is known to be a major degradation issue in the Ni-YSZ anode which can affect the electrical conductivity or loss of TPBs [12–15]. In the case of Ni-YSZ, Ni and YSZ provide the electronic and ionic conductivity, respectively, and YSZ inhibits the growth of Ni at high temperatures [16]. In addition, thermal

expansion mismatch at the electrode/electrolyte interface will be reduced compared to pure nickel metal as the electrode [1]. Using a Ni-YSZ cermet, the reaction zone is extended 10-20 microns away from the electrolyte into the active anode thickness which is referred to anode functional layer (AFL) [1,17].

In an oxygen ion conducting SOFC (Figure 2-1a), hydrogen fuel is oxidized inside the porous Ni-YSZ anode and oxygen in air is reduced at the cathode side. The oxidation, reduction and the overall reactions are shown in eq. (1), (2) and (3) [18]. Steam and heat are produced by eq. (3). Water produced at the anode side should be removed for the reaction to continue. Correct design parameters such as proper gas flow channels for uniform distribution of fuel and preheating the fuel/air improve the performance of the cells.



In the case of a proton conducting electrolyte SOFC (Figure 2-1b), hydrogen fuel is oxidized at the anode side (eq. (4)) with protons and electrons generated as a result. The electrons move through the external circuit while protons pass through the electrolyte and are reduced at the cathode side to produce water (eq. (5)). The chemical potential gradient is the driving force for this process [18]. Comparing eq. (1) and eq. (4), one can notice that water is not generated inside the anode in a proton conducting SOFC which is considered an advantage due to easier removal of water from the thin cathode in anode supported SOFCs.



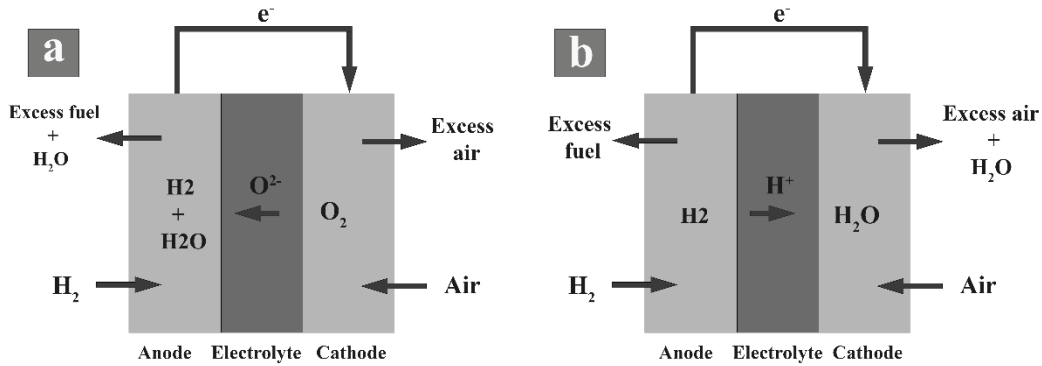


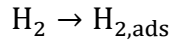
Figure 2-1. Schematic of (a) an oxygen ion conducting and (b) proton conducting SOFC.

Scanning electron microscopy (SEM) images of Ni-YSZ cermet at normal accelerated voltage (10-20 kV) collected using a backscattered electron (BSE) detector often have poor contrast due to similar backscatter coefficients of Ni and YSZ, making Ni and YSZ grains hard to differentiate. Thyden et al. [19] noticed that using secondary electron detector in a field emission SEM device at a low voltage, enables clear distinction between the two phases. Figure 2-2a shows a low voltage SEM image with Ni and YSZ phases.

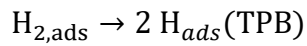
The anodic reaction (eq. (1)) takes place in electrochemically active regions called TPBs which are present within 10-20 μm from the electrolyte/anode interface known as the AFL. A schematic of a TPB is illustrated in Figure 2-2b. TPB is the line where three phases (oxygen ion conducting (i.e., YSZ), electronic conductor (i.e., Ni) and gas diffusive pores) share the same interface. The rate of an electrochemical reaction depends on the composition and morphology of the three phases inside the AFL. An ideal microstructure consists of a high density, active TPB network with enough porosity for gas diffusion.

The reaction mechanism at TPBs on the anode side (eq. (1)) takes place as below [1,6,20–22]:

1. Dissociation and adsorption of H₂ on Ni or electrolyte surface



2. H_{2,ads} diffusion to the TPB



3. Electrochemical reaction at the TPB

The oxygen ions from the electrolyte react with the adsorbed hydrogen at the TPB to form oxygen vacancy (V_O^{••}) and lattice oxygen at the electrolyte (O_O^x).

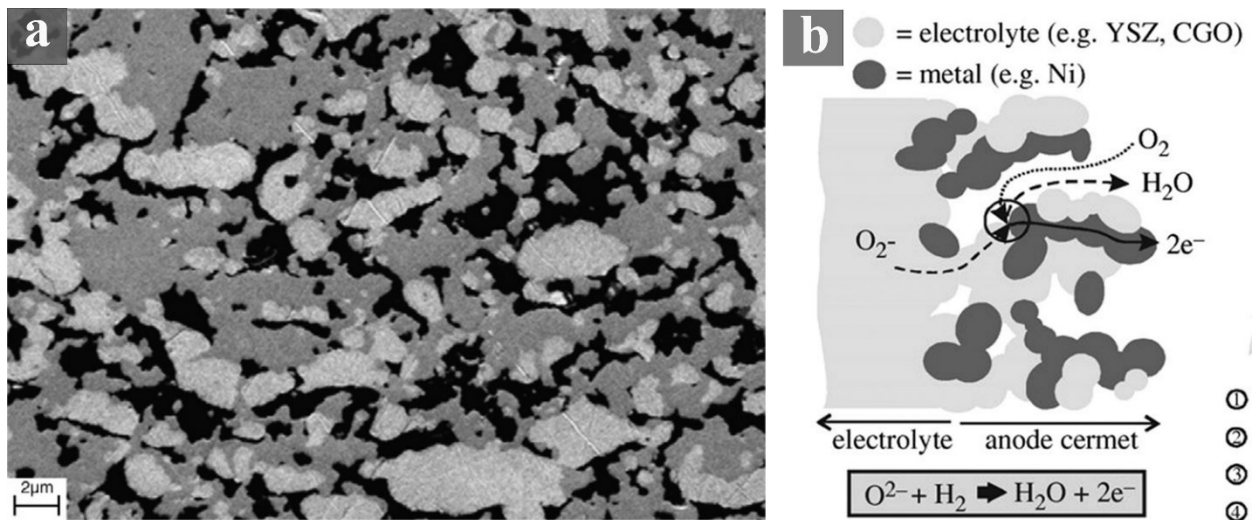
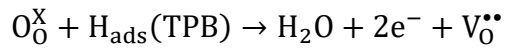


Figure 2-2. (a) SEM image taken by a low acceleration voltage (1kV) secondary electron detector. Bright, grey and dark colors are Ni, YSZ and epoxy, respectively [19]. (b) schematic of TPB region inside a typical Ni-YSZ anode functional layer [23].

Hereafter, in this paper, particle refers to raw NiO/Ni and YSZ powders used to fabricate Ni-YSZ cermets or nano-size infiltrated materials inside the electrodes. However, “grains” refer to NiO/Ni and YSZ grains in the sintered or/and reduced microstructure.

2.3 Microstructural features which impact the electrochemical performance of Ni-YSZ anodes

Electrical and ionic conductivities of the Ni-YSZ cermet and its mechanical and electrochemical properties depend highly on its microstructure which itself is a function of composition and particle size, sintering temperature, reduction temperature, fuel humidity, porosity and the tortuosity factor [22]. Electrode degradation in SOFCs is a result of an increase of resistance in the electrode due to loss of connectivity between percolating grains such as Ni, or reactions between different phases which leads to the formation of non-conducting phases which obstruct the electrical or ionic path or reduce the TPB length [3]. The Ni-YSZ electrode can appear in small thicknesses (20-30 μm) in electrolyte supported cells or as a support plus AFL at larger thicknesses (500-1000 μm) in anode supported cells. It should be noted that since the electrochemical reaction in the Ni-YSZ cermet occurs only inside the AFL, the Ni-YSZ support which provides the mechanical integrity for the cell needs to show mainly a high electrical conductivity for transport of electrons as well as a high porosity and low tortuosity for easier gas diffusion. Ionic conductivity in the anode support is not a necessary parameter as ions are not transported inside the support. Metal supported fuel cells do not have any ionic conductors in their metal support and show excellent performance. However, addition of small amounts of YSZ to a predominantly Ni support can suppress Ni coarsening and reduces crack formation during anode reduction [24]. On the contrary, the AFL needs to show high electronic and ionic conductivity as well as TPB density to promote electrochemical reactions [23].

In a fuel cell, there are different resistance components which lead to the loss of voltage at any operating current density which are: ohmic polarization due to the ohmic resistances of the electrolyte, electrodes and interfaces between the electrodes and electrolyte, and contact resistance

between the cell and current collector mesh/interconnect; concentration polarization at the electrodes due to the transport of gaseous fuel and air and reaction products through the anode and cathode; and activation polarization which is related to the oxygen reduction reaction at the cathode side and hydrogen oxidation at the anode side [25]. In this regard, Ni-YSZ microstructure directly impacts different cell resistance components and as such the performance which are explained in this section.

2.3.1 Size and ratio of Ni to YSZ

2.3.1.1 Size of Ni and YSZ

Electrochemical performance of the Ni-YSZ anode largely depends on the total length of active TPBs which increases when fine Ni and YSZ grains form the microstructure of the electrode, particularly in the functional layer where most of the electrochemical reactions occur [26–28]. It has been previously shown that finer Ni provides a lower resistance in the electrode and that the synthesis method of Ni highly affects its later performance. In a study, Yu et al. found that in Ni-YSZ cermet, fine NiO or YSZ particles improved the electrical and mechanical properties. When a coarse NiO was mixed with a fine YSZ the cermet electrical conductivity was low but its mechanical strength was suitable. However, when coarse YSZ and fine NiO were used in the cermet the reverse happened [29]. Hanifi et al. found that controlling the particle size of NiO and YSZ is crucial for developing ideal microstructures for fuel cell and electrolysis modes which can be quite different. They showed that providing sufficient porosity with large pore size is critical for an anode support used in electrolysis applications due to the transfer of fuel and reaction products under high humidity [30].

2.3.1.2 Ratio of Ni to YSZ

In a Ni-YSZ cermet the content of Ni and YSZ can vary which provides different microstructures for the support and functional layer. Traditionally, 40-50 vol.% Ni is used in the functional layer and in the support for a Ni-YSZ electrode. The thickness and grain sizes of both YSZ and Ni as well as the Ni/YSZ ratio also play a crucial role on the mechanical strength of the cell [31]. Increasing the content of Ni or YSZ leads to an increase in electronic conductivity or ionic conductivity of the electrode, respectively. The Ni/YSZ ratio also impacts the TPB length and excess amount of either phase can decrease the TPB length and increase activation polarization [32–35]. Xi et al. developed different Ni-YSZ cermets with varying contents of Ni (30-70 vol.%) by a co-precipitation technique and found that the sample containing 40 vol.% Ni, provided the finest and most homogenous microstructure which resulted in an improved TPB length and the lowest activation polarization [36]. Wilson et al. found that 50 vol.% Ni in the Ni-YSZ cermet provided the highest TPB length and the lowest polarization resistance [34]. Although increasing the Ni content can boost the electrical conductivity, it simultaneously increases the porosity and enhances Ni coarsening which facilitates cell degradation [35]. For the anode support, the content of Ni can be up to 90 vol.% to provide a high electrical conductivity and low concentration polarization but at least 10 vol.% YSZ is required to control Ni coarsening [24].

Vivet et al. studied the Ni-YSZ cermet with varying Ni content using focused ion beam-scanning electron microscopy (FIB-SEM) to reconstruct the microstructure and a passive voltage contrast (PVC) technique to estimate the degree of percolation of the electrically conducting Ni phase and found that, after an initial reduction, the Ni-YSZ composition with 40:60 volume ratio provided high electrical conductivity and the largest active TPB length in the anode cermet [37]. They also observed a sudden increase of electrical conductivity between 16-26 vol.% of Ni due to the start

of Ni percolation in the microstructure. In Figure 2-3 samples A1 (35pore:50YSZ:15Ni vol.%) and A2 (36pore:48YSZ:16Ni vol.%) showed a non-percolating Ni network and did not have any active TPB while sample A3 (39pore:35YSZ:26Ni vol.%) showed a percolating Ni network and the majority of TPBs in this sample were active electrochemical sites (58%).

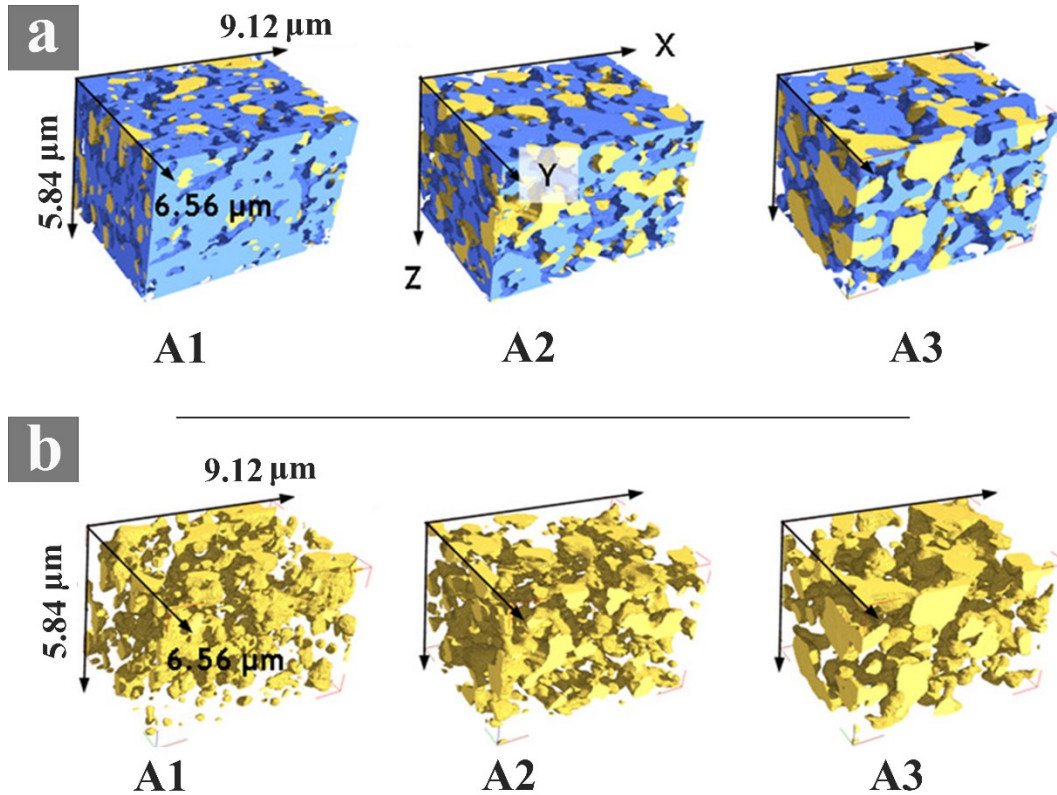


Figure 2-3. (a) Reconstructed 3D anode microstructures (Ni: yellow, 8YSZ: blue, pore: transparent), (b) the corresponding Ni phase of each sample illustrates that Ni grains are not percolated in samples A1 and A2 while they are almost totally percolated in sample A3 [37].

Percolation threshold is a factor of size of the starting NiO and YSZ and their size ratio, particle distribution and porosity content as well as the size and distribution of Ni and YSZ grains in the cermet [38]. Nam et al. [39] found out the optimized volume fraction of electronic to ionic phase in a random packing system of binary particles to be 0.45. In addition, they found reducing the

grain size of Ni and YSZ doesn't affect the activation loss at low current densities but greatly increases the performance at higher current densities. Pratihari et al. reported that the synthesis method of Ni has an important effect on the electrical conductivity of the Ni-YSZ anode as it affects the microstructure of the cermet. They found that the percolation thresholds for Ni-YSZ cermet for which Ni was prepared by solid-state and liquid-dispersion techniques were around 30 vol.% Ni while for electroless coating technique it was about 10-20 vol.%. Electroless coated samples showed the highest electrical conductivity due to a continuous coating of Ni on the YSZ grains [40]. In another study, Clemmer et al. developed Ni-YSZ composite microstructures by tape casting and co-sintering using different sources of nickel powder and pore-former, such as metallic Ni, NiO, graphite and Ni-coated graphite. By performing microstructural analysis and conductivity measurements, they found that Ni-coated graphite provided the lowest percolation threshold for Ni and the anode containing a large amount of graphite showed the highest percolation threshold [41]. The initial percolation threshold should be evaluated after a prolonged operation time to assess the effectiveness of the initial microstructure. However, this important parameter was not reported in the aforementioned papers.

2.3.2 Microstructural porosity

Sufficient porosity content is crucial for the Ni-YSZ anode especially inside the support in order to ease gas diffusion and removal of the reaction products. Numerical modeling using random packing system of binary spherical particles showed that higher porosity in the anode and lower porosity inside the cathode effectively increase the performance of SOFCs [39]. Typically, no additional pore-former is utilized inside the AFL as the pores generated due to the reduction of NiO are sufficient for diffusion of gas inside the thin AFL layer while maintaining high TPB density. However, too high an amount of porosity is undesirable since it adversely affects the

density of TPBs inside the AFL as well as the mechanical properties of the support [40,42–44]. Ni-YSZ electrode porosity is also important for solid oxide electrolysis (SOEC) mode where porosities in the range of 50 vol.% are recommended [30,45]. Hanifi et al. reported that a Ni-YSZ anode support containing calcined YSZ had higher porosity (46% vs. 34% for Ni-uncalcined YSZ) and lower concentration polarization which led to significantly better performance under SOEC mode for such a cell. However, both cells had shown similar performance under SOFC mode since the activation polarization of the electrode containing uncalcined YSZ was lower (due to a finer pore structure inside the functional layer) [30].

Laguna-Bercero et al. [46] studied the effect of different types of pore-formers (PMMA, graphite or an equal mixture of both) in a Ni-YSZ support on the electrochemical performance of tubular cells under both SOFC and SOEC modes. The cells did not have a coating of AFL during fabrication. However, an active functional layer containing fine grains of Ni and YSZ and no pore-formers is formed intrinsically during the slip casting process (in the outer layer of the tube which is in contact with the plaster mold). In these cells, electrochemical reactions take place adjacent to the anode/electrolyte interface. They concluded that the Ni-YSZ support containing graphite leads to a more porous anode support (51%) and formation of coarser pores (due to lower shrinkage of the graphite containing support) in the vicinity of the electrolyte which leads to a decrease of the TPBs. However, the cell containing PMMA (anode support porosity of 41%) had finer pores next to the electrolyte and improved TPB length and showed the highest performance under both SOFC and SOEC operational modes (818 and -713 mA·cm⁻² were obtained in SOFC and SOEC modes at 800°C). The cell containing a mixture of pore-formers (final porosity of 45%) showed intermediate results. All the cells had similar concentration polarization values revealing that even

the least porous cell (containing PMMA with a final porosity of 41%) provided sufficient porosity for gas flow in SOFC mode.

2.3.3 Impact of the characteristic pathway diameter

In recent years the concept of “characteristic pathway diameter” has been introduced as an important microstructural characteristic feature which helps to get a better understanding of the quality of the pathways connecting different phases in the Ni-YSZ cermet [47–49]. This diameter is introduced as the diameter of the largest sphere that can be squeezed through the network of Ni, YSZ or pores. Figure 2-4 shows the percolating TPBs and their pathways of electrons in the Ni phase and the “characteristic pathway diameter” is pointed out by red arrows. These parameters reveal the quality of the pathway connections of the different phases, i.e., the width of the pathway for electrons in Ni, oxygen in YSZ and gas in pores. Researchers from the Technical University of Denmark who introduced this concept concluded that if the percolation of TPB sites is through a narrow diameter of about 20 nm, then impurities such as carbon deposition can break the network connectivity and negatively affect the electrode percolation in the electrode. However, if this pathway is large in the range of 200 nm or more, the microstructural contiguity is less impacted by impurities [49].

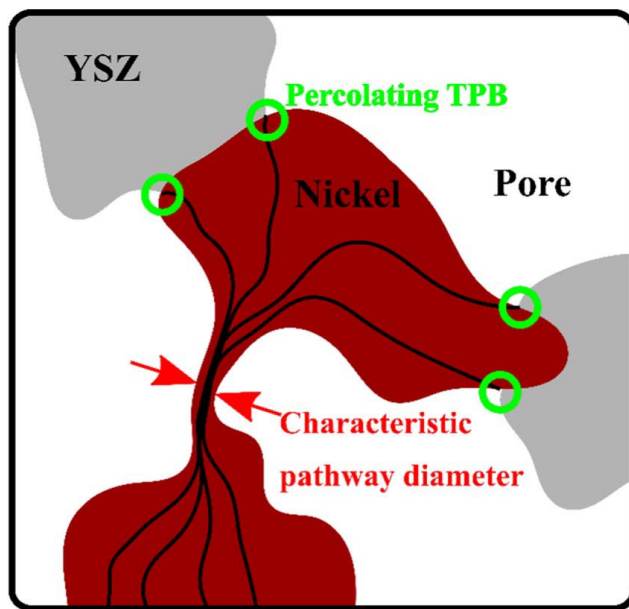


Figure 2-4. Schematic of the characteristic pathway diameter concept. (Red arrows highlight the characteristic pathway for the Ni phase, and percolating TPB between Ni (red), YSZ (gray) and pore (transparent) are circled in green) [49].

2.3.4 Tortuosity factor

Tortuosity factor is a crucial microstructural feature which impacts the cell electrochemical performance directly. This factor is different from tortuosity (the ratio of the average pore length to the thickness) of the porous cermet. Tortuosity factor has more significance than tortuosity as it is related to diffusivity or conductivity [50]. This factor is quantified using different methods such as random-walk simulation [51], or solving the Laplace equation with finite element method (FEM) [52] or lattice Boltzmann method (LBM) [53]. It decreases when the volume fraction of Ni, YSZ or pores increases in the microstructure [51]. Under the percolation threshold around 25 vol.%, the value of tortuosity factor increases drastically. In a study, it was shown that Ni coarsening might have positive impact on lowering the tortuosity factor for pores and facilitate gas diffusion in the support [54]. It is shown that for a suitable Ni-YSZ microstructure, Ni percolation from the anode surface to the anode/electrolyte interface is a crucial parameter since it determines the electrochemically active area of the cell [55]. Even though performance also depends on the

ionic conductivity as well as TPB density, Ni percolation has more pronounced effect on cell performance. When a suitable Ni percolation is guaranteed in the AFL and support microstructure, other microstructural features such as tortuosity factor for YSZ and pore can be optimized. TPB density can also increase by selecting proper ratios between Ni and YSZ as well as the particle size of starting materials, and sintering and reduction process conditions [55].

2.3.5 Reduction process

There are several works in the literature confirming that the reducing conditions of NiO-YSZ composites have a great effect on the final microstructure of the electrode. However, there is no general agreement on how these parameters affect the final sample properties. Possibly, there are several components competing in parallel (particle sizes, gas impurities, steam amounts, porosity and tortuosity, etc.) and then each sample could present different optimized reducing conditions. Supporting this trend, Pihlatie et al. [56] found that there are at least two overlapping processes contributing to the change of conductivity, depending on the initial particle size distribution of Ni and the cermet microstructure. Lee et al. [57] also studied different Ni-YSZ reducing conditions and found that the growth of Ni particles occurs by increasing the temperature and humidity, and thus decreasing the active TPB lengths. They also observed that increasing the temperature and humidity also increases the formation of cracks on the surface of the electrode. Similar effects were found for thin electrodes, as the anode polarization in electrolyte supported cells is also affected by the reducing conditions [58]. In addition to nickel species mobility, the reduction mechanism and kinetics play a role in the final morphology of the cermet. In this sense, Monzon et al. also observed that nickel mobility is significantly enhanced by the presence of steam [59]. They found that depending on the reduction conditions, pre-conditioning periods of up to several

days at the operation temperature are required in order to assure initial stabilization of the microstructure.

Jial et al. also studied the effect of the reduction procedure and temperature on the Ni-YSZ final microstructure in detail [60,61]. They showed that an anode reduced at 500°C showed poor performance and stability due to small interfacial area between Ni and YSZ, and formation of a highly porous nickel which facilitates Ni sintering at higher temperatures (Figure 2-5a-c). They found that the Ni-YSZ interface was destroyed after a temperature rise due to the existing gaps between Ni and YSZ (Figure 2-5b) which got worse following operation. Due to the presence of the pores in Ni in the sample that was reduced at 800°C, part of the Ni-YSZ interface was lost (Figure 2-5d and e) but more than half of the interface remained intact. A sample that was reduced at 1000°C had densified Ni and its attachment to YSZ was without any gap and there were no pores at the interface of Ni-YSZ following operation (Figure 2-5f-g). They concluded that the performance of the anode is not only a function of TPB length but also the interfacial bonding between nickel and YSZ in the AFL which can improve with an increase in reduction temperature leading to inhibition of nickel sintering and improving the anode stability during long-time operation. Pores can promote the sintering of Ni in high temperature operation. The small interfacial area between Ni and YSZ reveals weak interfacial bonding between Ni and YSZ which results from a low temperature reduction process. Ni sintering is enhanced by the presence of sub-micron closed pores inside Ni grains as well as weak Ni-YSZ interfacial bonding [61].

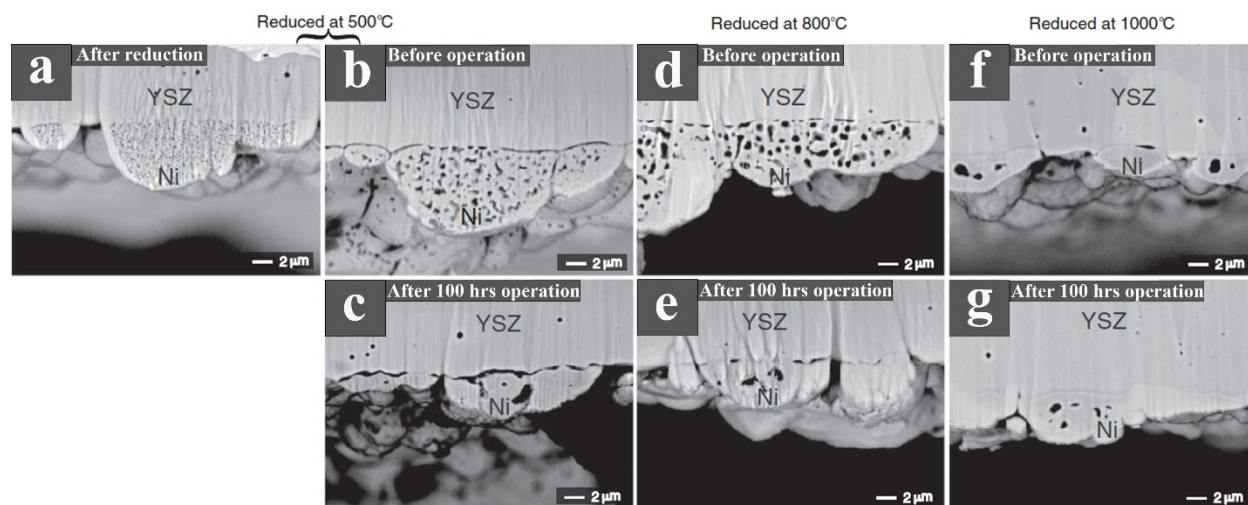


Figure 2-5. Cross-sections SEM images of (a)(b)(c) pure Ni anodes reduced at 500°C, (d)(e) 800°C and (f)(g) 1000°C, (a) right after reduction, (b)(d)(f) before operation and (c)(e)(g) after operation and kept at 800°C under humidified hydrogen for 100 h [61].

2.3.6 Interfacial designs

It is well established that the critical processes of fuel oxidation that define the performance of the cell occur at the surface [62]. As a consequence, for the particular case of Ni-YSZ cermets, Ni-YSZ interfaces will play a very important role in terms of reaction activity and stability. Although conventional Ni-YSZ anodes have been investigated in detail for many years, there is a lack of information regarding the atomic structure of the interfaces between nickel and YSZ [63]. Several years ago, Revcoleschi and Dhalenne [64] reported aligned metal-oxide composites by chemical reduction of directionally solidified (DSE) NiO – ZrO₂(stabilized by CaO) lamellar eutectics. They reported epitaxial relationships between the phases, forming the (111) Ni- (100) ZrO₂ interfacial plane. Similar eutectic compositions were later proposed as candidates for SOFC anodes by Merino et al. [65]. In addition to a lower polarization resistance in comparison with conventional Ni-YSZ cermets [66], they also present superior ageing stability, as the low-energy interfaces formed between the metallic Ni particles and the YSZ prevent particle coarsening [67]. In fact, further studies using transmission electron microscopy (TEM) and X-ray pole figure experiments

confirmed that during NiO reduction, nickel undergoes an interface-induced crystallographic reorientation to form a lower energy interface, and as a consequence more stable Ni is formed [68]. Transfer of oxygen takes place from NiO to the YSZ vacant sites, as also confirmed by in situ NiO reduction in the TEM [69]. These experimental results are also consistent with theoretical predictions for the stability of Ni/YSZ interfaces [70]. However, the study of conventional Ni-YSZ interfaces and their orientation relationships is much more complex than those mentioned for DSEs. For example, higher-index interfaces were observed, such as Ni (15 13 1)/ YSZ (4 4 10). It is supposed that various Ni/YSZ interfaces coexist in different energy states, and certainly the method of synthesis is crucial to define the grain orientation. These results confirm that preparation routes such as DSEs are essential to achieve high stability [71].

2.4 Development of novel Ni-YSZ anodes by infiltration of porous YSZ

2.4.1 Calcination and milling of YSZ

Infiltration of porous YSZ substrates with anode or cathode materials can provide electrodes with superior electrochemical performance compared with traditionally prepared electrodes. The authors developed different types of porous YSZ microstructures for infiltration by calcination of Tosoh YSZ (a commonly used YSZ powder for SOFC fabrication) at 1300-1500°C and milling the coarsened powder in an aqueous suspension for 72 h [72–76]. Calcination is an essential method for development of a porous substrate since as-received YSZ powder normally has fine particles (250 nm), a high surface area (12-13 m²·g⁻¹) and thus high sinterability. Even with incorporation of pore-formers inside the Ni-YSZ support, there are dense YSZ regions which increase the tortuosity for gas diffusion. The authors found that YSZ crystals and particles enlarge upon increasing the calcination temperature and following milling compared with the as-received powder. Thus, their ability to shrink is lowered during the sintering process. Calcination and

subsequent milling leads to the formation of particles with larger size (500-750 nm) and a lower surface area (3-5 m².g⁻¹). The particle size correlates with the calcination temperature (Figure 2-6) [75]. The reduced surface area of YSZ leads to generation of a porous structure following sintering at 1350-1400°C which contains interconnected pores (~20-25%) even without incorporation of any pore-formers. By controlling the particle size of the YSZ, a monolithic porous and dense layer through a multiple slip casting method was developed which significantly eases the electrode fabrication [75].

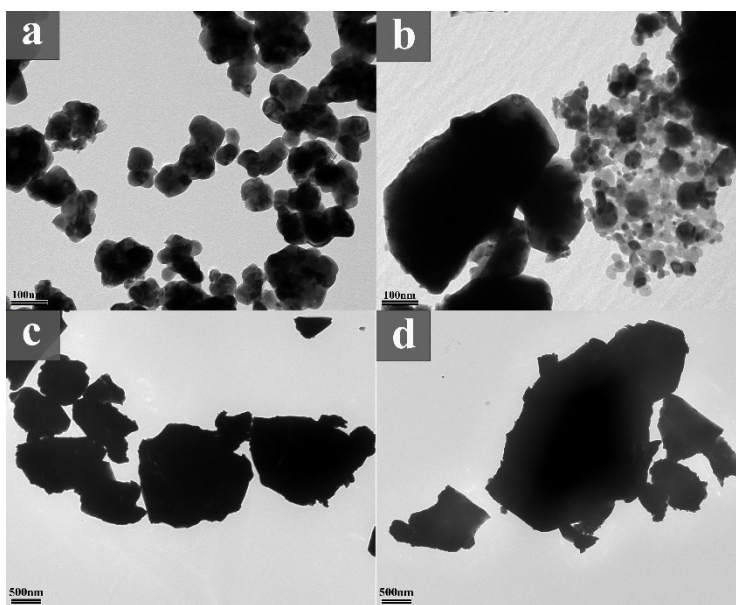


Figure 2-6. TEM images of YSZ powders after 72 h milling. (a) as-received Tosoh YSZ (b) calcined at 1300, milled for 72 h (c) calcined at 1400, milled for 72 h and (d) calcined at 1500, milled for 72 h [75].

It was also observed that calcination and subsequent milling shifted the isoelectric point (IEP) of a YSZ aqueous suspension towards lower pH values (Figure 2-7a) [72,76]. Following dispersion in water, yttrium and other positively charged ions precipitate on the powder surface and change the surface chemistry of the as-received YSZ. Calcination leads to a more stable YSZ structure that prevents yttrium leaching and explains the lower IEP observed for the calcined–milled

powders. Due to hydrogen bonding and formation of large agglomerates, the YSZ suspension shows a high viscosity and larger agglomerates at basic pHs which leads to a significantly porous structure. It was also concluded that while acidic YSZ slips are suitable for slip casting, the basic YSZ slips can be used for gel casting. Acid–base titration results also indicated a direct relationship between powder surface area and the amount of acid/base used for pH adjustment (Figure 2-7b) [72].

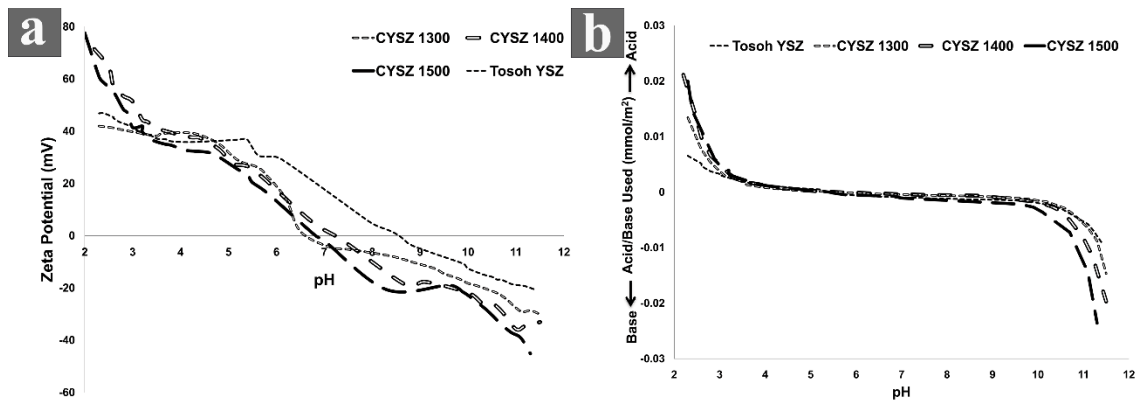


Figure 2-7. (a) YSZ zeta potential curve as a function of pH and (b) amount of acid or base per unit of YSZ surface consumed for pH adjustment [72].

2.4.2 Effect of pore-former on the microstructure of porous YSZ

In our research, different types of pore-formers such as graphite, starch, carbon black, polymethylmethacrylate (PMMA) and their mixtures were added to the Ni-YSZ electrode layer by a slip casting process in order to increase the pore content and ease the infiltration process. It was observed that when a high surface area YSZ is used in the slip, in order to generate sufficient amount of porosity (50 vol.%) for infiltration and gas diffusion, 60-70 vol.% pore-former (graphite or PMMA) is required. At low contents of pore-formers mainly closed pores are formed which are

not desirable for the electrode. However when calcined and milled YSZ powder is used for the slip, a low content of pore-former can create sufficient porosity (Figure 2-8) [75].

Recent trends to introduce porosity without using pore-formers, apart from the aforementioned calcination and milling process, are the phase inversion and the freeze casting methods. The uniqueness of these methods is that they produce uniformly aligned porosities. The phase inversion method is being widely used for microtubular SOFC fabrication in recent years [77,78]. The final asymmetrical microstructure presents finger-like pores in the inner part of the tube facilitating mass transport channels, while the sponge-like pores close to the electrolyte enlarge the TPBs. For example, a maximum power density of $0.75 \text{ W}\cdot\text{cm}^{-2}$ at 700°C was recently achieved for a Ni-YSZ/YSZ/LSM-YSZ cell [79]. As for the freeze casting method, it is also possible to radially align pore channels with a range of porosity by controlling the solid loading of the pastes [80]. For example, Chen et al. demonstrated a maximum power density of $1.28 \text{ W}\cdot\text{cm}^{-2}$ at 800°C [81]. They varied the porosity of tubular Ni-YSZ anode supports utilizing the freeze casting method in order to obtain a better understanding of the correlation between the porosity and concentration polarization losses in SOFCs. The porosity was controlled by varying the solids/water weight ratio when preparing anode slurries with all other processing variables kept constant. Additionally, the permeability and mechanical strength were characterized as a function of porosity. Efficient gas diffusion due to columnar pore formations inside the support reduced the concentration polarization and increased the performance of the cell as a result.

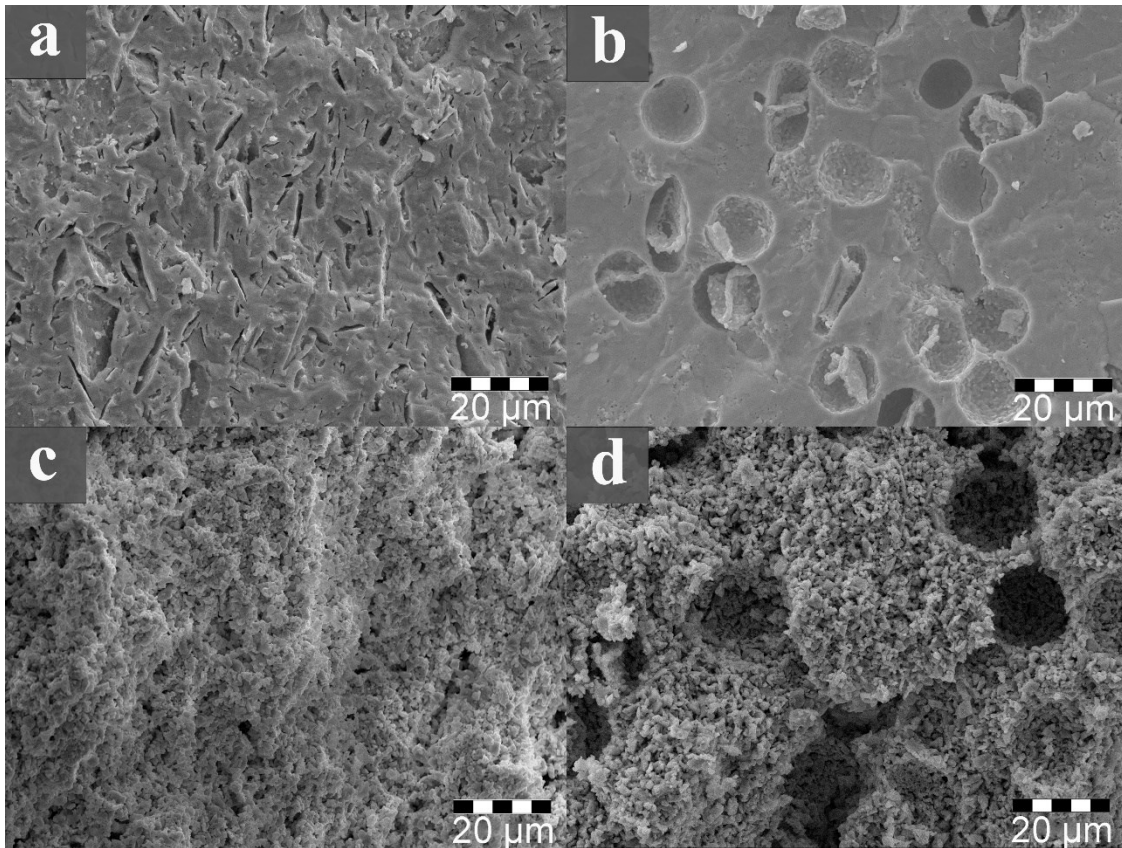


Figure 2-8. SEM images of the YSZ substrate sintered at 1350°C. (a) Tosoh YSZ + 20 vol.% graphite, (b) Tosoh YSZ + 20 vol.% PMMA, (c) calcined 1500°C-milled YSZ + 20 vol.% graphite and (d) calcined 1500°C-milled YSZ + 20 vol.% PMMA [75].

2.4.3 Infiltration of porous YSZ to form electrodes

Infiltration has been an important method for fabrication of high performing electrodes for fuel cells which provides unique microstructures in terms of the particle size and distribution. It not only improves the catalytic activity (through the presence of dispersed nano-particles), but also increases the ionic and electronic conductivity (through an interconnected network of nano-particles) which overall lead to an increase of TPB length and reduction of cell resistance. The nano-size particles form due to a lower heat treatment temperature used to decompose the nitrates of constituents (350-400°C) and form the final phases (600-700°C) compared with the conventional sintering process (1100-1400°C). Infiltration also prohibits any reaction of phases

with the electrolyte and formation of non-conducting phases due to the reduced temperature needed to form the desired phases. In addition, due to their enhanced electrochemical performance, infiltrated fuel cells can be operated at much lower temperatures, improving the long-term stability of the cell [82–84].

Infiltration has been widely used to fabricate novel electrode structures such as LSM [85,86], LSCF [87,88], LSBT [89,90] and Ruddlesden-Popper materials such as $\text{La}_{n+1}\text{Ni}_n\text{O}_{3n+1}$ ($n= 1, 2, 3$)-YSZ [91,92] or $\text{Nd}_2\text{NiO}_{4+\delta}$ [93,94]. These studies show that the infiltrated electrodes provided superior performance compared with the conventionally sintered electrodes. For instance, Hanifi et al. showed that SDC infiltration into a Ni-YSZ anode which forms a continuous network of nano-size SDC particles (Figure 2-9a), enhances the electrochemical reactions in both SOFC and even further in SOEC modes. Similarly, LSM infiltrated into a YSZ scaffold (Figure 2-9b) boosts the SOEC performance in comparison with standard LSM-YSZ composite electrodes [95]. Hanifi et al. had found that the morphology of the porous YSZ network significantly affects the surface area of the YSZ support, TPB length and, therefore, electrochemical performance of an infiltrated cell. Ni-YSZ supports fabricated using calcined/milled YSZ showed a uniform microstructure before and after infiltration with nano-size particles of LSM and led to a homogenous distribution of infiltrates and superior performance compared with the conventional LSM-YSZ cathodes [95,96].

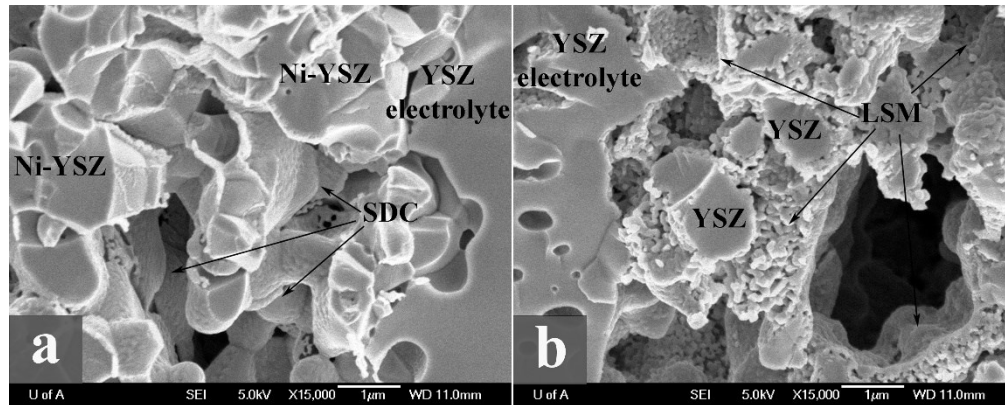


Figure 2-9. (a) Ni-YSZ coverage by SDC near the interface of the fuel electrode and electrolyte, (b) YSZ coverage by LSM near the interface of the cathode and electrolyte [95].

Infiltrated ceria-based materials improve the catalytic surface area for fuel oxidation in fuel cells [97,98]. For anode-supported cells, Cu infiltration has been investigated because it is a coke-tolerant electrical conductor and can be incorporated in large volumes [99,100]. As a replacement for conventional Ni-YSZ anodes, porous YSZ scaffold infiltrated with Ni can lower the thermal stresses arising from the mismatch of the coefficient of thermal expansion (CTE) between anode materials and the electrolyte as well as it can improve the mechanical strength of the anode support due to higher content of YSZ in the anode structure [34].

A major benefit of Ni infiltration can be enhancement of the cell's resistance to redox cycling. Formerly, Tucker et al. showed that when Ni was infiltrated into a thin YSZ porous layer in metal supported cells, redox resistance of the cell improved [101]. This is due to the fact that nano-sized Ni particles can reach the electrical percolation at a much lower limit (minimum of ca. 9 vol.%) [41,102]. Unlike the Ni component in standard Ni-YSZ cermets, the infiltrated Ni with its low content and fine particles is not a structural element in the composite Ni-YSZ anode and during an oxidation cycle cannot cause stresses which lead to anode or electrolyte cracking. Infiltration of Ni-YSZ had been previously shown to be very effective in enhancing cell performance, and

thermal and redox cycling. Howe et al. showed when SDC was infiltrated into the Ni-YSZ electrode, it improved the mixed ionic and electronic conductivity, TPB length and decreased the cell degradation after 56 aggressive thermal cycles ($100^{\circ}\text{C}\cdot\text{min}^{-1}$ heating and cooling rates) [103]. Buyukaksoy et al. also infiltrated a $10\ \mu\text{m}$ porous YSZ layer on a $170\ \mu\text{m}$ YSZ electrolyte and obtained $310\ \text{mW}\cdot\text{cm}^{-2}$ power density at 800°C and stable performance following 15 redox cycles [104]. However, they used an electrolyte supported cell which due to its thick electrolyte and also thin anode cannot be a suitable representative for redox cycling tests.

Redox effect is more pronounced when an anode supported cell with a thin electrolyte is tested. Hanifi et al. developed fully infiltrated electrodes for a fuel cell by infiltration of Ni-SDC ($\text{Sm}_{0.2}\text{Ce}_{0.8}\text{O}_{1.9}$) into a $600\ \mu\text{m}$ porous YSZ scaffold (anode side) and Nd_2NiO_4 into a $30\ \mu\text{m}$ thin porous YSZ (cathode side). The microstructure of the infiltrated cell showed a suitable distribution of particles ($50\text{--}100\ \text{nm}$) inside both electrodes. The cell delivered a power density of about 190, 260 and $300\ \text{mW}\cdot\text{cm}^{-2}$ at 600 , 650 and 700°C , respectively (Figure 2-10a) and showed excellent redox cycling resistance at 650°C by full recovery of open circuit voltage (OCV) even with room temperature air purging into the anode (Figure 2-10b) [105]. However, Ni infiltrated cells still suffered from degradation (25% in 140 h) due to Ni sintering at the operation temperature which led to a reduction in TPB length as well as loss of electrical conductivity [13,98,101]. Figure 2-11 compares the SEM images of a porous YSZ support infiltrated with Ni-SDC (Figure 2-11a) and a sample infiltrated solely with Ni (Figure 2-11b). It was observed that co-infiltration of Ni and SDC could control the Ni particle coarsening ($50\text{--}100\ \text{nm}$ infiltrate particle size) while in the SDC-free sample, Ni particles can grow up to $500\ \text{nm}$ and appear as isolated particles. Such particles are likely less interconnected electronically. The infiltrated SDC could electronically connect the non-

percolated Ni particles due to electronic conductivity of doped ceria under a reducing atmosphere and overall decreases the negative impact of Ni sintering [13].

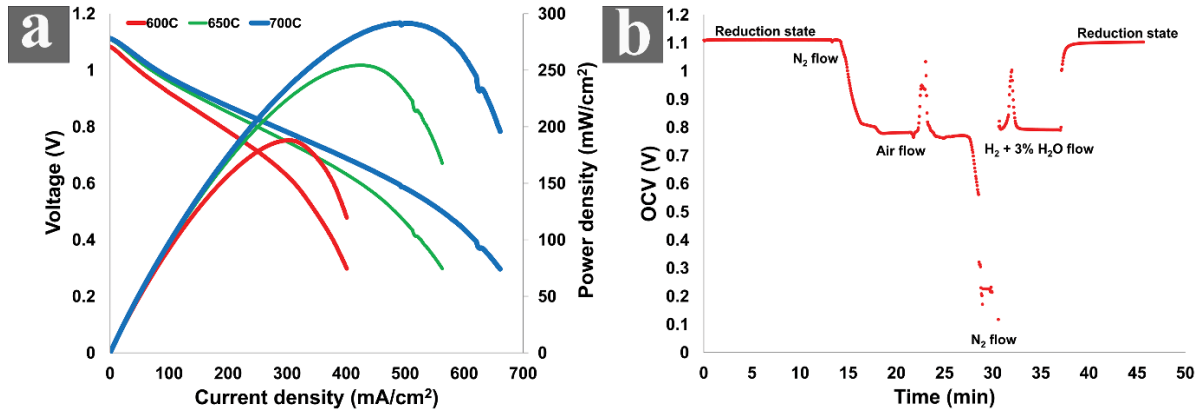


Figure 2-10. (a) Electrochemical performance of the Ni-SDC infiltrated cell at different temperatures, (b) open circuit voltage curve during a redox cycling test at 650°C [105].

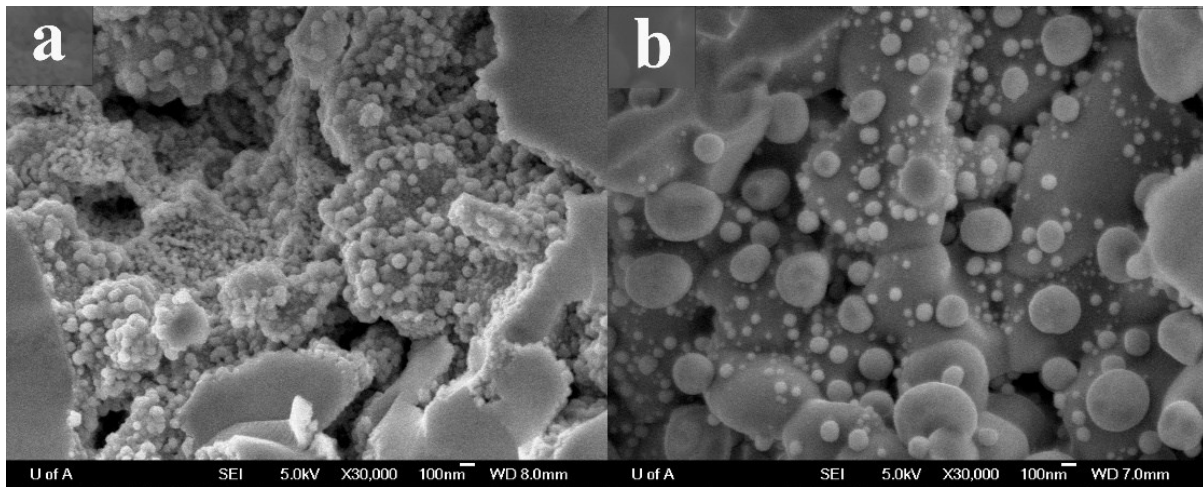


Figure 2-11. SEM images showing the microstructure of infiltrated porous YSZ support structures (a) Within the Ni-SDC infiltrated porous YSZ anode and (b) Within the middle of a typical Ni infiltrated porous YSZ support [13].

Buyukaksoy et al. showed that the stability of a Ni-YSZ cermet formed by infiltration of Ni depends highly on the pore size of the YSZ substrate. When Ni is infiltrated into the YSZ scaffold with fine grains and pore size (~200 nm each), it shows a uniform distribution of Ni particles

(Figure 2-12a), low resistance and high stability ($0.10 \text{ ohm}\cdot\text{cm}^2$ per electrode at 800°C , which increased by 10% following 100 h of operation). They concluded that the fine structure of the porous YSZ scaffold appears to constrain Ni agglomeration. However, when Ni was infiltrated into a porous YSZ substrate with 500 nm YSZ grains and larger pores (0.5 and $5 \mu\text{m}$) (Figure 2-12b), a lower stability and electrochemical performance were observed due to a less constraining effect of YSZ ($0.5 \text{ ohm}\cdot\text{cm}^2$ per electrode at 800°C , which increased by 140% following 100 h of operation) [106]. Overall results show that despite the fact that coarsening of Ni can be reduced using co-infiltration or decreasing the pore size, it cannot be fully controlled and full infiltration of porous YSZ with Ni to provide an electrical conduction path has not yet been a practical method for commercialized Ni-YSZ cermet fabrication. Another major challenge for Ni infiltration is the laborious process which involves up to 25 to 30 times of infiltration for a $500 \mu\text{m}$ porous support to achieve sufficient Ni to percolate [13,105,107]. This makes the infiltration process impractical especially for commercial applications regardless of the stability of the cell.

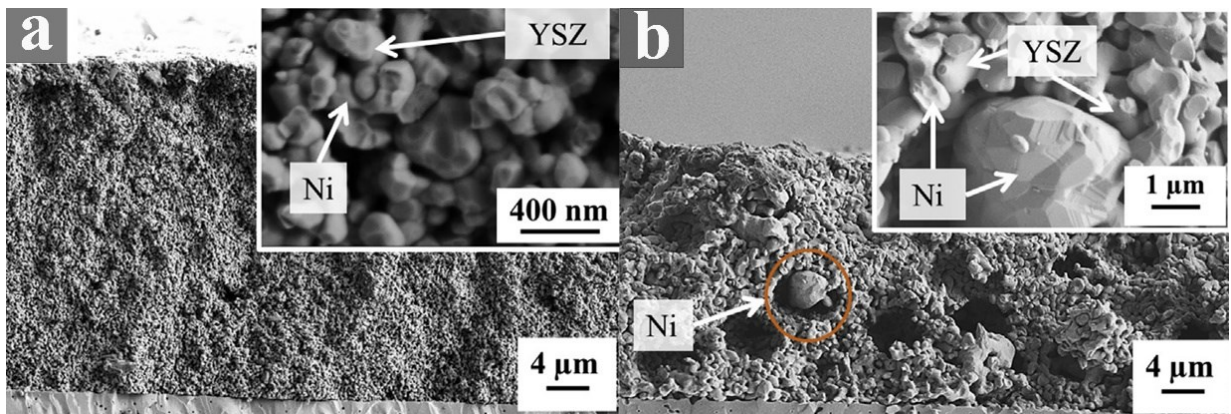


Figure 2-12. SEM images of the cross-section of the anode after running under humidified hydrogen for 150 h. (a) substrate with fine YSZ grains and pores (b) substrate with large pores [106].

2.5 Application of Ni-YSZ in fabrication of proton conducting fuel cells

Barium cerate-based proton conductors such as $\text{BaZr}_{0.1}\text{Ce}_{0.7}\text{Y}_{0.1}\text{Yb}_{0.1}\text{O}_{3-\delta}$ (BZCYYb) show a high proton conductivity but they are not chemically stable under reducing atmospheres and electronically conducting species can form from them. Ni-YSZ with excellent mechanical properties and chemical stability has shown promising results to be used as a support in such proton conducting cells [24,108–110]. Hanifi et al. manufactured a cell based on proton conducting BZCYYb electrolyte and Ni-YSZ support. The cell configuration was Ni-YSZ anode support (375 μm), Ni-BZCYYb AFL (20 μm), BZCYYb electrolyte (10 μm) and LSCF-BZCYYb cathode (25 μm). They achieved maximum power density values of 166, 218, and 285 $\text{mW}\cdot\text{cm}^{-2}$ at 600, 650, and 700°C, respectively. In order to achieve a coherent sintering shrinkage across the support and electrolyte in addition to improving electrolyte densification, they used fine NiO (50 nm) and YSZ (250 nm) powders [110]. Figure 2-13 shows the interfaces of this cell where there is a smooth transition between the Ni-YSZ support, Ni-BZCYYb functional layer and the BZCYYb proton conducting electrolyte. In another study, they reduced the content of YSZ to 0 and 10 wt%. The cell containing 10 wt% YSZ in the support showed stable operation for 67 h without any degradation revealing that the stable Ni-YSZ electrode has good potential to be used as the support for proton conducting electrolytes and lower the manufacturing cost related to the more expensive proton conductor powders [24].

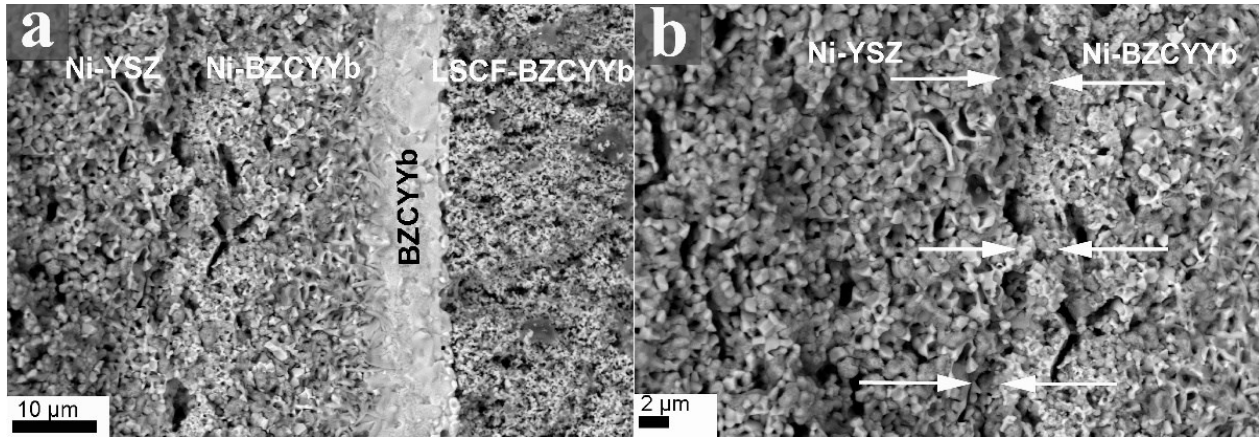


Figure 2-13. SEM images of the cell following testing. (a) interfaces between cathode, electrolyte, and part of the cell anode, (b) interface between Ni-YSZ support and Ni-BZCYYb anode functional layer [110].

2.6 Degradation of Ni-YSZ supported SOFCs

Lack of stability of the SOFCs is known to be a major parameter that has affected the commercialization of fuel cells. Using YSZ electrolyte supported cells requires increasing the operation temperature to 800 to 1000°C which itself can accelerate the degradation rate due to the increased chemical reaction and thermomechanical load of the components [111,112]. Anode supported cells have the advantage of operating at lower temperatures which enables using lower price interconnect materials available [111]. Regardless of higher power densities of anode supported cells in general, different parameters affect the stability of the Ni-YSZ electrode. The Ni-YSZ support not only maintains the mechanical integrity of the cell, but also provides interconnected fuel channels, reactive electrochemical regions inside the AFL and conveys the generated electrons to the current collectors. By stacking SOFCs for higher electrical output, other parameters such as interconnects take part in degradation of the cells. In the following sections, parameters affecting the degradation of Ni-YSZ supported cells will be thoroughly discussed. In the last section, possible solution for controlling the degradation will be provided.

2.6.1 Degradation of the Ni-YSZ electrode

Stationary commercial application of solid oxide fuel cells requires 40,000 to 80,000 h of operation including four or five thermal cycles per year for maintenance purposes [113]. Therefore, long term tests are required to understand the degradation mechanisms close to the actual operational conditions. Any defects in the design components or the microstructural parameters of the cells should be eliminated to reach the long-term milestones. In addition, the main reasons for degradation in Ni-YSZ anode supported cells are discussed and the important data such as cell configuration, operating conditions, degradation rates, reasons for degradation and any attempts to lower the degradation rate are summarized in Table 2-1.

2.6.1.1 Mechanisms of Ni-YSZ electrode degradation

The degradation of Ni-YSZ is known to be a major cause of overall fuel cell degradation. Agglomeration of Ni grains and loss of contact between nickel grains, change of nickel morphology, fracture of the ceramic matrix, phase separation, change of anode porosity, delamination, coke formation and poisoning by sulfur and other elements are some of the reasons for anode degradation [3,114–116]. In the Ni-YSZ cermet, there are three mechanisms which control the degradation rate: (1) material transport mechanisms, (2) deactivation and passivation mechanisms and (3) thermomechanical mechanisms. These mechanisms can act individually or collectively and each of them can become the dominant degradation mechanism depending on the operational conditions of the single cell or the fuel cell stack. Change of Ni surface morphology, increase of Ni grain size and loss of Ni-Ni grain contact are major transport mechanisms which occur due to the tendency of Ni grains to reduce their surface area. Nickel can be transported by diffusion or evaporation and subsequent condensation depending on the temperature and humidity level. The loss of catalytically active sites decreases the rate of electrochemical reactions and

increases activation polarization. In addition, loss of contact as a result of Ni grain growth leads to a decrease of electrical conductivity or increase of cell ohmic resistance. Improper materials combinations or the presence of impurities lead to a chemical gradient which itself is a driving force for transport of Ni inside the Ni-YSZ cermet [117].

More recently, Khrustov et al. studied the degradation of Ni-cermet using a combination of numerical simulation and experimental data. They identified the electrical conductivity of Ni-YSZ cermets before and after long terms tests (300 h, 1000 h and 3000 h). By performing image processing, modeling of the microstructure, and electrical conductivity simulation using a finite element method, they concluded that the electrical resistance of Ni-YSZ and the degradation rate are related directly to the decrease in the volume fraction of the connected nickel clusters [118].

Deactivation and passivation mechanisms become dominant degradation mechanisms when there are impurities in the hydrocarbon fuels which can cause carbon formation [119,120] or sulfur poisoning [121,122] which both lead to a reduction of active sites and increase of activation polarization.

Ni coarsening and loss of Ni grain contact may occur due to diffusion and sintering of nickel grains or due to Ni migration in a gaseous form. Ni sintering can occur due to diffusion of vacancies, grains and grain boundaries. Size, curvature and surface energy affect the Ni coarsening through the diffusion process. Small grains have high surface energy and tend to agglomerate to lower their energy. Because of the varying pressure in proximity to two grains with different radii, a diffusivity vacancy flux is introduced which controls the growth kinetics. In long operations, grains normally reach a single size and coarsening will stop due to Ostwald ripening effect [3,123]. Formation of Ni(OH)₂ can also significantly accelerate the Ni grains sintering and loss of Ni in the Ni-YSZ anode. At high temperatures (above 900°C) even with a small amount of humidity Ni(OH)₂ can

form which can precipitate in low humidity regions of the cermet as Ni and form larger grains. Both Ni growth and depletion of Ni in some areas of the cermet have been observed which was attributed to hydroxide formation [123,124].

2.6.1.2 Long-term degradation inside the Ni-YSZ electrode

By extending the operation time of SOFCs, the initial microstructure of Ni-YSZ varies to adapt to thermodynamic equilibrium at high temperature. Brus et al. [125] evaluated the Ni-YSZ anode morphology in a 100 W stack composed of six single cells over 3700 h of SOFC operation by the FIB-SEM 3D reconstruction method (Table 2-1, row 1). Commercial single cells were provided by SOFC Power Co. Three regions of the cell were examined after the test: inlet, middle and outlet to understand the variations of the microstructure according to design parameters. The inlet of the cell is where the fuel is first in touch with the active anode surface (by horizontal fuel channel grooves inside the interconnect) and the outlet is the end of the fuel channel where most of the fuel has already reacted in electrochemical reaction. Figure 2-14 demonstrates the three areas where samples were taken.

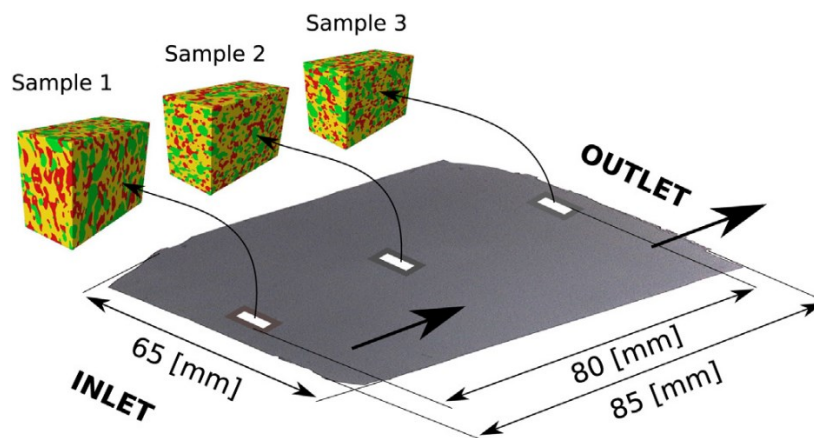


Figure 2-14. Location of the samples taken from the inlet, middle and the outlet of the cell [125].

FIB-SEM reconstructed data revealed that the inlet of the cell (8 cm long) had the most reduction in TPB length. Figure 2-15 shows the variation of TPB according to the evolution of Ni, YSZ and pores before and after 3700 h of the test.

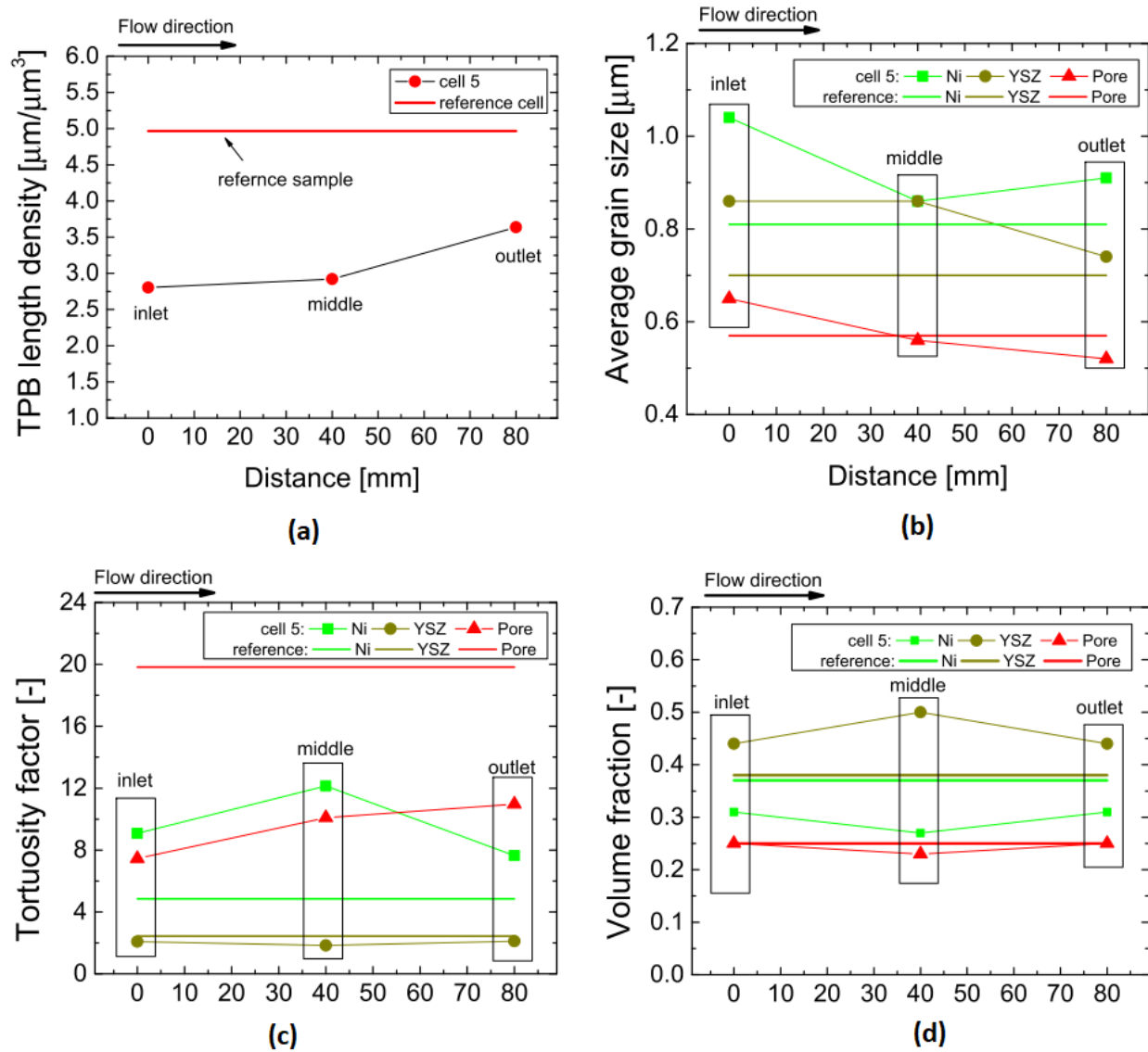


Figure 2-15. Quantified microstructure parameters conducted for the reference sample and the sample after 3700 h of long-term SOFC operation for (a) TPB length density (b) average grain size (c) tortuosity factor and (d) volume fraction. Samples were taken at different locations of the cell in the vicinity of the anode/electrolyte interface [125].

Ni grains for all three regions of the cell (fuel inlet, middle and outlet) were coarser compared with the initial microstructure of the reference cell (Figure 2-15b). Since the inlet section was fuel-rich and current density was high, the generated heat was higher in this region. Thus, the Ni grains of the inlet were coarser than the ones in the middle of the cell. Also, Ni grains at the fuel outlet were larger than the middle due to the proximity of the cell outlet to the perimeters of the box furnace. Ni grain coarsening can follow the charging capacitor law [11,126]:

$$r(t) = (r^{max} - r^0)[1 - \exp(k_{s,cap}t)] + r^0 \quad (1)$$

where r^0 and r^{max} are the initial and maximum grain radius and $k_{s,cap}$ and t are the rate of grain growth and time, respectively. In addition to nickel coarsening, the volume ratio of Ni:YSZ inside the functional layer was reduced from 50:50 to 31:44 due to the diffusion of Ni from the AFL into the support. TPB density in the proximity of the electrolyte was reduced from 5 to $2.7 \mu\text{m}\cdot\mu\text{m}^{-3}$ at the fuel inlet and $3.7 \mu\text{m}\cdot\mu\text{m}^{-3}$ at the fuel outlet position. Reduction of the TPB is a result of both Ni migration and coarsening. As can be seen from Figure 2-16, all six single cells of the stack did not undergo any voltage degradation during the operation time considering the degradation of the anode. The voltage fluctuation of cell number six is due to a contact wire issue. As the authors explained, the electrochemical reaction rate inside the LSCF cathode gradually improves during the operation time and this nullifies the degradation of the anode [127]. As a consequence, the overall cell degradation is zero. There are two parameters that should be considered: first, the design factors such as the local temperature or local fuel utilization variations inside the stack affect the microstructure of the anode support locally. Therefore, providing efficient gas distributor channels and heat management of the stack is crucial to reduce the degradation rates. Second, in order to monitor the effect of anode degradation on the overall performance of the cell, more than 3700 h for the stability test is needed.

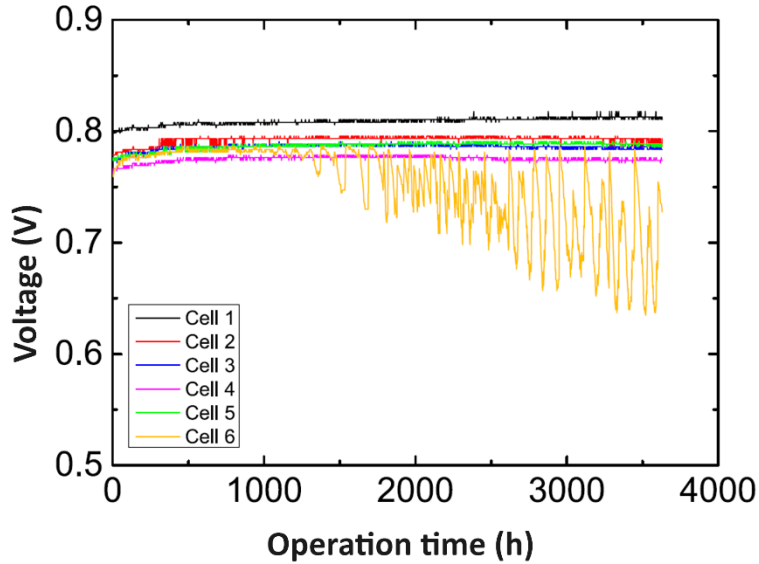


Figure 2-16. Stability test for a stack operating at 700°C with 0.5 A·cm⁻². The fluctuations of the voltage for cell 6 are due to a contact wire issue and not degradation [125].

Lee et al. [128] studied 5000 h of SOFC operation at 700°C for a commercial stack with 60 thermal cycles (Table 2-1, row 2). Cells are composed of Ni-YSZ anode, YSZ electrolyte and gadolinium doped ceria (GDC)-LSCF cathode. The thermal cycles were divided into two stages (I: 700-250°C and II: 700-50°C). The heating/cooldown ramp of the cycles was 1°C·min⁻¹ which doesn't resemble the real work condition of SOFCs such as 10°C·min⁻¹. Post-mortem microstructural analysis revealed that Ni agglomeration was the main reason for degradation in long-term testing before initiating the thermal cycles. By applying 60 thermal cycles, vertical cracks inside the cathode appeared and separation of the LSC/GDC interface took place due to CTE mismatch [129]. Their result showed that Ni agglomeration and new pore formation inside the anode support was part of the intrinsic degradation process of this commercial cell while almost no degradation took place inside the cathode before the thermal cycling procedure. According to the authors, increasing the temperature to 800°C and holding the stack for 4 h at this temperature eliminated the water produced during the reaction and the power density recovered 8.1%. As mentioned earlier [111],

returning back to full OCV is another indication that SOFC performance has recovered in long-term operation.

2.6.1.3 Redox cycling

During redox cycling, oxidation of nickel to form nickel oxide leads to 70% volume expansion in the nickel phase. Such an expansion causes swelling on a macroscopic scale, and it can damage the electrolyte drastically [130]. In addition, thermal and redox cycling can change the microstructure and introduce instability in the Ni-YSZ anode [131–133]. The kinetics of NiO formation is dominated by the diffusion of Ni and oxygen through the oxidized layer. When NiO-YSZ is reduced again, Ni nuclei appear on the surface of NiO grains. Reduction causes volume decrease of NiO and makes the newly formed Ni grains accessible to the reducing gas. The kinetics of redox is controlled by surface reaction instead of diffusion. The driving force for lowering the surface energy on Ni grains leads to sintering of Ni grains and formation of larger Ni grains by formation of Ni(OH)₂ and precipitation on the preferred sites in the microstructure [131,134]. The net result is a more rapid coarsening of the Ni grains as a result of redox cycling.

In addition, redox cycling causes a decrease of ionic conductivity of YSZ [134]. This can occur either due to phase transformation from cubic to tetragonal or the mobility of zirconium species under SOFC operational conditions [115]. Figure 2-17 visualizes the Ni, YSZ and pores following a redox cycle as reported by Holzer et al. [135]. According to FIB-tomography shown in Figure 2-17, Ni shows a heterogeneous distribution. While in some local regions the number of connections is high, between those regions Ni connection is low due to Ni agglomeration. Both YSZ and pore phases are homogeneously distributed in the microstructure. Local resistive losses (Joule heating) can be related to local phase changes in the microstructure. Gas transport/electrical losses originate from high loss locations at bottlenecks of the phases, so-called constrictions. They

attributed the loss of electronic conductivity following redox cycling to a reduction of Ni percolation and the decrease of ionic conductivity to a decrease in the constriction factor. However, redox cycling led to smoother gas diffusion due to a higher pore volume fraction and a higher constriction factor [135].

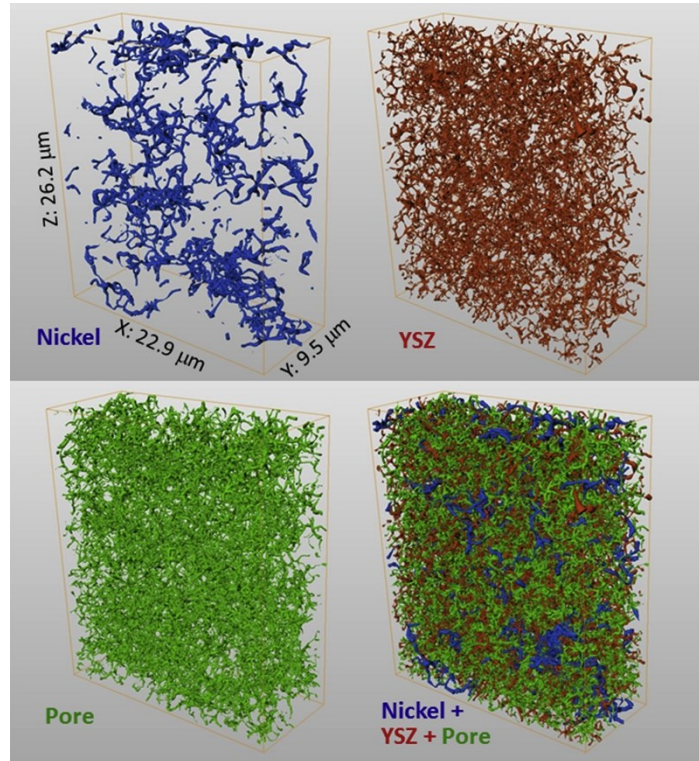


Figure 2-17. Visualization of skeletonized phase networks in the anode sample after redox cycling for Ni (top left), YSZ (top right), pores (bottom left) and all three skeletons superimposed [135].

Pecho et al. [136] found that although finer Ni-YSZ anode microstructures have higher initial conductivities, they undergo more severe Ni coarsening following redox cycling at 950°C. However, coarser anode microstructures have a more stable Ni phase but show lower YSZ stability due to lower sintering activity. In the coarse microstructures, YSZ necks are weak and mechanical stresses induced by redox cycling can lead to connection loss between YSZ grains and as such a drop in percolation. They proposed that, in order to improve redox stability, mixtures of fine and

coarse starting powders in appropriate amounts should be used for the anode functional layer and the support.

They also reported that there is no simple relationship between TPB length and activation polarization. In addition, degradation following redox cycling depends on the initial microstructure. Following a redox cycle, finer microstructures showed less reduction for both TPB and polarization values. In fine microstructures, TPB reduction occurs due to Ni coarsening while in coarse microstructures TPB loss is due to a reduced YSZ percolation. These scenarios are based on a model for coupled charge transfer and transport, which allows using TPB and effective properties as input. Despite the severe microstructural changes for the coarse microstructures upon redox cycling, the performance did not decrease proportionally. They concluded that the loss of YSZ percolation in the entire microstructure is not detrimental since the electrochemical reactions occur in a narrow functional layer area [137]. In the next sections we will explain about other mechanisms affecting the degradation of Ni-YSZ anode supported cells inside SOFC stacks.

2.6.2 Long-term degradation due to interconnects

In addition to Ni-YSZ electrode degradation, design parameters such as the gas distributor channels, temperature variations at different locations of the cell, water management and efficient extraction of the produced water, and sealing material and its chemical reaction with the other components can also affect the degradation of the cells in long-term use. For an SOFC to operate safely for extended periods, all parameters contributing to the degradation of the cell should be controlled or eliminated. Long-term SOFC operation is important in a way that the parameters affecting the degradation can appear after a specific operation time span which might be hidden during earlier SOFC operation periods.

Researchers at Forschungszentrum Julich noticed that chromium (Cr) evaporation from the stainless-steel interconnect is the main reason for the long-term degradation of the Ni-YSZ supported SOFC stacks. Malzbender et al. [138] studied the stability of a four-cell stack with Ni-YSZ anode, YSZ electrolyte and LSM-YSZ cathode (Table 2-1, row 3). The composition of the cells and the operation conditions are provided in Table 2-2 (F1004-08). A stack stability graph at 800°C for 19,000 h is shown as Figure 2-18. The total degradation rate of the stack was 0.5%·kh⁻¹. Cr evaporation from the interconnect oxide scales can result in a Cr₂O₃ sediment at the cathode/electrolyte interface and fill the pores. The pores inside the cathodes are gradually filled and the number of active TPB points are reduced. Therefore, they applied MnCo_{1.9}Fe_{0.1}O₄ (MCF) as a Cr-retention protective layer to suppress Cr diffusion into the cathode. In addition, they found out that by applying a well-developed perovskite cathode contact layer (LaMn_{0.45}Co_{0.35}Cu_{0.2}O_{3-δ} (LCC10) developed at Julich) onto the interconnect, Cr-retention ability can be increased even further. The MCF Cr-retention layer was coated by the atmospheric plasma spray (APS) method and successfully suppressed Cr diffusion into the cathode. Although initial Ni coarsening might be inevitable, the researchers at Julich noticed controlling the Cr evaporation at the cathode side interconnect is the dominant factor for reducing long-term degradation of their stacks. During 19,000 h of SOFC operation, they noticed that diffusion of Mn from the LSM structure into the YSZ grain boundaries caused short circuiting in the cell and fracture of the YSZ electrolyte. They concluded that LSCF can be a better candidate as the cathode for long-term operation of stacks compared to LSM.

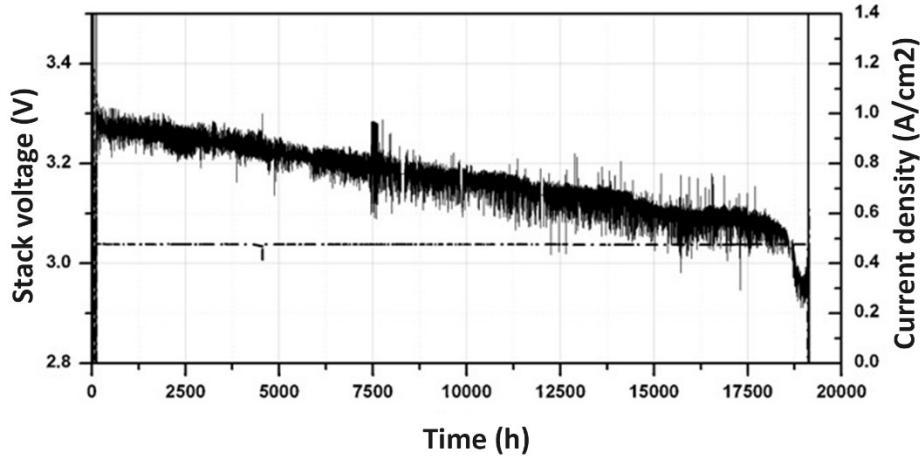


Figure 2-18. The F1004-08 four-cell stack with LSM/YSZ cathode fabricated at Julich operated at 800°C for 19,000 h. The composition of the single cells can be found in Table 2-2 [138].

In the case of using LSCF as the cathode, there is also a chance of Cr reaction with the cathode. A two-cell stack (F1002-95) was tested for 17,000 h at Julich. Single cells are composed of Ni-YSZ anode, YSZ electrolyte, LSCF cathode and GDC buffer layer (Table 2-1, row 4). Mn_2O_3 Cr-retention layer and $\text{La}_{0.97}\text{Mn}_{0.4}\text{Co}_{0.3}\text{Cu}_{0.3}\text{O}_{3-\delta}$ (LCC12) contact layer were coated onto the interconnect at the air side by a wet spray method. The average voltage drop was $1\% \cdot \text{kh}^{-1}$. Energy-dispersive X-ray spectroscopy (EDX) images confirmed the formation of SrCrO_4 at the surface of the cathode attached to the interconnect girders. No SrCrO_4 was formed between the girders (not in contact with the interconnect). Gradual growth of the oxide layer with lower conductivity than the cathode (almost 300 times) leads to a reduction of the electrical contact between the cathode and the interconnect.

Also, due to Cr evaporation from the interconnect, there were some iron oxide spots formed adjacent to the interconnect/Cr-retention layer. The authors tried applying the Cr-retention layer in other Julich stacks with the APS method which inhibits Cr migration to the cathode side more efficiently.

Table 2-1 Summary of the long-term stack and single cell tests mentioned in the text. SP, FL, TC, CD, FU, OU, WPS and T stand for screen print, functional layer thermal cycling, current density, fuel utilization, oxygen utilization, wet powder spray and temperature, correspondingly.

Year	Anode	Electrolyte	Cathode	Studied parameters	Reason for degradation	Improving factor	Degradation rate (%·kh ¹)*	Test condition	Duration (h)	Ref
1	2015	Ni-YSZ 240µm	YSZ	GDC + LSCF/ GDC 50 µm	- Ni-YSZ anode microstructure - FIB-SEM 3D reconstruction	- Ni coarsening specially at the inlet of the cell - Reduction of Ni:YSZ ratio from 50:50 vol.% to lower value → a sign of the diffusion of Ni from FL to the supp - Reduction of TBP density from 5 to 3 µm·um ⁻³ close to the electrolyte	0	T: 800°C H ₂ 1.8 L·min ⁻¹ N ₂ 1.2 L·min ⁻¹ Air 18 L·min ⁻¹ FU 75% Air inlet 630°C Fuel inlet 550°C	3700	[125]
	6-cell stack SOFC power Co.	LSCF contact layer								
2	2017	Ni-YSZ 500 µm	3-YSZ	GDC (2 µm) + LSC (10-20 µm)	- Performance of the stack at high flow of H ₂ and air - Performance of the stack at low flow of H ₂ and air - 60 thermal cycles (700-250°C and 700-50°C)	- For long-term test before the thermal cycles: Ni agglomeration at anode (also new pore formation) - After thermal cycles: Vertical cracks inside the cathode + cathode/GDC interface separation (CTE mismatch)	1.16 for I 2.64 for II	T: 700°C I: 3000 h: H ₂ 0.8 L·min ⁻¹ and air 2 LPM II: 2000 h: H ₂ 0.5 LPM and air 1.5 LPM CD 0.4 A·cm ⁻² TC 1°C·min ⁻¹	5000	[128]
	Commercial cell	Ni-YSZ FL 12 µm								
3	2012	Ni-YSZ	YSZ	LSM	- The effect of spinel protective coating onto the interconnect to suppress Cr species evaporation and migration at cathode side	- Mn diffusion from LSM into the YSZ grain boundary → YSZ fracture + short circuiting the cell	0.5	T 800°C FU 39.8% OU 26.6% CD 0.5 A·cm ⁻²	19000	[138]
	4-cell stack									
4	2011	Ni-YSZ	YSZ	GDC (7µm) + LSCF (40µm)	- Post-mortem analysis of the microstructure and composition	- Interaction between LSCF and Cr evaporated from the interconnect - SrCrO ₄ crystals formation at interconnect/cathode interface and forming insulating layer gradually - iron oxide corroded spots close to the interconnect/protective coat interface due to the lack of Cr inside the interconnect	1	T 700°C CD 0.5 A·cm ⁻² Fuel: 3% humidified H ₂ FU 40% Air	17660	[139]
	2-cell stack	Cr-retention layer								
	F1002-95									
5	2013	Ni-8YSZ (1 mm)	YSZ 10 µm	GDC (5 µm SP) + LSCF (SP)	- The effect of protective layer coated onto the interconnect on the stability of the cell - coating methods of layers	- Cr poisoning of the cathode from the interconnect - thermomechanical stress onto the sealing material - temperature gradient inside the large cell surface and stress into the sealing → gas leakage	0.9 (before 4 kh) 0.3 (40 kh-70 kh) 0.6% (0-70 kh average)	T 700°C CD 0.5 A·cm ⁻² H ₂ 1.400 SLM H ₂ O 0.373 SLM Air 5.280 SLM (dried with dew point of -40°C) FU 40% OU 25%	45000	[140]
	Stack	MnOx protective layer + LCC12 contact layer by WPS								
	F1002-97									

6	2013	Ni-8YSZ	8-YSZ	GDC/LSCF	- The effect of protective layer coated onto the interconnect on stability - coating methods of layers	-	- Compared to 45000 h: - Coating GDC layer by PVD for a denser layer → less unwanted diffusions into the electrolyte - interconnect protective layer is coated by atmospheric plasma spray method → denser layer and less Cr diffusion into the cathode	0.12	T 700°C Air 5280 SLM H2 1400 SLM H2O 0.373 SLM FU 40% CD 0.5 A.cm ²	15000	[140]
	4-cell Stack										
	F1004-21										
7	2018	Ni-YSZ Supp. 500 μm	YSZ 10 μm (SP)	GDC (PVD 1 μm) + LSCF 50 μm	- Post-mortem microstructural analysis - Providing a hypothesis for degradation reason	- Delamination of the anode/electrolyte interface (Mn diffusion from contact layer coated onto the interconnect to the YSZ grain boundaries) → manganese oxide containing secondary phase formation inside YSZ grain boundaries → YSZ fracture and possibly gas leakage	- Cr-retention layer was coated by atmospheric plasma spray → denser layer to suppress Cr diffusion into the cathode - Very low Cr content inside the cathode was found after the test → low degradation rate is attributed to low Cr species inside the cathode - Volatize manganese oxide species should be avoided at cathode contact layer → replacing contact layer to a contact layer without Mn	0.2	T 700°C CD 0.5 A.cm ² H2 2.8 NL.min ⁻¹ H2O 0.747 NL.min ⁻¹ Air 6.64 NL.min ⁻¹ FU 40%	35000	[141]
	4-cell Stack	FL 7 μm		LCC12 contact WPS							
	F1004-21	Tape cast		Cr-retention layer APS)							
8	2020	Ni-YSZ	YSZ	GDC + LSCF	- different protective coatings for Cr retention (WPS MnOx vs APS-MCF) - different contact layer on cathode side (LCC12, LCC10, LSCF) - different interconnect material (ITM vs Crofer 22 APU) - operation temperature (700°C vs 800°C) - different fuel utilizations - different fuels (H ₂ vs CH ₄)	- Increasing the operation T by 100°C, increases the degradation rate by a factor of 1.5-2 - Applying cathode protective coat with WPS cannot suppress Cr diffusion into the cathode completely - Mn diffuses from the contact layer (in the case of existing Mn inside contact layer) or LSM (being as the cathode) into the electrolyte grain boundaries	- changing the coating method of Cr retention layer from WPS to APS → denser layer for suppressing Cr diffusion into the cathode - No remarkable change in degradation using interconnect materials - Changing the Mn containing contact layer to LSFC possibly reduces Mn diffusion into the YSZ grains - Applying GDC by PVD method instead of SP method → denser layer and less Sr-zirconate formation at electrolyte surface - No change in degradation rate is noticed by increasing the FU or changing the fuel to liquid natural gas - Changing the cathode from LSM/YSZ to LSCF without Mn - Glass ceramic crystallization at 850°C for 10 h → no interaction with the interconnect	0.2 (the least voltage degradation value reported by them)	T 700°C and 800°C CD 0.5 A.cm ² Fuels: H2 (20% humidified) Dry H2 CH ₄ /H ₂ FU 40-80%	For different stacks (5450-~93kh)	[113]
	julich stacks comparison			LSM-YSZ							
	Electrolyte-supported cell	Ni:YSZ Vol ratio = 60:40	1500°C sinter								
9	2018	Ni-YSZ	YSZ	LCN-YSZ	- Degradation of the interfaces (anode/electrolyte/cathode current collector interface)	- Oxidation of interconnect at cathode side due to leakage of hydrogen and accelerating the iron oxides formation	- Coating Ni paste at anode side between Ni foam and the anode - Mn2O3-LCN layer formation at oxide scale of the interconnect on cathode side → lowering the contact resistance and suppressing the oxidation of steel interconnect	1.5	T 750°C H2: 1.67 SLM Air: 3 SLM CD 335 mA.cm ²	4400	[142]
	5-cell stack										

Table 2-2 Components for different stacks developed at Julich. SP, WPS and IC stand for screen print, wet powder spray and interconnect. All cells are composed of Ni-YSZ anode and YSZ electrolyte.

Stack (reference)	Composition					Operation parameter						Ref
	Cathode	Barrier layer	Cathode contact layer	IC Cr- retention layer	IC	Tem p (°C)	Current density (A.cm ⁻²)	Fuel	Fuel utilization (%)	Operation time	Voltage degradatio n rate (%kh ⁻¹)	
F1002-95	LSCF	GDC (SP)	LCC12	WPS-MnOx	Crofer22APU	700	0.5	H ₂	40	17660	1-1.4	[139]
F1002-97	LSCF	GDC (SP)	LCC10	WPS-MnOx	TIM	700	0.5	H ₂	40	>93000	~1/0.55	[111]
F1004-21	LSCF	GDC (PVD)	LCC12	APS-MCF	Crofer22APU	700	0.5	H ₂	40	34500	0.2	[141]
F1004-67	LSCF	GDC (SP)	LSCF	APS-MCF	Crofer22APU	700	0.5	H ₂	40	>23500	0.3	[143]
F1002-132	LSCF	GDC (SP)	LCC12	WPS-MnOx	ITM	800	0.5	H ₂	40	15144	1.5	[144]
F1004-08	LSM/8Y SZ	-	LCC10	APS-MCF	Crofer22APU	800	0.5	H ₂	40	19036	0.4	[138]
F**2018-07	LSCF	GDC (SP)	LCC10	APS-MCF	Crofer22APU	700	0.5	CH ₄ / H ₂	70-80	5450	0.3	[145]

Blum et al. [140] reported the long-term performance of a two-cell stack (F1002-97) at 700°C in Julich, designed for stationary applications. The stack is composed of two single cells (Table 2-1, row 5) with Ni-YSZ anode, YSZ electrolyte and LSCF-GDC cathode. Ni-YSZ supports were tape cast and subsequent layers including the GDC barrier layer and LSCF cathode were screen printed. Table 2-2 provides detailed information on the stack composition. The details of the Julich stacks design and test conditions are described elsewhere [146]. Later on [147], they optimized their tape cast process to first cast the electrolyte, anode functional layer and the support layers, and then co-sintered them together at 1400°C in one step to reduce the fabrication costs. The stack operated since 2007 for over 93,000 h and was shut down before 2020. This test is believed to be the longest SOFC operation with hydrogen fuel and Ni-YSZ supported cells reported in the literature. The post-mortem microstructural analysis of the stack is not published yet. The stability result of this stack (F1002-97) can be seen in Figure 2-19.

As mentioned earlier [138] (Table 2-1, row 3), it was revealed that in the case of a contact layer containing manganese, unwanted Mn diffusion might destroy the electrolyte. Apparently, the best option as the contact layer for the LSCF cathode in their stacks is the LSCF itself. The degradation of the stack up to the first 40,000 h of operation was about $0.9\% \cdot \text{kh}^{-1}$. According to the authors, the low degradation rate of the stack was directly related to proper protective and contact layers being coated onto the Fe-Cr alloy interconnect material (ITM, produced by Plansee SE [148]). By frequently returning back to the open circuit voltage (OCV) state between 40,000 to 70,000 h, the degradation rate decreased to $0.3\% \cdot \text{kh}^{-1}$ [111]. The average degradation rate for this stack up to 70,000 h of SOFC operation was about $0.6\% \cdot \text{kh}^{-1}$.

A four-cell stack with enhanced design and composition properties was fabricated at Julich (Stack 1004-21, Table 2-1, row 6) to improve the performance of the stack already discussed (stack F1002-97, Table 2-1, row 5). The operational conditions (temperature, fuel utilization and humidity ratio) were kept constant for the sake of comparison. Single cells were composed of Ni-YSZ anode, YSZ electrolyte, LSCF cathode and GDC interdiffusion protective layer. The composition of single cells is provided in detail in Table 2-2. There are two variations in the composition of these two stacks (F-1004-21 vs. F1002-97). In order to further improve the durability of the cell, the MCF Cr-retention layer was applied by the APS method (rather than WPS method) with the objective to provide a denser Cr-retention layer. Also, the GDC barrier layer was applied by physical vapor deposition (PVD) (rather than screen printing) with $1 \mu\text{m}$ thickness but denser in order to suppress Sr diffusion into the electrolyte [140]. The LCC12 contact layer was coated onto the interconnect and cell frames on the air side by the WPS method. As a result, the degradation rate decreased from 0.9 to $0.12\% \cdot \text{kh}^{-1}$ during 15,000 h of SOFC operation.

During several years of experiments, they reported that the choice of interconnect material (commercial steel Crofer 22 APU vs. ITM) did not affect the durability of the cell [113].

The aforementioned stack (Table 2-1, row 6) with PVD coated GDC and APS coated Cr-retention layer (F1004-21) was shut down at 35,000 h of operation due to a rapid degradation rate of one of the cells after 28,000 h of operation inside the stack (Figure 2-20).

Menzler et al. [141] studied the post-mortem characterization of this stack (Table 2-1, row 7). The main reason of degradation was the diffusion of manganese from the interconnect contact layer (coated onto the interconnect by APS method) and formation of a manganese oxide containing secondary phase inside YSZ grain boundaries, leading to electrolyte/anode interface delamination. Applying the Cr-retention layer by the APS method successfully kept the Cr content inside the cathode to a very low level ($4-8 \mu\text{g}\cdot\text{cm}^{-2}$). The same effect regarding migration of manganese from interconnect contact/protective layers has been formerly discussed (Table 2-1, row 3).

Later on, they changed the contact layer to LSCF in another stack F1002-132 and avoided manganese oxide formation inside the YSZ electrolyte [113,144].

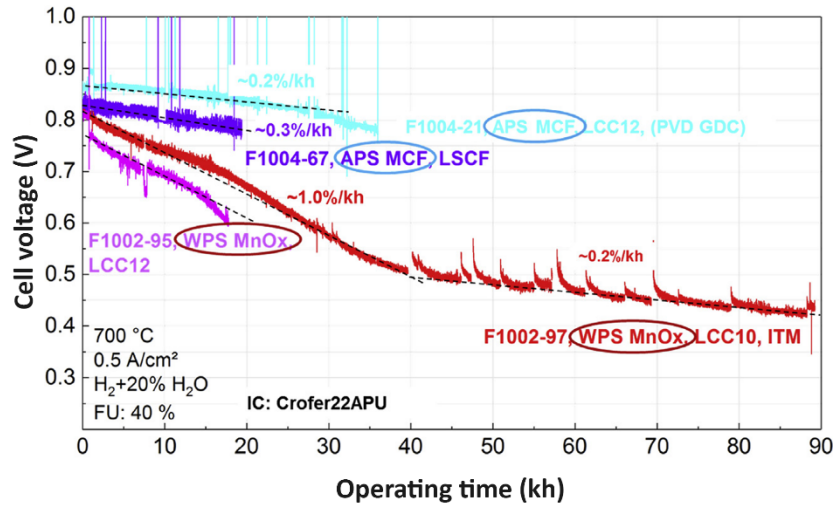


Figure 2-19. Stability tests of stacks developed at Julich with different interconnect protective coating, cathode contact material and interconnect materials (Crofer 22 APU vs. ITM) [113].

A brief summary of the important stacks manufactured at Julich is provided by Blum et al. [113] (Table 2-1, row 8). As Cr poisoning is the main reason for degradation of their stacks, wet powder sprayed (WPS) coatings cannot completely suppress Cr evaporation as described elsewhere [149,150]. Changing the coating method of the MCF Cr-retention layer onto the interconnect from WPS to APS is shown to be more effective due to a higher density since it reduced the degradation rate from 1% to $0.3\% \cdot \text{kh}^{-1}$. Using different interconnect material (ITM vs. Crofer 22 APU) or cathode contact material (LSCF, LCC10, LCC12) did not have any remarkable effect on the performance but it is preferred not to use contact layers containing volatile manganese species. Figure 2-19 shows a comparison of important Julich stacks by varying different interconnect protective coatings, cathode contact materials and interconnect materials. The stack components are described in Table 2-2.

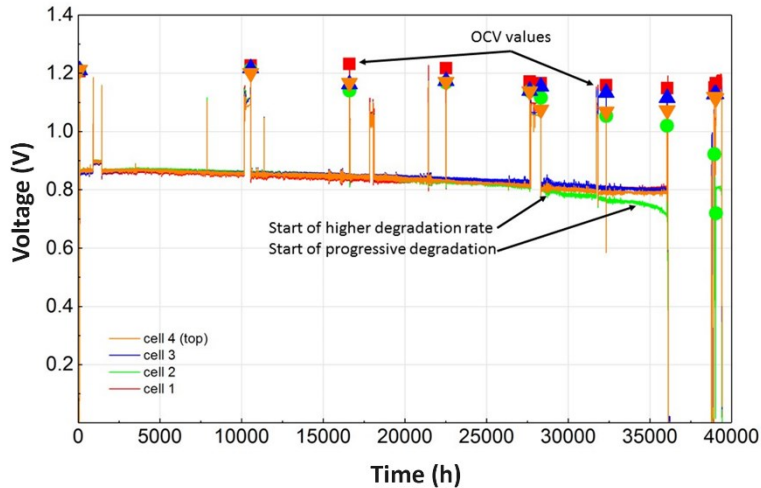


Figure 2-20. Stability test of the stack F1004-21 fabricated at Julich [141]. Details of the test condition are described in Table 2-2.

The effect of increasing the temperature on degradation rate was studied for different Julich stacks with WPS coated Cr-retention layer interconnects. Results are provided in Figure 2-21. Increasing the operation temperature from 700 to 800°C increased the degradation rate from 1 to 1.5%·kh⁻¹ (factor of 1.5) during 13,000-18,000 h of operation (F1002-132 at 800°C vs. F1002-95 and F1002-97 at 700°C). The cells being compared are made of Ni-YSZ anode, YSZ electrolyte, LSCF cathode and GDC buffer layer. The same behavior was also confirmed for the stack with interconnects containing APS coated protective layers when tested at 700 and 800°C for 20,000 h (increasing the degradation rate by a factor of 1.3-2 from 0.2% and 0.3%·kh⁻¹ at 700°C to 0.4%·kh⁻¹ at 800°C) [138,141,143]. Finding the safe operation temperature is crucial especially when targeting commercialization. Reducing the operation temperature might be necessary to compensate for better long-term stability.

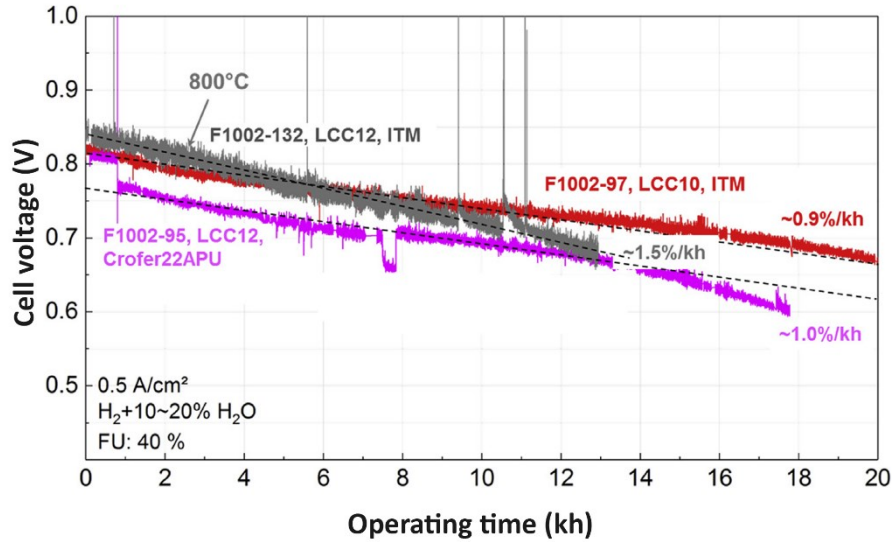


Figure 2-21. Stability of different stacks developed at Julich with WPS-MnOx protective coating onto the interconnect at 700°C and 800°C. As can be seen, changing the interconnect material did not affect the degradation rate [113].

The effect of fuel utilization and the type of fuel on Julich stacks are shown in Figure 2-22. Two stacks composed of Ni-YSZ anode, LSCF cathode and screen printed GDC layer operating at 700°C and 0.5 A·cm⁻² were compared (Table 2-2, F1004-67 vs. F2018-07). Stack F1004-67 consists of four single cells (10×10 cm²) and 130 W electrical power with 40% fuel utilization for 20,000 h. Stack F2018-07 consists of 18 single cells (20×20 cm²) and 2.5 kW power output [145]. As can be seen, changing the fuel utilization of stack F2018-07 from 40% to 70-80% for 430 h did not change the degradation rate compared to F1004-67. In addition, changing the fuel for stack F2018-07 from dry hydrogen to liquified natural gas with internal reforming for the next 4500 h (70-77% fuel utilization) did not affect the degradation rate as well.

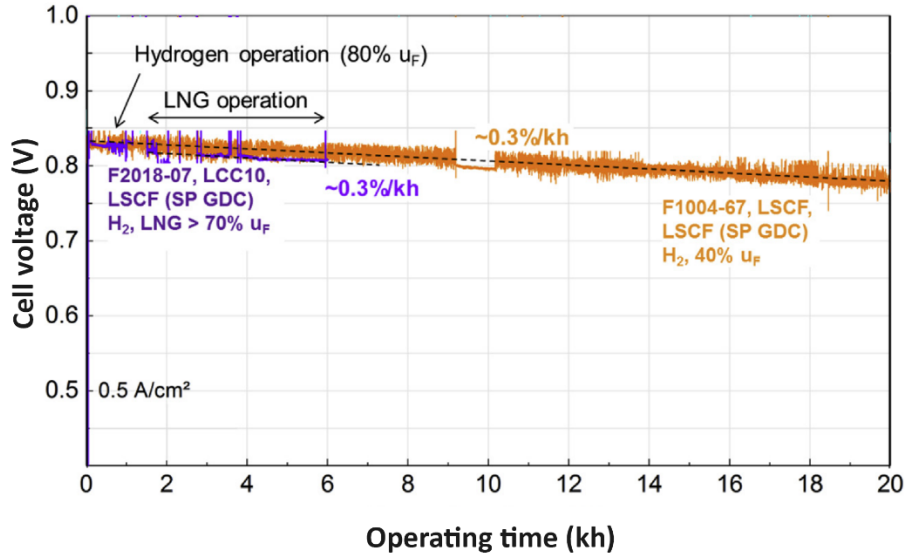


Figure 2-22. The effect of fuel type and fuel utilization on the stability of two stacks at 700°C developed at Julich. The composition of the single cells is described in Table 2-2. Stack 2018-07 undergoes a change of fuel utilization from 40% to 80% and type of fuel from hydrogen to liquified natural gas [113].

In the case of using LSM-YSZ as the cathode [138] or when Mn exists in the contact layer, Mn diffuses into the YSZ grains causing crack formation inside the grains or separation of the interface (Table 2-2, F1004-08). Increasing the temperature from 700 to 800°C accelerated the Mn diffusion process by a factor of 1.9 [113].

2.6.3 Long-term degradation due to the test design parameters

Design parameters and test conditions also affect the degradation of SOFCs during prolonged operation. Water management inside the Ni-YSZ electrode in SOFC mode is discussed by Matsui et al. [151]. They studied different H₂O:H₂ volume ratios up to 100 h at 1000°C. At 20 vol.% H₂O and 0.8 V, the cell showed ~26% degradation during 100 h of operation. Increasing the water ratio to 30 vol.% increased the degradation to ~52% during 70 h. Operating at 40 vol.% H₂O caused severe degradation just in the first 10 h and switching to OCV condition did not recover the cell performance. Another research group achieved less than 1%.kh⁻¹ degradation when running a cell

under 20 vol.% H₂O for 93,000 h of operation [113]. The results of this research are important as water management in SOFCs can be related to test setup design and how efficiently the produced water (especially at higher current densities) can be transported away from the reactive interface.

Yang et al. [142] studied the relationship between the microstructural changes at the interfaces (electrodes, contact material and current collector) and the degradation inside a five-cell planar SOFC stack of 340 W. They reported 1.5%·kh⁻¹ degradation in a period of 4400 h at 750°C (Table 2-1, row 9). They claimed a newly developed cathode contact material LaCo_{0.6}Ni_{0.4}O_{3-δ} (LCN) and external manifold design of the stack led to a reduced degradation rate. In addition to the importance of gas distributor channels and manifolds, sintering the contact material, cathode current collector paste (LCN) and the cathode together for a long-term test is important to achieve low degradation rates. The main reason for degradation was the formation of porous iron oxide structures at bipolar plates on the cathode side. The same effect related to the interconnect material was observed by another research group [139] (Table 2-1, row 4).

Scaling up from single cell tests to stack tests introduces new challenges. Developing a reliable sealing material with low volatility for long-term tests in stacks is crucial. The stacks developed at Julich usually used optimized glass sealings that are allowed to crystallize at 850° C for 100 h to produce a thermodynamically stable seal. In this case, no interaction between the glass sealing and the interconnect takes place [141]. Yang et al. studied the effect of the sealing material on degradation of commercial Ni-YSZ anode supported cells running with hydrogen fuel and 10 ppm H₂S for 3000 h. They noticed that the degradation was not inherent to the Ni-YSZ anode but was related to the sealant. While former studies with cells being sealed by Ceramabond 552 (Aremco) showed continuous degradation [152], changing the sealing material to G18 (BaO-CaO-Al₂O₃-

SiO₂-B₂O₃) glass developed at the Pacific Northwest National Laboratory suppressed the degradation during 3000 h of operation [153].

By increasing the surface area of the cells inside the stack, the temperature gradient at the surface of the cell leads to thermomechanical stress in the sealing material, which caused gas leakage [140]. BaO-CaO-SiO₂ glass ceramic with YSZ particles as the reinforcing material has been specially developed for better compatibility with the cell and interconnect material in long runs [154,155].

2.7 Strategies to improve the electrochemical performance and durability of SOFCs

In order to improve the performance of Ni-YSZ anode supported cells, the anode structure should be graded in terms of composition and porosity content. For long-term operation of SOFCs at elevated temperatures, composition of the AFL needs to comprise Ni grains which are not too fine (not less than 500 nm). Otherwise, Ni grain growth takes place and electrical conductivity and TPB length decreases. Large Ni grains (> 1 μm) can also negatively affect the TPB length and electrical conductivity. Coarse YSZ grains lower the mechanical properties and redox cycling tolerance of the cell. Apparently, grain sizes of 500 nm to 1 μm for both Ni and YSZ in the final microstructure of the AFL appear to be ideal. The Ni content in the AFL can be around 50 vol.% to maximize the TPB length but it can increase from 50 vol.% to 70-90 vol.% in the anode support. This leads to an increase of the electrical conductivity and porosity of the support which are the main requirements for Ni-YSZ supports. However, the porosity content of the support should not be enough to negatively affect the mechanical properties. The increased porosity (50-60%) can lower the tortuosity and concentration polarization, and ease the diffusion of gas and removal of the reaction products.

Addition of small amounts of YSZ (10-30 vol.%) to the support can suppress Ni sintering and provide better mechanical integrity for the support while maintaining a high electrical conductivity. Using calcined-milled YSZ enables development of a Ni-YSZ support with high porosity and less tortuosity, which is suitable for gas diffusion especially under SOEC modes. Infiltration of Ni into the porous YSZ scaffold to form a Ni-YSZ anode can improve the redox and thermal cycling; however, such cells suffer from continuous Ni sintering which to some extent can be reduced by co-infiltration with doped ceria and by controlling the size of the pores in the microstructure. It is postulated that infiltration of porous YSZ with Ni to form the electrical conduction path has been a failure since Ni sintering lowers the cell conductivity and increases the degradation rapidly. Infiltration appears to be more promising for the cathode or when a Ni-YSZ composite is infiltrated with doped ceria alone or together with Ni for improving its catalytic activity and ionic conductivity while the conduction path is already established due to a sufficient content of Ni. The reduction process should be performed at temperatures where the interfacial bonding between nickel and YSZ in the AFL remains coherent and there is no separation and crack formation at this interface due to any remaining porous Ni which has a high tendency for growth. However, a high reduction (above 850°C) temperature can also lead to the reduction of TPB length and 700-800°C appears to be the most suitable temperature for cell reduction.

Long-term operation of SOFCs provide the most valuable data which represent the actual reliability of these cells. Unfortunately, the number of academic publications which provide long-term SOFC data is limited. Meanwhile, operation for long term is not viable for many research groups due to limited access to equipment at their laboratories. Typically, it takes about 100 h for the SOFCs to reach to a minimum level of stability the cell components and sealing material. It is

strongly recommended that at least over 100 h of SOFC operation be studied prior to publishing SOFC results especially for authenticating novel materials and methods.

Efforts from well-known research groups show a systematic approach towards fabrication of the stacks with less than $1\% \cdot \text{kh}^{-1}$ degradation rates by varying one parameter at a time while keeping the rest of the parameters constant. It is believed that sealing material and current collector design in addition to anode microstructure have a crucial impact on degradation of SOFCs in the long term. Reaching the 40,000h requirement of commercial SOFCs won't be possible except by developing proper gas distributor channels, interconnects and sealing materials. Humidity plays an important role in degradation of the Ni-YSZ electrode because of the effects of nickel hydrolysis and subsequent re-deposition of Ni throughout the electrode, which can enhance Ni coarsening. Well-designed interconnects with continuous stable contacts to the electrode surfaces and proper grooves to supply the fuel and air are critical for a continuous provision of fuel/air to the AFL and removing the produced water vapor from the anode. As mentioned earlier, when all these parameters are fulfilled, durable Ni-YSZ supported SOFCs can be achieved.

Apart from all the microstructural features of the actual cell components, the reasons for triggering SOFC degradation might be hidden inside external variables such as stack/single cell test rig design parameters. Chromium evaporation from steel interconnects can lead to SOFC stack failure at high temperatures after a long operation time. A suitable Cr-retention protective layer is essential for long-term stability of the stacks. Operating at high temperatures apparently leads to unwanted Mn diffusion from the commonly believed stable LSM cathode as well. Operation temperatures of SOFCs can be reduced by development of new materials for the electrodes especially the cathode, formation of nano-structured electrodes by the infiltration technique, reducing the thickness of the electrolyte to about 2-3 μm and engineering the microstructures of the electrodes. It is highly

implausible to reach a stable SOFC over the long term without controlling all parameters affecting degradation.

Publishing SOFC performance in conjunction with measurement of the stability needs to be a new must practice in the SOFC community. It is recommended the standard testing protocols be followed in order to compare the results from different groups.

Conclusions

The current review discussed the significance of parameters that affect the microstructure of Ni-YSZ. It is concluded that proper selection of starting NiO and YSZ powders and their ratio is important to achieve a high mixed electronic and ionic conductivity as well as sufficient porosity and TPB length in the AFL or support of the cell. By calcination and milling it is possible to control the sintering ability of YSZ inside the anode support and develop a porous microstructure which is less tortuous. Such a porous structure is suitable for gas diffusion and removal of reaction products from the anode support as well as infiltration for boosting the electrochemical performance. Infiltration of Ni into a porous YSZ support forms a new Ni-YSZ cermet which is highly robust against thermal and redox cycles. However, apart from the laborious infiltration process, such an anode shows rapid degradation due to Ni sintering during operation. By controlling the pore size in the porous YSZ support as well as co-infiltration of Ni with doped ceria, the rate of degradation decreases but is not fully controlled. Infiltration of doped ceria enhances the electrochemical performance and thermal cycling of non-infiltrated Ni-YSZ. Infiltration is also recommended for thin porous YSZ layers to form novel high performing cathodes such as $\text{Nd}_2\text{NiO}_{4+\delta}$.

Long-term experiments are the gateways to commercialization of SOFCs. Regardless of how well the SOFCs might operate for short periods, long-term tests provide us the advantage of anticipating the costs and redesigning our set points for choice of materials and methods. The aforementioned research results combined with Table 2-1 information suggest the design complexities in SOFC stacks add unforeseen parameters which might lead to degradation of single cells. Reliability of SOFC stacks are more critical as they better represent possible commercial applications. For the final step towards commercialization, semi-commercial SOFC projects in Europe (such as PACE)

help to evaluate stack operation in real life conditions before widespread production of the stacks as the ultimate goal of the SOFC community.

Acknowledgements:

The authors would like to acknowledge Future Energy Systems and Ministerio de Ciencia e Innovación of Spain (grant no. PID2019-107106RB-C32) for financial support of the research carried out at the University of Alberta and Instituto de Ciencia de Materiales de Aragón (CSIC-Unizar) and during preparation of the current manuscript.

Chapter 3: Development of Proton Conducting Fuel Cells Using Nickel Metal Support

Sajad Vafaeenezhad^{1*}, Navjot Kaur Sandhu¹, Amir Reza Hanifi¹, Thomas H. Etsell¹ and Partha Sarkar²

1. Department of Chemical & Materials Engineering, University of Alberta, Edmonton, Alberta T6G 1H9, Canada

2. Innotech Alberta, Edmonton, Alberta T6N 1E4, Canada

Abstract

This research reports the fabrication of a metal supported fuel cell based on the well-known proton conducting electrolyte (PCE) BaZr_{0.1}Ce_{0.7}Y_{0.1}Yb_{0.1}O_{3-δ} (BZCYYb) material. The impact of the addition of YSZ on the anode microstructure is also described. This solid oxide fuel cell (SOFC) consists of Ni:yttria stabilized zirconia (YSZ) support (with different weight ratios of Ni:YSZ), Ni-BZCYYb anode functional layer (AFL), BZCYYb electrolyte and LSCF-BZCYYb cathode. The results show that addition of only 10 wt% YSZ to the support improves the microstructure of the cell by preventing severe Ni grain growth inside the support, and providing more accessible triple phase boundaries (TPBs) at the contact surface of the support/AFL and better distribution of the fuel gas to the accessible TPBs. As a result of microstructural improvement, polarization resistance of the cells with 10 wt% YSZ decreases compared with the cell having pure Ni metal. The cell containing YSZ in the support shows 67 h of stable operation under potentiostatic SOFC condition without any degradation. The current metal supported tubular fuel cell shows promising electrochemical and microstructural features which has the possibility to replace the conventional (Ni-PCE) or even Ni-YSZ anode supports.

Keywords: Metal-supported; Proton Conductor; Microstructure; BZCYYB; Nickel; YSZ

3.1 Introduction

An SOFC is a high temperature electrochemical conversion device that converts chemical energy into electricity and heat. The key advantages of SOFCs include high efficiency, flexibility of operation for a wide range of applications, continuous energy production and low pollutant emissions [17,42,156]. They can be incorporated into modular designs to fabricate stacks [157] and adapted to different application scales [15]. The majority of SOFC development recently has focused on anode-supported SOFCs with YSZ electrolyte. This has led to significant improvements in the reduction of electrolyte thickness ($<20 \mu\text{m}$) and reduction in the cell operating temperatures (below 800°C), hence enabling the use of economical stacks and balance-of-plant materials [158].

Since the introduction of proton conducting electrolytes by Iwahara et al. [159], significant research and development has concentrated on reducing the operation temperature. The activation energy for proton conduction is lower than oxygen ion conduction at intermediate temperatures [160–162]. Reducing the operation temperature of SOFCs can decrease the degradation rate [163,164]. BaZrO_3 and BaCeO_3 are the base of most PCEs due to their high proton conductivities [165–168]. BaZrO_3 shows superior stability under H_2O and CO_2 compared with BaCeO_3 but has lower proton conductivity [167,169].

In PCE fuel cells fed with hydrogen fuel, water is formed on the cathode side which reduces the necessity of having a high porosity anode support [110,170,171]. While NiO sinters at 1100°C , the sintering temperature of the proton conductors can occur at higher temperatures [108,172,173] which leads to severe NiO grain growth inside the NiO-PCE cermet during the sintering process. Consequently, the coating of subsequent thin films such as Ni-PCE AFL or the electrolyte is not

possible without polishing the surface of the support to remove the large Ni particles [174]. High temperature sintering of PCEs can lead to Ba diffusion from the perovskite structure to an alumina crucible and formation of compounds such as BaAl_2O_4 or evaporation of BaO . This leads to a reduction of the performance and stability of the fuel cell [175–178]. Doping small quantities of Ni as a sintering aid for the PCE reduces the required sintering temperature to 1400°C or below [160,179,180].

The poor chemical stability of barium cerates as proton conductors in H_2O and hydrocarbon environments is a well-known issue [181,182]. Partial substitution of the Ce with Zr can improve the stability of the proton conductor [177]. PCE materials based on yttrium doped BaCeO_3 such as $\text{BaCe}_{0.8}\text{Y}_{0.2}\text{O}_{3-\delta}$ (BCY), $\text{BaZr}_{0.1}\text{Ce}_{0.7}\text{Y}_{0.2}\text{O}_{3-\delta}$ (BZCY) and BZCYYb have been widely used due to their excellent protonic conductivity [171,183–186]. Rainwater et al. [171] fabricated a Ni-BZCYYb | BZCYYb | LSCF-BZCYYb cell with different amounts of pore former inside the Ni-BZCYYb support (Ni:BZCYYb volume ratio = 1:1). Their results indicated that the sample with 37 vol.% porosity (produced after reduction of the support and without addition of pore former) resulted in the electrochemical performance of $1.2 \text{ W}\cdot\text{cm}^{-2}$ at 750°C .

The possibility of using non-proton conductor cermet supports with a PCE electrolyte has been studied by different researchers. Bae et al. [108] deposited a Ni-BCZY ($\text{BaCe}_{0.55}\text{Zr}_{0.3}\text{Y}_{0.15}\text{O}_{3-\delta}$) AFL, BCZY electrolyte and BSCF ($\text{Ba}_{0.5}\text{Sr}_{0.5}\text{Co}_{0.8}\text{Fe}_{0.2}\text{O}_{3-\delta}$) cathode on top of a Ni-YSZ anode support (Ni:YSZ = 40:60 vol.%) with pulsed laser deposition (PLD). The reason for replacing Ni-BCZY with Ni-YSZ is better chemical and mechanical stability of the conventional Ni-YSZ support. In addition, deposition of a thin film AFL and the electrolyte on top of a Ni-YSZ support layer is easier compared with fabrication and sintering of a Ni-PCE support. Bae et al. obtained a power density of $742 \text{ mW}\cdot\text{cm}^{-2}$ at 650°C which is higher than a cell based on a Ni-BCZY support

[187]. In another study Hanifi et al. [110] used a Ni-YSZ support (NiO:YSZ = 65:35 wt.%) for a BZCYYb electrolyte on a tubular SOFC cell in order to improve the chemical stability and mechanical strength of the PCE cell. The authors reported that a careful selection of raw materials in terms of particle size and surface area is the key to match the shrinkage differences between the Ni-YSZ support, Ni-BZCYYb functional layer and BZCYYB electrolyte during sintering to fabricate a cell.

Conventional cermet supported fuel cells are limited to stationary applications because of the slow start-up and high operation temperature [188]. The high thermal conductivity and ductility of the metallic support (MS) improve the thermal shock resistance and lower the internal temperature gradients thereby allowing a quicker start-up [42]. In addition, metal supports are mechanically robust to severe redox cycling [158,188–190]. Redox cycling tolerance lets the cells tolerate interruption in fuel supply which reduces the complexity of the design [189]. If successful, MS-SOFC technology is capable of expanding traditional fuel cell applications to portable rugged SOFCs [188,190]. Metal-supported SOFCs using stainless steels for instance can reduce the material cost and increase the competitiveness of SOFCs [158,189,191]. Different alloys such as 430, 409, 410 and 441 are being used for metal supports. The thermal expansion coefficient of ferritic stainless steel supports is compatible with YSZ electrolyte (10-12 ppm°C⁻¹) [189]. Ferritic steel also bonds well with the ceramics which is considered an advantage. Recently, a symmetrical metal supported cell fabricated by Lawrence Berkeley National Laboratory (LBNL) has shown promising performance of 1.9 W.cm⁻² at 800°C [190]. The porous and symmetric ferritic stainless steel support (both at anode and cathode side) attached to a YSZ scaffold infiltrated with catalysts (LSM infiltrated at the cathode side and Ni-samarium doped ceria (SDC) infiltrated at the anode side) could withstand both anodic and cathodic environments. The same cell has been subjected to

severe temperature changes (675-800°C in 6.6 min) for more than 100 cycles while the current density variations have been tracked [192]. However, the inter-diffusion of Fe, Cr and Ni at the Fe-Cr support/AFL interface is a common issue for stainless steel metal supports. Consequently, formation of oxide scales on Ni particles followed by structural change of the support degrades cell performance. Addition of a diffusion barrier layer between the support and the AFL mitigates the degradation rate of the cell [193–195] but this can negatively impact performance. Rapid depletion of Cr in the support can also help the formation of iron oxide species inside the support [191]. Sintering the ferritic steel support must be carried out in reducing atmosphere or vacuum to prevent formation of chromium oxide which reduces the catalytic activity of the cathode and limits the choice of cathode material [189]. In anodic condition, a Ni support benefits high performance at low temperatures due to its high catalytic activity at a reasonable price. There is no need for a diffusion barrier layer to be used for Ni supports and it can be sintered in an oxidizing environment. Ni supports are more stable than ferritic supports in term of chemical compatibility with Ni-PCE functional layers without formation of any Ni-Fe-Cr alloy inside the anode. Ideally, as long as the microstructural features of the Ni support are kept optimized, there is no need for any extra component inside the support (that may just increase the net cost of the cell). Any undesired microstructural feature changes such as severe grain growth of Ni particles or crack formation inside the Ni support reduce the fraction of percolated particles or in more severe cases affect the interfaces of support/AFL/electrolyte by bending, separation or cracking. Special attention is required to keep the microstructural features of the support optimized.

A tubular fuel cell design has several advantages over the planar design such as higher thermal shock resistance, improved thermomechanical properties, higher thermal cycling ability, less sealing and faster start up/shut down time [196–198]. A combination of advantages such as using

a Ni metal support, highly conducting electrolyte and a tubular design appears to be very attractive for an efficient fuel cell. The aim of the current study is to fabricate such a fuel cell and study its electrochemical performance and microstructure. Another objective of this work is to shed light on the impact of YSZ on the microstructure of Ni-YSZ supports.

3.2 Experimental procedures

The metal supported PCE fuel cell was based on the Ni-YSZ (0 or 10 wt% YSZ) (support) | Ni-BZCYYb (AFL) | BZCYYb (electrolyte) | LSCF-BZCYYb (cathode) configuration. The tube diameter, length and active surface area of the fuel cells studied were 6 mm, 4 cm and $\sim 1.6 \text{ cm}^2$, respectively.

3.2.1 Fabrication of the anode support

Slip casting was used for fabrication of the two supports. Different weight ratios of NiO:YSZ were studied to understand the microstructural behavior of the support by increasing the content of YSZ. To form the slip, as received YSZ powder (TZ8Y, 8 mol% Y_2O_3 , Tosoh) was mixed with NiO (Sigma Aldrich, particle size $< 50 \text{ nm}$) in different YSZ:NiO weight ratios of 0:100, 10:90, 15:85, 25:75 and 35:65. The powder:water weight ratio was set to 1:1. Graphite (Sigma Aldrich, < 325 mesh) amounting to 30 vol.% was added as the pore former. The details of the slip casting process can be found in previous publications [86,110]. Hereafter, the cells with 0, 10, 15, 25 and 35 wt% of YSZ in the support are referred to Ni100, Ni90, Ni85, Ni75 and Ni65, respectively.

3.2.2 Synthesis of BZCYYb powder

The proton conductor, $\text{BaZr}_{0.1}\text{Ce}_{0.7}\text{Y}_{0.1}\text{Yb}_{0.1}\text{O}_{3-\delta}$ (BZCYYb) powder was synthesized by a sol-gel modified Pechini process and is explained elsewhere [170]. Briefly, stoichiometric contents of

nitrate forms of the constituents were dissolved in deionized water. Ethylenediaminetetraacetic acid (EDTA) and citric acid were used as chelating and complexing agents and ammonium hydroxide was added to promote the dissolution of EDTA in deionized water. The molar ratio of nitrate powder, EDTA and citric acid was set to 1:2:2. The final gel was heated at 350°C in a furnace to decompose the nitrates and sintered at 1100°C for the formation of single phase BZCYYb.

3.2.3 Coating of the anode functional layer and the electrolyte

The anode functional layer (AFL) suspension preparation method is explained elsewhere [110]. Briefly, the dip coating suspension was prepared by mixing 4 g each of NiO and BZCYYb powder (50:50 weight ratio) in 16 g of ethanol and 2.16 g binder (6 wt% ethyl cellulose in terpineol). The suspension was ball milled for 24 h at 250 rpm using zirconia balls (balls:powder weight ratio of 6:1). Supports were dip coated inside the AFL suspension once, dried and sintered at 1000°C (in air) for 3 h before application of the electrolyte. The BZCYYb electrolyte suspension was prepared by mixing the sol-gel BZCYYb powder, ethanol and binder (6 wt% ethyl cellulose in terpineol) with a 25% solid loading, as described elsewhere [170]. The electrolyte was dip coated on top of the AFL, dried at room temperature and sintered at 1450°C for 3 h before coating of the cathode layer.

3.2.4 Coating of the cathode layer

The cathode preparation method is explained elsewhere [170]. In summary, $\text{La}_{0.6}\text{Sr}_{0.4}\text{Co}_{0.2}\text{Fe}_{0.8}\text{O}_{3-\delta}$ (LSCF, Fuel Cell Materials) and BZCYYb powder were mixed with azeotrope (toluene/ethanol) solvent, binder and dispersant. The resulting mixture was ball milled for 12 h and dip coated on

the electrolyte. The cathode was dried at 100°C, following by heat treatment at 250°C for 1 h and sintering at 1100°C for 3 h.

3.2.5 Fuel cell setup and electrochemical testing

The tubular cell was attached to a mullite tube using Ceramabond 552-VFG (Aremco). Hot wax was used to seal the outlet of the mullite tube. Rolled nickel mesh (Alfa Aesar) was used as the current collector on the anode side. The mesh was pushed inside the tube to make a good contact with the anode. Platinum wires were connected to the nickel mesh as an extension of the current collection. Gold paste and wires were used as the current collector on the cathode side. The fuel cell was placed inside the hot zone of a tubular furnace. Two thermocouples record the temperatures continuously in the hot zone. The SOFC tests were performed in the temperature range of 600-750°C. Nitrogen was fed to the anode side at 10 mL·min⁻¹ by a stainless steel needle from room temperature up to 600°C. Reduction of the anode took place by switching gradually from nitrogen to humidified hydrogen (3 vol.% H₂O) over 24 h. The cells were tested under two flow rates of 10 and 25 mL·min⁻¹. Air was introduced to the cathode side at 50 mL·min⁻¹. Open circuit voltage (OCV), I-V and electrochemical impedance spectroscopy (EIS) measurements were carried out by a four probe configuration using a Solartron 1255 frequency response analyzer in combination with a Solartron 1287 electrochemical interface.

Microstructural analyses were carried out using a scanning electron microscope (SEM), JEOL 6301F. Transmission electron microscopy (TEM) was used for estimation of the initial particles size and morphology using a Philips Morgagni 268 TEM at 80 kV (Philips, Eindhoven, The Netherlands). X-ray diffraction (XRD) analysis was carried out using a Rigaku diffractometer RU-200B equipped with a rotating Cu anode (40 kV, 110 mA) and a graphite monochromator. Archimedes method was used to estimate the density and open porosity of the anode supports.

3.3 Results and discussion

3.3.1 Initial characterization of the support

Figure A 1 in appendix A represents the XRD pattern of NiO-BZCYYb functional layer following the sintering process. According to the XRD pattern, single phases of NiO and BZCYYb were obtained without the formation of any secondary phases.

Transmission electron microscopy (TEM) images of the different powders used for fabricating the cell are show in Figure 3-1. BZCYYb powder is composed of 10-20 nanometer-size particles agglomerated into 100-300 nm sizes. Similarly, NiO powder is composed of 10 nanometer-size particles agglomerated into 100-400 nm while YSZ powder contains individual 90 nm particles agglomerated into 250 nm particles. It should be noted that the initial particle size of the ceramic phases affect the sintering properties of the support and functional layer. Suitable particle sizes are essential in order to provide a smooth transition between the support and AFL.

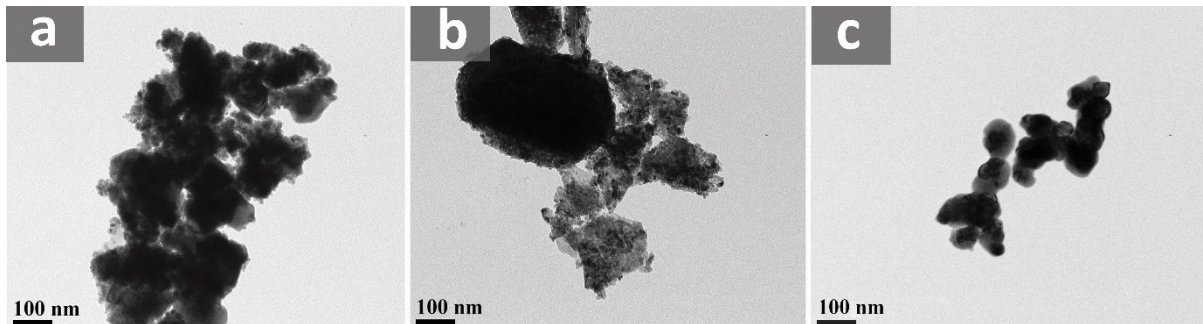


Figure 3-1 TEM images of fine (a) BZCYYb (b) NiO and (c) YSZ powder.

Pellets (1.5 cm diameter, 3 mm height) of NiO-YSZ, NiO-BZCYYb and BZCYYb were slip cast, sintered at 1450°C and reduced under hydrogen gas in a horizontal furnace. Table 3-1 shows the corresponding shrinkages (measured following sintering) and open porosities (measured following reduction) of the different pellets. According to this table, shrinkage of the NiO-BZCYYb falls

between the shrinkage of NiO-YSZ and the BZCYYb layer. Consequently, AFL as a buffer layer between the support and the electrolyte, alleviates the shrinkage mismatch and helps inhibit crack formation inside the electrolyte [110]. A disruptive shrinkage mismatch can affect the contact resistance between the layers. It can also be noted that as the content of NiO increases, open porosity increases from 37 to 49%. This is due to the formation of new open porosities around the reduced Ni grains which help the percolation of the larger pores formed by the pore former. Due to the small difference in composition of Ni90 and Ni85, the values of open porosity for these samples are close to each other. In addition, porosity measurement by Archimedes method contains specific errors. The standard deviation of each measurement is included in the table.

Table 3-1 Shrinkage and open porosity of different slip casted pellets, sintered at 1450°C and reduced by hydrogen gas. The NiO-YSZ pellets contained 30 vol.% graphite as pore former.

	BZCYYb	Ni:BZCYYb	Ni100	Ni90	Ni85	Ni75	Ni65
NiO:YSZ (wt%)	-	-	100:0	90:10	85:15	75:25	65:35
Ni:YSZ (vol.%)	-	-	100:0	82:18	75:25	61:39	50:50
Shrinkage (%)	17.0	25.0	31.5	34.2	34.1	34.1	33.5
Open Porosity (%)	-	-	48.79 ±0.17	42.51 ±0.69	42.85 ±0.38	37.69 ±0.71	37.01 ±0.92

Scanning electron microscopy (SEM) images of the slip cast support pellets containing 0, 10, 15, 25 and 35 wt% YSZ are provided in Figure 3-2. Pellets were sintered at 1450°C and reduced under humidified hydrogen. Similar magnifications provided in Figure 3-2 facilitate comparison of the microstructures. Based on Figure 3-2a and b, the nickel support (Ni100) (without the addition of YSZ) is highly susceptible to extensive grain growth following sintering at 1450°C (grain size between 2-8 μm). Figure 3-2b shows the formation of large cracks of the order of 10-20 μm inside

the slip cast pellet which can affect the mechanical integrity of the cell. It should be noted that part of the high open porosity of Ni100 is due to the formation of the aforementioned large cracks. Such cracks inside the support of the actual cell can lead to high ohmic and polarization resistance. The higher magnification in Figure 3-2a shows severe intergranular fracture and the formation of some voids most probably where smaller Ni grains are joined. The formation of large cracks inside sample Ni100 may increase the error in the values of shrinkage and open porosities of this sample in Table 3-1.

According to Figure 3-2c, addition of 10 wt% YSZ to the support improves the microstructure of the metal support significantly by inhibiting Ni grain growth. The initial grain size of Ni100 (2-8 μm) is reduced to 1-2 μm in Ni90. This represents a 50-75% decrease of grain size. Preventing the excessive Ni sintering with Ni90 provides a higher percolation of the gas diffusion channels. This is due to an increase in smaller interconnected pores in Ni90 rather than large intergranular pores in the Ni100 pellet. It has been shown that multi-scale architecture of anode supported cells with feature size decreasing from the support to the AFL (instead of an abrupt transition with large particle size difference) improves the thermomechanical properties of the fuel cell [199]. Figure 3-2d shows how reducing the grain size in Ni90 inhibited the formation of large cracks inside the pellet. The intergranular fractures existing in Ni100 can coalesce and turn into larger cracks (Figure 3-2a). Well joined nickel particles in Ni90 prevent crack propagation following sintering and reduction. Figure 3-2e-j show how addition of 15, 25 and 35 wt% YSZ affects the microstructure. Ni65 is the conventional Ni-YSZ support with 50:50 vol.% of Ni:YSZ which is widely being used by fuel cell researchers. As can be seen, the microstructural features show no significant differences compared with Ni90.

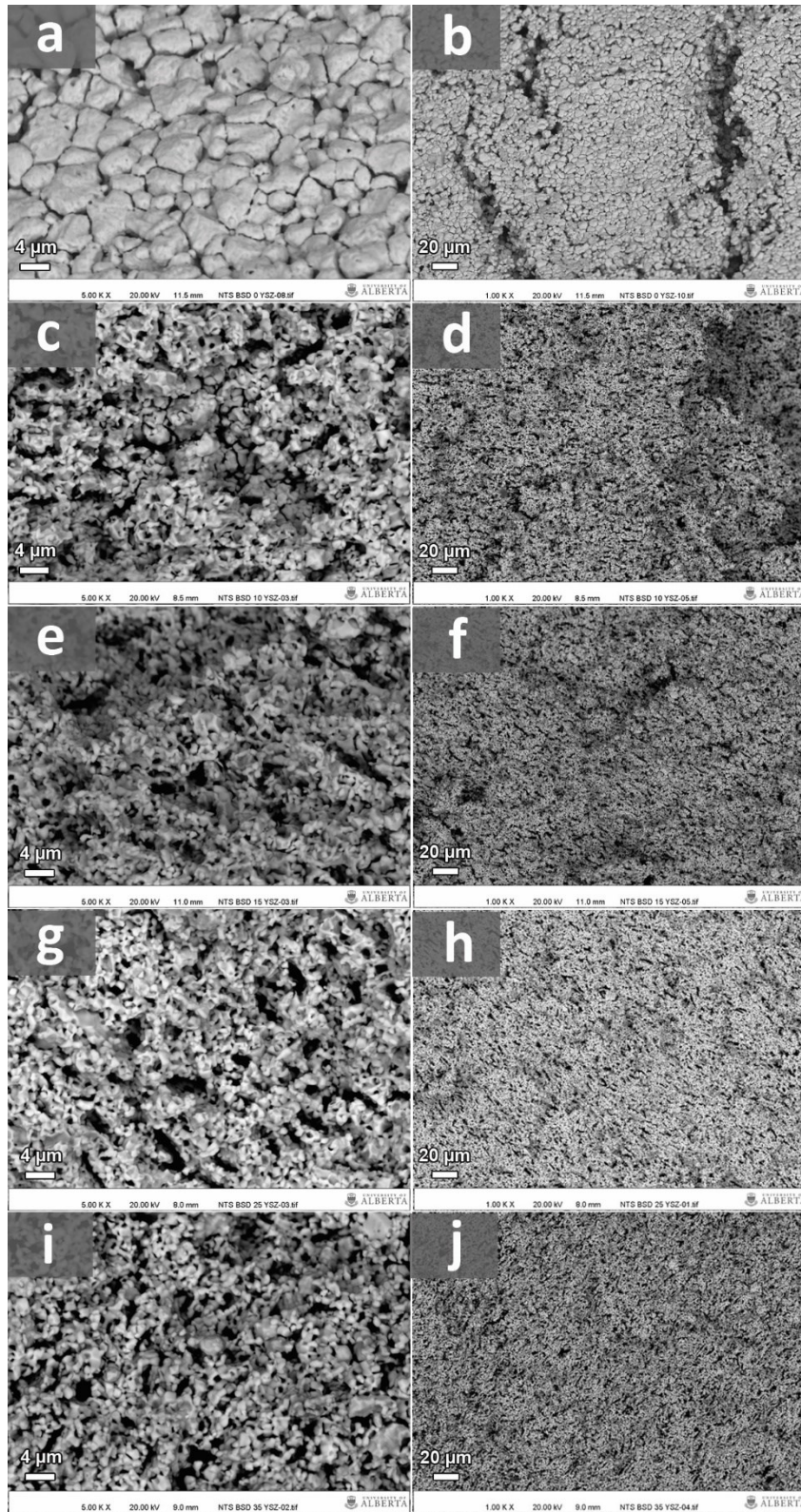


Figure 3-2 SEM micrographs of Ni-YSZ slip cast pellets with different weight ratios of NiO:YSZ for (a, b) Ni100 (c, d) Ni90 (e, f) Ni85 (g, h) Ni75 (i, j) Ni65. Pellets are described in Table 3-1.

Shrinkage data in Table 3-1 indicate that the Ni90 support has 34% shrinkage while Ni100 support has 32% shrinkage. The electronic conductivity of Ni-YSZ cermet doesn't follow a linear trend upon increasing the nickel content but rapidly increases when the Ni content reaches to ~ 30 vol. % [200]. At high Ni contents, the conductivity of the cermet follows a plateau [41,200,201]. The Ni90 support not only enjoys the high electrical conductivity of the metal supports but also has a more uniformly distributed porosity and higher mechanical strength than the Ni100 support. Based on this initial characterization, two fuel cells were fabricated using Ni100 and Ni90 as potential candidates for metal supported tubular SOFCs. The electrochemical performance and post-mortem microstructural variations are discussed in the following sections.

3.3.2 Post-mortem SEM analysis of the cells

Cross-sectional SEM micrographs of the cells following SOFC operation are shown in Figure 3-3. According to Figure 3-3a, b and c, the support of the Ni100 cell experienced large Ni grain growth accompanied by 50-100 μm cracks. Bae et al. [174] have also reported extensive Ni growth in Ni-BaZr_{0.85}Y_{0.15}O_{3- δ} AFL at 1450°C for 10 h which made coating of the subsequent thin layer difficult. Due to the difference in the thermal expansion coefficient of Ni and BZCYYB phases, there is extensive grain growth of Ni grains as well as large crack formation inside the support of the Ni100. This caused deformation of the AFL and the electrolyte as shown in Figure 3-3a. The attachment of large grains of Ni (10 μm) inside the support of the Ni100 cell in Figure 3-3b is full of cracks similar to the intergranular fractures taking place in Figure 3-2a (in the pellet sample). In both cases, severe Ni growth affected the Ni-Ni contact surface. Studies on in-situ reduction of NiO-YSZ composites show that reduction of Ni grains initiates at the NiO-YSZ interface or at the NiO free surface and is gradually extended to the bulk of the NiO grains [202]. The reduction of NiO to Ni produces nanoporosity due to volume contraction of more than 40% [203]. By increasing

the reduction temperature, the produced nanopores coalesce and Ni particles become porous as evidenced in Figure 3-3b.

Figure 3-3d and e show the microstructure of cell Ni90. Addition of 10 wt% YSZ prevented large crack formation inside the support. Furthermore, the electrolyte and AFL are intact with no visible deformation (Figure 3-3d). Elongated flake-like pores from the graphite are visible inside the anode support (Figure 3-3e). It is noteworthy that the contact surface of the support/AFL is very uniform and the AFL as a buffer layer can effectively moderate the mechanical stress induced in the electrolyte during sintering and reduction steps. One of the beneficial impacts of YSZ is to inhibit Ni growth as has been mentioned by the other researchers [204–206]. In the current study we clearly experienced this constructive function of YSZ in the Ni-YSZ anode support.

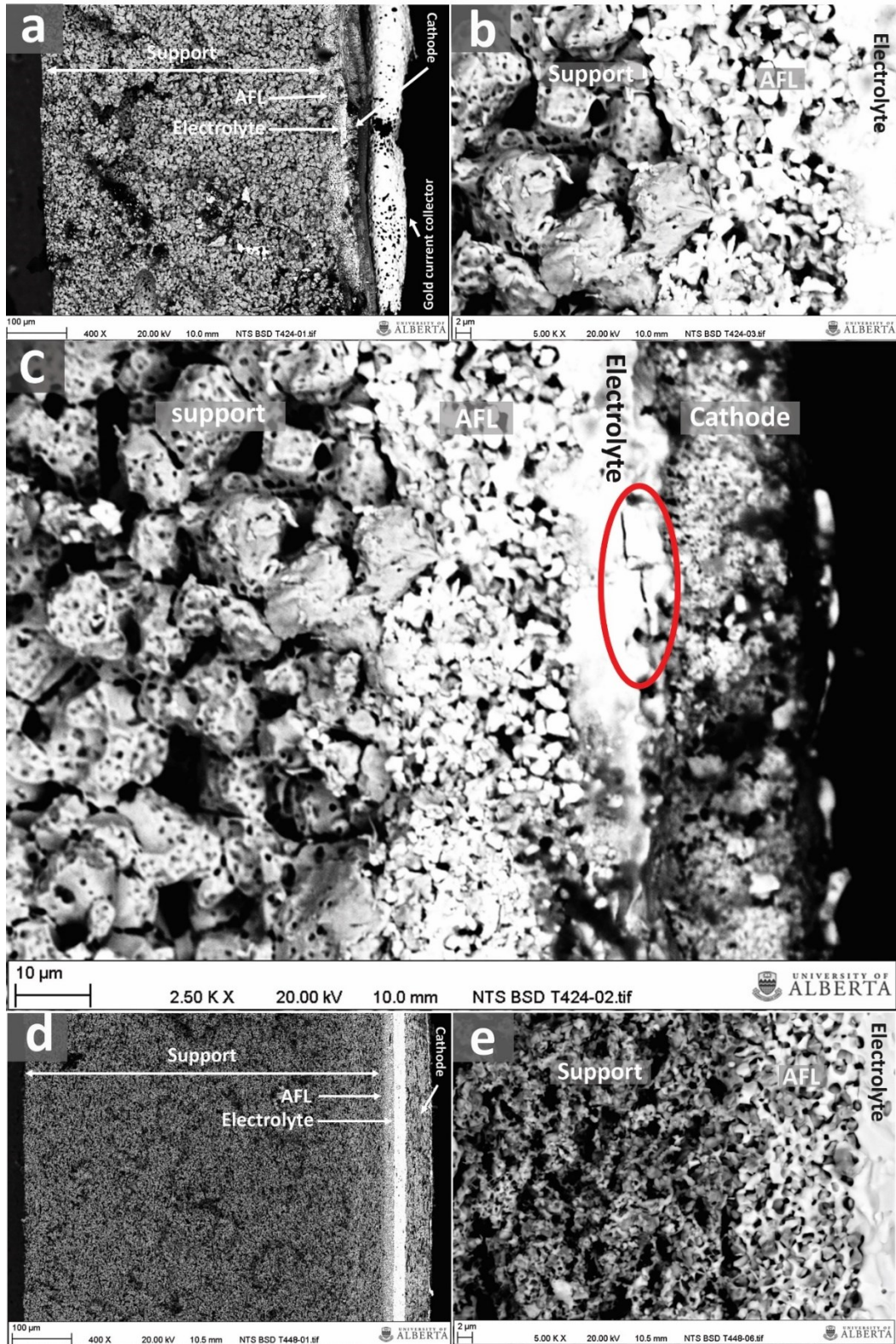


Figure 3-3 Post-mortem SEM micrographs of the cells after SOFC testing for (a, b and c) Ni100 cell and (d, e) Ni90 cell. The red oval in (c) shows the crack formed inside the electrolyte.

3.3 SOFC electrochemical performance under humidified hydrogen

The current-voltage-power curves and EIS spectra for cells Ni100 and Ni90 are shown in Figure 3-4. Both cells were tested with 3 vol.% humidified hydrogen and a flow rate of $10 \text{ mL} \cdot \text{min}^{-1}$. The open circuit voltage (OCV) values of the cell Ni100 in Figure 3-4a are 0.94, 0.91, 0.88 and 0.85 V at 600, 650, 700 and 750°C, respectively, which are less than the corresponding OCV values of the cell Ni90 (1.08, 1.05, 1.02 and 0.98 V) in Figure 3-4b. According to Figure 3-3b, severe Ni grain growth up to $10 \mu\text{m}$ took place inside the Ni100 support. The mechanical stress arising during Ni grain growth and following reduction of the large Ni particles caused crack formation inside the electrolyte of cell Ni100 (Figure 3-3c). In a lower magnification in Figure 3-3a, deformation of the electrolyte can also be noticed which can be affected by the large cracks formed inside the support. Due to such microstructural defects, the OCV of cell Ni100 decreased from the theoretical value at each temperature. Addition of 10 wt% YSZ to the support in cell Ni90 optimized the microstructure of the cell (Figure 3-3d and e) and the OCV value was recovered as can be seen in Figure 3-4b. The peak power density (PPD) of the two cells is almost the same according to Figure 3-4e with values of 109, 146, 178 and 205 $\text{mW} \cdot \text{cm}^{-2}$ for cell Ni90 at 600, 650, 700 and 750°C, respectively. Regardless of the similar PPD of the two cells, the non-optimized microstructure of cell Ni100 did not show a high OCV and was unstable at fuel flow rates above $10 \text{ mL} \cdot \text{min}^{-1}$.

The Nyquist plots of the cells are shown in Figure 3-4c and d. The high frequency intersection of the impedance with the real axis is attributed to the ohmic resistance of the cell (R_{ohm}). The values of R_{ohm} decreased by increasing the temperature due to an improved ionic conductivity of the YSZ electrolyte. According to Figure 3-4f, the R_{ohm} of the two cells show similar values at each temperature with a slightly increased R_{ohm} for cell Ni100 at lower temperatures. However, the difference in polarization resistance of the two cells is more noticeable in Figure 3-4f. The total

polarization resistance of cell Ni100 is 68%-123% more than cell Ni90. Based on Figure 3-4f, the value of the activation energies for R_{ohm} of Ni100 and Ni90 are 0.17 and 0.34 eV, respectively, while for R_p they are 1.25 and 1.24 eV. Despite having similar activation energies for R_p , the value of R_p is reduced for the cell Ni90 by tailoring the microstructure.

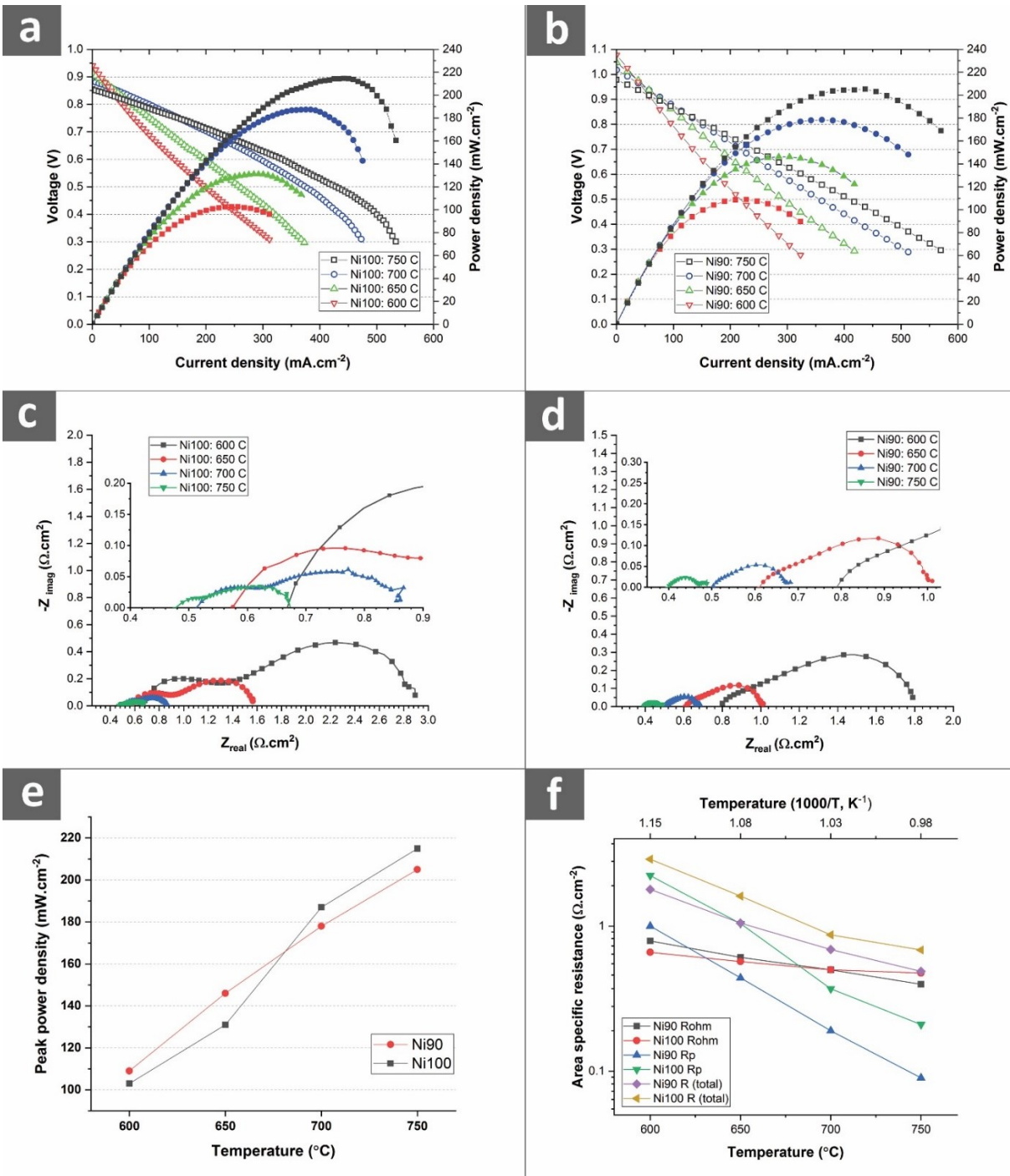


Figure 3-4 (a) Current density-voltage-power curves of (a) cell Ni100 and (b) cell Ni90 at different temperatures. The flow rate of the fuel (3 vol.% humidified hydrogen) was $10 \text{ mL} \cdot \text{min}^{-1}$. (c) Nyquist plot of the cell Ni100 and (d) cell Ni90. (e) Peak power densities of the cells. (f) Area specific resistance of the cells Ni100 and Ni90 as temperature varied.

Distribution of relaxation times (DRT) plots for the two cells are shown in Figure 3-5. Four peaks are noticeable in Figure 3-5: the high frequency peaks of R1 and R2, medium frequency peak of R3 and low frequency peak of R4. DRT graphs reveal that the characteristic frequency of the same peak is higher for cell Ni100 compared to cell Ni90. The corresponding area specific resistances (ASR) at different operating temperatures are extracted from the Nyquist plots by an equivalent ohmic resistance (R_{ohm}) in series with four R-CPE elements and summarized in Table 3-2. Peak R4 which takes place at low frequencies is insignificantly influenced by the temperature variations and is attributed to concentration polarization inside the electrodes. Concentration polarization in proton conductor SOFCs is not dominant at Ni-PCE electrodes since the electrochemical reactions occur and the resulting water product forms in the thin cathode layer. Therefore, the anode of PCE cells and its support do not need to be as porous as oxygen ion conducting SOFCs [171]. Peak R1 takes place at high frequencies and its values increase at lower temperatures. The characteristic frequency of peak R1 shifts to higher frequencies by reducing the temperature according to the DRT plots in Figure 3-5a and b.

Studies on DRT analysis for PCE SOFCs are limited in the literature. Attribution of individual DRT peaks to the anodic or cathodic reaction requires changing the fuel or oxidant concentration at the anode or cathode side. A recent study on an SOFC with Ni-BaCe_{0.55}Zr_{0.3}Y_{0.15}O_{3- δ} (Ni-BCZY) anode [207], revealed the high frequency peak R1 is more dependent on variations of hydrogen gas at the anode side. The value of the peak R1 increases at lower temperatures. As mentioned, the characteristic frequency of peak R1 shifts to higher frequencies by reducing the temperature according to the DRT plots in Figure 3-5a and b. According to Table 3-2, the value of R1 at 600°C reduces from 0.45 for cell Ni100 to 0.22 $\Omega \cdot \text{cm}^2$ for cell Ni90. This reduction in the resistance can be attributed to improved support/AFL interface in the anode of cell Ni90 which

facilitates hydrogen dissociation, oxidation and diffusion to the accessible TPBs and the anode/electrolyte interface.

The medium frequency peak R3 is attributed to the electrochemical reactions taking place at the cathode [207]. The characteristic frequency of peak R3 shifts to lower frequencies at lower temperatures. According to Table 3-2, there is still higher resistance for R3 of cell Ni100 than cell Ni90. Considering the relatively fast kinetics of proton diffusion at the cathode/electrolyte interface for the production of hydroxide/water, the intrinsic properties as well as the microstructural features of the cathode can be the rate determining factors for oxygen dissociation, reduction and diffusion at TPBs inside the cathode. Regardless of the fact that both cathodes had the same composition, comparing the microstructure of the cathodes in Figure 3-3a and d shows the cathode of cell Ni100 is affected by the mechanical stress induced by the large Ni particles inside the support while the cathode of cell Ni90 seems intact. Figure 3-3a shows how the whole electrolyte and cathode are susceptible to be deformed by deformation of the support. Changing the microstructure of the cathode can change the distribution of TPBs close to the cathode/electrolyte interface and increase the resistance of peak R3 as can be seen in Table 3-2. This shows a non-optimized support as the thickest component of the cell can readily affect the other components of the cell. Peak R2 takes place at frequencies between R1 and R3 and disappears at temperatures above 650°C for Ni90 as shown in Figure 3-5b. Due to the uncertainty in the accuracy of fitting the value of the R2-CPE element at 700 and 750°C, this element was neglected for the aforementioned temperatures. Peak R2 might be the sum of two resistances in the anode and cathode with similar time constants which are affected either by changing the concentration of the oxidant or the fuel. Further studies on SOFCs based on the BZCYYb electrolyte are required to elucidate the nature of this peak. According to Table 3-2, the values of

R1 and R3 as the main contributors to the polarization resistance are lower for cell Ni90. The reduction in polarization for cell Ni90 can be related to:

1. The higher density of active TPBs at the AFL/support interface with smaller Ni grains and higher surface area.
2. The uniform distribution of the fuel at the AFL/support interface with highly interconnected pores inside the support.
3. Higher charge-transfer rates at the electrolyte/electrode interface when the electrolyte is not deformed due to mechanical stresses induced by large Ni grains inside the support.

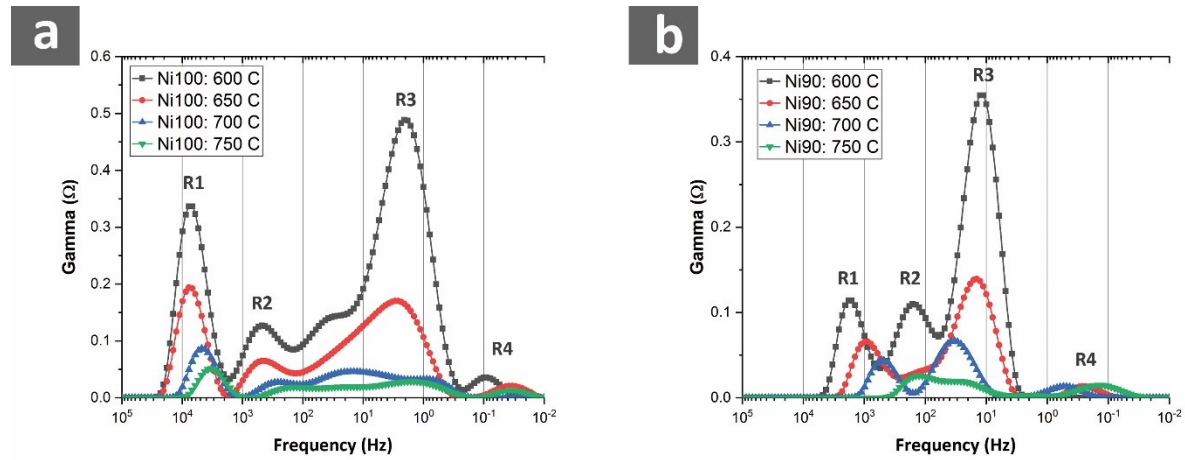


Figure 3-5 Distribution of relaxation times (DRT) for (a) cell Ni100 and (b) cell Ni90 at different temperatures.

Table 3-2 The values of area specific resistance components for cells Ni90 and Ni100 fitted with the equivalent circuit of the Nyquist plots in Figure 3-4c and d.

	Temperature (°C)	R_{ohm} ($\Omega \cdot cm^2$)	R1 ($\Omega \cdot cm^2$)	R2 ($\Omega \cdot cm^2$)	R3 ($\Omega \cdot cm^2$)	R4 ($\Omega \cdot cm^2$)	R_p ($\Omega \cdot cm^2$)	R_{total} ($\Omega \cdot cm^2$)
Ni100	600	0.66	0.45	0.55	1.20	0.03	2.23	2.89
	650	0.57	0.30	0.16	0.57	0.01	1.04	1.61
	700	0.50	0.12	-	0.23	0.02	0.37	0.87
	750	0.48	0.06	-	0.13	0.02	0.21	0.69
Ni90	600	0.79	0.22	0.29	0.48	0.02	1.01	1.8

	650	0.59	0.12	0.06	0.23	0.03	0.44	1.03
	700	0.50	0.08	-	0.12	0.02	0.22	0.72
	750	0.39	0.02	-	0.06	0.03	0.11	0.5

Figure 3-6 shows the higher power performance of the as fabricated Ni-supported cell (Ni90) with the conventional Ni-YSZ supported cell (Ni65) at 600 and 700°C. While the peak power densities of the Ni65 cell are 166 and 285 $\text{mW}\cdot\text{cm}^{-2}$ at 600 and 700°C, the peak power densities for cell Ni90 are 189 and 326 $\text{mW}\cdot\text{cm}^{-2}$ at corresponding temperatures. This stands for a 14% boost in the cell performance. It should be noted that the fuel flow rate for cell Ni90 is half of the fuel flow rate for cell Ni65. At the same fuel flow rates, the boost in performance would be even more noticeable for Ni90. This comparison of performance shows that it is possible to decrease the content of YSZ in the Ni-YSZ support to as low as 10 wt% to benefit the high electrical conductivity of the support as well as to ease current collection similar to other metal supported fuel cells.

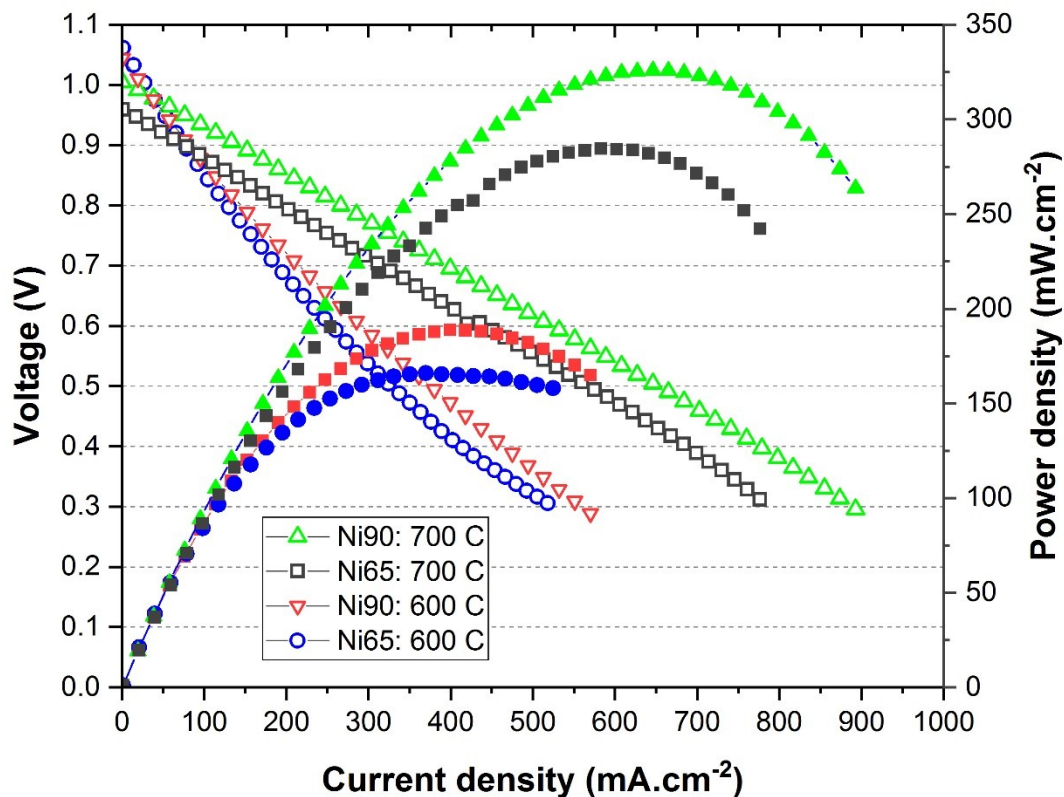


Figure 3-6 Power densities of the two cells Ni90 and Ni65 at 600 and 700°C. The fuel (3 vol.% humidified hydrogen) flow rate for cell Ni90 was 25 mL·min⁻¹ and the fuel flow rate for cell Ni65 was 50 mL·min⁻¹.

The nanometer-sizes of the initial Ni particles are highly susceptible to grain growth at the elevated temperatures. The use of YSZ as a growth inhibitor for Ni is better reflected when using very fine Ni particles as the raw material. In this study very fine NiO particles were used to fabricate a PCE cell based on a Ni-YSZ support since using fine NiO particles enables matching the sintering shrinkage among the support, AFL and PCE electrolyte. To shed more light on the importance of adding YSZ as a Ni growth inhibitor, a half-cell with initially larger NiO particles (J. T. Baker, average particle size: 250 nm) was fabricated with the same support composition as the Ni100 cell. Comparing the two support microstructures in Figure 3-7a and Figure 3-7b indicates that the initial

larger particles of NiO-Baker led to final microstructural features (grain size, porosities) to be smaller than the corresponding support microstructure of the Ni100 cell which used 50 nm NiO particles. Nanometer-size NiO particles of the Ni100 support are more susceptible to grain growth during sintering compared with NiO-Baker. The sponge-like porous Ni morphology after reduction can also be noticed for the cell with NiO-Baker in Figure 3-7b. Addition of 10 wt% YSZ to the Ni100 cell (Figure 3-7c) modified the metal support in terms of microstructural stability and kept the microstructural features even finer than the NiO-Baker cell. Using a small amount of YSZ, a stable microstructure for a PCE cell can be engineered.

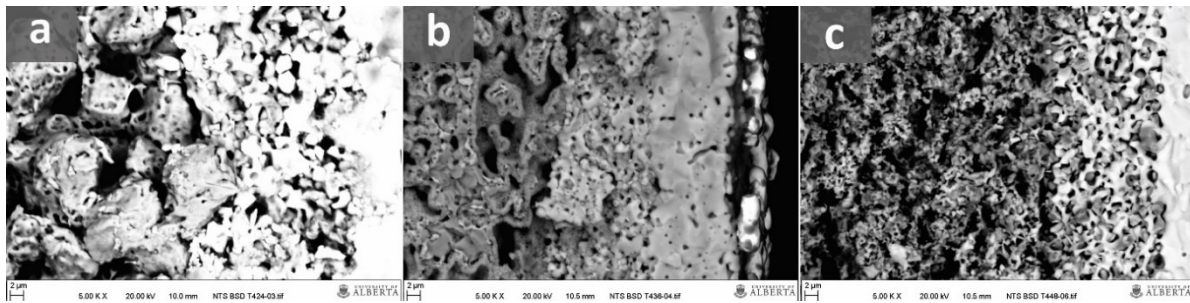


Figure 3-7 SEM micrograph of (a) Ni100 cell (b) half-cell with 100 wt% Ni metal support, Ni-BZCYYb AFL and BZCYYb electrolyte. The initial NiO powder used to fabricate this cell is NiO Baker. (c) Ni90 cell. All cells were sintered at 1450°C and reduced by hydrogen

Figure 3-8a shows a potentiostatic test of the cell Ni90 for 67 hours at 0.7 V. No degradation took place during the period of testing. A slight improvement in the performance of the cell is noticeable at the beginning of the stability test which reaches a plateau. A similar behavior was observed by another research group on a SOFC with a Ni-BZCYYb anode [171]. Comparing the EIS results before and after the potentiostatic test in Figure 3-8b reveals a decrease of ohmic resistance after the potentiostatic test. The initial improvement in the stability test can be due to completion of the reduction process and reorientation of Ni grains inside the support (considering the high Ni content

inside the support). Consequently, a higher electrical conduction path will be provided gradually until stabilization of the microstructure and reaches a plateau after 40 h of operation in Figure 3-8a.

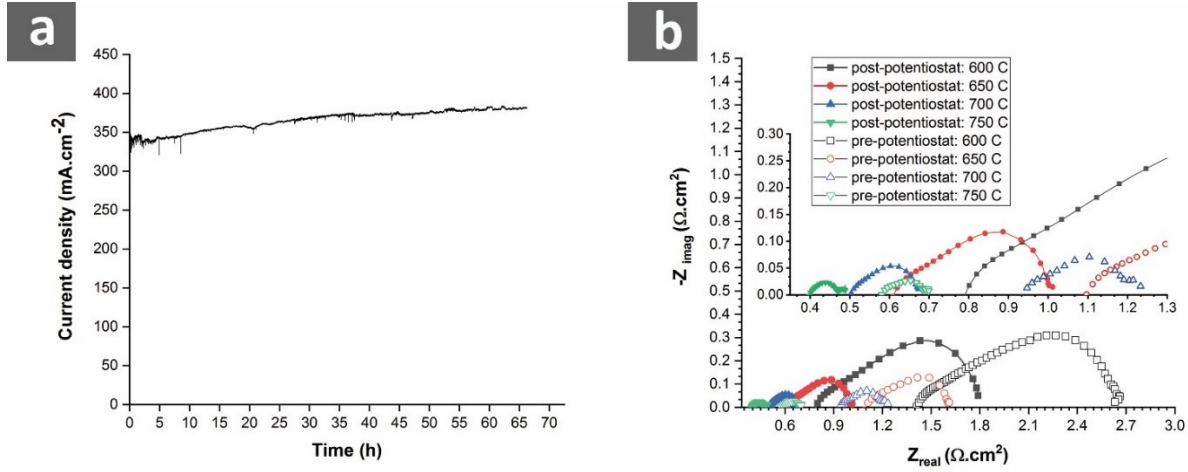


Figure 3-8 (a) Potentiostatic operation of the cell Ni90 for 67 hours at 0.7 V and 700°C in SOFC mode. The flow rate of the fuel (3 vol.% humidified hydrogen) was 10 mL·min⁻¹. (b) Nyquist plot of the cell Ni90 before (pre-potentiostat) and after (post-potentiostat) the potentiostatic test at 600, 650, 700 and 750°C.

3.4 Conclusions

In this study nickel supported proton conducting fuel cells were fabricated for low temperature applications. The results show that the addition of 10 wt% YSZ to the Ni support (Ni90 cell) prevented severe Ni grain growth inside the Ni support (Ni100) and stopped crack formation inside the support and the electrolyte. The Ni90 cell shows higher OCV and lower polarization resistance compared to the Ni100 cell due to more accessible TPB sites at the support/AFL contact surface, better distribution of the fuel gas at the AFL surface and a more relaxed microstructure (less internal stress on different layers). The performance of the metal supported cell (Ni90) was also compared with the conventional Ni65 (NiO:YSZ = 65:35 wt%) fuel cell which showed superior performance. This shows the importance of optimization and utilization of metal supported cells in SOFC applications. The slip casting method used to fabricate the metal supports is a well-

established approach to fabricate fuel cells. The long-term stability and thermal shock resistance of the new cells will be tested in the future to assess the feasibility for mobile applications for which a rapid temperature increase is a necessity.

Acknowledgments

The authors would like to acknowledge Future Energy Systems (FES) and the Climate Change and Emissions Management Corporation (CCEMC) of Canada for funding this research.

Chapter 4: Tailoring the SOFC Anode-support Composition and Microstructure for Low-temperature Applications

Sajad Vafaeenezhad^{1*}, Amir Reza Hanifi^{1,2}, Mark Cuglietta³, Mohtada Sadrzadeh², Partha Sarkar¹ and Thomas H. Etsell¹

¹Department of Chemical & Materials Engineering, University of Alberta, Edmonton, Alberta T6G 1H9, Canada

²Department of Mechanical Engineering, University of Alberta, Edmonton, Alberta T6G 1H9, Canada

³C-FER Technologies, Edmonton, Alberta T6N 1H2, Canada

Abstract

In this research, the performance of a tubular fuel cell based on a Ni-YSZ (yttria stabilized zirconia) anode support containing 82 vol.% of Ni (Ni82) is compared with a cell containing the conventional Ni-YSZ support with 50 vol.% Ni (Ni50). A Ni-YSZ buffer layer with a tailored microstructure was added to the Ni82 support layer to provide intermediate porosity, higher ionic conductivity and to reduce the thermal expansion mismatch with the anode functional layer. Both cells were tested using infiltrated $\text{Nd}_2\text{NiO}_{4+\delta}$ (NNO) cathodes. High peak power densities of 790 and 478 $\text{mW}\cdot\text{cm}^{-2}$ were achieved at 600 and 550 °C, respectively, for the Ni82 cell which were 25% and 87% higher than the performances for the conventional cell at respective temperatures. In addition, no degradation was found during four redox cycles at 550 °C, making this support an attractive candidate for low-temperature SOFC applications.

Keywords: Electrolyte, Microstructure, Ni-YSZ, SOFC, YSZ.

4.1 Introduction

Solid oxide fuel cells (SOFCs) are devices that directly convert the chemical energy of hydrogen or hydrocarbons [208] into electricity and heat using electrochemical reactions [209–211]. The operating procedure of SOFCs doesn't involve the burning process [212] which turns them into high-efficiency energy conversion devices. Traditionally, SOFCs operate at high temperatures (800-1000 °C) due to the limitation of the electrolyte's conductivity at lower temperatures. But operating at high temperatures accelerates the degradation of the cell components. Thus, the SOFC community has been constantly trying to reduce the operation temperature of SOFCs while maintaining the stability and high performance of the cells.

Low-temperature SOFCs (LT-SOFCs) operate at 400-650 °C. Thermally-induced microstructural changes are slower at lower temperatures which lengthens the life span of SOFCs. Therefore, lower-cost materials for the balance of plant and interconnects can be used [213]. In addition, heat exchange costs and thermal insulation requirements will be reduced [6]. For this purpose, lowering the different polarization components, particularly ohmic and activation polarization, is important. Thickness of the electrolyte, electronic conductivities of the electrodes, attachment of the different layers inside the cell, and contact resistance at the points of current collection also affect the measured ohmic resistance of the cell.

Using anode supported SOFCs, fabrication of thinner electrolytes down to 2.5 μm is possible which can further reduce the operation temperature of SOFCs [214]. As a result, the ionic transfer path inside the electrolyte is shortened which lowers the ohmic resistance of the cell. A mixture of Ni and YSZ to make a composite anode extends the effective electrochemical reaction zone from the 2D anode/electrolyte interface into a 3D region [215] called the anode functional layer (AFL). This leads to an increase in the number of three-phase boundary (TPB) sites, a reduction of the

activation polarization at the anode and improvement of the electrical efficiency. YSZ provides ionic conductivity for the anode, inhibits Ni grain growth during sintering and operation, and reduces the thermal expansion coefficient (TEC) mismatch between the anode and electrolyte [215]. An AFL with 40-50 vol.% Ni content is the established composition for stable and high performing conventional SOFC anodes [216]. Electrochemical performance of the anode is largely limited by the density of active TPBs between Ni, YSZ and pores [137,216] as well as interconnected gas diffusion paths inside the anode [217]. These parameters are strongly influenced by microstructural features such as the size, composition and distribution of Ni, YSZ and pore phases [37,218]. The anode support is responsible for transferring the generated electrons to the current collector and also providing mechanical integrity for the cell. The percolation threshold for electrical conductivity of the anode is at 30 vol.% Ni [219]. Below this volume fraction, the support is mainly an ionic conductor while above this value, the conductivity can reach three orders of magnitude higher at 60 vol.% Ni [219].

A large TEC mismatch can lead to cracking of the electrode or the electrolyte [220]. Metal-supported SOFCs (MS-SOFCs), for example, using nickel or ferritic steel as the support, offer an attractive alternative to conventional SOFC designs because of the durability that can be imparted to the cell by the support. Metal supports are also cheaper than conventional Ni-YSZ supports, and provide better stability during rapid thermal and redox cycling due to their high ductility and thermal conductivity [221–223], and offer fast start-up capability [224]. MS-SOFCs are capable of expanding the traditional fuel cell applications to portable SOFCs [188,190]. In addition, the thermal expansion coefficient of ferritic stainless steel supports is compatible with the YSZ electrolyte [189]. However, there are challenges associated with nickel or stainless steel MS-SOFCs such as oxidation or coarsening of the metal support [225,226], and interdiffusion of Fe,

Cr and Ni at the support/AFL interface in the case of stainless steels [189,227,228]. These effects necessarily limit operation of a metal-supported SOFC to temperatures typically less than or equal to 800 °C, which nevertheless makes them perfectly suitable for LT-SOFC designs. Diffusion of Ni into a ferritic stainless steel support causes the ferritic matrix to partially change into an austenitic structure and the coefficient of thermal expansion increases, which leads to internal cracks in the support [193]. Addition of a diffusion barrier layer between the support and AFL can limit the diffusion [194].

A Ni support offers benefits of high performance and conductivity due to its superb catalytic activity in reducing environments. Moreover, there is no need for barrier layers since no oxide scales or unwanted diffusion takes place in the Ni supports during normal cell operation. However, severe Ni coarsening, which can lead to pore shrinkage or expansion, particularly at higher temperatures or in the presence of steam (e.g., at high fuel utilization rates), as well as redox instability in pure Ni supports can induce mechanical stress due to the associated volume change in the support. This leads to crack formation and its propagation to the electrolyte [189,229,230].

To reduce the operation temperature even more, optimization of the electrode microstructure and utilization of materials with higher catalytic activity are necessary. Choosing cathode materials with higher ionic and electronic conductivities can significantly reduce the operation temperature of the cell by increasing the oxygen reduction reaction (ORR) rate. Conventional manganese-based perovskite cathodes such as $\text{La}_{1-x}\text{Sr}_x\text{MnO}_3$ (LSM) have a low ionic conductivity at low temperatures [231]. In addition, many of the mixed electronic and ionic perovskites such as $\text{La}_{0.6}\text{Sr}_{0.4}\text{Co}_{0.2}\text{Fe}_{0.8}\text{O}_{3-\delta}$ (LSCF) with faster ORR at lower temperature suffer from Sr segregation [232]. By contrast to conventional perovskite cathodes, Ruddlesden-Popper perovskite materials such as NNO and $\text{Pr}_2\text{NiO}_{4+\delta}$ (PNO) show excellent stability and oxygen exchange kinetics at low

temperatures since they don't contain alkaline earth metals and can avoid segregation problems [233].

There are two approaches for applying of cathode layer. The conventional approach includes synthesis of the cathode particles and heat treating them at 1000-1100 °C for single phase formation. Then applying the cathode onto the electrolyte using methods such as screen printing and sintering at elevated temperatures [234–237]. Infiltration of oxygen electrode material inside a porous scaffold can be an alternative approach for fabrication of high performing LT-SOFCs. Infiltrated particles, which are often calcined at temperatures below 1000 °C, have higher surface area compared to conventional cathode materials, which are sintered at 1100-1200 °C. Using an infiltrated cathode, a high active TPB length is achievable which increases the ORR rate at lower temperatures [83]. Laguna-Bercero et al. achieved a peak power density (PPD) of $400 \text{ mW} \cdot \text{cm}^{-2}$ at 600 °C in a Ni-YSZ/YSZ/NNO infiltrated YSZ scaffold [93]. Chen et al. [94] infiltrated NNO into a scandia stabilized zirconia (SSZ) scaffold and used a SSZ electrolyte and Ni-YSZ support. They achieved a PPD of $280 \text{ mW} \cdot \text{cm}^{-2}$ at 650 °C ($\text{H}_2:\text{H}_2\text{O} = 50:50 \text{ vol.}\%$) under SOFC mode. They also noticed that the activation polarization was higher when screen printed NNO was used compared with infiltrated NNO. Dogdibegovic et al. [224] studied the performance of different infiltrated Ruddlesden-Popper cathodes including NNO and PNO. They achieved a PPD of $1 \text{ W} \cdot \text{cm}^{-2}$ at 700 °C using NNO infiltration inside the cathode scaffold and co-infiltration of Ni and Sm-doped ceria (SDC) inside the anode scaffold.

Minimizing electron pathways length for current collection in SOFCs is critical to lower the ohmic resistances [238,239]. Due to the geometric design of tubular cells, current collection takes place in radial and axial directions (current collection pathway in Figure 4-1) which increases the current collection pathway length. In addition, mechanical compression is not easily provided in the

tubular design. If the support is not highly conductive, gradual loss of contact due to lack of mechanical pressure between the current collector and the support increases the ohmic resistance of the cell and leads to power loss [209]. Different methods have been used to improve current collection of the tubular SOFCs including a current collector brush with carbon fiber bristle and Inconel stem [240], or using pure nickel foam [241]. Previously, the authors studied the possibility of using a slip cast porous nickel metal support as the current collector in proton conducting SOFCs. It was found out that addition of small amounts of YSZ to the Ni support plays an important role in preventing crack formation inside the support, preventing Ni grain growth and aiding densification of the YSZ electrolyte [229].

In the present study, a high performing LT-SOFC is fabricated using a high nickel content support, by engineering its microstructure and addition of a buffer Ni-YSZ layer between the support and the anode functional layer (AFL). The performance of the new cell is compared with a conventional cell having an identical cathode, electrolyte and AFL. Finally, robustness of the cell is validated using four redox cycles at 550 °C. The high nickel content support has low ohmic resistance, shows the characteristics of metal supports and is an attractive support and current collector candidate for LT-SOFCs.

4.2 Experimental procedures

Two cells (2 cm² active area each) with different anode support compositions were fabricated: Ni50 cell with conventional Ni:YSZ volume ratio of 50:50 (NiO:YSZ weight ratio = 65:35) and Ni82 cell with Ni:YSZ volume ratio of 82:18 (NiO:YSZ weight ratio = 90:10). Ni82 cell has an additional thin (40 μm) Ni-YSZ buffer layer with Ni:YSZ volume ratio of 50:50 and additional porosity between the highly conductive anode support and the functional layer. This buffer layer

reduces the thermal expansion differences between the two layers and eliminates the possibility of crack formation. The rest of the layers including the electrolyte and cathode layer are identical for both cells.

4.2.1 Fabrication of the anode support

Slip casting was used for fabrication of the anode supports. Two different supports were slip cast using NiO (J. T. Baker, average particle size of 250 nm) to YSZ (Tosoh TZ8Y, 8 mol% Y_2O_3) weight ratios of 65:35 or 90:10. Powders were added to the water (weight ratio of 40:60) and zirconia balls. pH of the slip was set to 4.0 using hydrochloric acid to obtain a stable slip. The mixture was milled for 2 h using a rotary ball mill at 70 rpm. Afterwards, graphite (30 vol.% with 4.5 μm average particle size) was added to the suspension and milled again for 15 minutes. Finally, the slip was sonicated using an ultrasound bath for 3 minutes and cast into plaster molds. Supports were dried at room temperature and pre-sintered at 950 °C for 3 h.

4.2.2 Coating of the anode buffer layer and functional layer

For the Ni82 cell, an additional thin NiO-YSZ layer (buffer layer) was coated before coating the anode functional layer (AFL). Buffer layer slurry for dip coat is prepared by mixing NiO:YSZ powders (65:35 weight ratio), graphite (30 vol.%), ethanol (1:4 weight ratio) and binder (6 wt% ethyl cellulose in terpineol) using a ball mill for 2 h. Ultrasound bath was used for one minute before each dip to provide a homogenous suspension. The buffer layer was coated onto the Ni82 supports using 5 dip coats and 10 minutes drying time between each coat. Then the supports were dried at room temperature and heat treated at 900 °C for 3 h. AFL slurry was prepared similarly without the addition of any graphite. Two dips of AFL were coated onto the Ni82 and Ni50 supports, dried at room temperature and heat treated at 900 °C for 3 h.

4.2.3 Coating of the electrolyte layer

A thin YSZ electrolyte layer was coated onto the cells using a dip coating method. YSZ and ethanol (1:8 weight ratio) and binder (6 wt% ethyl cellulose in terpineol) were milled for 1 h using zirconia balls in a planetary mill. The suspension was then sonicated for 3 minutes using an ultrasound bath. Dip coating was performed by dipping the supports into the electrolyte suspension once and holding it for 10 seconds. They were then dried at room temperature and sintered at 1400 °C for 3 h. Another set of dip coating was performed following sintering with a YSZ suspension with 1:10 solid loading and sintered again at 1400 °C for 3 h to achieve better sealing.

4.2.4 Coating of the YSZ scaffold and cathode infiltration

An infiltration method was used for fabricating the cathode. First, a thin YSZ scaffold layer was coated onto the electrolyte using dip coating. To generate sufficient porosity inside the scaffold, Tosoh YSZ powder (250 nm average particle size) was calcined at 1500 °C for 3 h and then milled for 48 h. The dip coat suspension was prepared by mixing calcined and milled YSZ powder with ethanol, dispersant (Menhaden fish oil in azeotropic solvent) and binder (6 wt% ethyl cellulose in terpineol). The scaffold was heat treated at 1300 °C for 3 h to achieve proper attachment with the electrolyte. NNO was infiltrated into the YSZ scaffold. Briefly, neodymium and nickel nitrates with stoichiometric ratios were mixed with water (5 M) and surfactant (Triton X-100) using a magnetic stirrer. The temperature of the viscous solution was increased to 70 °C and a few drops were added onto the YSZ scaffold. The excess infiltrate solution was cleaned using a tissue and the cell was heat treated at 350 °C for 15 minutes for the nitrates to decompose. This process was repeated twice and the solid loading of the nitrates in the YSZ scaffold reached 30 wt%.

4.2.5 Fuel cell setup and electrochemical testing

Schematic of the test setup is shown in Figure 4-1. The tubular cells were attached to mullite tubes using Ceramabond 552 (Aremco) cement. Hot glue was used to seal the outlet of the mullite tube. Ag paste (Fuel Cell Materials) was coated onto the anode and Ag wire (Alfa Aesar) was wrapped around the anode as the anode current collector. In the Ni50 cell which had lower support conductivity, copper mesh (Alfa Aesar) was also rolled and pushed inside the anode to help with current collection. Gold paste (Heraeus) and gold wires were used as the cathode current collector. The cell was placed in the hot zone of a tubular furnace and a thermocouple was placed next to the testing area. Anode was reduced using a mixture of nitrogen and humidified hydrogen (3 vol.% H₂O) with flow rates of 45 and 5 SCCM, respectively, over 24 h. Then the gas mixture was gradually switched to 0 SSCM of nitrogen and 50 SSCM of hydrogen in 1 hr. Flow of air to the cathode side was set at 150 SCCM. Electrochemical impedance spectroscopy (EIS), IV and OCV measurements were performed using a Metrohm Autolab potentiostat with 10 A booster and FRA32M module for impedance measurements in four probe configurations.

Microstructural analysis was carried out using a Zeiss Sigma 300 VP-FESEM scanning electron microscope. Image J software was used to analyze the SEM images of the polished samples. Matlab optimization toolbox with combination of DRTtools was also used to extract distribution of relaxation time (DRT) data from EIS graphs based on Tikhonov regularization with continuous function discretization [242]. Contribution of different types of polarization in DRT was measured using peak fitting in origin software.

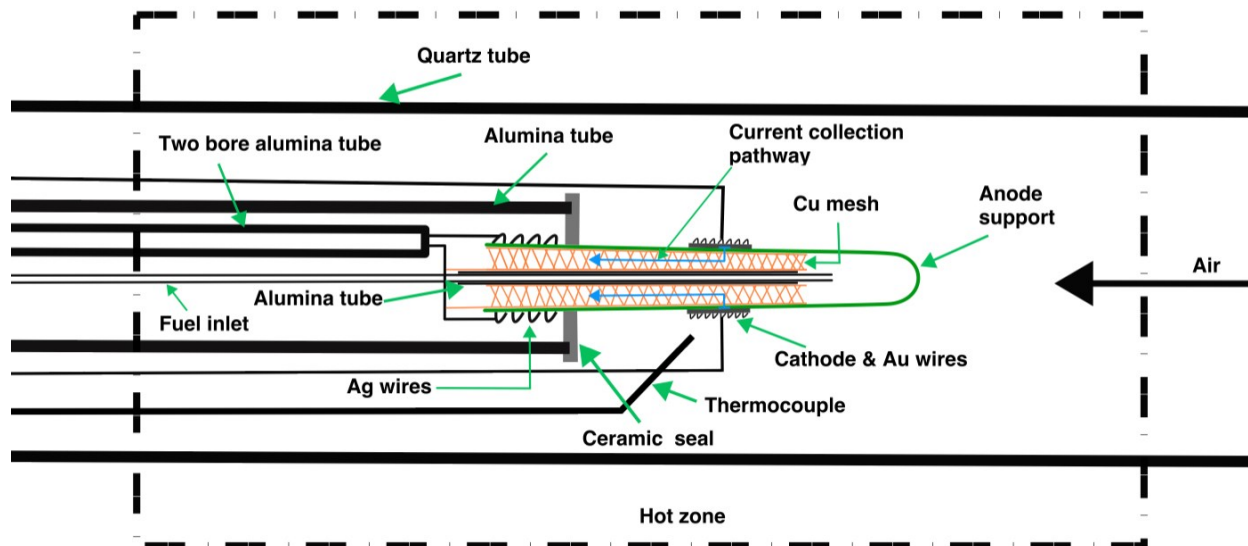


Figure 4-1. Schematic of the tubular SOFC test setup used for these experiments.

4.3 Results and discussion

4.3.1 Post-mortem SEM analysis of the cells

Figure 4-2a and b show the SEM micrographs of two cells Ni82 and Ni50. According to Figure 4-2a and b, the thickness of the AFL in both cells was about 20 μm . In addition, a 40 μm buffer layer with microstructure feature size in between the AFL and the support in the Ni82 cell is noticeable in Figure 4-2c. The composition (Ni:YSZ ratio = 50:50 vol.%) of the buffer layer in the Ni82 cell was the same as the composition of the Ni50 support. According to Figure 4-2e and f, the thickness of the electrolyte and infiltrated cathode layer were identical for both cells. The electrolyte in the Ni82 cell had slightly higher closed porosity compared with the Ni50, potentially due to lower shrinkage of the support in the Ni82 cell as increasing the Ni content reduces the Ni-YSZ support shrinkage [243]. Figure 4-2g and h show the cathode infiltrates to the electrolyte/cathode interface. Both cells acquire 30 wt% of cathode infiltrates for the purpose of comparison. Figure 4-2c shows a coherent attachment between the support/buffer layer/AFL of

the Ni82 cell after the test. In addition, Figure 4-2e and f show a coherent attachment of the YSZ scaffold at the cathode/electrolyte interface.

A closer view of the support microstructures with their corresponding energy dispersive spectroscopy (EDS) maps is provided in Figure 4-3. Comparing Figure 4-3a and b shows higher content of porosity for the Ni82 support. Moreover, YSZ grains in the Ni82 support are smaller and uniformly distributed between nickel grains. Comparing the EDS maps in Figure 4-2c and d also reveal the higher nickel content in the microstructure of the Ni82 cell.

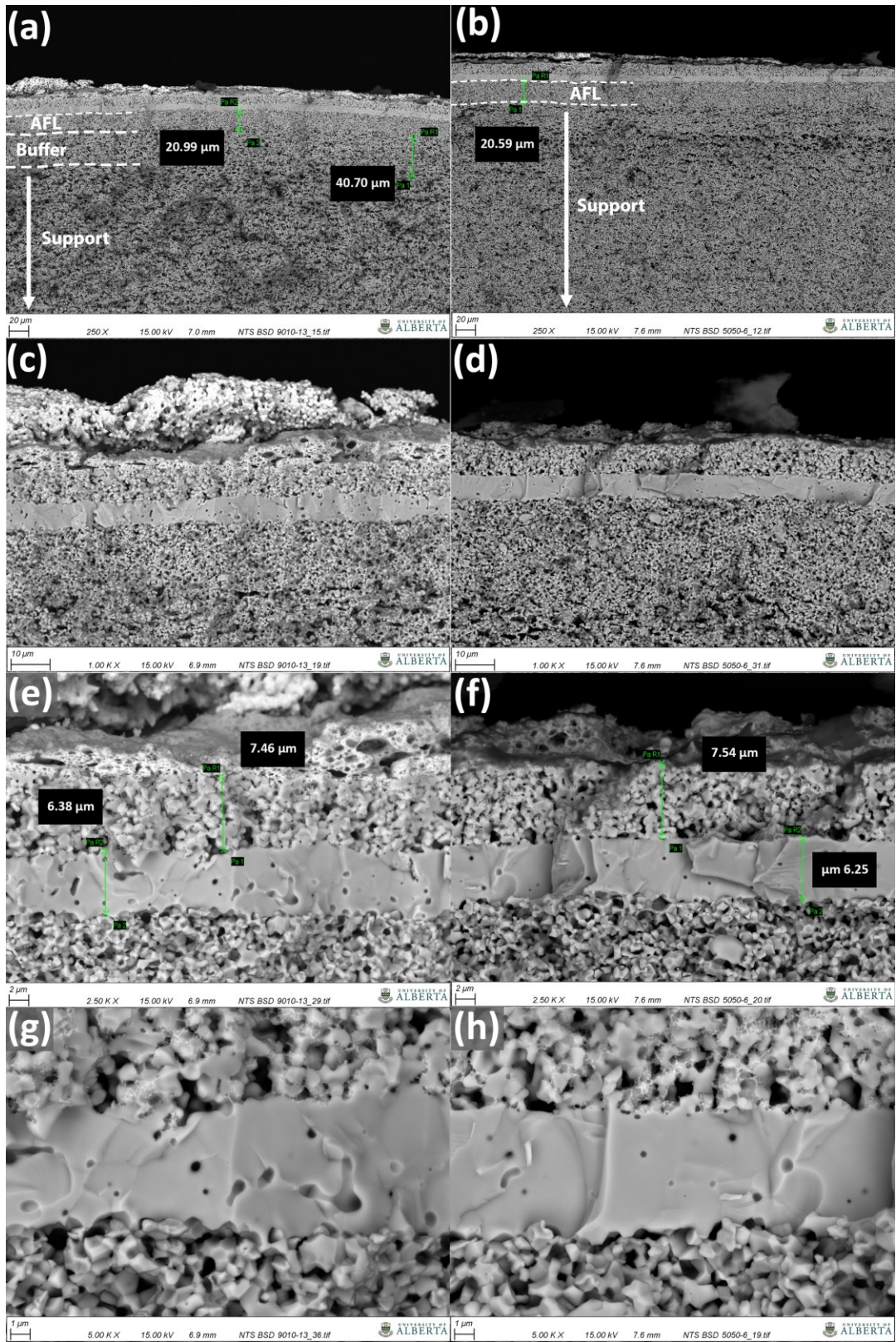


Figure 4-2. Post mortem SEM micrographs of (a, c, e, g) Ni82 cell and (b, d, f, h) Ni50 cell.

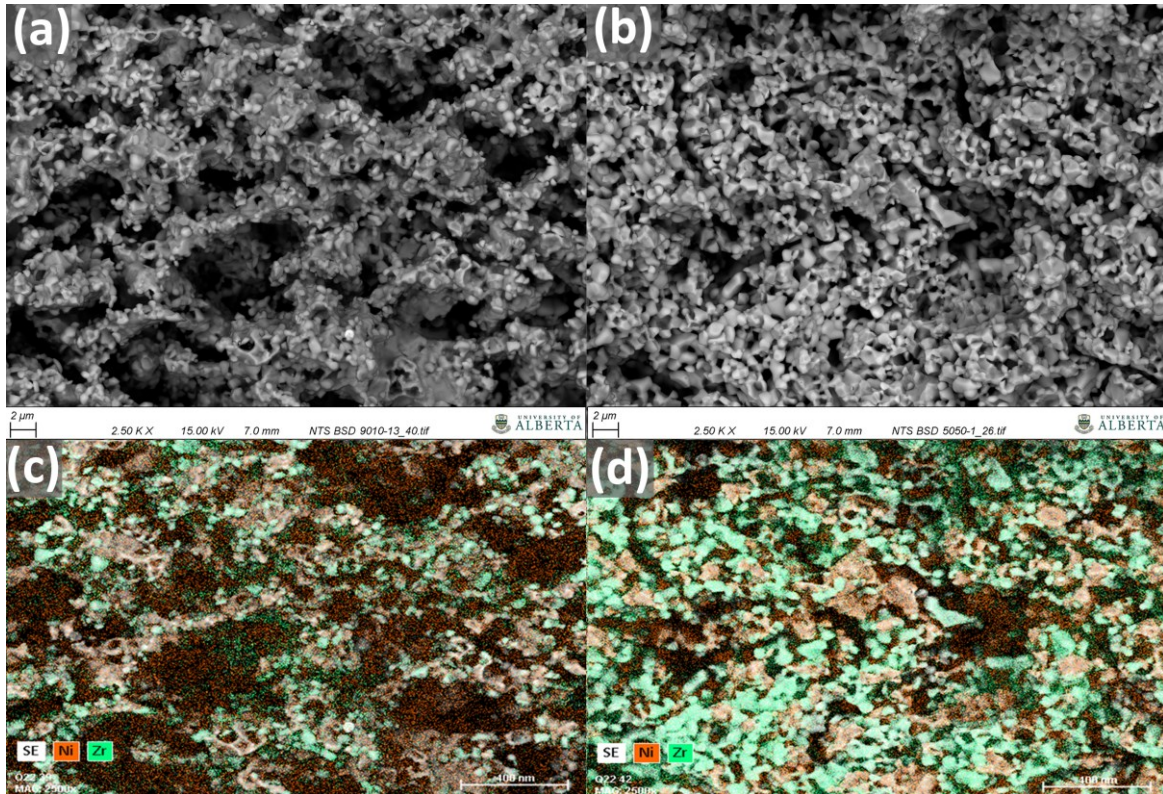


Figure 4-3. Post mortem SEM micrographs of the support in (a) Ni82 and (b) Ni50 cell and their corresponding EDS maps for (c) Ni82 and (d) Ni50 cell.

For a better comparison of microstructural features, both samples were polished and mounted using epoxy resin. Low accelerating voltage SEM images of the cross section of the polished samples are provided in Figure B 1 of the appendix B. Three different phases can be detected: Ni, YSZ and pores. Figure B 1a and b show the microstructure of AFL for Ni82 and Ni50 cells while Figure B 1c and d show the microstructure of the support for the corresponding cells. According to Figure B 1c, Ni grains inside the support of the Ni82 cell were larger than the support of the Ni50 cell due to higher Ni content. It has been proven that 10 wt% YSZ in the initial NiO-YSZ composition still limits Ni grain growth and prevents crack formation inside the support [229]. Without the addition of YSZ, Ni grains could grow to over 10 μm as seen in Figure 3-3. All Ni

grains in the Ni82 support are interconnected (otherwise the color contrast would be different at low acceleration voltage). Comparing Figure B 1c and d reveals the larger pores inside the support of the Ni82 cell compared with Ni50.

Quantitative comparison of the microstructural features was performed by image analysis of the polished samples. For size analysis, multiple horizontal lines are drawn onto the images and the average intersection length of the lines with each phase is measured. For volumetric fractions, area fraction of each phase is measured based on color contrast of each phase. Volume fractions of different phases inside the anode of both Ni82 and Ni50 cells are compared together in Figure 4-4. The functional layer of both anodes (20 μm) contains almost the same volume fraction of phases (Ni:YSZ:pore = 46-48:40:14-12 vol.%) and the least amount of total porosity consisting of a fine distribution of smaller pores to keep the active surface area as high as possible. The support layer of Ni82 contains a higher amount of porosity (Ni82:Ni50 porosity = 33:24 vol.%) and Ni compared to the Ni50 cell (Ni82:Ni50 Ni = 59:43 vol.%). Higher porosity values were achieved during the reduction of NiO to Ni. The thick buffer layer (40 μm) in the Ni82 cell contained higher YSZ and a lower amount of porosity compared with its support. The volume fraction of YSZ in all the layers was slightly lower than the initial volume fraction of YSZ added during fabrication of the anode. This similar error in all three layers for both cells suggests that some of the YSZ particles were removed during the polishing process due to its brittleness.

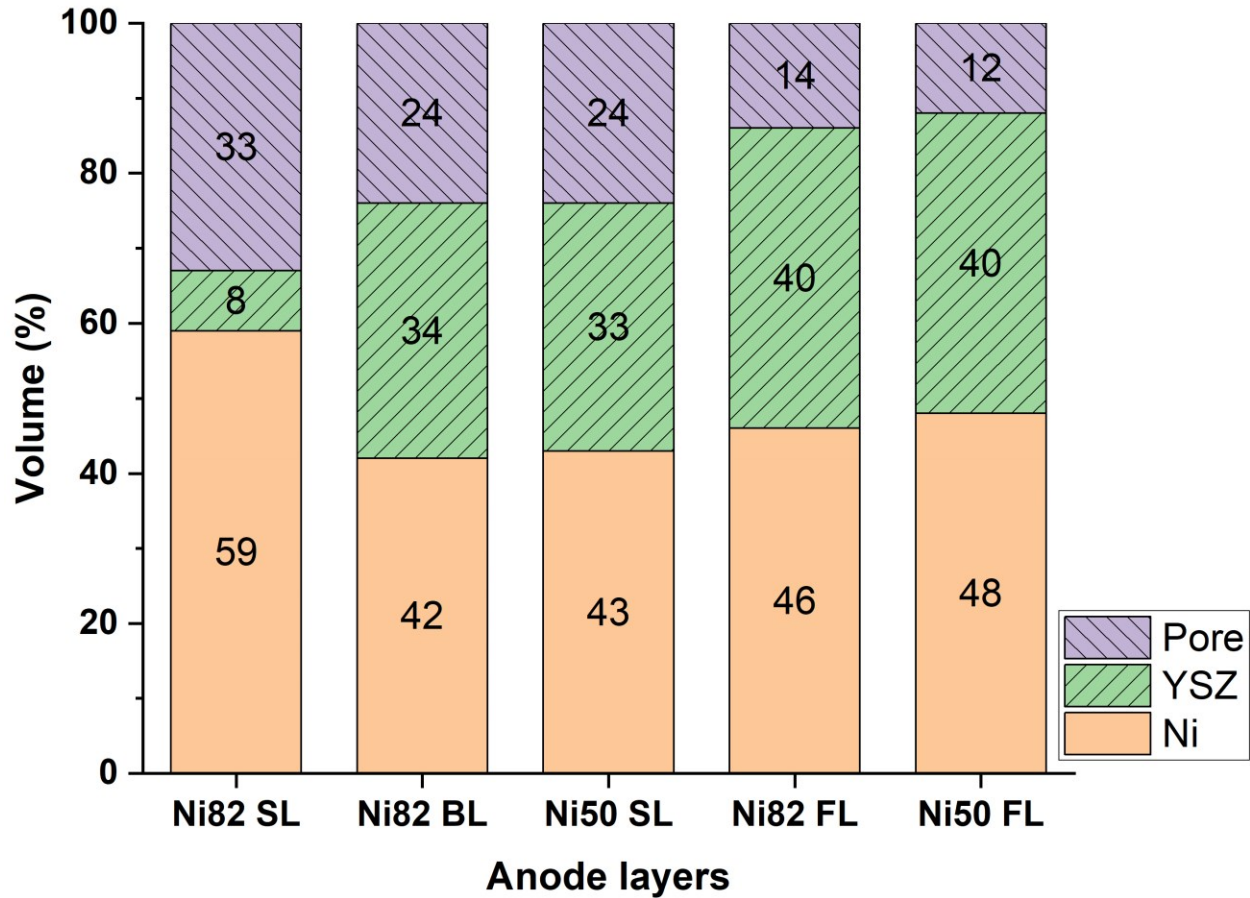


Figure 4-4. Volume fraction of Ni, YSZ and pores inside different layers of Ni82 and Ni50 cells. SL: support layer, BL: buffer layer, FL: functional layer.

Figure 4-5 shows the size distribution of different phases inside different layers of the Ni82 cell. A very narrow distribution of YSZ grain sizes can be observed inside the support. YSZ grains deposited between Ni grains have unique purposes of limiting Ni grain growth and increasing the mechanical integrity of the support. Meanwhile both Ni and pores have similar size of about 3 μm . By transitioning from the thick support layer to the 40 μm thick buffer layer, YSZ grain size increases from 500 nm to about 1.5 μm due to increased volume ratio of YSZ content. As a result, YSZ particles are more likely in contact with each other leading to faster rates of material transfer due to surface diffusion. Ni and pore size decrease to about 1.8 μm . This intermediate buffer layer

can suppress possible mechanical stress created in the AFL or the electrolyte during reduction of the highly conductive support layer. Ni and YSZ grains are slightly smaller compared to the buffer layer while pore size is much lower inside the AFL. Pores inside the AFL are generated mostly due to NiO reduction to Ni. Average grain size comparison in Figure 4-5d shows that the pore size was linearly reduced from the support to the functional layer while Ni grain size had a nonlinear trend. The support layer of the Ni82 cell can be considered as a highly conductive and porous layer with the least amount of tortuosity for both current collection and gas diffusion. The AFL with a finer pore distribution and the lowest amount of total porosity combined with the high surface area of Ni and YSZ contributes to the electrochemical reactions at the anode. The buffer layer had intermediate Ni grain size and pore volume between the support and AFL layers for efficient transfer of the electrons from the AFL to the support and mechanically stabilizing the electrode.

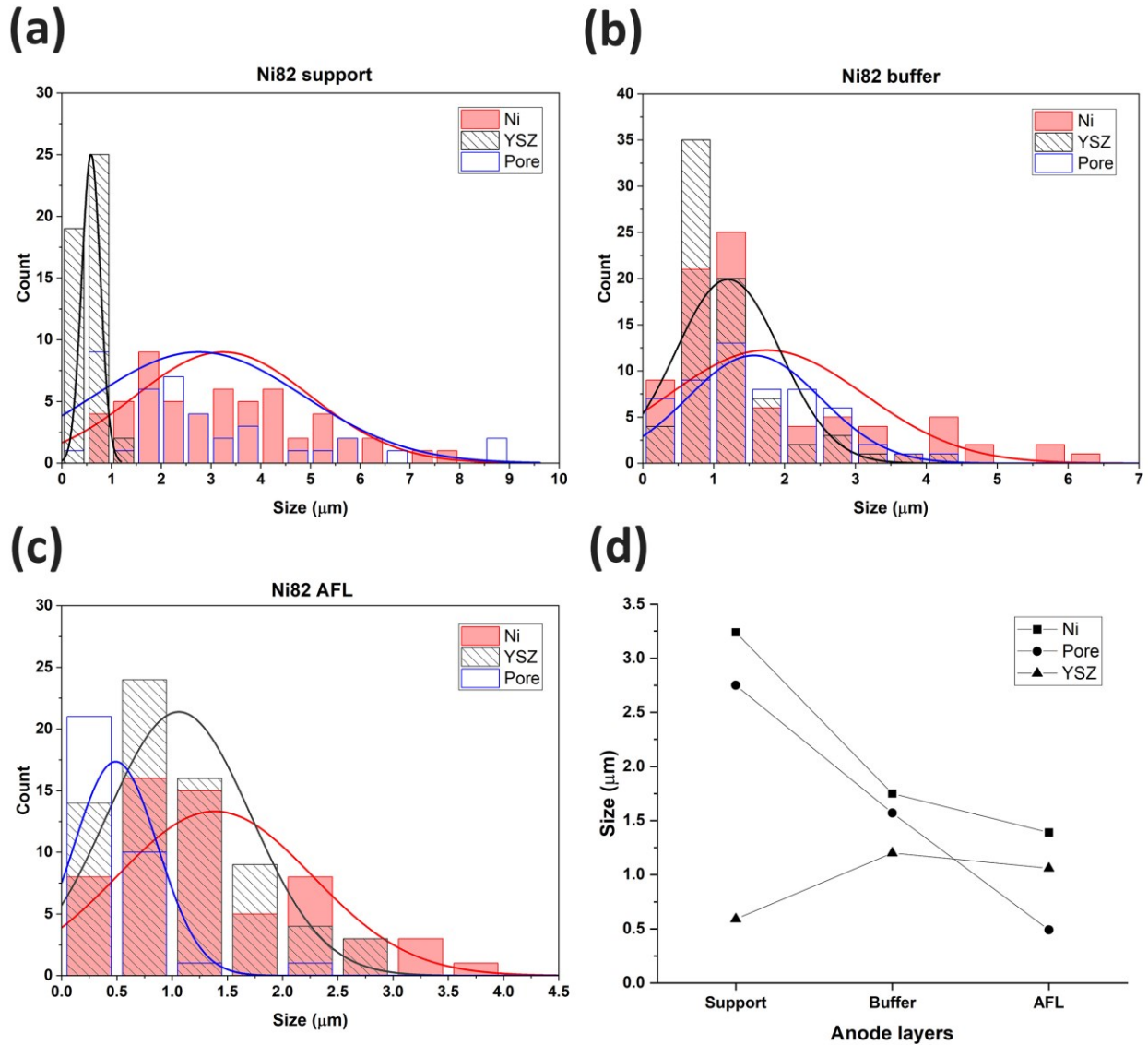


Figure 4-5. Distribution of Ni, YSZ and pore sizes inside different layers of the Ni82 anode: (a) support layer (b) buffer layer (c) AFL. (d) Comparison of average phase sizes in different layers of the Ni82 anode.

4.3.2 Electrochemical performance of the cell

The current density-voltage-power density plots of Ni50 and Ni82 cells are shown in Figure 4-6a and b, respectively. The corresponding PPD at each temperature is compared for the two cells in Figure 4-6c. According to Figure 4-6c, the Ni82 cell shows a 25%, 87% and 86% increase in PPD compared with the conventional Ni50 cell at 600, 550 and 500 °C, respectively.

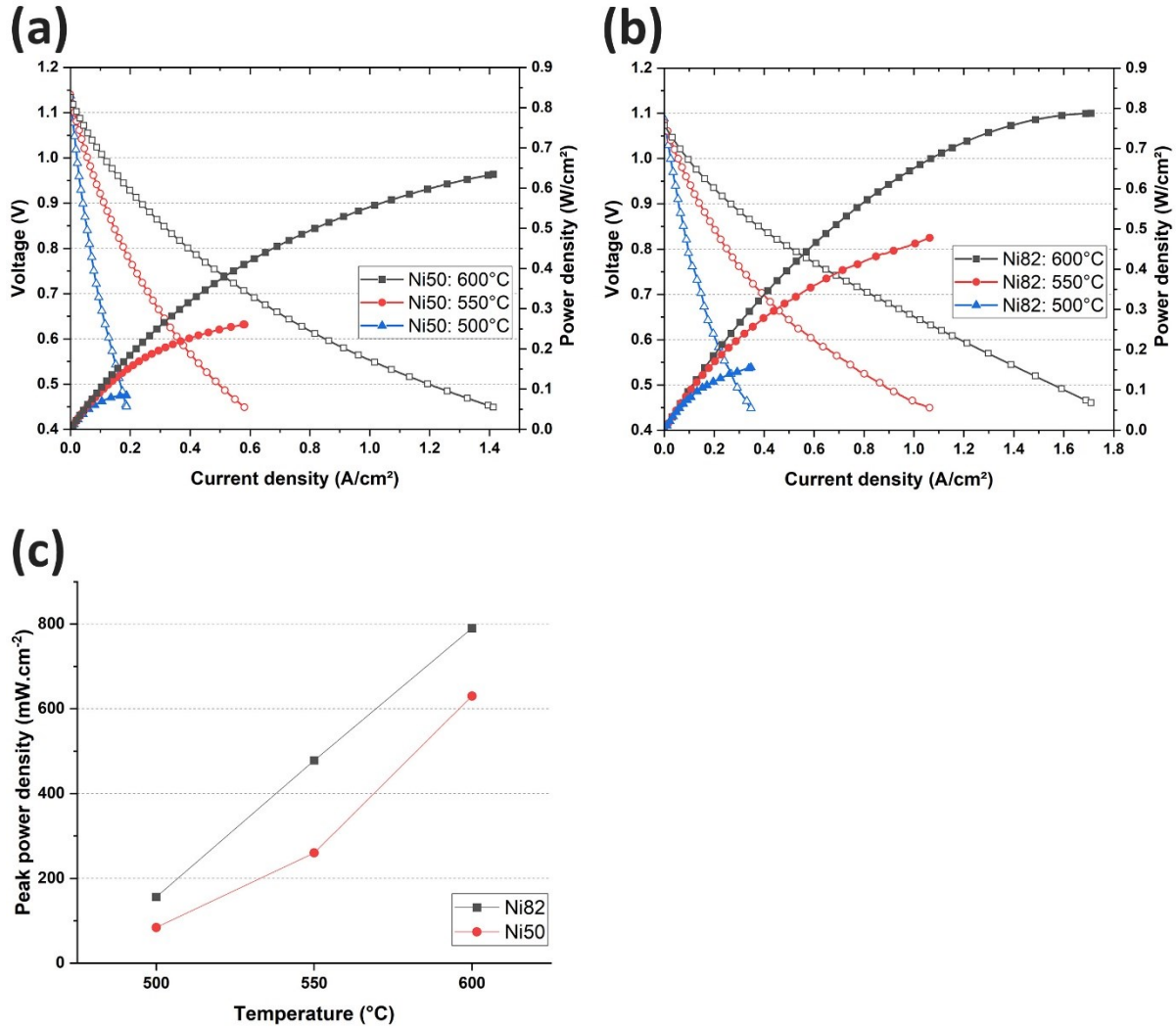


Figure 4-6. Current density-voltage-power density plot of (a) Ni50 and (b) Ni82 cell at different temperatures (c) comparison of peak power density of Ni82 and Ni50 cells at different temperatures.

Figure 4-6b shows the PPD of the Ni82 cell reaching 790 and 478 $\text{mW}\cdot\text{cm}^{-2}$ at 600 and 550 °C, respectively, which can be considered a high performance for low temperature SOFCs with a YSZ electrolyte. According to Figure 4-2g and h, the thickness of the electrolyte for both cells is similar. Nyquist plots of both cells are compared together in Figure 4-7a, b and c. As can be seen, the ohmic resistance for the Ni82 cell is lower at each temperature compared with the Ni50 cell. This is due to higher electronic conductivity of the Ni82 support compared with Ni50. To better interpret

the Nyquist plot, DRT data is extracted from the Nyquist data and shown in Figure 4-7d, e and f for corresponding temperatures. DRT computation is based on Tikhonov regularization with the gaussian discretization method. For the sake of comparison, DRT parameters including full width half maximum (FWHM) coefficient (0.5) and regularization parameter λ (0.001) were kept constant for both samples. As can be observed in Figure 4-7a, b and c, DRT data have excellent fitting with the EIS data (points vs solid lines). Choosing the right DRT parameter is essential for reliability of the fitting. To measure the value of polarization resistance associated with each peak in the DRT plots of Figure 4-7, peaks were isolated using OriginPro software. Isolated peaks and the fraction of their surface area to the total surface area under DRT curves are shown in Figure B 2 of the appendix B. Table 4-1 shows values of the resistance and capacitance for five R-CPE elements in each cell at different temperatures. Capacitance values (C) were calculated using the characteristic frequency (f) and the resistance (R) for each peak according to the following equation [244]:

$$RC = \frac{1}{2\pi f}$$

Table 4-1 The value of different resistance and capacitance corresponding to the peaks in Figure 4-7 for Ni82 and Ni50 cells.

	T (°C)	C-CPE 1			C-CPE 2		C-CPE 3		C-CPE 4		C-CPE 5		R _p (total)
		R _{ohm} (Ω.cm ²)	R1 (Ω.cm ²)	C1 (F.cm ⁻²)	R2 (Ω.cm ²)	C1 (F.cm ⁻²)	R3 (Ω.cm ²)	C1 (F.cm ⁻²)	R4 (Ω.cm ²)	C1 (F.cm ⁻²)	R5 (Ω.cm ²)	C1 (F.cm ⁻²)	
Ni82	500	0.78	0.52	7.6E-05	2.21	1.4E-04	0.85	0.005	0.17	0.47	0.15	3.49	3.9
	550	0.42	0.30	1.3E-04	0.95	2.8E-04	0.12	0.014	0.13	1.81	0.06	13.98	1.55
	600	0.24	0.37	2.2E-04	0.14	3.7E-03	0.02	0.095	0.23	0.70	0.02	359.23	0.78
Ni50	500	1.25	0.30	1.3E-04	4.48	1.8E-04	0.79	0.010	0.24	0.22	0.24	6.58	6.05
	550	0.52	0.31	1.3E-04	1.73	3.1E-04	0.04	0.214	0.36	0.22	0.19	8.57	2.62
	600	0.32	0.28	2.9E-04	0.54	9.8E-04	0.09	0.089	0.33	0.24	0.19	4.15	1.43

According to the DRT data, there are five peaks contributing to the resistance of the cells. One extra peak is noticeable for DRT data at low frequencies in Figure 4-7 compared to Figure 3-5 due to microstructural difference (thickness of the cathode, addition of buffer layer). This can

contribute to different concentration polarization values for anode and cathode. High frequency peaks are related to activation polarization of the anode or cathode. Peak R1 (capacitance of $7.6 \times 10^{-5} - 2.9 \times 10^{-4} \text{ F.cm}^{-2}$) with the characteristic frequency of 3000-4000 Hz has almost the same value for both cells at each temperature (resistance values of 0.30 and 0.31 $\Omega.\text{cm}^2$ for Ni82 and Ni50 cell, respectively, at 550 °C). In contrast, peaks R2 (capacitance of $1.4 \times 10^{-4} - 3.7 \times 10^{-3} \text{ F.cm}^{-2}$) with characteristic frequency of 300 Hz have much larger contributions to the total polarization resistance of the Ni50 cell compared with Ni82 cell (R2 value of 0.54, 1.73 and 4.48 for the Ni50 cell compared with 0.14, 0.95 and 2.21 $\Omega.\text{cm}^2$ for the Ni82 cell at 600, 550 and 500 °C, respectively).

As previously reported [93,245] for cells with a Ni-YSZ anode, YSZ electrolyte and NNO cathode, the high frequency peak R1 is associated with oxygen ion transfer at the cathode/electrolyte interface and mid frequency R2 is associated with anode charge transfer. Since the cathode microstructure and thickness are identical for both cells, the peak R1 contribution is similar for both cells. In addition, anode charge transfer kinetics are faster in the Ni82 cell due to higher rate of fuel supply from the highly porous support to the AFL/electrolyte interface.

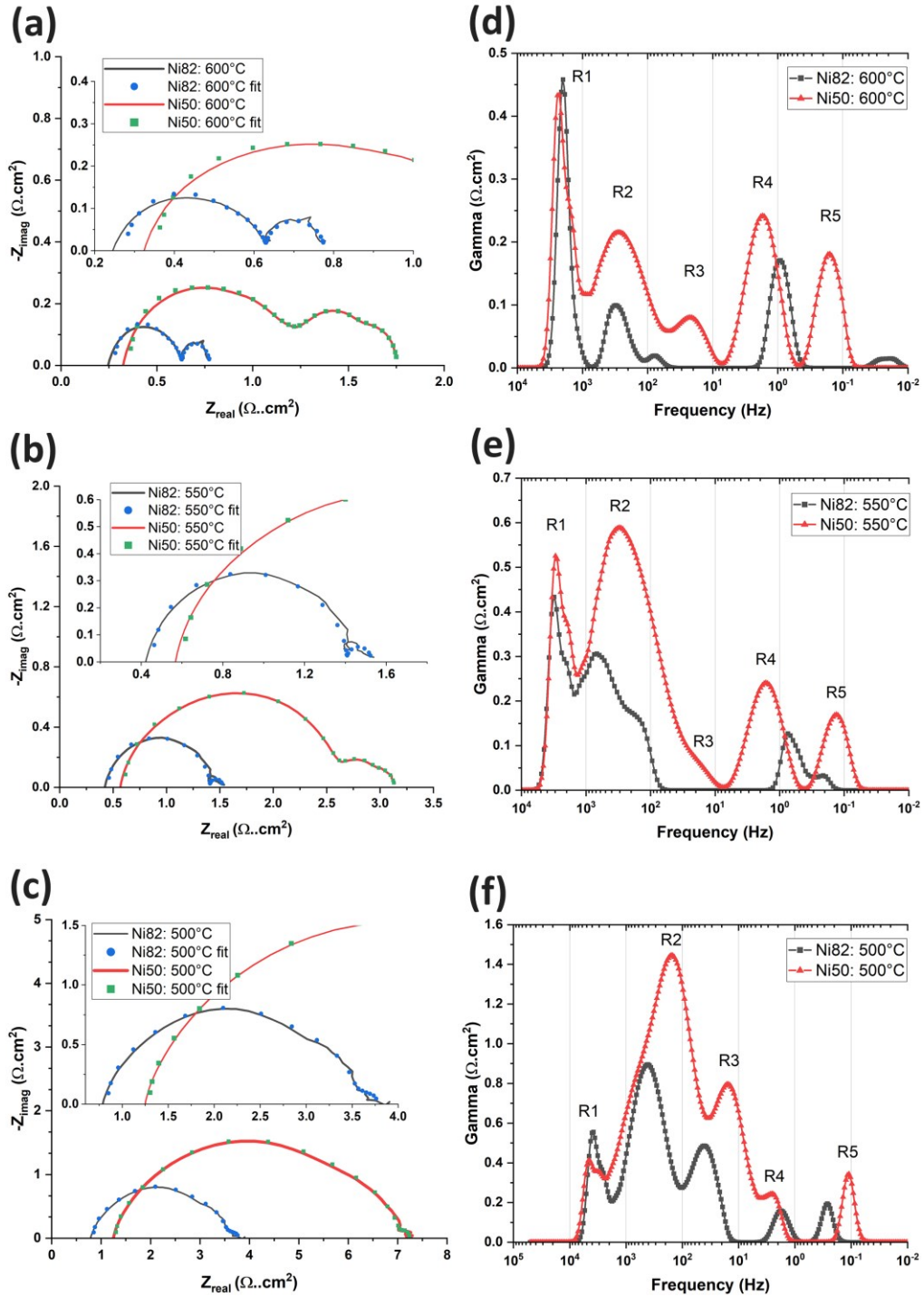


Figure 4-7. EIS comparison of Ni82 and Ni50 cells at (a) 600 °C (b) 550 °C and (c) 500 °C. The inset is the zoomed view of the same graph. Square and circle points show the fitting on experimental EIS using the DRT method. Corresponding DRT data for each temperature are shown in d, e and f.

The values of peaks R4 and R5 don't change much by changing temperature from 600 to 550 °C for both cells. This behavior is related to concentration polarization inside the anode or the cathode [93]. To better identify the contribution of concentration polarization, fuel flow was decreased from 50 to 20 SCCM for the Ni50 cell. Corresponding EIS and DRT data are shown in Figure B 3 of the appendix B. As shown in Figure B 3b, the value of the peak associated with the lowest characteristic frequency (0.1 Hz) markedly increased by reducing the fuel flow rate. This shows that peaks R4 and R5 in Figure 4-7 are associated with concentration polarization inside the cathode and anode, respectively. According to Figure 4-7d and f, the R5 peak contribution for Ni82 is lower than Ni50 (0.19, 0.19 and 0.24 for the Ni50 cell compared with 0.02, 0.06 and 0.15 $\Omega \cdot \text{cm}^2$ for the Ni82 cell at 600, 550 and 500 °C, respectively) which is due to the higher amount of porosity inside the Ni82 cell. Anode support porosity has been proven to improve the performance of the cell [246] due to providing a higher amount of accessible fuel to the active area and faster removal of water from the cell. This can also contribute to peaks R2 and R3 in Figure 4-7d, e and f.

4.3.3 Redox cycles

In the lifetime of an SOFC, the cell may undergo several reduction and oxidation (redox) cycles which can cause crack formation inside the anode and their propagation to the electrolyte followed by cell failure. The higher the Ni content in the support, the greater chance for cell cracking. Temperature is also an important factor in accelerating crack propagation upon redox cycles. To evaluate the redox cycling resistance of the Ni82 cell, it was exposed to four redox cycles at 550 °C. EIS and IV measurements were performed before each cycle. Hydrogen was stopped for 1 h and then re-introduced to the anode. The OCV of the cell was tracked during redox cycle periods and the result is shown in Figure 4-8a. The OCV of the cell dropped initially to 0.2-0.3 V when

hydrogen was unavailable. By introducing hydrogen back, the OCV fully recovered to 1.08 V after each cycle. Performance of the cell before and after each redox cycle was measured and is shown in Figure 4-8b. According to Figure 4-8b, performance of the cell increased after four redox cycles. Figure 4-8c shows how the contribution of the mid frequency semicircle to the total polarization resistance of the cell was reduced by increasing the number of redox cycles.

As discussed before, mid frequency peaks are attributed to anode charge transfer. Improvement in performance of the cell in successive redox cycles can be due to the formation of smaller Ni grains [69,247,248] inside the AFL and increasing the TPB length. Pihlatie et al. studied the effect of porosity on redox stability of Ni based SOFCs [249]. According to them, porosity accommodates the volumetric expansion of Ni during oxidation. Increasing the porosity of the electrode can reduce the cumulative redox strain and increase the ability of the cell to recover from the induced stress during the redox cycle. It is worth mentioning that the buffer layer can also play an important role in improving the redox cycling resistance by providing a smooth microstructural change between the support and the AFL. The thermal expansion coefficient of Ni-YSZ cermet increases linearly by increasing Ni content [250]. Thus, a buffer layer with intermediate Ni content between the support and AFL can lead to a reduction of the stress induced in the electrolyte and AFL during redox cycles. Figure 4-8c shows that the ohmic resistance of the cell did not increase which proves that the electrolyte remained intact after four redox cycles. It is possible that such a cell could fail during high temperature (>700 °C) redox cycles. Therefore, it is recommended to operate this cell at temperatures below 650 °C as the support is designed for low temperature applications.

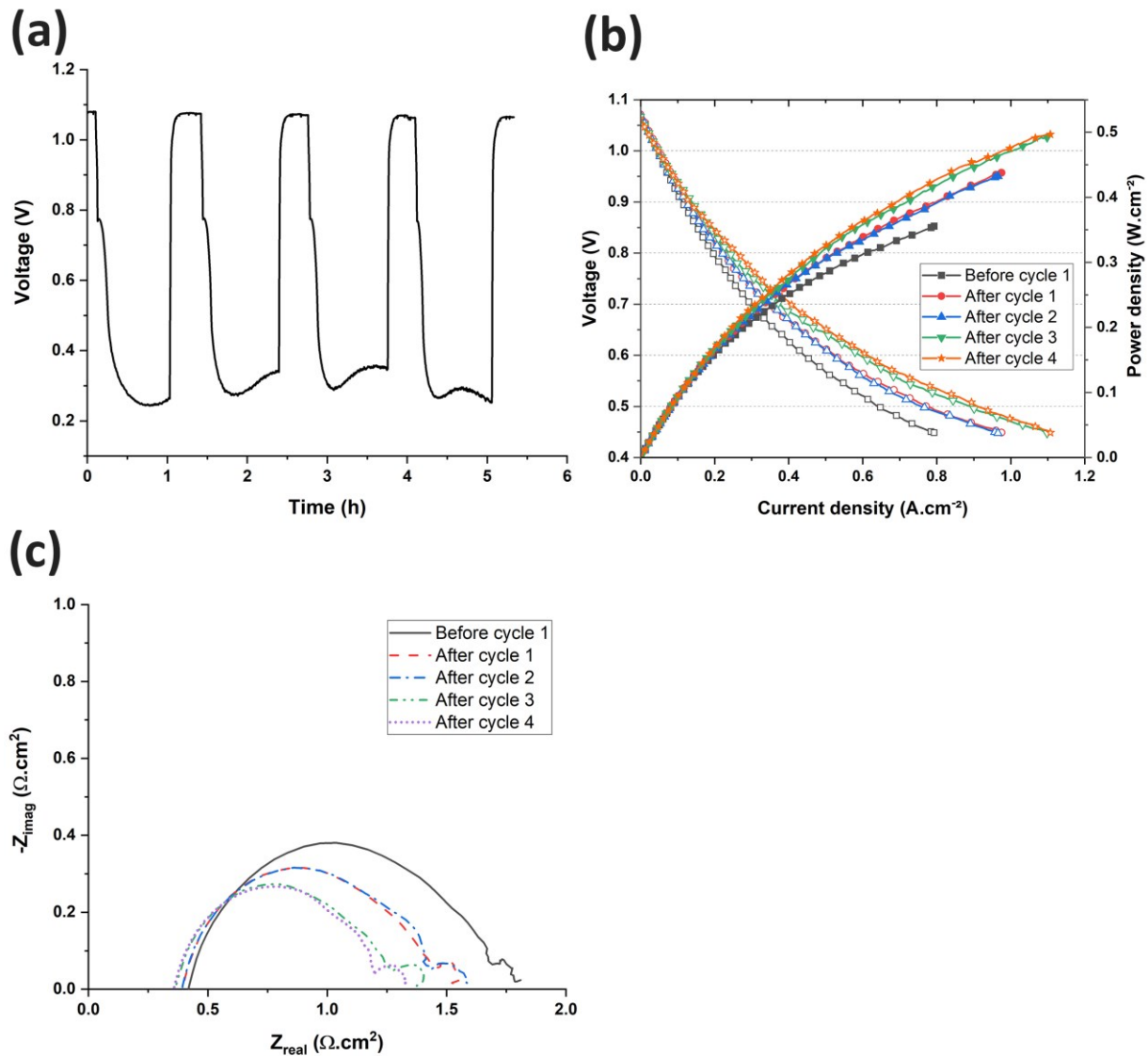


Figure 4-8. (a) OCV graph of the Ni82 cell redox cycles at 550 °C. (b) IV curves and (c) Nyquist plots before and after each redox cycle. Hydrogen was cut off for 1 h and introduced again for 15 min during each cycle.

4.4 Conclusions

The results of the current study suggest that by providing a highly conductive yet porous support, it is possible to operate an SOFC based on a YSZ electrolyte and Ni-YSZ functional layer at low temperatures, even below 600 °C. The cell showed excellent PPD of 790 and 478 $\text{mW}\cdot\text{cm}^{-2}$ at 600

and 550 °C, respectively, which were 25% and 87% higher than the conventional cell performance at similar temperatures. Addition of a small amount of YSZ to Ni secures the microstructural integrity and avoids crack formation during cell reduction. The cell showed excellent redox cycling resistance at 550 °C. DRT results show better diffusion of the fuel inside the anode support which led to a decrease in concentration polarization and increase in the anode charge transfer kinetics. The improved conductivity of the support is believed to be an important advantage for current collection in tubular cells with known current collection problems.

Acknowledgements

The authors would like to acknowledge Future Energy Systems Research Initiative (grant number RES0031233) for funding this research.

Chapter 5: Performance and Stability of Infiltrated Praseodymium Nickelate Cathodes for Low-temperature Fuel Cell Applications

Sajad Vafaeenezhad^{1*}, Miguel A. Morales-Zapata², Amir Reza Hanifi¹, Miguel A. Laguna-Bercero², Ángel Larrea², Partha Sarkar¹ and Thomas H. Etsell¹

¹Department of Chemical & Materials Engineering, University of Alberta, Edmonton, Alberta T6G 1H9, Canada

²Instituto de Nanociencia y Materiales de Aragón, CSIC-U. Zaragoza, c/ María de Luna 3, 50018, Zaragoza, Spain

Abstract

The electrochemical performance and stability of infiltrated praseodymium nickelate (PNO) as the cathode for solid oxide fuel cell (SOFC) applications was studied. PNO cathode ($\text{Pr}_2\text{NiO}_{4+\delta}$) was infiltrated into gadolinium-doped ceria (GDC) scaffolds and tested in two different anode-supported cells with tubular geometry: i) tubular cell A with Ni-YSZ (yttria-stabilized zirconia) support, Ni-YSZ anode functional layer (AFL), and thin ($\sim 7 \mu\text{m}$) electrolyte and; ii) microtubular cell B with Ni-YSZ support, without AFL and thick ($34 \mu\text{m}$) electrolyte. The peak power densities for cell A were 770, 470, and 274 $\text{mW}\cdot\text{cm}^{-2}$ at 750, 700 and 650°C, respectively. Both cells were stable during 91 h and 260 h of stability testing and experienced a reduction in total polarization resistances. Post-mortem X-ray diffraction (XRD) analysis confirmed PNO's partial transformation into the $\text{Pr}_4\text{Ni}_3\text{O}_{10}$ phase with higher electrical conductivity and thermal stability. The cathode composition was changed to better interpret the distribution of relaxation time (DRT) peaks. Improvement in the oxygen reduction reaction and gas conversion rates during the stability

tests was confirmed using DRT analysis. This finding confirms that PNO infiltrated into GDC scaffold can be considered a promising cathode for SOFC applications.

Keywords: SOFC, YSZ, Praseodymium, Nickelate, Cathode, PNO.

5.1 Introduction

Currently, there is an emerging interest in the development of advanced electrodes for intermediate-to-low temperature (between 500 and 750 °C) SOFC operation in order to lower the fuel cell degradation. However, long-term electrode stability issues must be solved for its implementation on a wide industrial scale. In full cell configurations that employ thin, anode-supported standard YSZ electrolytes, there is a limitation of performance at lower operating temperatures evidenced by a high polarization resistance contribution from the cathode [251,252]. The SOFC cathode configuration with mixed conducting perovskites shows a relatively high impedance at temperatures below 750 °C in lanthanum strontium manganite (LSM)-YSZ composites [253], lanthanum strontium cobaltite (LSC) [254], lanthanum strontium ferrite (LSF) [255] and lanthanum-strontium cobalt ferrite LSCF [256], where some reactivity with YSZ ($\text{La}_2\text{Zr}_2\text{O}_7$, SrZrO_3) at high temperatures is present [253,257–259]. The same is also occurring for nickelates [260], where an insulating zirconate phase ($\text{Ln}_2\text{Zr}_2\text{O}_7$, with Ln = La, Pr, Nd) is formed during high-temperature sintering in neodymium nickelate (NNO), lanthanum nickelate (LNO) and PNO with YSZ composites.

To mitigate this effect, cathode materials with conductivity and stability are required. Recent works have shown that electrode fabrication and modification by infiltration of active components into a porous scaffold at both anode and cathode can result in outstanding electrochemical performance [224,261].

The process of nanoparticle infiltration for electrode performance enhancement has been successfully implemented over the last decade by several research groups [83,93,214,262,263]. In this process, a thin porous scaffold is first deposited on top of the dense electrolyte and then the active cathode catalyst is infiltrated into it. The resulting infiltrated particles give higher surface area which leads to higher three-phase boundary (TPB) density inside the cathode. Most of the electrochemical reaction occurs at the cathode/electrolyte interface and it is a common practice to split the electrode into a functional and current collection layer. The current collection layer is specifically optimized for the electronic conductivity, with enough porosity for the diffusion of reactants to the electrolyte interface. Solid loading of the infiltrated solution is an important aspect for a successful nanoparticle-infiltrated electrode as contact surfaces increase by their addition on the surface of the backbone electrode (scaffold). Moreover, the rate of increasing the infiltrate solid load decreases after each subsequent infiltration [264].

Lanthanum, praseodymium and neodymium nickelates such as $\text{La}_2\text{NiO}_{4+\delta}$ (LNO) [265], $\text{Pr}_2\text{NiO}_{4+\delta}$ (PNO) [262,266,267], $\text{Nd}_2\text{NiO}_{4+\delta}$ (NNO) [268], and also the single oxide PrO_x [224,269] have replaced the conventional LSM as cathode catalyst compositions, where the active infiltrated nanocatalyst in selected porous scaffolds has provided and enhanced charge transfer in a metal supported SOFC [224]. The authors emphasized the optimization of infiltrate solution compositions, thickness of layers, sintering conditions, the scaffold's porosity and catalyst firing temperature.

Among the nickelates, PNO shows the highest oxygen diffusion and surface exchange coefficients, making it appealing as an oxygen electrode [270]. Therefore, high-performance PNO cathodes, including highly ordered Ruddlesden-Popper phases, have been successfully developed for SOFCs [271–273] and reversible [274] cells in recent years. For instance, Vibhu *et al.* [275] obtained a

power density at 0.5 V of $1.6 \text{ W}\cdot\text{cm}^{-2}$ at $800 \text{ }^\circ\text{C}$ using the single cell configuration Ni-YSZ/YSZ/CGO/ $\text{Pr}_4\text{Ni}_3\text{O}_{10-\delta}$. They also measured the electrolysis performance of the cell and could reach a current density of $1.6 \text{ A}\cdot\text{cm}^{-2}$ at $800 \text{ }^\circ\text{C}$ and 1.54 V with a PNO cathode [276]. Regarding the nickelate infiltrations into porous scaffolds, the purity of the nickelate phase in ceramic electrodes plays an important role in the electrochemical performance [261,277–279] and the reproducibility [280] of the cell. To the best of our knowledge, there are only a few papers in the literature on PNO-infiltrated cathodes for SOFC application to date. Railsback *et al.* [262] obtained a low non-ohmic resistance at $650 \text{ }^\circ\text{C}$ ($0.11 \text{ }\Omega\cdot\text{cm}^2$) in symmetrical cells using PNO infiltrated into an LSGM scaffold. Nicollet *et al.* [266] fabricated and tested the electrochemical characteristics of PNO infiltrated into GDC scaffold oxygen electrodes and YSZ electrolyte symmetrical cells. They managed to obtain a lower annealing temperature ($900 \text{ }^\circ\text{C}$) using N_2 atmosphere than air ($1000 \text{ }^\circ\text{C}$) [262]. They could obtain very low polarization resistance values ($0.075 \text{ }\Omega\cdot\text{cm}^2$ at $600 \text{ }^\circ\text{C}$) using this method. Dogdibegovic *et al.* reported a peak power density of $0.6 \text{ W}\cdot\text{cm}^{-2}$ at $700 \text{ }^\circ\text{C}$ using a metal-supported SOFC with YSZ electrolyte [224]. SOFC stability using PNO-based electrodes has been performed before [267,271,273,281–283]; however, their stability as a cathode fabricated by infiltration in a complete SOFC cell during operation have not yet been fully tested.

In the present work, we intend to study the performance and stability of infiltrated PNO cathodes. First, the reactivity of the PNO phase with GDC and YSZ scaffolds was studied to select the most appropriate scaffold. Then, infiltrated PNO cathodes were studied in two different types of tubular SOFCs using in-depth EIS and DRT analysis in parallel with post-mortem XRD and microstructural characterization.

5.2 Experimental procedures

Two different fuel cells were fabricated and tested using a PNO cathode to understand the stability of the PNO cathode with different anode support and electrolyte thicknesses. Table 5-1 shows the composition and the thickness of each layer. Cell A was composed of a slip-cast Ni-YSZ support with 390 μm thickness fabricated at the University of Alberta, Canada. Cell B used an extruded support of 640 μm fabricated at the University of Carlos III, Madrid, Spain. In addition, the electrolyte in cell A was thinner compared to the electrolyte of cell B (7.9 μm vs. 36-38 μm). A gadolinium-doped-ceria (GDC) cathode scaffold was coated onto the electrolyte of both cells and PNO was infiltrated into it as the active cathode material. Cathode development for both cells and the subsequent testing were performed in Canada.

Table 5-1 Composition and thickness of different layers in cells A and B.

Cell	Anode Support				AFL		Electrolyte		Cathode	
	Method	Composition	volume ratio	Thickness (μm)	Composition	Thickness (μm)	Composition	Thickness (μm)	Composition	Thickness (μm)
A	Slip-cast	Ni:YSZ: Gr	30:30:40	390	Ni:YSZ	20	YSZ	7.9	PNO-GDC	10
B	Extrude	Ni:YSZ:Starch	25:25:50	640	-	-	YSZ	36	PNO-GDC	20

5.2.1 Fabrication of the anode support

Cell A's support was fabricated using slip casting. Initially, NiO powder (Fuel Cell Materials, average particle size of 1 μm) was milled using a ball mill at 70 rpm for 24 h. Milled NiO was mixed with YSZ (Tosoh TZ8Y, 8 mol% Y_2O_3) with a 65:35 weight ratio. Powders were added to water (1:1 weight ratio) and zirconia balls. The pH of the slip was set to 4 using hydrochloric acid to gain a stable slip. The mixture was milled for 2 h using a ball-mill at 70 rpm. Next, graphite (40 vol.% with 4.5 μm average particle size) was added to the suspension and milled again for another 15 minutes. Finally, the slip was sonicated using an ultrasound bath for three minutes and cast into

plaster molds. Supports were dried at room temperature and pre-sintered at 850 °C for 3 h. The average outer diameter of cell A was 5.3 mm.

Cell B's anode support was fabricated using the extrusion method. The details of the method are explained elsewhere [284]. In brief, YSZ (Tosoh TZ8Y) was added to NiO (Hart Materials, average particle size of 0.7 μm) and corn starch (particle sizes between 4-10 μm), then mixed with a thermoplastic multicomponent mixture of a polymer, wax and surfactant. The temperature of the mixture was controlled carefully before extrusion of the microtubes using a modified commercial extruder. Raw tubes were collected for applying the electrolyte and co-sintering. The average outer diameter of cell B was 3.1 mm. Actual cells before the test are shown in Figure C 1 of appendix C for comparison.

5.2.2 Coating of the AFL

An AFL was coated onto the support of cell A by the dip coating method. AFL slurry was prepared by mixing NiO (J. T. Baker, average particle size of 250 nm):YSZ powders (65:35 weight ratio), ethanol (1:4 powder:ethanol weight ratio) and binder (6 wt% ethyl cellulose in terpineol) using zirconia balls in a planetary mill for 2 h. The slurry was homogenized in an ultrasound bath for one minute before the dip coat. Two dips of AFL were applied to the support, dried at room temperature and pre-sintered at 850 °C for 3 h.

5.2.3 Coating of the electrolyte layer

A thin YSZ layer was coated onto cell A by dip coating. YSZ and ethanol (1:7 weight ratio) and binder (6 wt% ethyl cellulose in terpineol) were milled using zirconia balls in a planetary mill at 300 rpm for 1 h. Afterward, the suspension was sonicated for three minutes using an ultrasound bath. The anode support was dipped once into the electrolyte suspension for 10 seconds. The YSZ-

coated supports were dried first at room temperature and then co-sintered at 1400 °C for 3 h. Another dip coat was applied after sintering using YSZ suspension (1:10 solid ratio) and sintered at 1400 °C for 3 h to make sure a gas-tight YSZ electrolyte was achieved. The electrolyte of cell B was also coated using a dip coat. Briefly, YSZ and propanol (1.25:1 weight ratio) and binder (5 wt% polyvinyl butyral in propanol) were mixed using a magnetic stirrer at 300 rpm for 15 minutes. The suspension was sonicated for 1 minute using an ultrasound bath. The anode support was dipped three times into the electrolyte suspension for about 1 second. Finally, the supports were first dried at room temperature and then sintered at 1500 °C for 2 h.

5.2.4 Coating of the GDC scaffold and cathode infiltration

Infiltration of PNO into a porous GDC scaffold was used to fabricate the cathode. Initially, a porous and thin GDC scaffold was coated onto the electrolyte of both cells using a dip coat. The suspension was prepared by milling GDC powder with ethanol, dispersant (Menhaden fish oil in azeotropic solvent), and binder (6 wt% ethyl cellulose in terpineol). Cell A was dipped once and cell B was dipped twice into the scaffold suspension. Afterward, the scaffold was dried at room temperature and heat-treated at 1300 °C for 3 h. PNO was infiltrated into the GDC scaffold as the active cathode material. Briefly, Pr and Ni nitrates with stoichiometric ratios were mixed with water (7 molar) and surfactant (Triton-X) using a magnetic stirrer. Cells were dipped into the infiltrate suspension while put inside a high vacuum chamber for two minutes. Afterward, the excess was removed using a damp tissue. The cells were heat-treated at 350 °C for 15 minutes for the nitrates to decompose. This process was repeated three times and the solid load of the nitrates in the GDC scaffold reached 30 wt%.

5.2.5 Preparation of scaffolds for X-ray diffraction (XRD) analysis

Preliminary XRD analysis is performed on two candidates for PNO scaffolds: YSZ and GDC. Both scaffolds were prepared using slip casting. YSZ powder was first calcined at 1500 °C for 2 h and then milled for 24 h using a ball mill at 72 rpm to generate more porosity after sintering. Then, YSZ (or GDC) powder was mixed with water (1:1 weight ratio) and the pH of the suspension was set to 4 using hydrochloric acid to improve the stability of the suspension. The suspension was milled using a planetary mill and zirconia balls at 300 rpm for 2 h. Subsequent to milling, it was sonicated for two minutes and then cast onto a flat plaster mold. After drying at room temperature, the flat plates were sintered at 1300 °C for 3 h. PNO was infiltrated once into the scaffolds and decomposed at 350 °C. Then it was heat treated at different temperatures (700 – 1000 °C) for 5 h and XRD analysis was performed from the top surface of the infiltrated scaffolds.

5.2.6 Fuel cell setup and electrochemical testing

The tubular cells were attached to mullite tubes using Ceramabond 552 (Aremco) cement. Hot glue was used to seal the outlet of the mullite tube. Ag paste (Fuel Cell Materials) was coated onto the anode and Ag wire (Alfa Aesar) was wrapped around the anode as the anode current collector. Copper mesh (Alfa Aesar) was also rolled and pushed inside cell A (with a larger diameter) as the current collector. Ag paste was coated onto the cathode and dried at 200 °C. A Ag mesh was tightly wrapped around the cathode using Ag wires. The cell was placed in the hot zone of a tubular furnace and a thermocouple was placed close to the cathode to monitor the temperature. The anode was reduced using a mixture of nitrogen and humidified hydrogen (3 vol.% H₂O) with flow rates of 43 and 7 standard cubic centimeters per minute (SCCM), respectively, over 24 h. Then the gas mixture was gradually switched to 0 SCCM of nitrogen and 50 SCCM of hydrogen in 1 h.

Synthetic air with 100 SCCM was used on the cathode side. Electrochemical impedance spectroscopy (EIS), IV and OCV measurements were performed using a Metrohm Autolab potentiostat with 10A booster and FRA32M module for impedance measurements in four probe configurations.

Microstructural analysis was carried out using a Zeiss Sigma 300 VP-FESEM scanning electron microscope. Image J software was used to analyze the SEM images of the polished sample. Matlab optimization toolbox with a combination of DRT tools was used to extract distribution of relaxation time (DRT) data from EIS graphs based on Tikhonov regularization with continuous function discretization [242]. XRD patterns of the cathode samples were directly collected over the surface of the tubes using a Rigaku Ultra IV diffractometer equipped with a cobalt tube as the radiation source.

5.3 Results and discussion

5.3.1 PNO reactivity with YSZ and GDC scaffolds

Although PNO can be obtained as a pure phase up to 1350 °C by different methods [260], there is evidence of PNO's decomposition in an oxidizing atmosphere at temperatures below 900 °C [285]. The minimum temperature for PNO single-phase formation has been reported to be between 950 and 1000 °C [262,286,287]. This questions the suitability of PNO as cathode material for intermediate temperature SOFC applications [288]. Due to the limited literature data on the stability of infiltrated PNO, the stability of PNO infiltrate is studied on two different cells.

5.3.1.1 Reactivity of PNO and YSZ

Planar YSZ scaffolds were prepared by slip casting YSZ suspension onto a flat plaster mold, drying at room temperature and subsequent sintering at 1300 °C. Figure 5-1a compares the XRD data for

PNO infiltrated into a YSZ scaffold and heat-treated for 5 h between 700-1000 °C. At 700 and 800 °C, the dominant phases are Pr₆O₁₁ with the main YSZ scaffold peaks. NiO peaks could not be identified in this temperature range as the intensity counts are at the background level. However, by increasing the temperature to 900 °C, the nickel oxide phase is present alongside Pr₆O₁₁. At 1000 °C, the formation of the PNO phase is confirmed in the YSZ scaffold, while the NiO phase is still detectable. In addition, the appearance of Pr₂Zr₂O₇ and Pr₂Sr₂O₇ phases confirm the reaction of PNO and the YSZ scaffold at 1000 °C. Sr impurities could have been present in the raw material. Pr₂Zr₂O₇ has been identified as a product of Pr and YSZ reaction in other studies using conventional synthesis methods [260,289]. This reaction occurred gradually and the intensity increased during long annealing times up to 1000 °C.

At temperatures lower than 1000 °C, the Pr zirconate phase is not visible, a behavior that has been observed in previous work [290] for the LNO/YSZ reactivity for four hours. This result is beneficial as with fewer secondary phases, the infiltrated electrode is more stable during SOFC operation.

As explained previously by Montenegro-Hernández *et al.* [260], the reactivity between PNO and YSZ using the solid-state reaction method is more a consequence of the decomposition of PNO in air at less than 900 °C. However, this is not the case with the infiltration method as the temperature at which the PNO phase is formed (1000 °C) is not in this range.

5.3.1.2 Reactivity of PNO and GDC

Figure 5-1b shows the XRD result of PNO infiltration into a GDC scaffold after subsequent heat treatment at 700-1000 °C. At lower temperatures, Pr₆O₁₁ is the predominant phase with low-intensity NiO peaks. In addition to these phases, the formation of a Ce-Pr-Gd phase is also present

(CPGO phase [291]). The calculated lattice parameters of this phase at 700, 800 and 900 °C are 5.4124(7), 5.4123(6) and 5.4102(8) Å, respectively. Laguna *et al.* [292] have previously confirmed the diffusion of Pr into the GDC lattice in PNO-GDC powder mixtures at temperatures higher than 1100 °C. According to this study, this phase is formed at much lower temperatures when infiltrated. By increasing the temperature to 1000 °C, single-phase PNO forms with low-intensity Pr₆O₁₁ and traces of NiO. However, the phase formation of PNO, as in the previous case with PNO-infiltrated YSZ, occurs at 1000 °C. No evidence of reactivity between PNO with GDC is found up to 1000 °C.

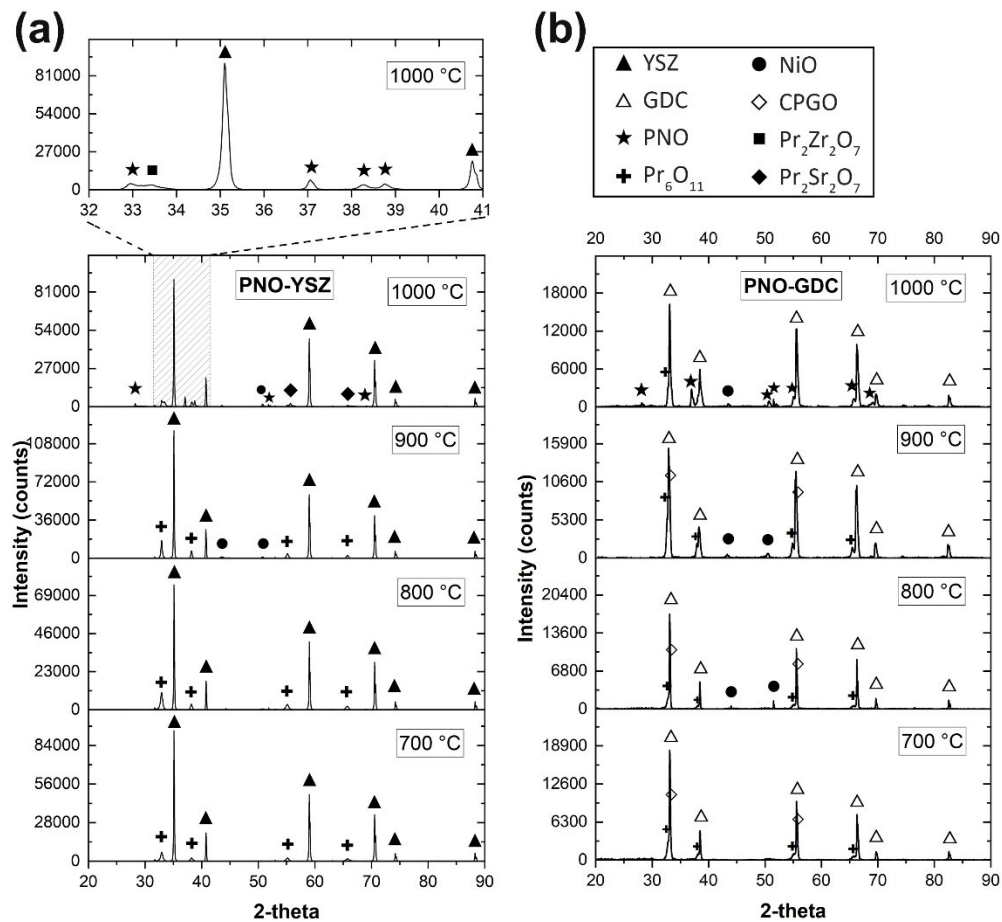


Figure 5-1. XRD diffractograms of (a) PNO-infiltrated YSZ and (b) PNO-infiltrated GDC scaffolds in samples annealed between 700 and 1000 °C for five hours using one infiltration.

The PNO peaks in the YSZ substrate of Figure 5-1a are less clear in comparison with the PNO-infiltrated GDC sample (Figure 5-1b) probably due to the formation of $\text{Pr}_2\text{Zr}_2\text{O}_7$ with the YSZ scaffold. Based on these XRD results, GDC was chosen as the scaffold for PNO infiltration.

5.3.2 Post-mortem SEM analysis of the cells

Post-mortem SEM micrographs of cells A and B are shown in Figure 5-2a-f. The contrast of the low-kV images of the polished specimens shows three distinct phases in the anode support and AFL. Contrast mechanisms of Ni-YSZ SOFC anodes using low-kV electrons are explained by Thyden *et al.* [19]. Conductive and percolating Ni particles shine brightly, while insulating YSZ, and epoxy-filled pores are in dark and light grey, respectively. According to Figure 5-2a and b, both cells have interconnected Ni particles inside the anode support after the stability tests. There is no sign of Ni migration from the anode/electrolyte interface as well. In addition, the anode/electrolyte or cathode/electrolyte interface is intact without any sign of delamination. The thickness of the anode support in cell B is higher than cell A. Comparing Figure 5-2e and f shows the average pore size in the anode support of cell B is larger than cell A. This can ease fuel diffusion to the electrode/electrolyte interface, considering the fact that the thickness of the support in cell B is much larger than cell A. A 20 μm AFL can be detected in Figure 5-2e with less porosity compared to the attached support layer. Comparing Figure 5-2c and d shows that the thickness of the electrolyte in cells A and B is 8 and 37 μm , respectively. As a result, the ohmic contribution of the electrolyte will be higher in cell B. The thickness of the infiltrated cathode for cells A and B is 10 and 22 μm , respectively, providing the possibility to study the effect of infiltrated cathode thickness on the performance of the fuel cells as well. Some traces of silver can be seen (bright) at the cathode/electrolyte interface in Figure 5-2c and d, which could have been entrapped during the polishing or cutting process. Due to embedding the post-mortem cells inside epoxy, PNO infiltrates

are not easily visible inside the cathode. A reference cell was fabricated with PNO being infiltrated inside the GDC scaffold and the resulting cathode microstructures of fractured specimens are shown in Figure 5-2g and h. Figure 5-2g shows the cathode/electrolyte interface and Figure 5-2h shows the top section of the cathode and the infiltration direction. As can be seen, GDC grains are uniformly covered by PNO infiltrates from top to the bottom of the cathode thickness, while leaving porosity for air diffusion inside the cathode.

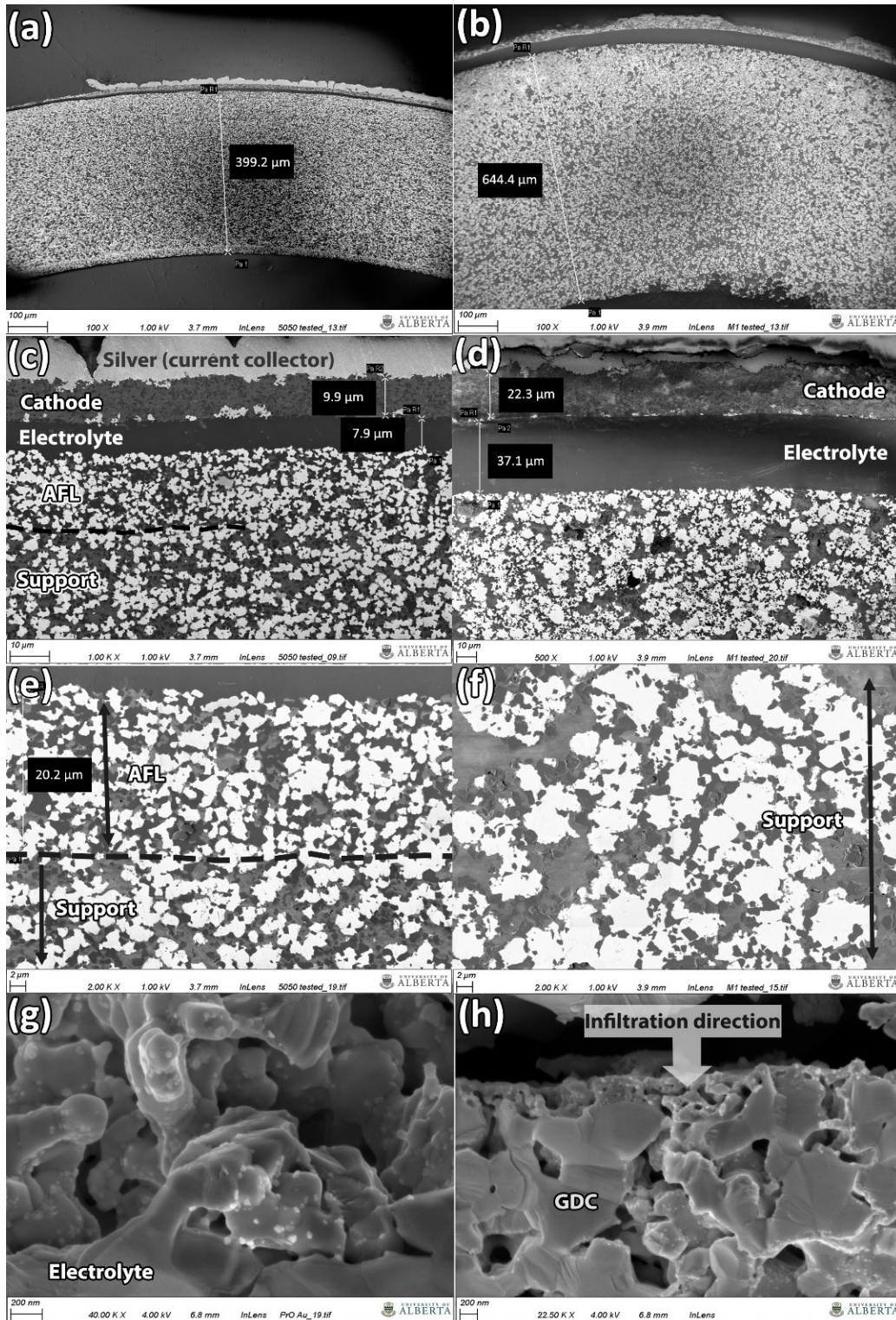


Figure 5-2. Post-mortem 1 kV secondary electron in-lens SEM images of epoxy-embedded polished specimens from cell A (a, c and e) and cell B (b, d, f). Contrast shows different phases in AFL and support. Ni, YSZ and pores are bright, dark grey and light grey, respectively. 4 kV secondary electron in-lens SEM images of fractured specimens from the reference cell are shown in g and h.

5.3.3 Electrochemical performance of the cells

Performances of cells A and B at different temperatures are shown in Figure 5-3a and b. According to Figure 5-3a, peak power density (PPD) for cell A is 770, 470 and 274 $\text{mW}\cdot\text{cm}^{-2}$ at 750, 700 and 650 °C, respectively. The performance of cell B is shown in Figure 5-3b with PPD of 660, 380 and 210 at 750, 700 and 650 °C, respectively. According to Figure 5-3c, the PPD of cell A is 17, 23 and 30 % more than cell B at 750, 700 and 650 °C, respectively.

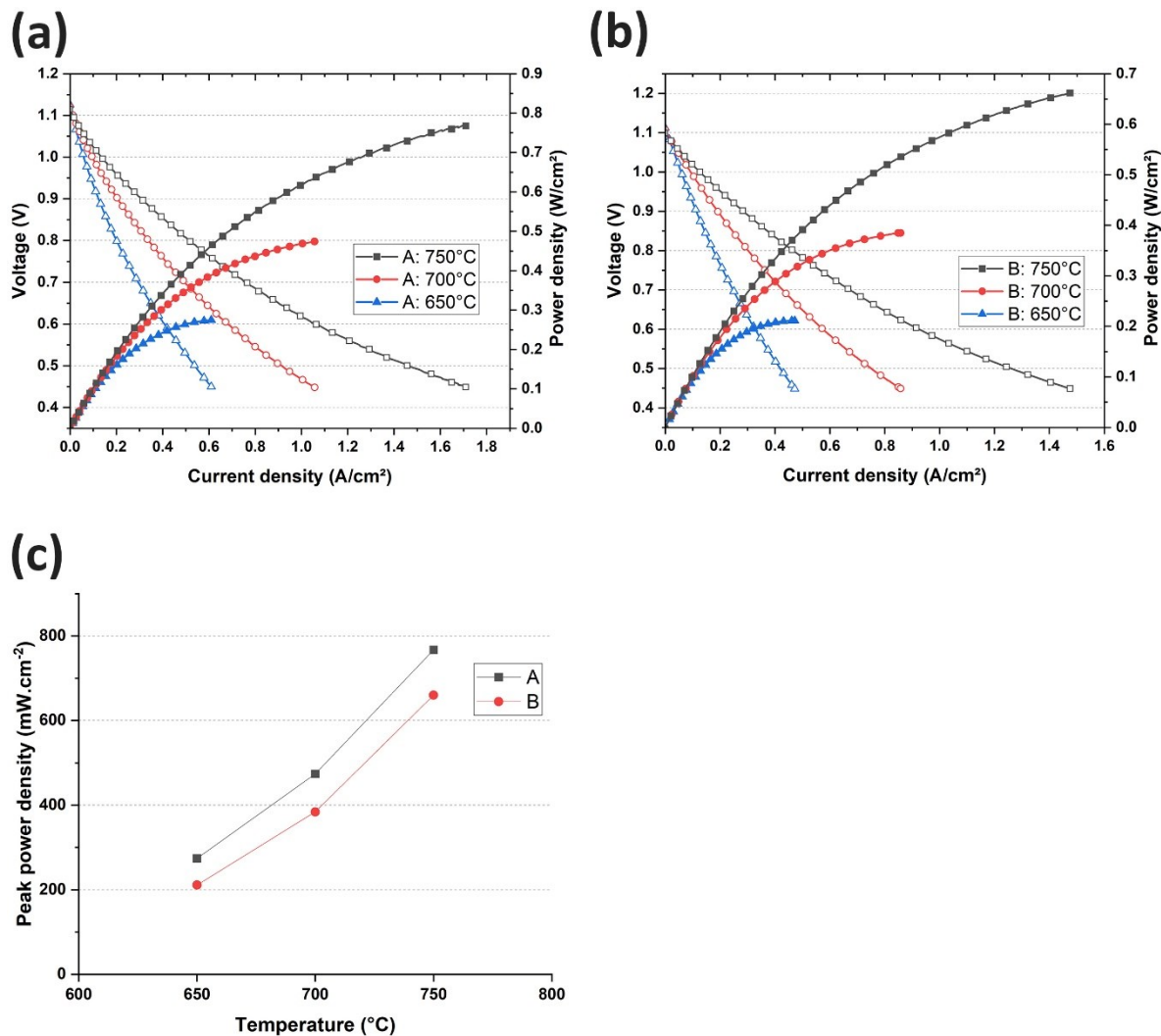


Figure 5-3. Current density-voltage-power density graphs of (a) cell A and (b) cell B at different temperatures with 50 SCCM H₂ (3 vol.% humidified) on the anode side and 100 SCCM air on cathode side; (c) comparison of peak power densities of cell A and B at different temperatures.

Nyquist plots of both cells at each temperature are compared together in Figure 5-4. According to Figure 5-4a, b and c, the ohmic resistance of cell A is lower than cell B. The reason for the difference in ohmic resistance is related to the thinner electrolyte of cell A compared to cell B as shown in Figure 5-2c and d. DRT graphs of the EIS data were extracted and shown in Figure 5-4d, e and f. DRT computation is based on Tikhonov regularization with gaussian regularization

method. DRT parameters including full width half maximum (0.5) and regularization parameter (0.001) were constant for both cells. As can be seen in Figure 5-4a, b and c, DRT data is well fitted with the corresponding EIS data (dots vs line). Four resistance-constant phase elements (R-CPE) equivalent to four peaks are detectable in DRT data for both cells except for the peak R5 with a

characteristic frequency of 1 Hz at 650 °C for cell B. The difference in the microstructure of both cells makes the comparison of the DRT data complex.

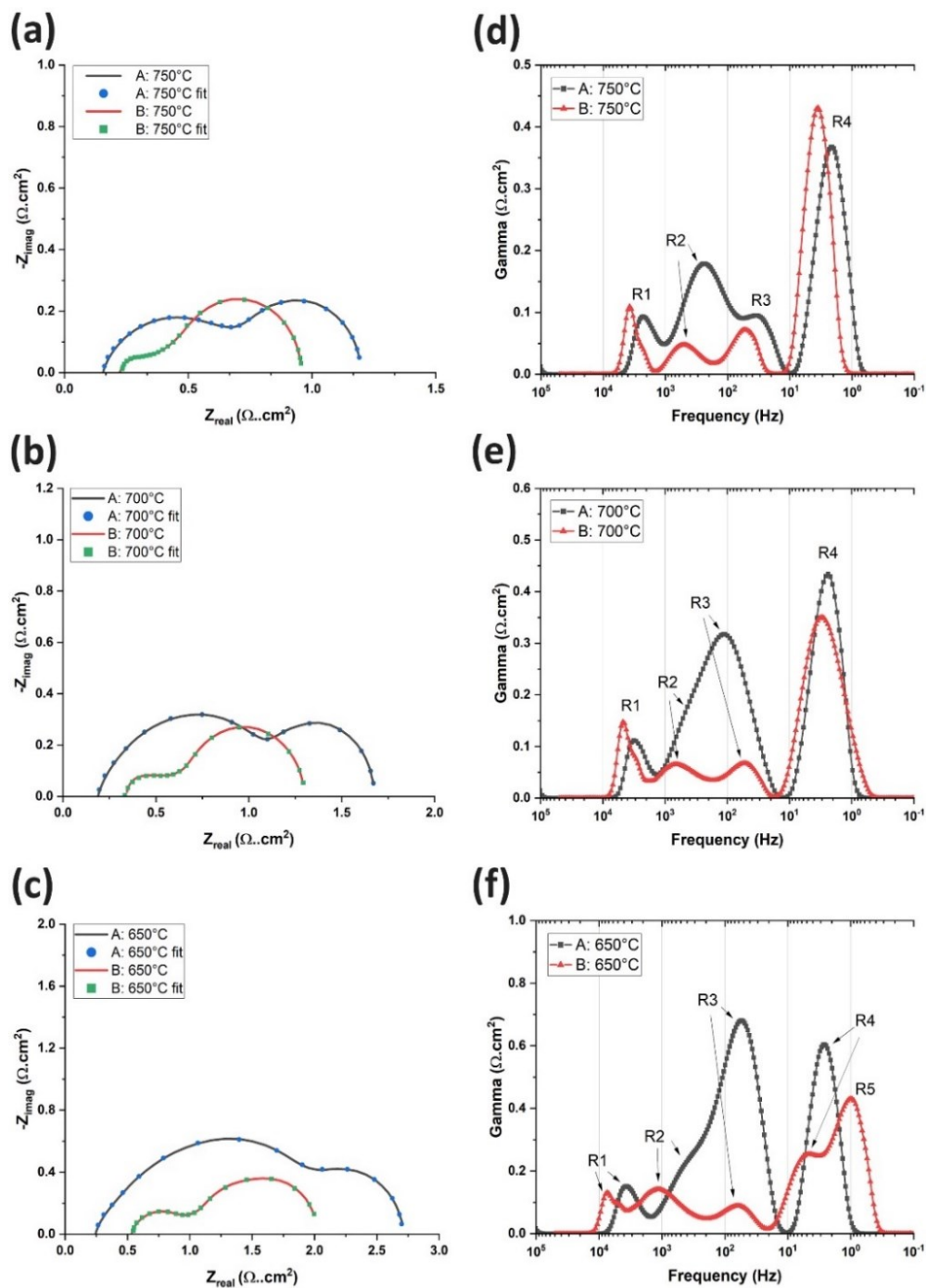


Figure 5-4. EIS comparison of cells A and B at (a) 750 °C (b) 700 °C (c) 650 °C. Blue circles and green squares show the fittings on experimental EIS data using the DRT method. Corresponding DRT data for each temperature are plotted in d, e and f.

Due to the novelty of such infiltrated cathodes, limited data are available in the literature on EIS analysis of infiltrated nickelates. Changing either the anode or the cathode's microstructure can help to understand the contribution of each peak as suggested by others [293]. For this reason, praseodymium oxide (PO = Pr₆O₁₁) was infiltrated into similar GDC scaffolds and used as a new cathode material for cells A and B. The rest of the variables (porosity, thickness, etc.) were kept similar for both cells. DRT data of cell A with PNO and PO cathodes at different temperatures are compared together in Figure 5-5a, b and c. For the sake of comparison, fuel and air flow rates were kept constant for both cathodes. As can be seen for cell A, high-frequency peak R1 with a characteristic frequency between 2000-3000 Hz is not affected by changing the cathode. Peak R1, almost unaltered with temperature, is assigned to oxygen ion transfer in air and fuel electrodes, as previously reported by other researchers [245,294–296]. Peak R2 with a characteristic frequency of 100-1000 Hz is also not affected by changing the cathode, especially at 650 and 700 °C. Increasing the temperature to 750 °C the value of peak R2 is slightly reduced, which can have overlap with the R3 contribution. Peak R2 is associated with charge transfer resistance at the anode/electrolyte interface [93,295]. The fact that peak R2 is not much affected by changing the cathode confirms this hypothesis. Interestingly, the value of peaks R3 and R4 are reduced by changing the cathode from PNO to PO while keeping the other components of the cell similar. Peak R3 with a characteristic frequency between 10-100 Hz is associated with oxygen ion surface exchange [295] and charge transfer inside the cathode.

DRT data for cell B with PNO and PO cathodes are shown in Figure 5-5d, e and f. To better understand the contribution of peak R3 and R4, the cathode gas atmosphere is changed for cell B, in addition to changing the cathode. Three different cathode atmospheres were used at 650 °C and 700 °C. According to Figure 5-5d, the value of the low-frequency peak R5 is reduced when PO

cathode is used at 650 °C (black vs. red graphs). By using pure oxygen on the cathode side (blue vs red graph), the R5 peak is eliminated. Also, when atmospheric air is used with the PO cathode compared to 100 SCCM air (green vs red graph), the peak R5 value increased. These results suggest that low-frequency peak R5 can be related to concentration polarization and gas diffusion in the cathode. By increasing the temperature to 750 °C in Figure 5-5e, peak R5 for the PO cathode appeared at lower frequencies (0.7 Hz) when atmospheric air is used. In contrast to cell A, peak R3 for cell B was not much affected by changing the cathode or changing the cathode gas atmosphere. At 750 °C, the most dominant difference in DRT peaks of cell B was the low-frequency peak R4. The variation of the DRT graph for cell B upon changing the hydrogen pressure is shown in Figure C 2 of the appendix C. As can be seen, peak R4 is affected by both changing the flow rate of hydrogen on the anode side as well as changing the flow rate of oxygen on the cathode side. In addition, increasing the total flow rates increases the characteristic frequency of peak R5 from 2 to 10 Hz. This behavior at low frequency is attributed to gas conversion. Gas conversion and total flow rates have an inverse relationship [297–299]. In low steam partial pressures, gas conversion can be the highest contributor to cell resistance [299]. It was demonstrated by Flura *et al.* that an EIS setup with poor gas diffusion network conversion contribution will dominate, especially at low oxygen partial pressure [300]. Formation/consumption of gas generated by EIS *ac* perturbation on top of the electrode is the reason for gas conversion polarization which its value increases in poor gas flow channels and lower gas flow rates. This can be worse for most of the tubular cell test setups, because air on the cathode side is not pressurized compared to planar designs. When the cathode gas was switched from atmospheric air to oxygen (using hydrogen = 50 SCCM as fuel), peak R5 was revealed in

Figure C 2 as a gas diffusion contributor in the cathode. This implies that conversion and diffusion mechanisms in the SOFC are coupled, as confirmed by others [299].

Figure 5-5 and Figure C 2 were useful to find out the contribution of each peak in Figure 5-4. However, interpretation of the DRT data should be performed with caution. Further studies with anodic and cathodic symmetrical cells are required to fully understand the nature of each peak. Moreover, anodic and cathodic peaks can have overlapping contributions, as the time constant for one component can limit the electrochemical reaction of the other.

According to Figure 5-4d, e and f, no peak with characteristic frequencies less than 1 Hz is detected in Figure 5-4. It can be concluded that no concentration polarization is taking place either in the anode or the cathode of cell A or B with a PNO cathode. When comparing Figure 5-4d to Figure 5-4f, the peak R3 value for cell A in Figure 5-4e is significantly reduced at 750 °C compared to 650 °C suggesting that the respective cathodic contribution is highly thermally activated. In addition, the R3 peak in cell A with a relatively thinner cathode is more affected by temperature variations. The lower performance of cell B can be related to the ohmic resistance due to the thicker electrolyte. Cell B anode support, however, contains higher pore volume due to higher added pore former and higher binder content in the extrusion process with a larger average pore size (compare Figure 5-2e and f). The importance of pore content on the performance of SOFC has already been

discussed by other researchers [301]. This might compensate for the lack of AFL in cell B by providing fuel channels with faster flow rates inside the anode to the anode/electrolyte interface.

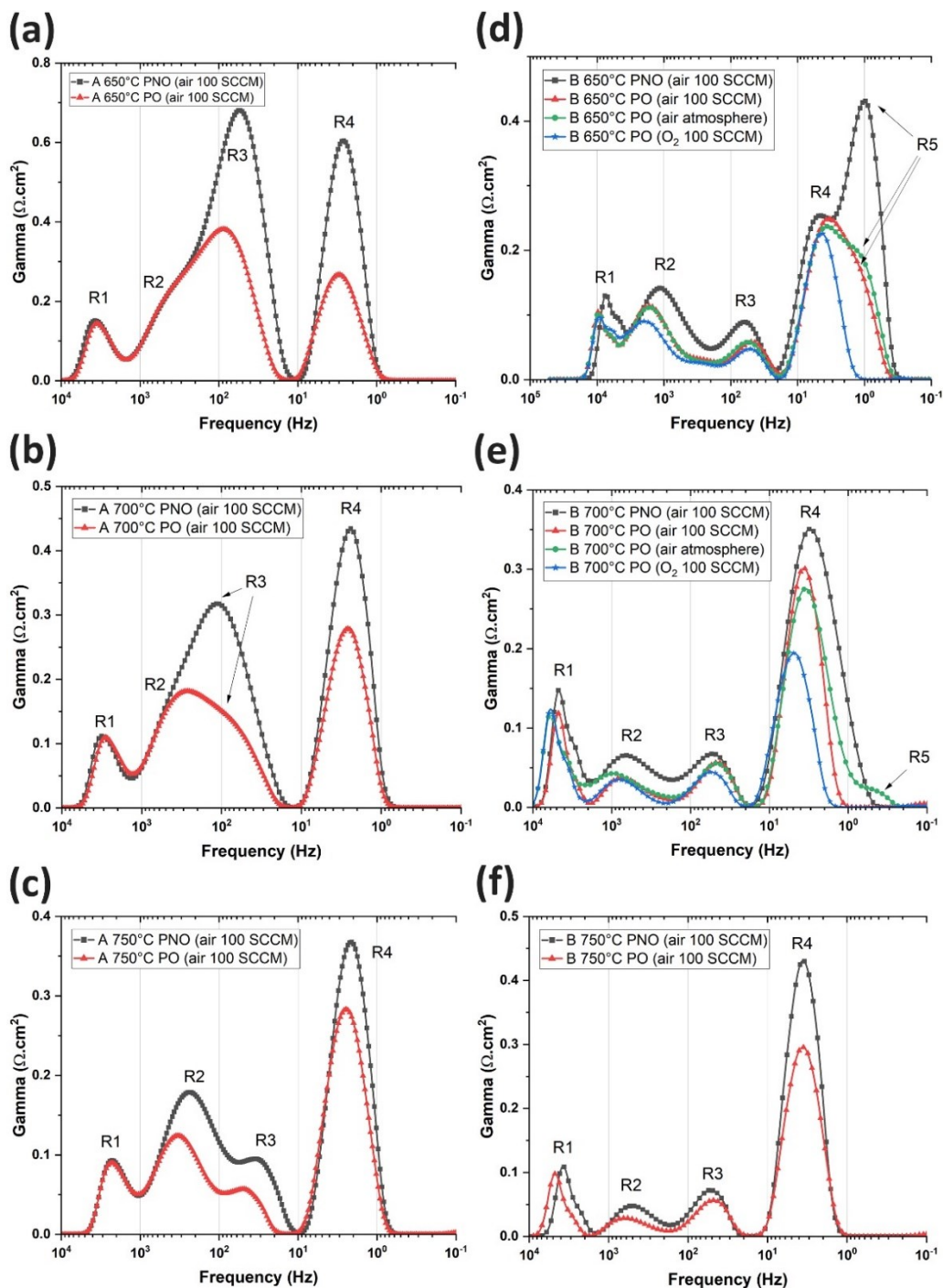


Figure 5-5. Comparison of DRT results of cell A and B with PNO and PO (Pr_6O_{11}) cathodes exposed to different cathode atmospheres. (a, b and c) cell A. (d, e and f) cell B. Humidified hydrogen with 50 SCCM was used as fuel on the anode side for both cells.

5.3.4 Stability test

Figure 5-6 shows the result of the potentiostatic tests for cells A and B at 0.7 V and 650 °C. Fuel and air flows were 50 and 100 SCCM, respectively, for both cells. According to the Figure 5-6, cells A and B are stable for 91 and 260 h of the test period, respectively. An improvement in the current density is noticeable for both cells at the beginning of the stability test. In addition, the behavior of both cells seems similar for the initial 91 h, which shows the repeatability of the test. The sudden increase in current density of cell B at 186 h is due to a slight increase in the fuel pressure inside the fuel chamber. The fuel outlet gas - composed of unreacted hydrogen and produced water - was placed inside a water container. Proper bubbling of the fuel outlet during the stability test ensures sealings are gas-tight. The water inside the container gradually evaporates and refilling the water container slightly increased the fuel pressure.

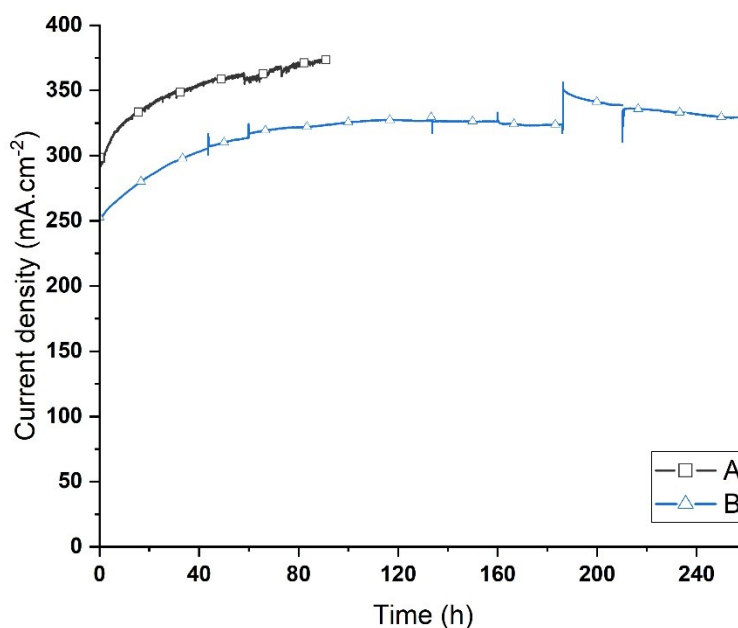


Figure 5-6. Potentiostatic test of cell A and B at 650 °C and 0.7 V. Fuel and air were provided on anode and cathode sides with 50 and 100 SCCM, respectively.

The performance and resistances of both cells before and after the potentiostatic tests are compared together in Figure 5-7. According to Figure 5-7a, cell A's performance increased from 274 to 360 $\text{mW}\cdot\text{cm}^{-2}$ (31 % improvement) during the test. Comparing the Nyquist plots in Figure 5-7b and c reveals a reduction in total impedance value after 91 h of the stability test. Ohmic resistance did not change, which shows stable electrical contact during the experiment. Figure 5-7c shows the corresponding DRT curves for the Nyquist plots in Figure 5-7b. According to this figure, peaks R3 and R4 showed a reduction which is the reason for the performance improvement during the stability test.

Figure 5-7d shows how the performance of cell B improves during the first 161 h of the test from 211 to 277 $\text{mW}\cdot\text{cm}^{-2}$ (31 % improvement). For the rest of the test, the performance slightly decreases from 277 to 267 $\text{mW}\cdot\text{cm}^{-2}$. Figure 5-7e shows the Nyquist plot at different time intervals of the stability test for cell B. As shown, the total polarization resistance continuously decreases from 1.46 $\Omega\cdot\text{cm}^2$ at the beginning of the test to 0.95 $\Omega\cdot\text{cm}^2$ after 260 h. However, ohmic resistance starts to increase from 0.5 to 0.6 $\Omega\cdot\text{cm}^2$ between 160 h and 260 h of the test. The DRT data in Figure 5-7f show a reduction in the value of peak R4 as the experiment progresses. Also, peak R5 is completely removed in the first 60 h of the experiment. Peak R2 slightly increases from the start of the test up to 160 h, then returns to the initial value at 260 h. As discussed before, this peak is related to charge transfer resistance in the anode which accelerates by operating at high temperatures and steam content. The increasing value of peak R1 and R2 can be attributed to the degradation of the Ni-YSZ TPB by agglomeration of Ni particles or contamination of the electrode [295]. However, this process is not reversible. In contrast, refilling the outlet water container at 163 h and returning the fuel pressure to the initial pressure might be the reason for this behavior. Increasing the ohmic resistance of cell B can be the reason for a slight decrease in the performance

between 160-260 h of the test. The increase in ohmic resistance of the cell can be related to the current collector contact during the experiment. As mentioned earlier, changing the cathode can vary the contribution of peak R4. Post-mortem XRD analysis was performed on the cathode to further understand the underlying reason for the R4 peak decreasing.

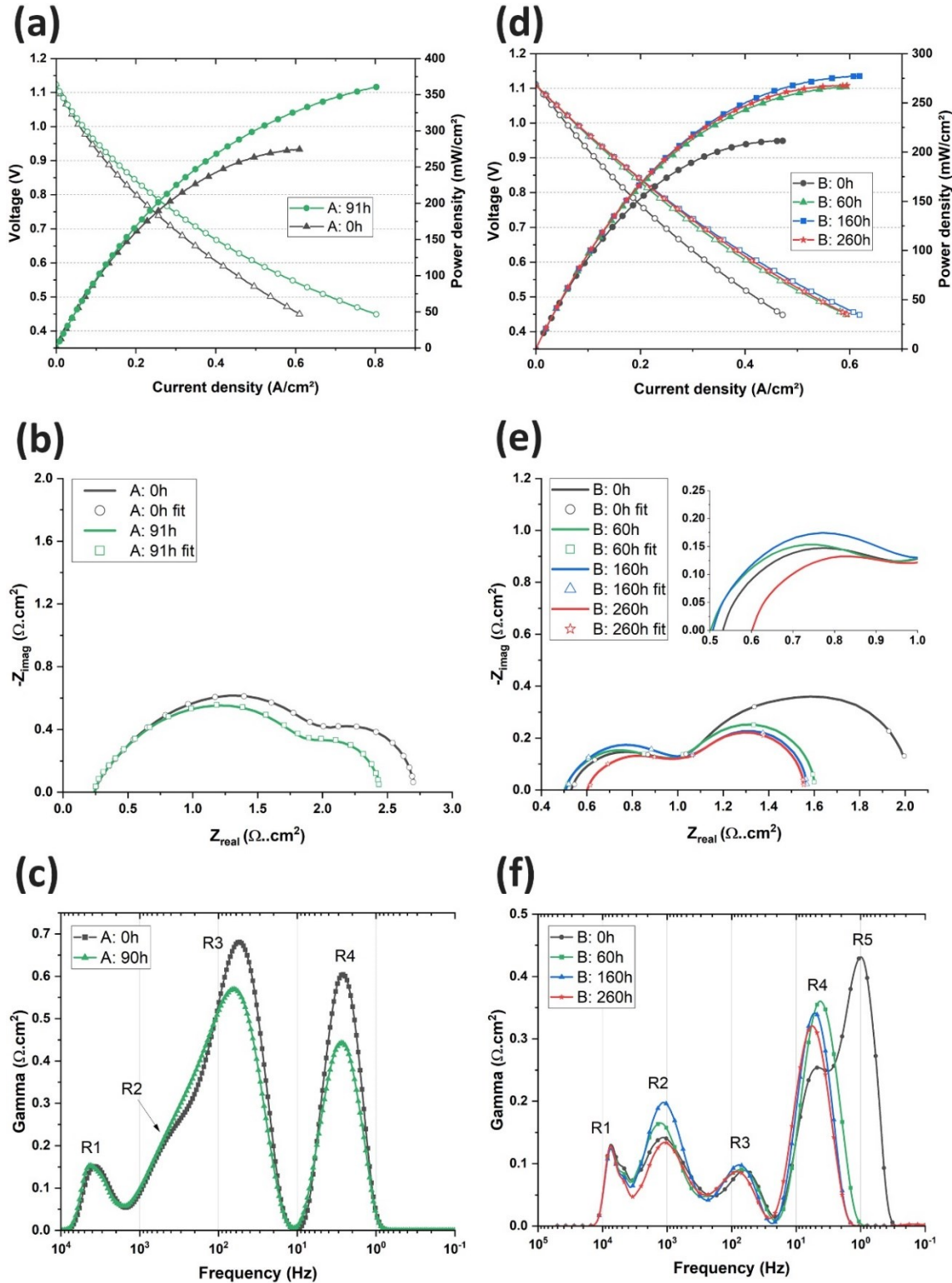


Figure 5-7. I-V-P, Nyquist plots and corresponding DRT graphs for cell A (a, b and c) and cell B (d, e and f). The solid line in (b) and (e) are experimental Nyquist data while the points on the curve show the accuracy of corresponding DRT fitting. Inset in (e) shows the zoomed Nyquist data.

5.3.5 Post-mortem XRD phase analysis

As mentioned in section 5.3.1.2, no evidence of reactivity of the PNO phase with GDC was found in the samples heat-treated at 1000 °C for five hours, but subsequent decomposition of PNO under SOFC operation due to prolonged heat treatment and evolving into a high-order nickelate is possible [287]. To study this possibility, two fuel cells were fabricated identical to cells A and B with PNO cathodes as reference cells to compare them with post-mortem XRD results. The active area of each cell was cut and XRD was performed for cathode phase analysis. For post-mortem XRD measurements, the silver current collector coat was carefully peeled off to expose the cathode surface.

Figure 5-8 shows the XRD comparison for reference cells and post-mortem cells. Due to the small surface area of each cell, XRD peak intensities are lower than Figure 5-1. Reference cells A and B consist of GDC scaffold alongside PNO peaks and traces of Pr₆O₁₁. Interestingly, the intensity of the 33 ° peak has increased and a new peak at 38.4° emerged for both cells after the experiments. These peaks are characteristic of the decomposition of PNO into PO and Pr₄Ni₃O₁₀ as previously observed by Montenegro-Hernández et al. [260]. The Pr₄Ni₃O₁₀ phase appeared as an effect of the heat treatment under air which facilitates the oxidation of Ni²⁺ to Ni³⁺ [287], increasing the electrical conductivity of the Ruddlesden–Popper cathode [302]. Reduction in the R4 peak value of Figure 5-7c and f during the stability tests can be attributed to an improvement in the conductivity of the cathode. Even so, the intensity of Pr₄Ni₃O₁₀ (at ~38°) is low and interferes with the base PNO peaks, so one should be cautious reaching a definitive conclusion. No further phase evolution was observed during this analysis even though both samples have a considerable difference in the operation time (91 to 260 hours).

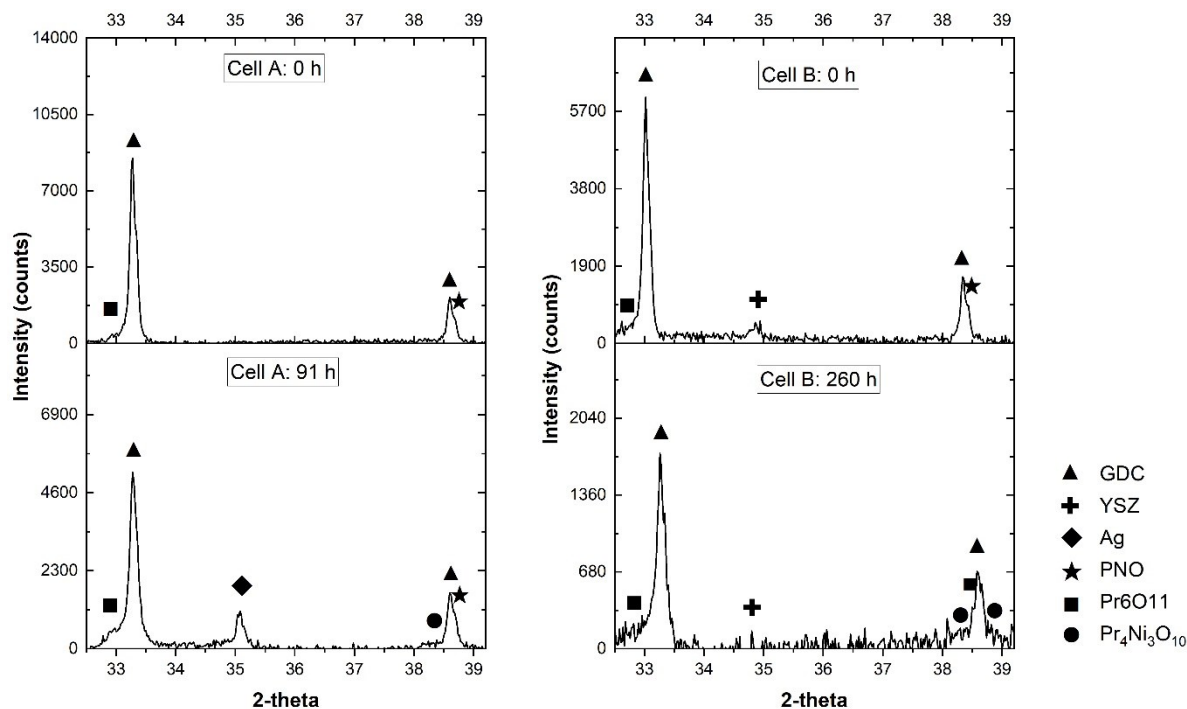


Figure 5-8. Background-subtracted XRD in the 32 to 39° range of A (91 h test) and B (260 test) samples heat-treated at 1000 °C and operated at 650 °C in comparison with the reference cells (0 hours of operation) for the same heat treatment.

5.4 Conclusions

$\text{Pr}_2\text{NiO}_{4+\delta}$ (PNO) cathode was fabricated using infiltration into a GDC scaffold because it showed lower reactivity than YSZ scaffolds as confirmed by XRD analysis. The performance of the cathode was compared on two tubular SOFCs with different anode and electrolyte microstructure. Both cells showed promising performances at temperatures between 650-750 °C. Stability tests in the SOFC mode showed stable performances for both cells during 91 h and 260 h of potentiostatic tests at 650 °C and 0.7 V. Total polarization resistance of the cells reduced during the stability tests, which was associated with an enhancement in the oxygen reduction reaction and gas conversion rate according to DRT results. According to post-mortem SEM analysis, nickel particles inside the anode were interconnected showing no apparent microstructural degradation.

In addition, no delamination at the cathode/electrolyte interface was detected. Post-mortem XRD analysis of the cathodes showed partial PNO phase transformation into $\text{Pr}_4\text{Ni}_3\text{O}_{10}$ with improved conductivity and thermal stability. Based on the results of this study, PNO can be a promising cathode for low-temperature SOFC applications due to its high performance and stability.

Conflicts of interests

There are no conflicts to declare.

Acknowledgements

The authors would like to acknowledge Future Energy Systems Research Initiative (grant number RES0031233) and the Climate Change and Emissions Management Corporation of Canada, and grant PID2019-107106RB-C32 funded by MCIN/AEI/ 10.13039/501100011033 for funding this research.

Chapter 6: Degradation of Solid Oxide Electrolysis Cells with Infiltrated Praseodymium Nickelate Cathodes

6.1 Abstract

Stability of a cell with similar composition and microstructure to cell B in chapter 5 (PNO-infiltrated cathode and microtubular support) was measured in electrolysis mode. Severe degradation was noticed during 61 h of the potentiostatic test at 1.3 V and 700 °C. Post-mortem SEM analysis showed depletion of Ni from 100 μm away from the electrolyte towards the electrolyte, contributing to fuel electrode polarization resistance. In addition, DRT analysis revealed increased polarization resistance in air electrode during the stability test. Degradation of the electrode continued even in OCV condition which shows the effect of high steam content on degradation of the fuel electrode. The results of this study suggest further modification of both fuel and air electrode is required for the cell to operate in electrolysis mode.

6.2 Introduction

Avoiding the consequence of climate change requires modification of the current energy system from fossil fuels to low-carbon energy sources. Renewable energies available including solar and wind exceeds current energy demands several times. The challenge lies behind the infrastructure to fulfil the demand with continuous and flexible supply. In countries such as Denmark and Germany, the share of renewable electrical energy supply is reaching 40-50% [303]. By continuing the adaptation from other countries, the demand for large scale energy conversion devices increase. Analysis shows that 1600 GW of electricity and 7500 TWh of chemical storage might be needed to de-carbonize the heavy duty transport facilities such as trucks, ships and planes in Europe [304].

The huge scale for deploying electrolysis means there is enough room for different kinds of electrolyzers including alkaline, PEM and SOEC. SOECs have advantages in terms of conversion efficiencies, raw material availability and the ability to be integrated with downstream chemical synthesis [303]. Higher operating temperatures of SOECs give rise to two advantages over competing alkaline and PEM electrolyzers: (i) more favorable thermodynamics and (ii) faster kinetics [303]. In electrolysis of water, a water molecule is split into hydrogen and oxygen molecules as Eq. 6-1:



Total energy required for electrolysis is defined by enthalpy of formation (ΔH_f) of the reaction. In high-temperature steam electrolysis such as SOEC, ΔH_f is lower than liquid water electrolysis (e.g. PEM electrolyzers) by enthalpy of water evaporation (ΔH_{evap}). Electrolysis is preferred to operate at thermoneutral voltage (Eq. 6-2) [305].

$$E_{\text{th}} = \frac{\Delta H_{\text{th}}}{2F} \quad (6-2)$$

where 2 is the number of electrons per mole in the reaction and F is the Faraday constant. The reason is that at thermoneutral voltage (E_{th}), the heat required for the electrolysis reaction ($T \cdot \Delta S$, ΔS is the entropy change of the electrolysis reaction) equals the joule heat power ($ASR \cdot i^2$) formed by the loss in the electrolysis reaction. In other words, an electrolysis cell operating at E_{th} is generating enough power to supply the exact heat required for the electrolysis reaction without the need for external heating or cooling source. Equilibrium voltage (Eq. 6-3) is equivalent to the voltage of Gibbs free energy of formation ($\Delta G_f(T)$) at a given temperature.

$$E_{\text{eq}} = \frac{\Delta G_f(T)}{2F} \quad (6-3)$$

An electrolysis cell operating at $E_{\text{eq}} > E_{\text{cell}} > E_{\text{th}}$ requires external heat to keep the requested temperature and in the case of $E_{\text{cell}} > E_{\text{th}}$ the cell will heat up and needs cooling [305]. By increasing the operation temperature, the theoretical voltage required for splitting the H_2O or CO_2 is reduced by 20 to 30% [305]. An SOEC operating at thermoneutral voltage of 1.29 V will gain an electrolysis current density of $1.5 \text{ A}\cdot\text{cm}^{-2}$ whereas a PEM electrolyser at its thermoneutral voltage of 1.47 V gains a current density of $0.5 \text{ A}\cdot\text{cm}^{-2}$ with similar gas composition [303]. Lower operation voltages mean lower operation costs (lower electricity demand per quantity of produced gas) while higher current densities translate to lower capital cost (fewer electrolysers needed for production of hydrogen).

There have been superior improvements in SOEC stability in the past years. SOEC stack lifetime of 2.5 years has been experimentally demonstrated [306]. In addition, experimental tests with dry CO_2 electrolysis for over a year suggests SOEC is the most mature technology for electrochemical conversion of CO_2 into CO [307]. Nowadays, SOEC stack degradation is typically less than 1% per 1000 h and SOEC scalability is increasing at a fast pace [303]. It is worth mentioning that over 50,000 SOFC units with similar cells and stack components to SOECs are used for residential applications in Japan thus far [308].

Although SOEC technology is starting to scale up and commercialize by companies such as Topsoe, there have been several challenges for this technology. In the case of the fuel electrode, the partial pressure of oxygen can increase more than three orders of magnitude by increasing the steam content in the fuel composition from 3% to 50% H_2O in $\text{H}_2/\text{H}_2\text{O}$ [309]. As a result, nickel hydroxide formation and Ni surface transport accelerates [123]. Depending on operation conditions (current density, temperature, etc.), nickel can migrate toward [310] or away from the

electrolyte interface [311]. Ni relocation inside the fuel electrode can reduce the active TPB density and increase the polarization resistance contribution from the fuel electrode [312].

Air electrode degradation is also accelerated in electrolysis mode. A GDC barrier layer is usually used to prevent LSCF (lanthanum strontium cobalt ferrite) reaction with the YSZ electrolyte. SOEC tests at 800 °C showed fast degradation in the oxygen electrode during 50 h when a GDC layer is not implemented [313]. In many studies, formation of non-conductive SrZrO₃ is confirmed by diffusion of Sr into the GDC barrier layer, reacting with the YSZ electrolyte and increasing the ohmic resistance [311,314]. In the following section, the performance and stability of a similar cell to cell B in chapter 5 is measured in electrolysis mode and compared together. In addition, possible solutions to the challenges faced are suggested as future directions.

6.3 Experimental procedures and electrochemical testing

6.3.1 Electrochemical testing

The test setup for electrolysis tests is displayed in Figure 1-1. A heating tape (Omega) is wrapped around the fuel inlet as well as the cap of the impinger to avoid steam condensation. A thermocouple is placed inside the water impinger (close to where hydrogen bubbles inside the water). The hot plate controls the temperature of the water. The water impinger is placed inside silicon oil to uniformly transfer the heat from the hotplate to the water. The temperature of the water was increased to 82 °C for the saturated steam pressure above the water to reach to 0.5 atm. As a result, a ~ 50:50 mole ratio of steam:H₂ is achieved. The total fuel pressure was 1.01 atm (based on the digital flow meter reading). A hydrogen bubbler is placed ~ 10 cm deep inside water which increases the total pressure by 0.01 atm due to the water column in between the end of the bubbler and the water surface.

6.3.2 Electrolysis cell configuration

A cell was fabricated similar to cell B in chapter 5. Since the aforementioned cell was stable for about 260 h in SOFC mode, studying the performance and stability of a similar cell in electrolysis mode is the objective.

6.4 Results and discussion

6.4.1 Electrochemical performance of the cells

Initially, the performance of the cell was studied with a lower steam content ($\text{H}_2\text{O}:\text{H}_2 = 3:97$ mole ratio). The performance of the cell in fuel cell mode is shown in Figure 6-1a. The power densities at 650, 700 and 750 °C are 310, 550 and 880 $\text{mW}\cdot\text{cm}^{-2}$, respectively, which are slightly higher than the power density of the similar cell (cell B) in chapter 5. Figure 6-1b shows the EIS data in fuel cell mode at different temperatures. Part of improved performance can be attributed to lower ohmic resistances in this cell compared to cell B in chapter 5.

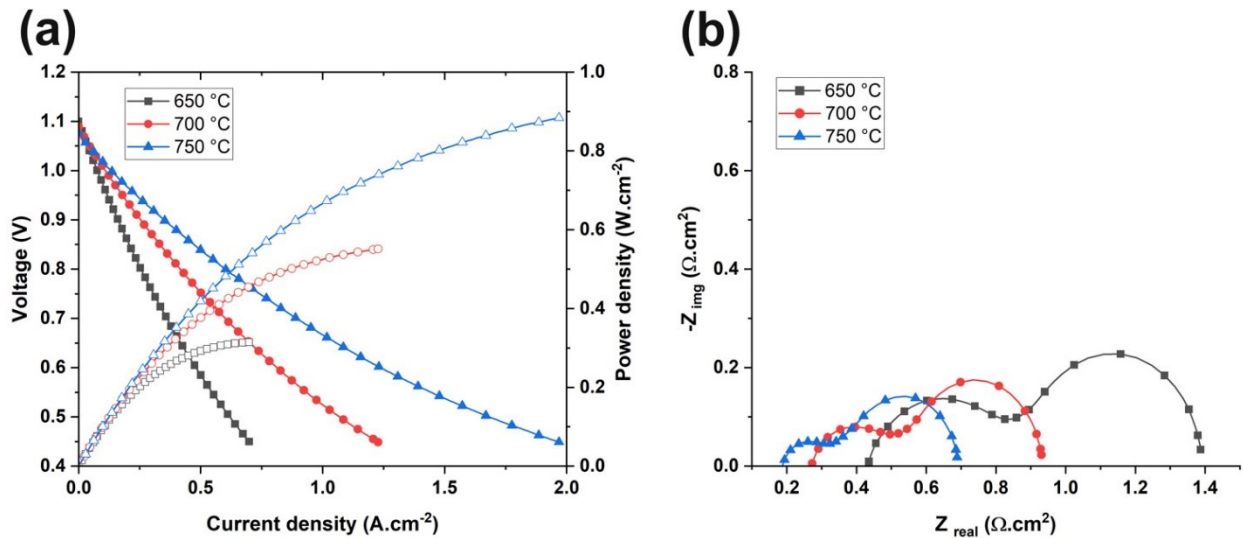


Figure 6-1 (a) I-V-P graph in fuel cell mode tested at different temperatures. (b) EIS graph measured at OCV. The fuel and air flow rates were 50 and 100 SCCM, respectively.

An electrolysis test was performed on the same cell by increasing the temperature of the water to 81 °C inside the impinger. Steam:H₂ molar ratio in the fuel composition is 1:1. Figure 6-2a shows the performance of the cell in both SOFC and SOEC modes. SOFC to SOEC transition on the I-V curve takes place linearly which suggests reversible behavior. Ohmic resistance at 700 and 750 °C are slightly higher than the corresponding ohmic resistances in Figure 6-2b (SOFC mode).

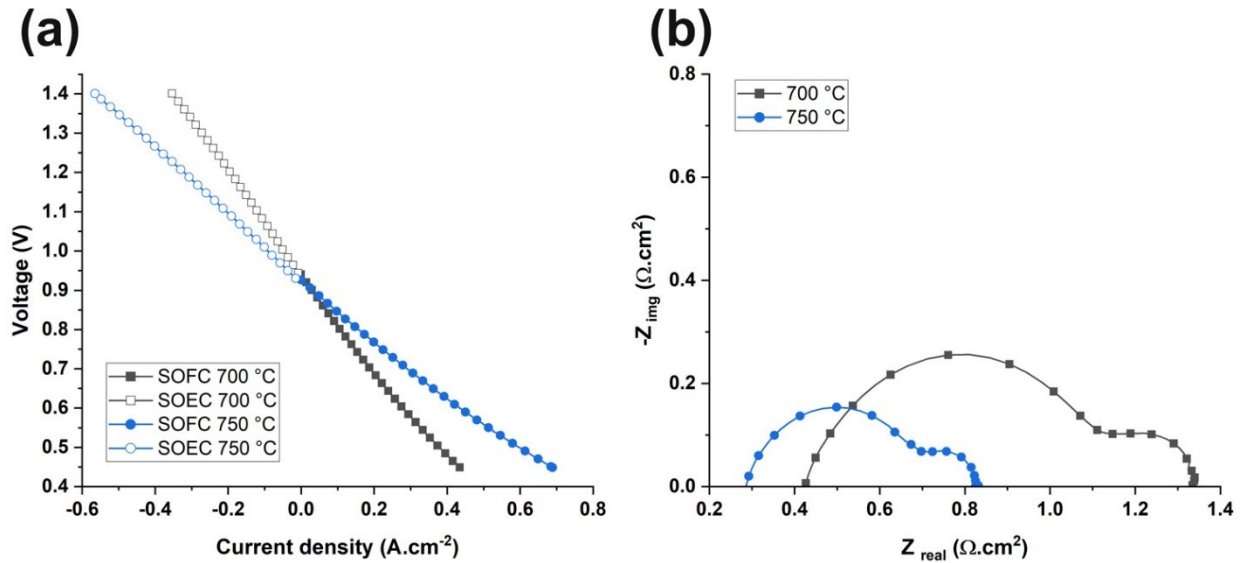


Figure 6-2 (a) Performance of the cell in fuel cell and electrolysis mode. (b) EIS data at OCV. Fuel composition was 50:50 mol ratio of H₂:H₂O.

6.4.2 Stability test

Figure 6-3 shows the stability test in SOEC mode at 1.3 V and 700 °C. The test was paused at 28 h and OCV was tracked to make sure the steam:H₂ ratio is not changing during the experiment. Figure 6-4a and b show OCV values recorded by pausing the stability test at 28-37 h as well as at the end of the stability test (61-84 h). Negligible fluctuation in OCV (+/- 5 mV) shows that the steam:H₂ composition is kept constant. This can be due to good insulation of the fuel line preventing steam condensation. Based on the stability test at 1.3 V, fast degradation takes place

from 0-28 h and then continues from 37-61 h with reduced degradation rate. In addition to the degradation during the test, the cell was degrading during 28-37 h in the OCV state. It can be concluded that degradation of the cell is related to the high steam content in fuel composition.

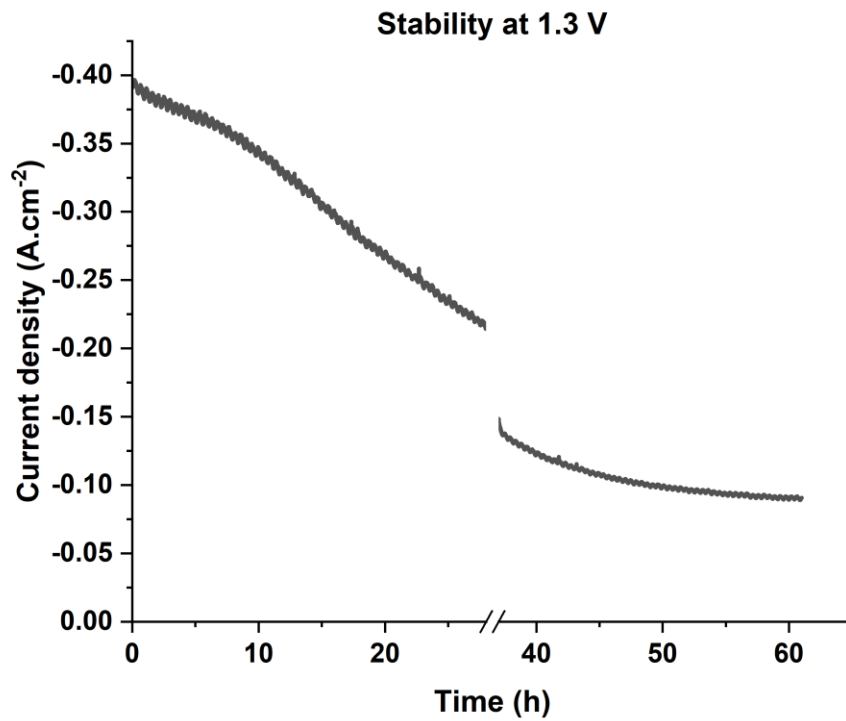


Figure 6-3 Stability test in electrolysis mode at 1.3 V. The stability test was stopped at 28h for 9h (OCV was measured during this period), then continued from 37h up to 61h. Fuel composition was 50:50 mole ratio of H₂:H₂O.

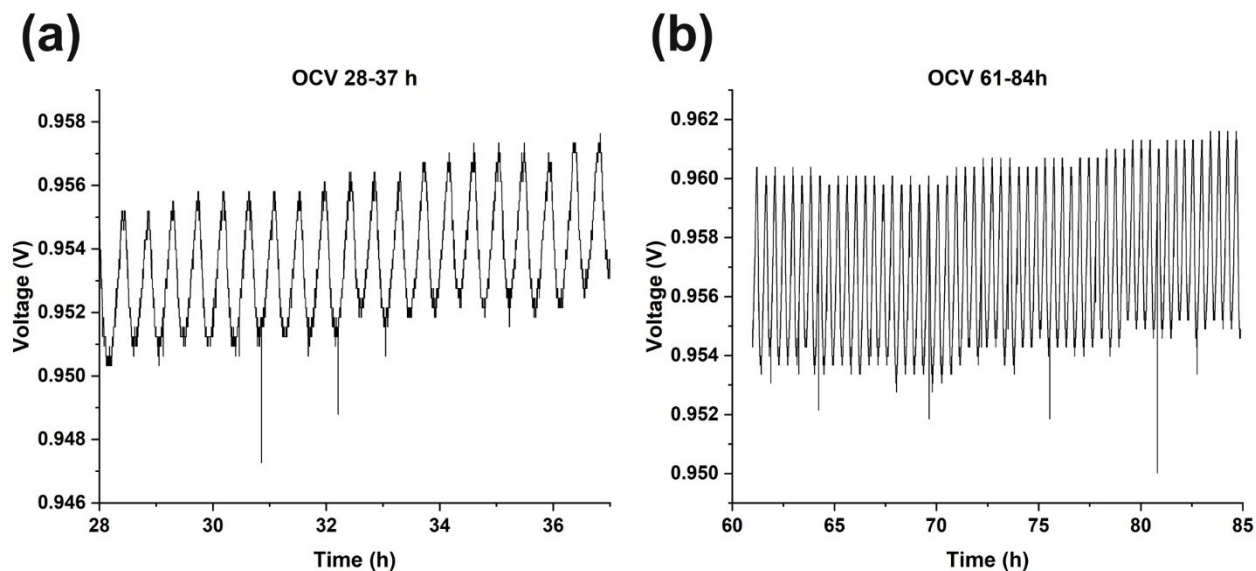


Figure 6-4 Tracking the OCV of the cell (a) in the middle of the stability test from 28 – 37 h and (b) at the end of the stability test from 61-84 h. Fuel composition was 50:50 mole ratio of H₂:H₂O. Note the OCV is plotted on an expanded scale.

The performances of the cell are compared at 0, 28h and 61 h of the stability test in Figure 6-5a. As can be seen, by continuation of the stability test, the cell's performance is degrading in both fuel cell and electrolysis mode. EIS measurements in Figure 6-5b show an increase of the total polarization resistance from $0.86 \Omega \cdot \text{cm}^2$ at the beginning of the test to $1.88 \Omega \cdot \text{cm}^2$ (at 28 h) and $4.1 \Omega \cdot \text{cm}^2$ (at 61 h). By deconvoluting the EIS data in Figure 6-5c, four R-CPEs are detected out of which peak R3 with characteristic frequency of 10-100 Hz is the main contributor to the degradation of the cell. In addition to peak R3, peak R4 contributed to the increase of polarization resistance during the stability test. As stated before in chapter 5, peaks R2 and R3 are associated with charge transfer processes at the fuel and air electrodes, respectively.

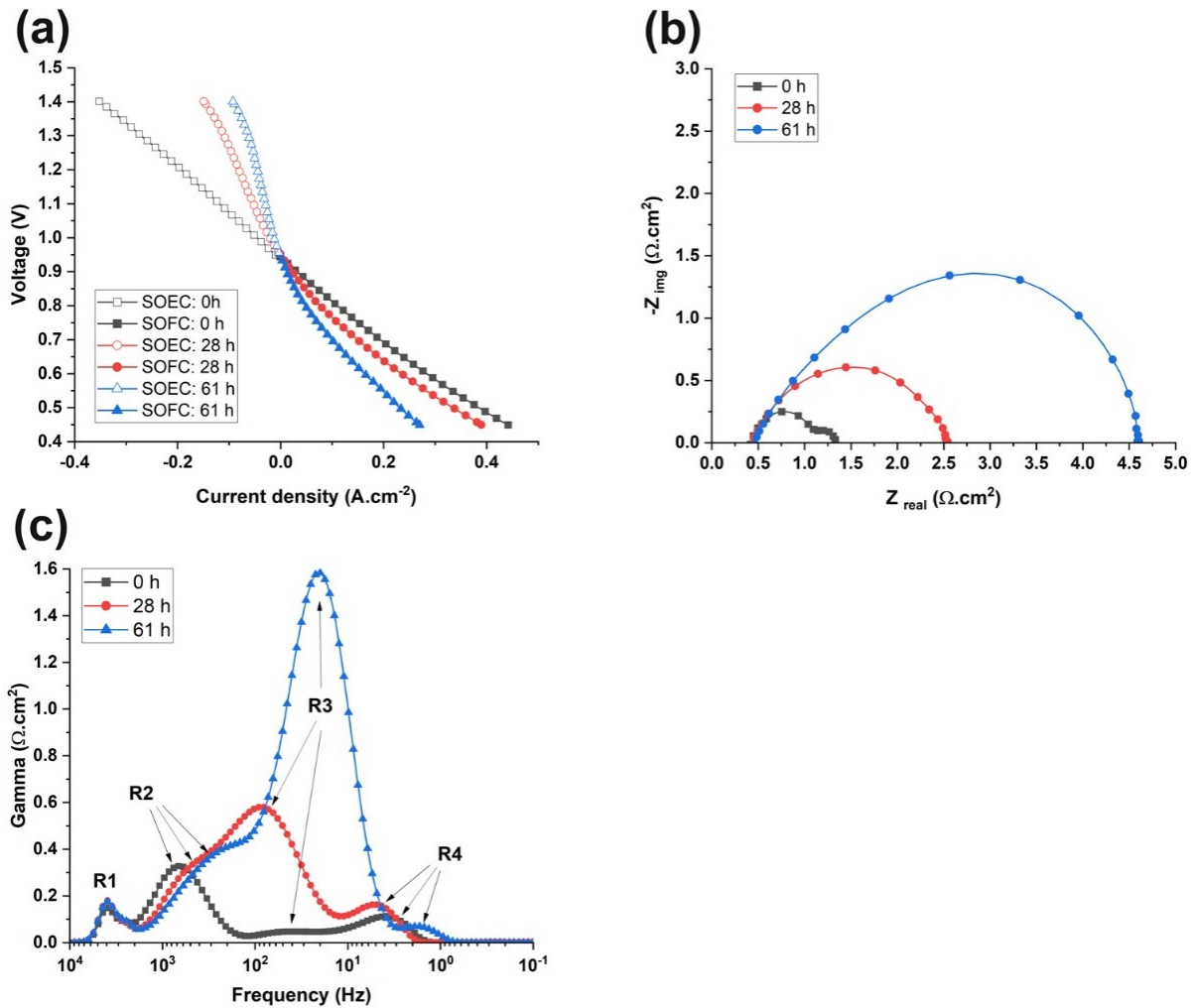


Figure 6-5 (a) I-V and (b) EIS measurement of the cell at different intervals during the stability test. (c) DRT graph corresponding to EIS data in (b).

Figure 6-6 shows the microstructure of the cell after the stability test in SOEC mode. As can be seen, the distribution of pores inside the support is not uniform and less porosity is detected in areas close to the electrolyte.

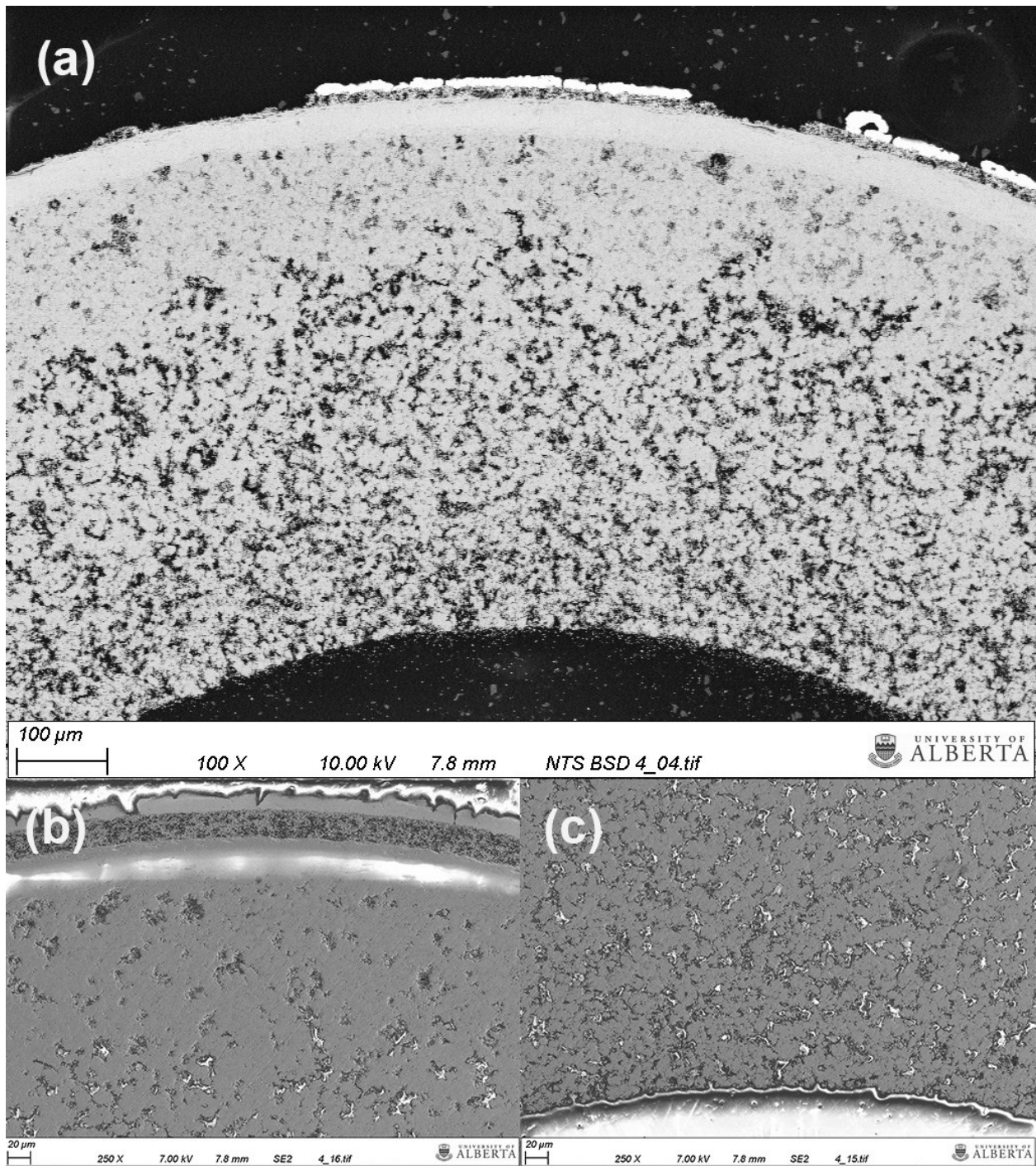


Figure 6-6 Post-mortem SEM images of the cell after the stability test (a) backscattered image showing the pore distribution from bottom to the top of the support (b) secondary image of support close to the electrolyte and (c) away from the electrolyte.

Figure 6-7 compares the post-mortem microstructure of the cell in this chapter following the stability test in electrolysis mode to cell B in chapter 5 following 260 h of stability test in fuel cell mode. Large pores up to 68 μm are detected in the Ni-YSZ support of the cell following the stability test in SOEC mode (Figure 6-7b) while no such large pores are detected in Figure 6-7a, corresponding to the cell operated in SOFC mode. The distribution of the pores in the support in Figure 6-7a is more uniform as well.

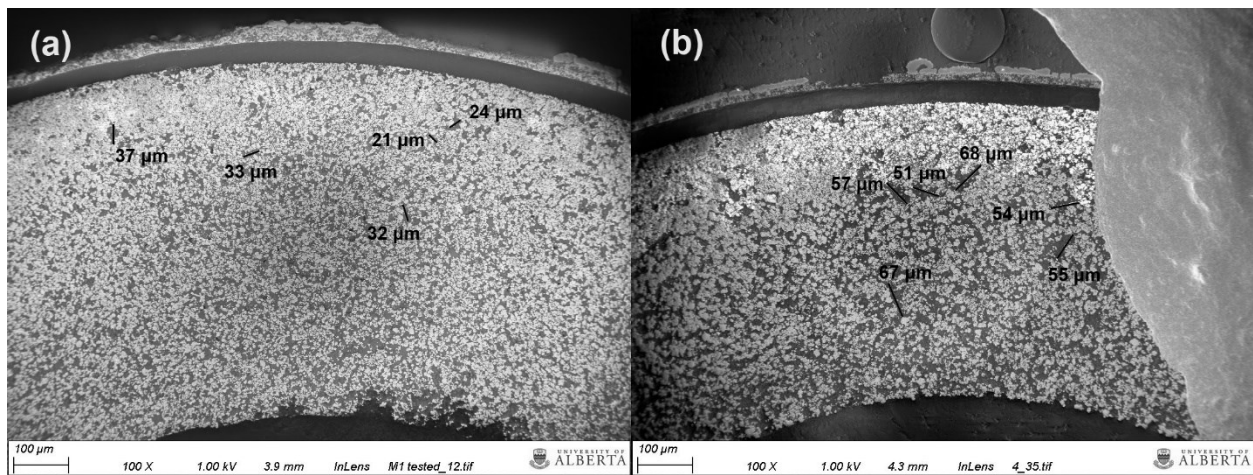


Figure 6-7 (a) Post-mortem SEM image of cell B in chapter 5 after 260 of stability test in SOFC mode. (b) Post-mortem SEM image of the cell in chapter 6 after the stability test in SOEC mode. The lines in the images show the length of the pores inside the support.

Ni migration to and away from the electrolyte has previously been reported for Ni-YSZ fuel electrodes in SOECs [315]. Ni migration can reduce the active TPBs close to the electrolyte and increase the R2 contribution in Figure 6-5c. Contribution of peak R3 is related to the PNO air electrode. In a similar study by Morales-Zapata *et al.* with a Ni-YSZ fuel electrode, YSZ electrolyte, GDC barrier layer and PNO air electrode (not infiltrated), the stability of the cell was studied in reversible mode [316]. They found an increase in R2 and R3 peaks during electrolysis mode and a temporary reduction in polarization resistance during fuel cell mode. Ni migration and

an increase in pore content of the support was also detected by them which was due to the high steam content in fuel composition and attributed to the peak R2. An increase in peak R3 value at the end of each electrolysis mode was also detected by them and attributed to the PNO air electrode.

By comparing the results of chapters 5 and 6, it appears that infiltrated PNO air electrode stability is affected by the high steam content in electrolysis mode. Further studies including XRD analysis of the infiltrated PNO air electrode exposed to high steam content is needed to fully understand the decomposition of the PNO air electrode in electrolysis mode. Modification of the fuel electrode support is necessary to achieve a stable Ni-YSZ support. Barnett *et al.* [317] found out infiltrating GDC nanoparticles into a Ni-YSZ electrode can reduce the electrode polarization resistance as much as three times by providing additional oxygen transport paths and enhancing the charge transfer process. Total polarization resistance of the GDC-infiltrated electrode in their study was stable for 1000 h of stability test. Park *et al.* [318] compared the stability of symmetrical Ni-YSZ fuel electrodes with and without GDC infiltration in SOEC mode for 1000 h. They found out GDC infiltration effectively reduced the polarization resistance of the Ni-YSZ electrode during the electrolysis operation at different steam contents. DRT analysis showed lower polarizations for oxygen ion transfer as well as Ni-YSZ charge transfer for a GDC-infiltrated electrode.

6.5 Conclusions

An infiltrated PNO air electrode was coated onto a microtube and tested in electrolysis mode. The microstructure and stability of this cell was compared to a cell (cell B in chapter 5) with similar composition operating in SOFC mode for 260 h. Results show Ni migration and increasing pore size inside the fuel electrode during the electrolysis test. Moreover, based on DRT data, the

infiltrated PNO air electrode was degrading during the electrolysis test. These results were comparable to the results of other researchers testing non-infiltrated PNO cathodes in SOEC mode. The results of this study suggest further modification of the air electrode as well as fuel electrode is necessary to increase the stability of the cell in electrolysis mode.

Chapter 7: Planar SOFC Performance and Stability

7.1 Abstract

The performance and stability of a planar SOFC based on tape cast support were studied. Tape cast parameters, electrolyte coating method as well as sintering parameters were optimized to achieve crack-free and dense electrolyte. The highly conductive anode support and buffer layer developed in chapter 4 were implemented for the cell in this study. Infiltrated NNO in YSZ scaffold was used as the cathode. The cell showed stable performance during 70 h of stability test at 0.7 V and 800 °C without any degradations. The results of the current study show the anode support composition developed in chapter 4 can be used for both tubular and planar SOFCs.

7.2 Planar cell design

Most of the experimental results of this thesis are based on tubular cells. However, the possibility of fabrication and testing planar SOFCs was studied as well. Schematic of the test setup used for testing the planar cells is depicted in Figure 7-1. An alumina tube was used as the main chamber. A smaller alumina tube was used as the fuel inlet and placed inside the larger alumina tube. To better demonstrate the internal components of the setup, the outside alumina tube is removed in Figure 7-1. The fuel inlet was attached to a high temperature resistant plastic tube. The plastic tube worked as a spring to push the fuel inlet onto the current collector on the anode side. Two ceramic rods attached to two springs applied force to the cathode current collector. An alumina ring transferred the force of the springs on the cathode current collector to assure proper contact with the cathode surface. Two different materials were tested as contact paste, mesh and wires: silver and gold.

Ceramabond 552 was used for sealing and is coated between the cell and outer alumina tube. After finishing the test, the sealing was removed using abrasive material and the setup was ready for the next test. Anode and cathode wires were passed through two-bore alumina rods to keep them separated before reaching the cell. Anode wires were passed inside the fuel chamber for simplicity in sealing. Hot glue was applied to the end of the two-bore alumina rods to keep the wires separated as well as preventing the penetration of air into the fuel chamber. A brass fitting was connected to the end of the outer alumina tube and could be detached from the tube by a screw mechanism (another fitting is placed inside the alumina tube and is threaded). 1/8 inch stainless steel tubes were attached to the brass fitting and connected the main fuel inlet line from the flowmeters to the brass fitting. Another stainless steel tube was connected to the brass fitting and diverted the outlet fuel into a water container to check the sealing as discussed already.

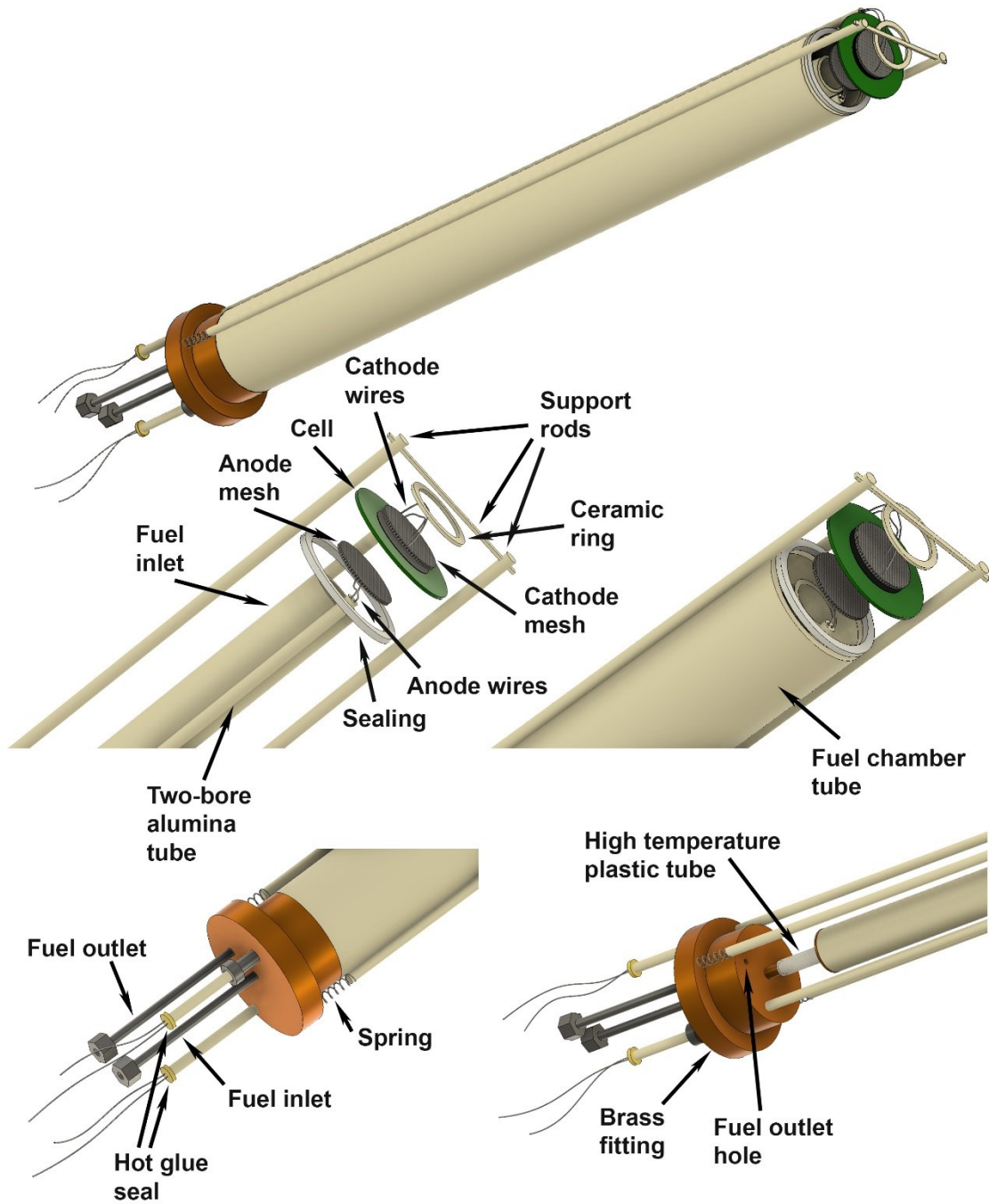


Figure 7-1 Schematic of the planar cell's test setup used in the thesis.

7.3 Experimental procedures

7.3.1 Fabrication of the support

Tape casting was used for fabrication of the planar anode supports. NiO:YSZ weight ratio inside the support was kept at 90:10 to achieve a highly conductive support. NiO powder was initially milled for 48 h to reduce the particle size. NiO and YSZ were added to the water (10 wt%), dispersant (BYK, D3005, 1 wt%), binder (BYK, B1000, 15 wt%), PMMA (30 vol.%, 10 μm average particle size) and were milled by a planetary mill at 300 rpm for 2 h (with 15 minutes interval and 5 minutes rest in between). Then, the viscous paste was transferred to a jar and rolled over a roller device overnight to remove entrapped air from the paste. A film applicator (10 cm wide blade) with digital calipers was used for tape casting. Two sides of the blade were calibrated on top of a flat glass surface. A light source was used for calibration purpose by detecting any light passing in between the glass and blade. An automatic tape cast applicator bed was used for precise tape casting. Tape casting was done on multiple surfaces (Mylar sheet, glass, thick plastic sheets with/without paraffin/shoe wax on top). The best result was achieved on top of the Mylar sheets without any wax. Paste was poured in front of the blade and tape cast with a speed of 5-10 $\text{mm}\cdot\text{s}^{-1}$.

Subsequent to tape casting, tapes were let dry at room temperature or drying was assisted by infrared lamps on top of the tapes. The ratio of the initial materials for the paste was optimized in such a way as to prevent crack formation during the drying process. It was found out that crack formation has a direct relationship with the water content inside the tape as well as the thickness of the tape. The final thickness of the tape was lower than the gap under the blade. Following the first layer, it was let dry and two subsequent layers were tape cast on top of the first layer (after

drying at room temperature) for the final thickness of the tape cast layer to reach to ~ 300-420 μm . Tapes were cut and presintered at 900-1100 $^{\circ}\text{C}$.

7.3.2 Coating of the anode functional layer, buffer layer and the electrolyte

Prior to coating the AFL or electrolyte layers, one side of the support was masked using parafilm. A Ni-YSZ buffer layer (NiO: YSZ = 65:35 weight ratio + 30 vol% PMMA (6 μm)) was coated prior to coating the AFL. Dip coating was used to coat the AFL and buffer layer onto the supports. The composition of the AFL was similar to the ones described in section 1.3.3.3. The buffer layer had a similar composition to the AFL with the addition of PMMA as a pore former.

Spray coating and dip coating were studied for coating the electrolyte. An airbrush (Iwata) with adjustable air flow was used to spray the electrolyte suspension onto the support. Dip coating method was performed similar to section 1.3.3.3. Figure 7-2 compares the microstructure of the electrolyte coated by dip coating and spray coating after sintering at 1400 $^{\circ}\text{C}$. As can be seen, less porosity is detectable using the dip coat method. In addition, large chunks of YSZ particles are visible on top of the electrolyte layer in the spray coated sample. The possible reason could be selective and non-agitative deposition of particles during the dip coat process. Deposition by spray coating is more susceptible to air entrapment and agglomerated particles depositing in the coating.

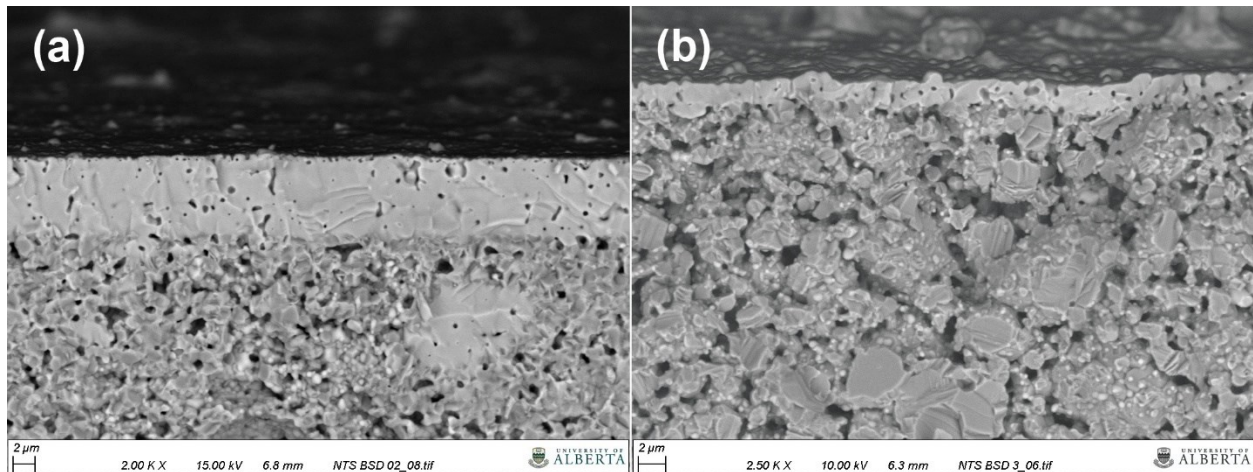


Figure 7-2 SEM micrograph of (a) dip coated and (b) spray coated electrolyte onto the presintered Ni-YSZ tape. Both electrolytes were sintered at 1400 °C for 3h.

7.3.3 Coating of the scaffold and cathode infiltration

Calcined and milled YSZ scaffold was coated onto the electrolyte using screen printing. Screen print paste was prepared by mixing 7.5 g of calcined and milled YSZ with 4 g of ink vehicle (Fuel Cell Materials). A screen (partially masked) was placed on top of the half cells, then YSZ paste was screen printed onto it and heat treated at 1250 °C for 3 h. NNO cathode was infiltrated into the scaffold as described in section 1.3.3.5, except vacuum was not used for infiltration.

The planar cell setup, sintered button cells and tape cast process are briefly depicted in Figure 7-3.

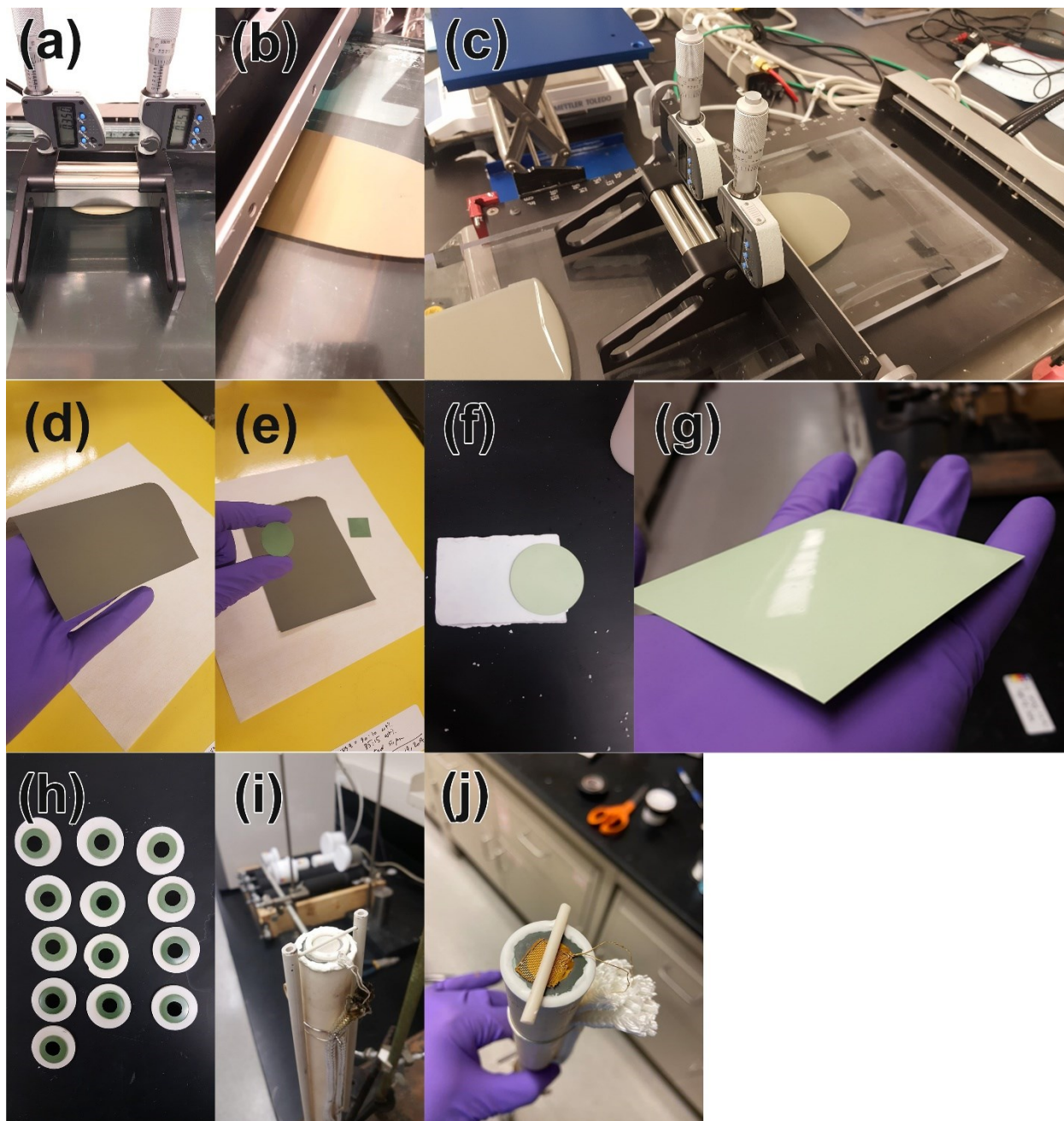


Figure 7-3 (a), (b) and (c) Tape cast process and coating of Ni-YSZ film onto the Mylar sheet (d) multilayered Ni-YSZ tape after drying in room temperature (e) one inch planar cell following sintering (f) presintered Ni-YSZ tape (g) 7.5x7.5 cm electrolyte coated Ni-YSZ support following sintering (h) button cells following coating the cathode and heat treatment (i) planar test setup with silver and (j) gold current collector.

7.4 Results and discussion

Performance and stability of the planar cell was tested in fuel cell mode at 800 °C. Figure 7-4 shows the stability of the cell at 800 °C and 0.7 V. Flow rates of hydrogen and air were 50 and 100 SCCM, respectively. As can be seen, no degradation is detected over 70 h of the stability test following the initial stabilization of the cell (initial 3-4 h).

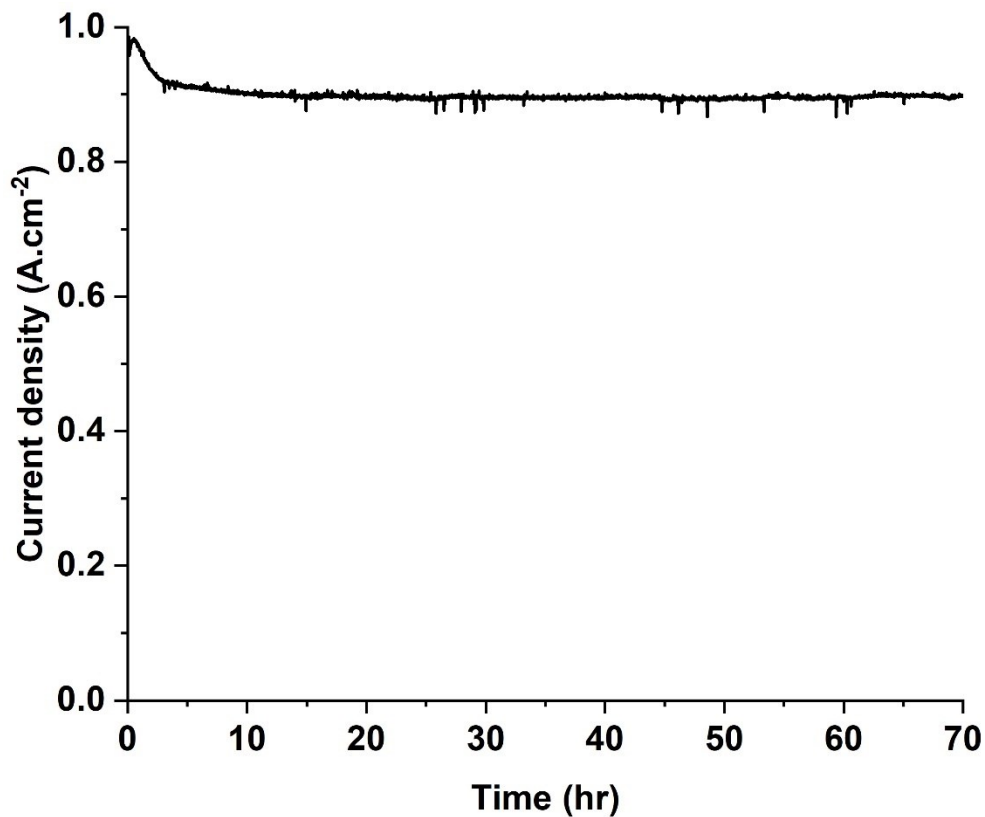


Figure 7-4 Stability test of the planar SOFC at 800 °C and 0.7 V.

Performance of the cell before and after the stability test is compared together in Figure 7-5a. Performance of the cell is slightly increased during the stability test. By looking at Figure 7-5b, a reduction in total polarization resistance of the cell after 70 h of stability test is noticeable. DRT

data extracted from the EIS graphs are demonstrated in Figure 7-5c. According to DRT data, an increase in peak R3 value with characteristic frequency of 10-100 Hz is seen. This peak has already been discussed in chapters 4 and 5 and attributed to the oxygen reduction reaction at the cathode. Further XRD analysis is required to reach to a final conclusion on cathode composition.

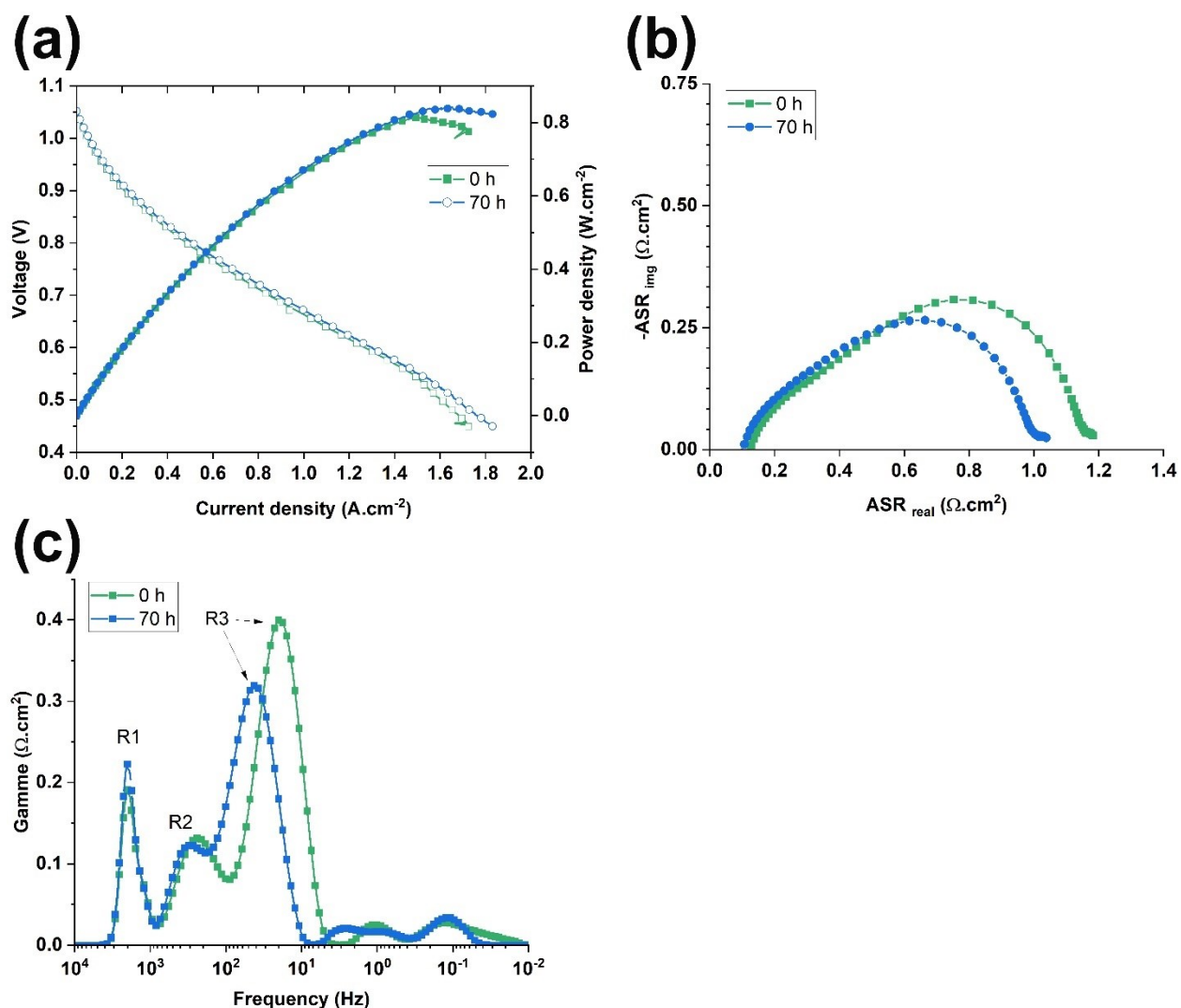


Figure 7-5 (a) I-V-P and (b) EIS measurements of the cell prior and after the stability test (c) DRT data collected from EIS measurement prior and after the stability tests.

Post-mortem SEM analysis of the cell is shown in Figure 7-6. Thickness of the tape cast support is about 295 μm with visible spherical pores created by 10 μm PMMA (Figure 7-6a). Figure 7-6b

shows the attachment of the support layer, buffer layer and the functional layer. The buffer layer (29 μm thick) can be differentiated from the support layer by smaller pores (smaller PMMA was used for the buffer layer). Electrolyte in Figure 7-6c is dense with good attachment to the cathode layer. Infiltrated NNO with 200-220 nm average agglomerate size can be seen Figure 7-6d reaching the cathode/YSZ interface due to open porosities provided by the calcined and milled

YSZ scaffold. The lower Ni content in the AFL and buffer layers is shown in the EDS map of Figure 7-6e.

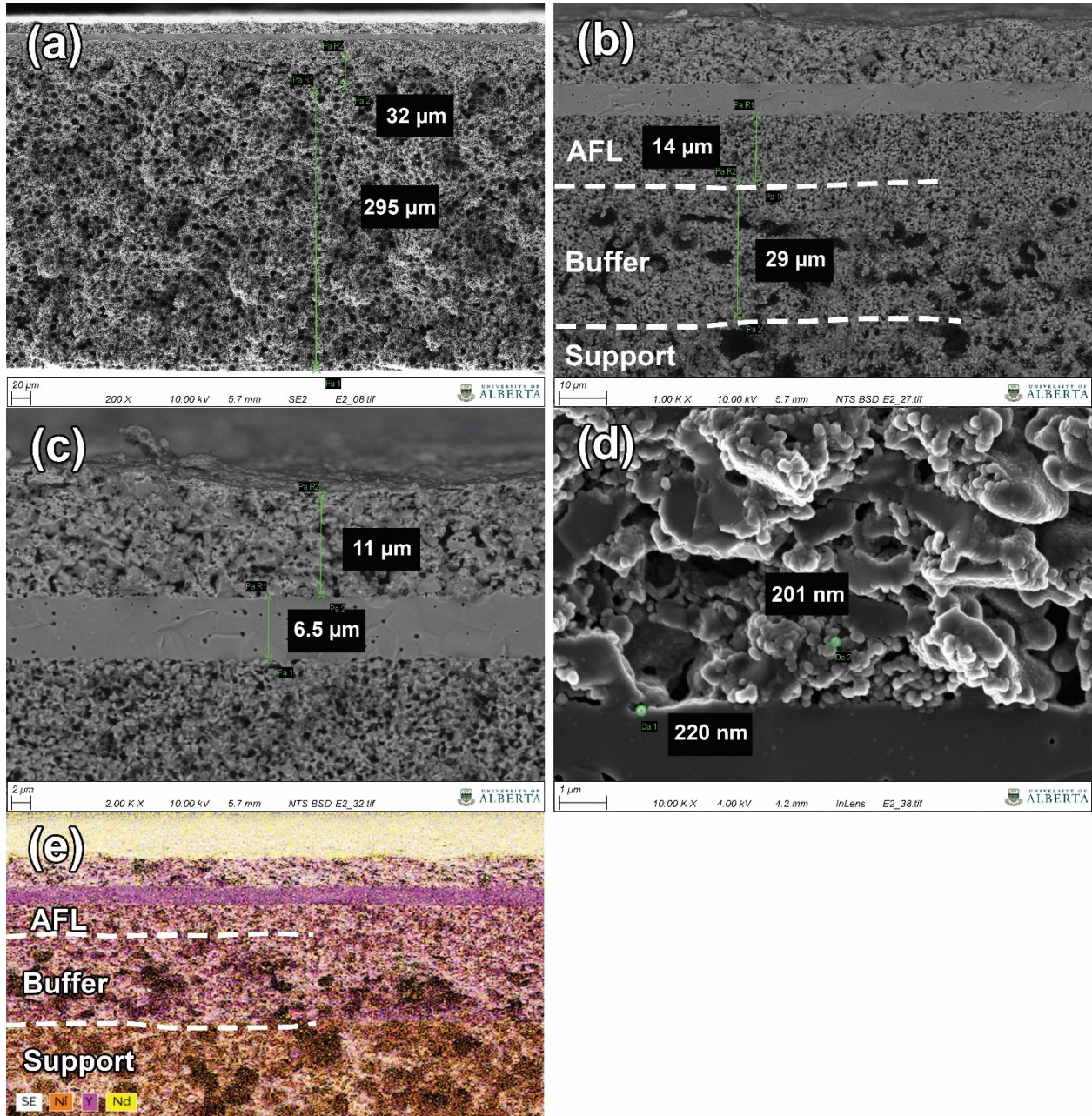


Figure 7-6 Post-mortem SEM micrographs of planar SOFC following 70 h of stability test at 850 °C. (a) 295 μm thick support (b) different components of the anode (c) thickness of the electrolyte and cathode (d) infiltrated cathode microstructure and (e) EDS map of the AFL, buffer and support layers in fuel electrode.

7.5 Conclusions

The possibility of fabrication and testing a successful planar cell was studied. The setup for testing the cell was fabricated as well as optimizing the tape cast parameters for a successful, crack-free multilayer support. The initial anode support composition contained 90 wt% NiO (in NiO-YSZ composite) before reduction to achieve high conductivity. Thermal expansion coefficient mismatch of the support and functional layers was alleviated using a 29 μm buffer layer with intermediate conductivity and porosity. Stability test in SOFC mode was performed at 800 °C for 70 h. Comparing the performance of the cell prior and after the stability test showed no degradation during the stability test. The result of this study suggests infiltrated NNO cathode is a good candidate for SOFC applications.

Chapter 8: Conclusions and Future Directions

8.1 Conclusions

The following conclusions are made in this study:

(i) Ni-YSZ electrode current collection paths in tubular cells are longer than planar cells. The composition and microstructure of the conventional Ni-YSZ electrode was modified. A novel metallic anode support was fabricated with high Ni content and low YSZ content to control Ni agglomeration. The novel anode support was used for tubular SOFCs with proton conductor as well as oxygen ion conductor electrolytes. Proton conductor cell showed stable potentiostatic results for 67 h and oxygen ion conductor SOFC showed 25 and 87% superior performance compared to conventional cells at 600 and 550 °C.

(ii) Stability of infiltrated praseodymium nickelate cathode in GDC scaffold was studied for 260 h in SOFC mode at 650 °C on two different tubular cells with different half-cell composition and geometry (tubular and microtubular). Preliminary XRD results were performed to achieve the best heat treatment temperature for the cathode. Results showed no degradation of the cathode and even slight improvement through a partial phase transformation into the $\text{Pr}_4\text{Ni}_3\text{O}_{10}$ phase with higher thermal stability.

(iii) The possibility of fabrication and testing a successful SOFC with the novel anode support composition and an infiltrated neodymium nickelate cathode was studied. A Ni-YSZ buffer layer with intermediate porosity and conductivity between the anode functional layer and highly conductive anode support was fabricated and placed between the two layers. Results show stable operation of the cell in SOFC mode for 70 h without any degradation.

(iv) The challenges for operating an SOFC in electrolysis mode were studied. Results showed that the cell was not stable during a stability test at 1.3 V. Large pores inside the Ni-YSZ support were detected in post-mortem SEM analysis. Based on DRT data, the main contributor to the degradation of the cell in SOEC mode was the oxygen evolution reaction at the air electrode. Further studies are required to better understand the nature of degradation in the air electrode as well as improving the fuel electrode microstructure due to the high steam content in SOEC mode.

(v) The main focus of the thesis was to reduce the degradation rate of SOFCs by isolating anodic and cathodic parameters contributing the degradation. Due to the complexity of fabrication and testing of SOFCs, reducing the number of variables and designing a systematic approach for fabrication and testing was critical. Degradation of stability can arise from parameters not directly related to the cell itself such as anode and cathode current collectors, conducting paste, fuel/air preheating temperature, furnace hot zone stability and condition, efficient flow of fuel/air onto the active area, choice of sealing (compression or ceramic paste), steam/water management in fuel chamber, impurities in the lab/furnace environment. For the SOFCs to consider a reliable power source and widespread application of them, reducing the operation cost is inevitable. By reducing the degradation rate or operating at lower temperature/higher voltages, overall cost of the SOFCs will reduce which helps wide scale commercialization of this technology. Thermal management and load distribution in real SOFC application such as residential micro-CHPs are the next topic which require collaboration of materials scientists with electrical/computer science field. In this thesis, the possibility of fabricating and testing stable (for less than 300 h) SOFCs in tubular and planar geometries were studied. Next step requires extending the stability of fabricated SOFCs to 1000 h as well as improving the stability of them in electrolysis mode.

8.2 Future directions

A planar stack is going to be fabricated for testing planar cells in SOFC mode. New challenges for fabrication of the stack including choosing the right interconnect material, design and testing the stack, proper Cr-retention coating of the interconnect material and choosing the right sealing material will be studied in short-term and long-term experiments. Continuing the electrolysis experiments, Ni-YSZ electrode microstructure will be modified by infiltration of GDC nanoparticles. Stability of the infiltrated air electrode material will be studied at anodic potentials.

8.3 Journal papers

- **Chapter 2:** Microstructure and Long-term Stability of Ni-YSZ Anode supported Fuel Cells: A Review. (Submitted to Materials Future)
- **Chapter 3:** Development of Proton Conducting Fuel Cells Using Nickel Metal Support (*Published: S. Vafaenezhad, N.K. Sandhu, A.R. Hanifi, T.H. Etsell, P. Sarkar, J. Power Sources 2019, 435, 226763*)
- **Chapter 4:** Tailoring the SOFC anode-support composition and microstructure for low-temperature applications (Submitted to Fuel Cells)
- **Chapter 5:** Performance and stability of infiltrated praseodymium nickelate cathodes for low-temperature fuel cell applications (Submitted to International Journal of Hydrogen Energy)

References

- [1] K.H. Ng, H.A. Rahman, M.R. Somalu, *Int. J. Hydrogen Energy* **2019**, 44, 30692.
- [2] Z. Zakaria, Z. Awang Mat, S.H. Abu Hassan, Y. Boon Kar, *Int. J. Energy Res.* **2020**, 44, 594.
- [3] M.S. Khan, S.B. Lee, R.H. Song, J.W. Lee, T.H. Lim, S.J. Park, *Ceram. Int.* **2016**, 42, 35.
- [4] S.P. Jiang, X. Chen, *Int. J. Hydrogen Energy* **2014**, 39, 505.
- [5] N. Shi, Y. Xie, Y. Yang, S. Xue, X. Li, K. Zhu, D. Huan, R. Peng, C. Xia, Y. Lu, *Mater. Renew. Sustain. Energy* **2020**, 9, 6.
- [6] Z. Gao, L. V. Mogni, E.C. Miller, J.G. Railsback, S.A. Barnett, *Energy Environ. Sci.* **2016**, 9, 1602.
- [7] N. Shaigan, W. Qu, D.G. Ivey, W. Chen, *J. Power Sources* **2010**, 195, 1529.
- [8] L. Fan, B. Zhu, P.-C. Su, C. He, *Nano Energy* **2018**, 45, 148.
- [9] Y. Chen, Y. Lin, Y. Zhang, S. Wang, D. Su, Z. Yang, M. Han, F. Chen, *Nano Energy* **2014**, 8, 25.
- [10] V. Verda, C. Ciano, in *Model. Solid Oxide Fuel Cells Methods, Proced. Tech.* (Bove, R. & Ubertini, S.) Springer Netherlands, 2008, 207.
- [11] P. Tanasini, M. Cannarozzo, P. Costamagna, A. Faes, J. Van Herle, A. Hessler-Wyser, C. Comninellis, *Fuel Cells* **2009**, 9, 740.
- [12] F. Abdeljawad, M. Haataja, *J. Appl. Phys.* **2013**, 114, 183519.
- [13] A.R. Hanifi, S. Paulson, A. Torabi, A. Shinbine, M.C. Tucker, V. Birss, T.H. Etsell, P. Sarkar, *J. Power Sources* **2014**, 266, 121.
- [14] F. Abdeljawad, B. Völker, R. Davis, R.M. McMeeking, M. Haataja, *J. Power Sources* **2014**, 250, 319.
- [15] Y.C.K. Chen-Wiegart, D. Kennouche, J. Scott Cronin, S.A. Barnett, J. Wang, *Appl. Phys. Lett.* **2016**, 108, 083903.
- [16] G. Xiao, F. Chen, *Front. Energy Res.* **2014**, 2, 1.
- [17] S.M. Haile, *Acta Mater.* **2003**, 51, 5981.
- [18] B. Singh, S. Ghosh, S. Aich, B. Roy, *J. Power Sources* **2017**, 339, 103.
- [19] K. Thyden, Y.L. Liu, J.B. Bilde-Sorensen, *Solid State Ionics* **2008**, 178, 1984.
- [20] J. Hanna, W.Y. Lee, Y. Shi, A.F. Ghoniem, *Prog. Energy Combust. Sci.* **2014**, 40, 74.
- [21] N. Mahato, A. Banerjee, A. Gupta, S. Omar, K. Balani, *Prog. Mater. Sci.* **2015**, 72, 141.

- [22] B. Shri Prakash, S. Senthil Kumar, S.T. Aruna, *Renew. Sustain. Energy Rev.* **2014**, 36, 149.
- [23] M. Rafique, H. Nawaz, M. Shahid Rafique, M. Bilal Tahir, G. Nabi, N.R. Khalid, *Int. J. Energy Res.* **2019**, 43, 2423.
- [24] S. Vafaenezhad, N.K. Sandhu, A.R. Hanifi, T.H. Etsell, P. Sarkar, *J. Power Sources* **2019**, 435, 226763.
- [25] F. Zhao, A. V. Virkar, *J. Power Sources* **2005**, 141, 79.
- [26] A. Atkinson, S. Barnett, R.J. Gorte, J.T.S. Irvine, A.J. McEvoy, M. Mogensen, S.C. Singhal, J. Vohs, *Nat. Mater.* **2004**, 3, 17.
- [27] M. Brown, S. Primdahl, M. Mogensen, *J. Electrochem. Soc.* **2000**, 147, 475.
- [28] J. Deseure, Y. Bultel, L. Dessemond, E. Siebert, *Electrochim. Acta* **2005**, 50, 2037.
- [29] J.H. Yu, G.W. Park, S. Lee, S.K. Woo, *J. Power Sources* **2007**, 163, 926.
- [30] A.R. Hanifi, M.A. Laguna-Bercero, N.K. Sandhu, T.H. Etsell, P. Sarkar, *Sci. Rep.* **2016**, 6, 27359.
- [31] M. Morales, M.Á. Laguna-Bercero, *ACS Appl. Energy Mater.* **2018**, 1, 2024.
- [32] M.A. Laguna-Bercero, *J. Power Sources* **2012**, 203, 4.
- [33] H. Koide, Y. Someya, T. Yoshida, T. Maruyama, *Solid State Ionics* **2000**, 132, 253.
- [34] J.R. Wilson, S.A. Barnett, *Electrochem. Solid-State Lett.* **2008**, 11, B181.
- [35] J.H. Lee, H. Moon, H.W. Lee, J. Kim, J.D. Kim, K.H. Yoon, *Solid State Ionics* **2002**, 148, 15.
- [36] X. Xi, H. Abe, M. Naito, *Ceram. Int.* **2014**, 40, 16549.
- [37] N. Vivet, S. Chupin, E. Estrade, A. Richard, S. Bonnamy, D. Rochais, E. Bruneton, *J. Power Sources* **2011**, 196, 9989.
- [38] H.S. Hong, U.-S. Chae, S.-T. Choo, *J. Alloys Compd.* **2008**, 449, 331.
- [39] J.H. Nam, D.H. Jeon, *Electrochim. Acta* **2006**, 51, 3446.
- [40] S.K. Pratihari, A. Dassharma, H.S. Maiti, *Mater. Res. Bull.* **2005**, 40, 1936.
- [41] R.M.C. Clemmer, S.F. Corbin, *Solid State Ionics* **2009**, 180, 721.
- [42] N.Q. Minh, *J. Am. Ceram. Soc.* **1993**, 76, 563.
- [43] M. Morales, M.A. Laguna-Bercero, M.E. Navarro, F. Espiell, M. Segarra, *RSC Adv.* **2015**, 5, 39350.
- [44] M. Morales, M.A. Laguna-Bercero, *RSC Adv.* **2017**, 7, 17620.
- [45] H. Monzón, M.A. Laguna-Bercero, A. Larrea, B.I. Arias, A. Várez, B. Levenfeld, *Int. J. Hydrogen Energy* **2014**, 39, 5470.

- [46] M.A. Laguna-Bercero, A.R. Hanifi, L. Menand, N.K. Sandhu, N.E. Anderson, T.H. Etsell, P. Sarkar, *Electrochim. Acta* **2018**, 268, 195.
- [47] P.S. Jørgensen, S.L. Ebbenhøj, A. Hauch, *J. Power Sources* **2015**, 279, 686.
- [48] M. Trini, P.S. Jørgensen, A. Hauch, M. Chen, P.V. Hendriksen, in *ECS Trans.* (Singhal, S. C. & Kawada, T.) 2017, 78, 3049.
- [49] M. Trini, P.S. Jørgensen, A. Hauch, J.J. Bentzen, P. V. Hendriksen, M. Chen, *J. Electrochem. Soc.* **2019**, 166, F158.
- [50] H. Iwai, N. Shikazono, T. Matsui, H. Teshima, M. Kishimoto, R. Kishida, D. Hayashi, K. Matsuzaki, D. Kanno, M. Saito, H. Muroyama, K. Eguchi, N. Kasagi, H. Yoshida, *J. Power Sources* **2010**, 195, 955.
- [51] M. Kishimoto, H. Iwai, M. Saito, H. Yoshida, *J. Power Sources* **2011**, 196, 4555.
- [52] J.R. Wilson, W. Kobsiriphat, R. Mendoza, H.Y. Chen, J.M. Hiller, D.J. Miller, K. Thornton, P.W. Voorhees, S.B. Adler, S.A. Barnett, *Nat. Mater.* **2006**, 5, 541.
- [53] J.R. Izzo, A.S. Joshi, K.N. Grew, W.K.S. Chiu, A. Tkachuk, S.H. Wang, W. Yun, *J. Electrochem. Soc.* **2008**, 155, B504.
- [54] H.Y. Chen, H.C. Yu, J. Scott Cronin, J.R. Wilson, S.A. Barnett, K. Thornton, *J. Power Sources* **2011**, 196, 1333.
- [55] M. Kishimoto, K. Miyawaki, H. Iwai, M. Saito, H. Yoshida, *Fuel Cells* **2013**, 13, 476.
- [56] M.H. Pihlatie, A. Kaiser, M. Mogensen, M. Chen, *Solid State Ionics* **2011**, 189, 82.
- [57] Y.H. Lee, H. Muroyama, T. Matsui, K. Eguchi, *J. Power Sources* **2014**, 262, 451.
- [58] S.W. Cheng, C.H. Tsai, S.H. Wu, C.K. Liu, Y.N. Cheng, R.Y. Lee, *Int. J. Hydrogen Energy* **2015**, 40, 1534.
- [59] H. Monzón, M.A. Laguna-Bercero, *Electrochim. Acta* **2016**, 221, 41.
- [60] T.S. Li, W.G. Wang, H. Miao, T. Chen, C. Xu, *J. Alloys Compd.* **2010**, 495, 138.
- [61] Z. Jiao, N. Shikazono, *J. Electrochem. Soc.* **2015**, 162, F571.
- [62] S.J. Skinner, *Adv. Mater. Interfaces* **2019**, 6, 1.
- [63] S.-S. Liu, Z. Jiao, N. Shikazono, S. Matsumura, M. Koyama, *J. Electrochem. Soc.* **2015**, 162, F750.
- [64] A. Revcolevschi, G. Dhalenne, *Nature* **1985**, 316, 335.
- [65] R.I. Merino, J.I. Peña, M.A. Laguna-Bercero, A. Larrea, V.M. Orera, *J. Eur. Ceram. Soc.* **2004**, 24, 1349.
- [66] A. Cubero, J.I. Peña, M.A. Laguna-Bercero, *Appl. Surf. Sci.* **2015**, 335, 39.
- [67] M.A. Laguna-Bercero, Á. Larrea, R.I. Merino, J.I. Peña, V.M. Orera, *J. Am. Ceram. Soc.* **2005**, 88, 3215.

- [68] M.A. Laguna-Bercero, Á. Larrea, *J. Am. Ceram. Soc.* **2007**, 90, 2954.
- [69] Q. Jeangros, A. Faes, J.B. Wagner, T.W. Hansen, U. Aschauer, J. Van herle, A. Hessler-Wyser, R.E. Dunin-Borkowski, *Acta Mater.* **2010**, 58, 4578.
- [70] M.C. Muñoz, S. Gallego, J.I. Beltrán, J. Cerdá, *Surf. Sci. Rep.* **2006**, 61, 303.
- [71] S.S. Liu, L.C. Saha, A. Iskandarov, T. Ishimoto, T. Yamamoto, Y. Umeno, S. Matsumura, M. Koyama, *Commun. Chem.* **2019**, 2, 1.
- [72] A.R. Hanifi, M. Zazulak, T.H. Etsell, P. Sarkar, *Powder Technol.* **2012**, 231, 35.
- [73] A.R. Hanifi, A. Torabi, T.H. Etsell, L. Yamarte, P. Sarkar, *Solid State Ionics* **2011**, 192, 368.
- [74] A.R. Hanifi, A. Torabi, A. Shinbine, T.H. Etsell, P. Sarkar, *J. Ceram. Process. Res.* **2011**, 12, 336.
- [75] A.R. Hanifi, A. Shinbine, T.H. Etsell, P. Sarkar, *Int. J. Appl. Ceram. Technol.* **2012**, 9, 1011.
- [76] A.R. Hanifi, B. Zahiri, D. Mitlin, A.L. Vincent, T.H. Etsell, P. Sarkar, *Ceram. Int.* **2016**, 42, 6755.
- [77] M.H.D. Othman, N. Droushiotis, Z. Wu, G. Kelsall, K. Li, *Adv. Mater.* **2011**, 23, 2480.
- [78] C. Ren, Y. Zhang, Q. Xu, T. Tian, F. Chen, *Int. J. Hydrogen Energy* **2020**, 45, 6926.
- [79] M. Ab Rahman, M.H.D. Othman, H. Fansuri, Z. Harun, A.F. Omar, H.A. Shabri, J. Ravi, M.A. Rahman, J. Jaafar, A.F. Ismail, N. Osman, *J. Power Sources* **2020**, 467, 228345.
- [80] B. Emley, D. Panthi, Y. Du, Y. Yao, *J. Electrochem. Energy Convers. Storage* **2020**, 17, 1.
- [81] Y. Chen, J. Bunch, T. Li, Z. Mao, F. Chen, *J. Power Sources* **2012**, 213, 93.
- [82] T.Z. Sholklapper, C.P. Jacobson, S.J. Visco, L.C. Dejonghe, *Fuel Cells* **2008**, 8, 303.
- [83] J.M. Vohs, R.J. Gorte, *Adv. Mater.* **2009**, 21, 943.
- [84] S.P. Jiang, *Int. J. Hydrogen Energy* **2012**, 37, 449.
- [85] T.Z. Sholklapper, C. Lu, C.P. Jacobson, S.J. Visco, L.C. De Jonghe, *Electrochem. Solid-State Lett.* **2006**, 9, A376.
- [86] M.A. Laguna-Bercero, A.R. Hanifi, T.H. Etsell, P. Sarkar, V.M. Orera, *Int. J. Hydrogen Energy* **2015**, 40, 5469.
- [87] T.E. Burye, H. Tang, J.D. Nicholas, *J. Electrochem. Soc.* **2016**, 163, F1017.
- [88] M. Shah, S.A. Barnett, *Solid State Ionics* **2008**, 179, 2059.
- [89] A.L. Vincent, A.R. Hanifi, J.-L. Luo, K.T. Chuang, A.R. Sanger, T.H. Etsell, P. Sarkar, *J. Power Sources* **2012**, 215, 301.
- [90] A.L. Vincent, A.R. Hanifi, M. Zazulak, J.L. Luo, K.T. Chuang, A.R. Sanger, T. Etsell, P.

- Sarkar, *J. Power Sources* **2013**, 240, 411.
- [91] S. Choi, S. Yoo, J.-Y. Shin, G. Kim, *J. Electrochem. Soc.* **2011**, 158, B995.
- [92] Y. Li, S.L. Zhang, C.X. Li, T. Wei, G.J. Yang, C.J. Li, M. Liu, *J. Therm. Spray Technol.* **2016**, 25, 392.
- [93] M.A. Laguna-Bercero, A.R. Hanifi, H. Monzón, J. Cunningham, T.H. Etsell, P. Sarkar, *J. Mater. Chem. A* **2014**, 2, 9764.
- [94] T. Chen, M. Liu, C. Yuan, Y. Zhou, X. Ye, Z. Zhan, C. Xia, S. Wang, *J. Power Sources* **2015**, 276, 1.
- [95] A.R. Hanifi, M.A. Laguna-Bercero, T.H. Etsell, P. Sarkar, *Int. J. Hydrogen Energy* **2014**, 39, 8002.
- [96] A. Torabi, A.R. Hanifi, T.H. Etsell, P. Sarkar, *J. Electrochem. Soc.* **2011**, 159, B201.
- [97] T.Z. Sholklapper, H. Kurokawa, C.P. Jacobson, S.J. Visco, L.C. De Jonghe, *Nano Lett.* **2007**, 7, 2136.
- [98] T. Klemensø, K. Thydén, M. Chen, H.J. Wang, *J. Power Sources* **2010**, 195, 7295.
- [99] S. Park, R.J. Gorte, J.M. Vohs, *Appl. Catal. A Gen.* **2000**, 200, 55.
- [100] V. Sariboğa, M.A. Faruk Öksüzömer, *J. Alloys Compd.* **2016**, 688, 323.
- [101] M.C. Tucker, G.Y. Lau, C.P. Jacobson, L.C. DeJonghe, S.J. Visco, *J. Power Sources* **2007**, 171, 477.
- [102] S.F. Corbin, X. Qiao, *J. Am. Ceram. Soc.* **2003**, 86, 401.
- [103] K.S. Howe, A.R. Hanifi, K. Kendall, M. Zazulak, T.H. Etsell, P. Sarkar, *Int. J. Hydrogen Energy* **2013**, 38, 1058.
- [104] A. Buyukaksoy, V. Petrovsky, F. Dogan, *J. Electrochem. Soc.* **2011**, 159, B232.
- [105] A.R. Hanifi, A. Torabi, X. Chen, S. Hill, P. Sarkar, T.H. Etsell, *J. Electrochem. Soc.* **2014**, 161, F391.
- [106] A. Buyukaksoy, S.P. Kammampata, V.I. Birss, *J. Power Sources* **2015**, 287, 349.
- [107] P. Keyvanfar, A.R. Hanifi, P. Sarkar, T.H. Etsell, V. Birss, *ECS Trans.* **2015**, 68, 1255.
- [108] K. Bae, H.S. Noh, D.Y. Jang, J. Hong, H. Kim, K.J. Yoon, J.H. Lee, B.K. Kim, J.H. Shim, J.W. Son, *J. Mater. Chem. A* **2016**, 4, 6395.
- [109] T. Amiri, K. Singh, N.K. Sandhu, A.R. Hanifi, T.H. Etsell, J.-L. Luo, V. Thangadurai, P. Sarkar, *J. Electrochem. Soc.* **2018**, 165, F764.
- [110] A.R. Hanifi, N.K. Sandhu, T.H. Etsell, P. Sarkar, *J. Am. Ceram. Soc.* **2017**, 100, 4983.
- [111] L. Blum, L.G.J. de Haart, J. Malzbender, N. Margaritis, N.H. Menzler, *Energy Technol.* **2016**, 4, 939.
- [112] A. Weber, E. Ivers-Tiffée, *J. Power Sources* **2004**, 127, 273.

- [113] L. Blum, Q. Fang, S.M. Groß-Barsnick, L.G.J. (Bert. de Haart, J. Malzbender, N.H. Menzler, W.J. Quadackers, *Int. J. Hydrogen Energy* **2020**, 45, 8955.
- [114] D. Simwonis, F. Tietz, D. Stöver, *Solid State Ionics* **2000**, 132, 241.
- [115] G.J. Nelson, K.N. Grew, J.R. Izzo, J.J. Lombardo, W.M. Harris, A. Faes, A. Hessler-Wyser, J. Van Herle, S. Wang, Y.S. Chu, A. V. Virkar, W.K.S. Chiu, *Acta Mater.* **2012**, 60, 3491.
- [116] T. Chen, W.G. Wang, H. Miao, T. Li, C. Xu, *J. Power Sources* **2011**, 196, 2461.
- [117] H. Yokokawa, H. Tu, B. Iwanschitz, A. Mai, *J. Power Sources* **2008**, 182, 400.
- [118] A. V. Khrustov, D.S. Pavlov, M. V. Ananyev, *Solid State Ionics* **2020**, 346.
- [119] N. Laosiripojana, S. Assabumrungrat, *J. Power Sources* **2007**, 163, 943.
- [120] H. He, J.M. Hill, *Appl. Catal. A Gen.* **2007**, 317, 284.
- [121] Y. Matsuzaki, I. Yasuda, *Solid State Ionics* **2000**, 132, 261.
- [122] Z. Cheng, M. Liu, *Solid State Ionics* **2007**, 178, 925.
- [123] L. Holzer, B. Iwanschitz, T. Hocker, B. Münch, M. Prestat, D. Wiedenmann, U. Vogt, P. Holtappels, J. Sfeir, A. Mai, T. Graule, *J. Power Sources* **2011**, 196, 1279.
- [124] Z. Jiao, N. Takagi, N. Shikazono, N. Kasagi, *J. Power Sources* **2011**, 196, 1019.
- [125] G. Brus, H. Iwai, A. Sciazko, M. Saito, H. Yoshida, J.S. Szmyd, *J. Power Sources* **2015**, 288, 199.
- [126] T. Parhizkar, R. Roshandel, *Energy Convers. Manag.* **2017**, 133, 20.
- [127] F.S. Baumann, J. Fleig, M. Konuma, U. Starke, H.-U. Habermeier, J. Maier, *J. Electrochem. Soc.* **2005**, 152, A2074.
- [128] D. Lee, J.K. Lin, C.H. Tsai, S.H. Wu, Y.N. Cheng, R.Y. Lee, *J. Electrochem. Energy Convers. Storage* **2017**, 14, 1.
- [129] J.W. Son, *U.S. Pat. No. 20120251917 A1* **2012**, 1.
- [130] H. Monzón, M.A. Laguna-Bercero, *Int. J. Hydrogen Energy* **2012**, 37, 7262.
- [131] D. Sarantaridis, A. Atkinson, *Fuel Cells* **2007**, 7, 246.
- [132] D. Waldbillig, A. Wood, D.G. Ivey, *Solid State Ionics* **2005**, 176, 847.
- [133] S. Primdahl, M. Mogensen, *J. Appl. Electrochem.* **2000**, 30, 247.
- [134] T. Klemensø, M. Mogensen, *J. Am. Ceram. Soc.* **2007**, 90, 3582.
- [135] L. Holzer, B. Iwanschitz, T. Hocker, L. Keller, O. Pecho, G. Sartoris, P. Gasser, B. Muench, *J. Power Sources* **2013**, 242, 179.
- [136] O.M. Pecho, O. Stenzel, B. Iwanschitz, P. Gasser, M. Neumann, V. Schmidt, M. Prestat, T. Hocker, R.J. Flatt, L. Holzer, *Materials (Basel)*. **2015**, 8, 5554.

- [137] O. Pecho, A. Mai, B. Münch, T. Hocker, R. Flatt, L. Holzer, *Materials (Basel)*. **2015**, 8, 7129.
- [138] J. Malzbender, P. Batfalsky, R. Vaßen, V. Shemet, F. Tietz, *J. Power Sources* **2012**, 201, 196.
- [139] N.H. Menzler, P. Batfalsky, S. Groß, V. Shemet, F. Tietz, *ECS Trans.* **2019**, 35, 195.
- [140] L. Blum, L.G.J. De Haart, J. Malzbender, N.H. Menzler, J. Rimmel, R. Steinberger-Wilckens, *J. Power Sources* **2013**, 241, 477.
- [141] N.H. Menzler, D. Sebold, O. Guillon, *J. Power Sources* **2018**, 374, 69.
- [142] J. Yang, W. Huang, X. Wang, J. Li, D. Yan, J. Pu, B. Chi, J. Li, *J. Power Sources* **2018**, 387, 57.
- [143] J. Zurek, N. Margaritis, D. Naumenko, N.H. Menzler, W.J. Quadackers, *Oxid. Met.* **2019**, 92, 353.
- [144] L.G.J. De Haart, I.C. Vinke, *ECS Trans.* **2019**, 35, 187.
- [145] Q. Fang, L. Blum, P. Batfalsky, N.H. Menzler, U. Packbier, D. Stolten, *Int. J. Hydrogen Energy* **2013**, 38, 16344.
- [146] L. Blum, U. Packbier, I.C. Vinke, L.G.J. De Haart, *Fuel Cells* **2013**, 13, 646.
- [147] N.H. Menzler, J. Malzbender, P. Schoderböck, R. Kauert, H.P. Buchkremer, *Fuel Cells* **2014**, 14, 96.
- [148] B. Tabernig, T. Franco, A. Venskutonis, H. Kestler, L. Sigl, in *Euro PM 2011*, 3, 449.
- [149] N.H. Menzler, D. Sebold, E. Wessel, *J. Power Sources* **2014**, 254, 148.
- [150] N.H. Menzler, D. Sebold, Q. Fang, *J. Electrochem. Soc.* **2015**, 162, F1275.
- [151] T. Matsui, R. Kishida, J. Kim, H. Muroyama, K. Eguchi, *ECS Trans.* **2019**, 25, 2023.
- [152] S. Zha, Z. Cheng, M. Liu, *J. Electrochem. Soc.* **2007**, 154, B201.
- [153] L. Yang, Z. Cheng, M. Liu, L. Wilson, *Energy Environ. Sci.* **2010**, 3, 1804.
- [154] Y. Zhao, J. Malzbender, S.M. Gross, *J. Eur. Ceram. Soc.* **2011**, 31, 541.
- [155] S.M. Gross, D. Federmann, J. Rimmel, M. Pap, *J. Power Sources* **2011**, 196, 7338.
- [156] N. Minh, J. Mizusaki, S.C. Singhal, *ECS Trans.* **2017**, 78, 63.
- [157] N.K. Sandhu, A.R. Hanifi, A. Woldnik, T. Amiri, T.H. Etsell, J. Luo, P. Sarkar, *Appl. Energy* **2016**, 183, 358.
- [158] P. Blennow, J. Hjelm, T. Klemensø, S. Ramousse, A. Kromp, A. Leonide, A. Weber, *J. Power Sources* **2011**, 196, 7117.
- [159] H. Iwahara, T. Esaka, H. Uchida, N. Maeda, *Solid State Ionics* **1981**, 3–4, 359.
- [160] Z. Liu, X. Wang, M. Liu, J. Liu, *Int. J. Hydrogen Energy* **2018**, 43, 13501.

- [161] K.D. Kreuer, *Solid State Ionics* **1999**, 125, 285.
- [162] P.S. Manning, J.D. Sirman, R.A. De Souza, J.A. Kilner, *Solid State Ionics* **1997**, 100, 1.
- [163] B.C.H. Steele, A. Heinzl, *Nature* **2001**, 414, 345.
- [164] S.C. Singhal, *Solid State Ionics* **2000**, 135, 305.
- [165] H. Iwahara, Y. Asakura, K. Katahira, M. Tanaka, *Solid State Ionics* **2004**, 168, 299.
- [166] T. Norby, *Solid State Ionics* **1999**, 125, 1.
- [167] K.D. Kreuer, *Annu. Rev. Mater. Res.* **2003**, 33, 333.
- [168] P. Babilo, S.M. Haile, *J. Am. Ceram. Soc.* **2005**, 88, 2362.
- [169] Y. Yamazaki, R. Hernandez-Sanchez, S.M. Haile, *J. Mater. Chem.* **2010**, 20, 8158.
- [170] A.R. Hanifi, N.K. Sandhu, T.H. Etsell, J.L. Luo, P. Sarkar, *J. Power Sources* **2017**, 341, 264.
- [171] B.H. Rainwater, M. Liu, M. Liu, *Int. J. Hydrogen Energy* **2012**, 37, 18342.
- [172] X. Chi, Z. Wen, J. Zhang, Y. Liu, *J. Eur. Ceram. Soc.* **2015**, 35, 2109.
- [173] X.Z. Fu, J.L. Luo, A.R. Sanger, N. Luo, K.T. Chuang, *J. Power Sources* **2010**, 195, 2659.
- [174] K. Bae, H.S. Noh, D.Y. Jang, M. Kim, H.J. Kim, J. Hong, J.H. Lee, B.K. Kim, J.W. Son, J.H. Shim, *J. Korean Ceram. Soc.* **2015**, 52, 320.
- [175] F.L. Chen, O.T. Sørensen, G.Y. Meng, D.K. Peng, *J. Eur. Ceram. Soc.* **1998**, 18, 1389.
- [176] A. Subramanian, J. Tong, R.P. O'Hayre, N.M. Sammes, *J. Am. Ceram. Soc.* **2011**, 94, 1800.
- [177] Z. Zhong, *Solid State Ionics* **2007**, 178, 213.
- [178] *Advances in Solid Oxide Fuel Cells and Electronic Ceramics*. John Wiley & Sons, Inc., 2015.
- [179] H. Shimada, T. Yamaguchi, H. Sumi, Y. Yamaguchi, K. Nomura, Y. Fujishiro, *Ceram. Int.* **2018**, 44, 3134.
- [180] B. Wang, L. Bi, X.S. Zhao, *J. Power Sources* **2018**, 399, 207.
- [181] K. Katahira, Y. Kohchi, T. Shimura, H. Iwahara, *Solid State Ionics* **2000**, 138, 91.
- [182] K.H. Ryu, S.M. Haile, *Solid State Ionics* **1999**, 125, 355.
- [183] F. Giannici, A. Longo, F. Deganello, A. Balerna, A.S. Arico, A. Martorana, *Solid State Ionics* **2007**, 178, 587.
- [184] W.G. Coors, D.W. Readey, *J. Am. Ceram. Soc.* **2002**, 85, 2637.
- [185] P. Sawant, S. Varma, M.R. Gonal, B.N. Wani, D. Prakash, S.R. Bharadwaj, *Electrochim. Acta* **2014**, 120, 80.

- [186] M. Liu, J. Gao, X. Liu, G. Meng, *Int. J. Hydrogen Energy* **2011**, 36, 13741.
- [187] Y. Guo, Y. Lin, R. Ran, Z. Shao, *J. Power Sources* **2009**, 193, 400.
- [188] J. Nielsen, Å.H. Persson, T.T. Muhl, K. Brodersen, *J. Electrochem. Soc.* **2018**, 165, F90.
- [189] M.C. Tucker, *J. Power Sources* **2010**, 195, 4570.
- [190] M.C. Tucker, *Energy Technol.* **2017**, 5, 2175.
- [191] O. Arevalo-Quintero, O. Kesler, *Fuel Cells* **2018**, 18, 466.
- [192] M.C. Tucker, *J. Power Sources* **2018**, 395, 314.
- [193] T. Franco, K. Schibinger, Z. Ilhan, G. Schiller, A. Venskutonis, *ECS Trans.* **2019**, 7, 771.
- [194] M. Brandner, M. Bram, J. Froitzheim, H.P. Buchkremer, D. Stöver, *Solid State Ionics* **2008**, 179, 1501.
- [195] V.V. Krishnan, *Wiley Interdiscip. Rev. Energy Environ.* **2017**, 6.
- [196] T. Suzuki, T. Yamaguchi, Y. Fujishiro, M. Awano, *J. Power Sources* **2006**, 160, 73.
- [197] K. Kendall, *Int. J. Appl. Ceram. Technol.* **2010**, 7, 1.
- [198] V. Lawlor, S. Griesser, G. Buchinger, A.G. Olabi, S. Cordiner, D. Meissner, *J. Power Sources* **2009**, 193, 387.
- [199] H.S. Noh, K.J. Yoon, B.K. Kim, H.J. Je, H.W. Lee, J.H. Lee, J.W. Son, *J. Power Sources* **2014**, 249, 125.
- [200] S.P. Jiang, S.H. Chan, *J. Mater. Sci.* **2004**, 39, 4405.
- [201] Z.C. Chen, Y. Sakane, T. Tsurumaki, Y. Ayame, F. Fujita, *ICCM Int. Conf. Compos. Mater.* **2007**, 1.
- [202] A. Faes, Q. Jeangros, J.B. Wagner, A. Hessler-Wyser, J. Van herle, A. Brisse, R. Dunin-Borkowski, *ECS Meet. Abstr.* **2009**, MA2009-02, 1330.
- [203] A. Faes, A. Nakajo, A. Hessler-Wyser, D. Dubois, A. Brisse, S. Modena, J. Van herle, *J. Power Sources* **2009**, 193, 55.
- [204] L. Pelegrini, J.B.R. Neto, D. Hotza, *Rev. Adv. Mater. Sci.* **2016**, 46, 6.
- [205] S.D. Kim, H. Moon, S.H. Hyun, J. Moon, J. Kim, H.W. Lee, *Solid State Ionics* **2007**, 178, 1304.
- [206] S.K. Pratihari, A. Das Sharma, R.N. Basu, H.S. Maiti, *J. Power Sources* **2004**, 129, 138.
- [207] S.M. Choi, H. An, K.J. Yoon, B.-K. Kim, H.-W. Lee, J.-W. Son, H. Kim, D. Shin, H.-I. Ji, J.-H. Lee, *Appl. Energy* **2019**, 233–234, 29.
- [208] M.D. Gross, J.M. Vohs, R.J. Gorte, *J. Mater. Chem.* **2007**, 17, 3071.
- [209] O. Hodjati-Pugh, A. Dhir, R. Steinberger-Wilckens, *Appl. Sci.* **2021**, 11, 1077.
- [210] Y. Lyu, J. Xie, D. Wang, J. Wang, *J. Mater. Sci.* **2020**, 55, 7184.

- [211] L. Fan, B. Zhu, P.C. Su, C. He, *Nano Energy* **2018**, 45, 148.
- [212] Z. Zakaria, Z. Awang Mat, S.H. Abu Hassan, Y. Boon Kar, *Int. J. Energy Res.* **2020**, 44, 594.
- [213] H. Su, Y.H. Hu, *Chem. Eng. J.* **2020**, 402, 126235.
- [214] B.-K. Park, S.A. Barnett, *J. Mater. Chem. A* **2020**, 8, 11626.
- [215] W.Z. Zhu, S.C. Deevi, *Mater. Sci. Eng. A* **2003**, 362, 228.
- [216] Y. Liu, Z. Shao, T. Mori, S.P. Jiang, *Mater. Reports Energy* **2021**, 1, 100003.
- [217] K. Lee, S. Choi, J. Kim, H. Lee, J. Lee, *J. Power Sources* **2005**, 140, 226.
- [218] C. Metcalfe, O. Kesler, T. Rivard, F. Gitzhofer, N. Abatzoglou, *J. Electrochem. Soc.* **2010**, 157, B1326.
- [219] E. Ivers-Tiffée, W. Wersing, M. Schießl, H. Greiner, *Berichte der Bunsengesellschaft für Phys. Chemie* **1990**, 94, 978.
- [220] S. MAJUMDAR, T. CLAAR, B. FLANDERMEYER, *J. Am. Ceram. Soc.* **1986**, 69, 628.
- [221] Z. Zhou, V.K. Nadimpalli, D.B. Pedersen, V. Esposito, *Materials (Basel)*. **2021**, 14, 3139.
- [222] M.C. Tucker, *J. Power Sources* **2017**, 369, 6.
- [223] M.C. Tucker, G.Y. Lau, C.P. Jacobson, L.C. DeJonghe, S.J. Visco, *J. Power Sources* **2008**, 175, 447.
- [224] E. Dogdibegovic, R. Wang, G.Y. Lau, M.C. Tucker, *J. Power Sources* **2019**, 410–411, 91.
- [225] M. Reisert, V. Berova, A. Aphale, P. Singh, M.C. Tucker, *Int. J. Hydrogen Energy* **2020**, 45, 30882.
- [226] N. Xu, M. Chen, M. Han, *J. Alloys Compd.* **2018**, 765, 757.
- [227] E. Dogdibegovic, R. Wang, G.Y. Lau, A. Karimaghloo, M.H. Lee, M.C. Tucker, *J. Power Sources* **2019**, 437, 226935.
- [228] M. Cuglietta, O. Arevalo-Quintero, O. Kesler, *Fuel Cells* **2019**, 19, 268.
- [229] S. Vafaenezhad, N.K. Sandhu, A.R. Hanifi, T.H. Etsell, P. Sarkar, *J. Power Sources* **2019**, 435, 226763.
- [230] H. Monzón, M.A. Laguna-Bercero, *ECS Trans.* **2015**, 68, 1229.
- [231] S.P. Jiang, *J. Mater. Sci.* **2008**, 43, 6799.
- [232] Y. Sun, S. He, M. Saunders, K. Chen, Z. Shao, S.P. Jiang, *Int. J. Hydrogen Energy* **2021**, 46, 2606.
- [233] P. Ding, W. Li, H. Zhao, C. Wu, L. Zhao, B. Dong, S. Wang, *J. Phys. Mater.* **2021**, 4, 022002.
- [234] R.K. Lenka, P.K. Patro, V. Patel, L. Muhmood, T. Mahata, *J. Alloys Compd.* **2021**, 860,

158490.

- [235] C. Lalanne, G. Prosperi, J.M. Bassat, F. Mauvy, S. Fourcade, P. Stevens, M. Zahid, S. Diethelm, J. Van herle, J.C. Grenier, *J. Power Sources* **2008**, 185, 1218.
- [236] S. Li, H. Tu, F. Li, M.T. Anwar, L. Yu, *J. Alloys Compd.* **2017**, 694, 17.
- [237] S. Li, H. Tu, L. Yu, M.T. Anwar, *Electrochim. Acta* **2016**, 212, 303.
- [238] R. Bove, *ECS Proc. Vol.* **2005**, 2005–07, 780.
- [239] R.J. Boersma, N.M. Sammes, C.J. Fee, *Solid State Ionics* **2000**, 135, 493.
- [240] H. Feng, D. Panthi, Y. Du, *ECS Meet. Abstr.* **2021**, MA2021-03, 18.
- [241] M.S. Arshad, N. Mushtaq, M.A. Ahmad, S. Naseem, S. Atiq, Z. Ahmed, R. Ali, G. Abbas, R. Raza, *Int. J. Hydrogen Energy* **2017**, 42, 22288.
- [242] T.H. Wan, M. Saccoccio, C. Chen, F. Ciucci, *Electrochim. Acta* **2015**, 184, 483.
- [243] T. Matsushima, H. Ohroi, T. Hirai, *Solid State Ionics* **1998**, 111, 315.
- [244] T. Paul, P.W. Chi, P.M. Wu, M.K. Wu, *Sci. Rep.* **2021**, 11, 12624.
- [245] A.R. Hanifi, M.A. Laguna-Bercero, N.K. Sandhu, T.H. Etsell, P. Sarkar, *Sci. Rep.* **2016**, 6, 27359.
- [246] B.-K. Park, R. Scipioni, Q. Zhang, D. Cox, P.W. Voorhees, S.A. Barnett, *J. Mater. Chem. A* **2020**, 8, 11687.
- [247] Y. Zhang, B. Liu, B. Tu, Y. Dong, M. Cheng, *Solid State Ionics* **2009**, 180, 1580.
- [248] T. Klemensø, C.C. Appel, M. Mogensen, *Electrochem. Solid-State Lett.* **2006**, 9.
- [249] M. Pihlatie, T. Ramos, A. Kaiser, *J. Power Sources* **2009**, 193, 322.
- [250] S.T. Aruna, M. Muthuraman, K.C. Patil, *Solid State Ionics* **1998**, 111, 45.
- [251] F. Tietz, Q. Fu, V.A.C. Haanappel, A. Mai, N.H. Menzler, S. Uhlenbruck, *Int. J. Appl. Ceram. Technol.* **2007**, 4, 436.
- [252] J. Fleig, J. Maier, *J. Eur. Ceram. Soc.* **2004**, 24, 1343.
- [253] M. Backhaus-Ricoult, *Solid State Ionics* **2006**, 177, 2195.
- [254] S.J. Skinner, *Int. J. Inorg. Mater.* **2001**, 3, 113.
- [255] Y. Huang, J.M. Vohs, R.J. Gorte, *J. Electrochem. Soc.* **2004**, 151, A646.
- [256] A. Esquirol, N.P. Brandon, J.A. Kilner, M. Mogensen, *J. Electrochem. Soc.* **2004**, 151, A1847.
- [257] H. Yokokawa, N. Sakai, T. Kawada, M. Dokiya, *Solid State Ionics* **1990**, 40–41, 398.
- [258] G.C. Kostogloudis, G. Tsiniarakis, C. Ftikos, *Solid State Ionics* **2000**, 135, 529.
- [259] Y. Huang, J.M. Vohs, R.J. Gorte, *J. Electrochem. Soc.* **2006**, 153, A951.

- [260] A. Montenegro-Hernández, J. Vega-Castillo, L. Mogni, A. Caneiro, *Int. J. Hydrogen Energy* **2011**, 36, 15704.
- [261] D. Ding, X. Li, S.Y. Lai, K. Gerdes, M. Liu, *Energy Environ. Sci.* **2014**, 7, 552.
- [262] J.G. Railsback, Z. Gao, S.A. Barnett, *Solid State Ionics* **2015**, 274, 134.
- [263] M.Y. Lu, T. Yang, R. Scipioni, Y.A. Chart, A. Furlong, S.A. Barnett, *J. Electrochem. Soc.* **2020**, 167, 164504.
- [264] M. Tafazoli, M. Baniassadi, A. Babaei, M. Shakeri, *Procedia Mater. Sci.* **2015**, 11, 428.
- [265] C. Nicollet, A. Flura, V. Vibhu, A. Rougier, J.M. Bassat, J.C. Grenier, *J. Power Sources* **2015**, 294, 473.
- [266] C. Nicollet, A. Flura, V. Vibhu, S. Fourcade, A. Rougier, J.M. Bassat, J.C. Grenier, *J. Solid State Electrochem.* **2016**, 20, 2071.
- [267] Z. Gao, X. Ding, D. Ding, L. Ding, S. Zhang, G. Yuan, *Int. J. Hydrogen Energy* **2018**, 43, 8953.
- [268] M.A. Laguna-Bercero, H. Luebbe, J. Silva, J. Van Herle, *Fuel Cells* **2015**, 15, 98.
- [269] C. Nicollet, A. Flura, V. Vibhu, A. Rougier, J.-M. Bassat, J.-C. Grenier, *Int. J. Hydrogen Energy* **2016**, 41, 15538.
- [270] E. Boehm, J.M. Bassat, P. Dordor, F. Mauvy, J.C. Grenier, P. Stevens, *Solid State Ionics* **2005**, 176, 2717.
- [271] X.D. Zhou, J.W. Templeton, Z. Nie, H. Chen, J.W. Stevenson, L.R. Pederson, *Electrochim. Acta* **2012**, 71, 44.
- [272] J.-M. Bassat, V. Vibhu, C. Nicollet, A. Flura, S. Fourcade, J.-C. Grenier, A. Rougier, *ECS Trans.* **2017**, 78, 655.
- [273] E. Dogdibegovic, C.J. Wright, X.D. Zhou, W.C. Wei, *J. Am. Ceram. Soc.* **2016**, 99, 2737.
- [274] M.A. Morales-Zapata, A. Larrea, M.A. Laguna-Bercero, *Int. J. Hydrogen Energy* **2020**, 45, 5535.
- [275] V. Vibhu, A. Rougier, C. Nicollet, A. Flura, S. Fourcade, N. Penin, J.C. Grenier, J.M. Bassat, *J. Power Sources* **2016**, 317, 184.
- [276] V. Vibhu, I.C. Vinke, R.A. Eichel, L.G.J. de Haart, *J. Power Sources* **2021**, 482, 228909.
- [277] W. Wang, M.D. Gross, J.M. Vohs, R.J. Gorte, *J. Electrochem. Soc.* **2007**, 154, B439.
- [278] R. Kiebach, C. Knöfel, F. Bozza, T. Klemensø, C. Chatzichristodoulou, *J. Power Sources* **2013**, 228, 170.
- [279] D. Ding, M. Liu, M. Liu, *ECS Trans.* **2013**, 57, 1801.
- [280] Y. Namgung, A. Kumar, J. Hong, I.H. Kim, S.J. Song, *J. Alloys Compd.* **2021**, 852, 157037.

- [281] R.K. Sharma, S.K. Cheah, M. Burriel, L. Dessemond, J.M. Bassat, E. Djurado, *J. Mater. Chem. A* **2017**, 5, 1120.
- [282] X. Chen, J. Wang, Q. Liang, X. Sun, X. Zhu, D. Zhou, J. Meng, *Solid State Sci.* **2020**, 100, 106108.
- [283] T. Zhang, Q. Zhou, Y. He, C. Zhao, S. Qi, M. Wang, T. Wei, D. An, *J. Mater. Sci. Mater. Electron.* **2020**, 31, 949.
- [284] B.I. Arias-Serrano, M.E. Sotomayor, A. Várez, B. Levenfeld, H. Monzón, M.A. Laguna-Bercero, A. Larrea, *RSC Adv.* **2016**, 6, 19007.
- [285] A.V. Kovalevsky, V.V. Kharton, A.A. Yaremchenko, Y.V. Pivak, E.N. Naumovich, J.R. Frade, *J. Eur. Ceram. Soc.* **2007**, 27, 4269.
- [286] J.M. Bassat, C. Allançon, P. Odier, J.P. Loup, M.D. Carvalho, A. Wattiaux, *Eur. J. Solid State Inorg. Chem.* **1998**, 35, 173.
- [287] C.Y. Tsai, A. Aguadero, S.J. Skinner, *J. Solid State Chem.* **2020**, 289, 121533.
- [288] J. Dailly, F. Mauvy, M. Marrony, M. Pouchard, J.-C. Grenier, *J. Solid State Electrochem.* **2011**, 15, 245.
- [289] A. Montenegro-Hernández, A. Soldati, L. Mogni, H. Troiani, A. Schreiber, F. Soldera, A. Caneiro, *J. Power Sources* **2014**, 265, 6.
- [290] H. Zhao, F. Mauvy, C. Lalanne, J.M. Bassat, S. Fourcade, J.C. Grenier, *Solid State Ionics* **2008**, 179, 2000.
- [291] R. Chiba, H. Taguchi, T. Komatsu, H. Orui, K. Nozawa, H. Arai, *Solid State Ionics* **2011**, 197, 42.
- [292] M.A. Laguna-Bercero, H. Monzón, A. Larrea, V.M. Orera, *J. Mater. Chem. A* **2016**, 4, 1446.
- [293] D.A. Osinkin, *Electrochim. Acta* **2021**, 372, 137858.
- [294] F. Mauvy, C. Lalanne, J.-M. Bassat, J.-C. Grenier, H. Zhao, L. Huo, P. Stevens, *J. Electrochem. Soc.* **2006**, 153, A1547.
- [295] S. Nugehalli Sampathkumar, P. Aubin, K. Couturier, X. Sun, B.R. Sudireddy, S. Diethelm, M. Pérez-Fortes, J. Van herle, *Int. J. Hydrogen Energy* **2022**, 47, 10175.
- [296] M.A. Laguna-Bercero, A.R. Hanifi, H. Monzón, J. Cunningham, T.H. Etsell, P. Sarkar, *J. Mater. Chem. A* **2014**, 2, 9764.
- [297] T. Jacobsen, P.V. Hendriksen, S. Koch, *Electrochim. Acta* **2008**, 53, 7500.
- [298] S. Primdahl, M. Mogensen, *J. Electrochem. Soc.* **1998**, 145, 2431.
- [299] P. Caliendo, A. Nakajo, S. Diethelm, J. Van, *J. Power Sources* **2019**, 436, 226838.
- [300] A. Flura, C. Nicollet, S. Fourcade, V. Vibhu, A. Rougier, J.-M. Bassat, J.-C. Grenier, *Electrochim. Acta* **2015**, 174, 1030.

- [301] B.K. Park, R. Scipioni, Q. Zhang, D. Cox, P.W. Voorhees, S.A. Barnett, *J. Mater. Chem. A* **2020**, 8, 11687.
- [302] J. Song, D. Ning, B. Boukamp, J.-M. Bassat, H.J.M. Bouwmeester, *J. Mater. Chem. A* **2020**, 8, 22206.
- [303] A. Hauch, R. Küngas, P. Blennow, A.B. Hansen, J.B. Hansen, B. V. Mathiesen, M.B. Mogensen, *Science (80-.)*. **2020**, 370.
- [304] D. Connolly, H. Lund, B. V. Mathiesen, *Renew. Sustain. Energy Rev.* **2016**, 60, 1634.
- [305] M.B. Mogensen, *Figshare (2020)*
- [306] J. Schefold, A. Brisse, H. Poepke, *Int. J. Hydrogen Energy* **2017**, 42, 13415.
- [307] R. Küngas, *J. Electrochem. Soc.* **2020**, 167, 044508.
- [308] T. Nakao, S. Inoue, S. Uenoyama, Y. Takuwa, M. Suzuki, *ECS Trans.* **2019**, 91, 43.
- [309] K. Chen, S.P. Jiang, **2016**, 163, 3070.
- [310] A. Hauch, S.D. Ebbesen, S.H. Jensen, M. Mogensen, *J. Electrochem. Soc.* **2008**, 155, B1184.
- [311] D. The, S. Grieshammer, M. Schroeder, M. Martin, M. Al Daroukh, F. Tietz, J. Schefold, A. Brisse, *J. Power Sources* **2015**, 275, 901.
- [312] E. Lay-Grindler, J. Laurencin, J. Villanova, P. Cloetens, P. Bleuet, A. Mansuy, J. Mougín, G. Delette, *J. Power Sources* **2014**, 269, 927.
- [313] S.J. Kim, G.M. Choi, *Solid State Ionics* **2014**, 262, 303.
- [314] P. Hjalmarsen, X. Sun, Y.L. Liu, M. Chen, *J. Power Sources* **2014**, 262, 316.
- [315] M.B. Mogensen, M. Chen, H.L. Frandsen, C. Graves, A. Hauch, P.V. Hendriksen, T. Jacobsen, S.H. Jensen, T.L. Skafté, X. Sun, *Fuel Cells* **2021**, 21, 415.
- [316] M.A. Morales-Zapata, A. Larrea, M.A. Laguna-Bercero, *Int. J. Hydrogen Energy* **2020**, 45, 5535.
- [317] S.A. Barnett, B.-K. Park, R. Scipioni, *ECS Trans.* **2019**, 91, 1791.
- [318] B.K. Park, D. Cox, S.A. Barnett, *Nano Lett.* **2021**, 21, 8363.

Appendix A

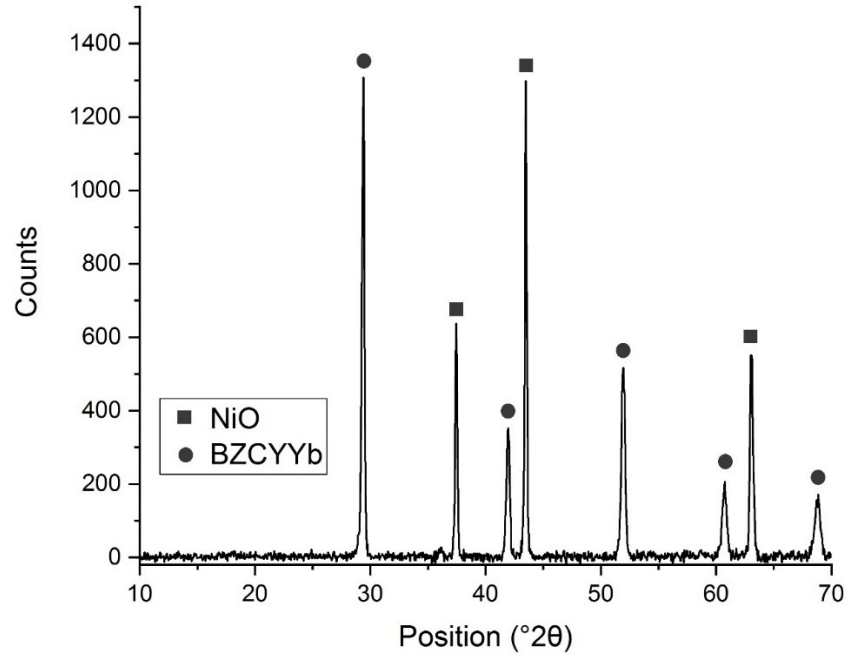


Figure A 1 XRD pattern of NiO-BZCYYb functional layer following sintering at 1450°C for 3 h.

Appendix B

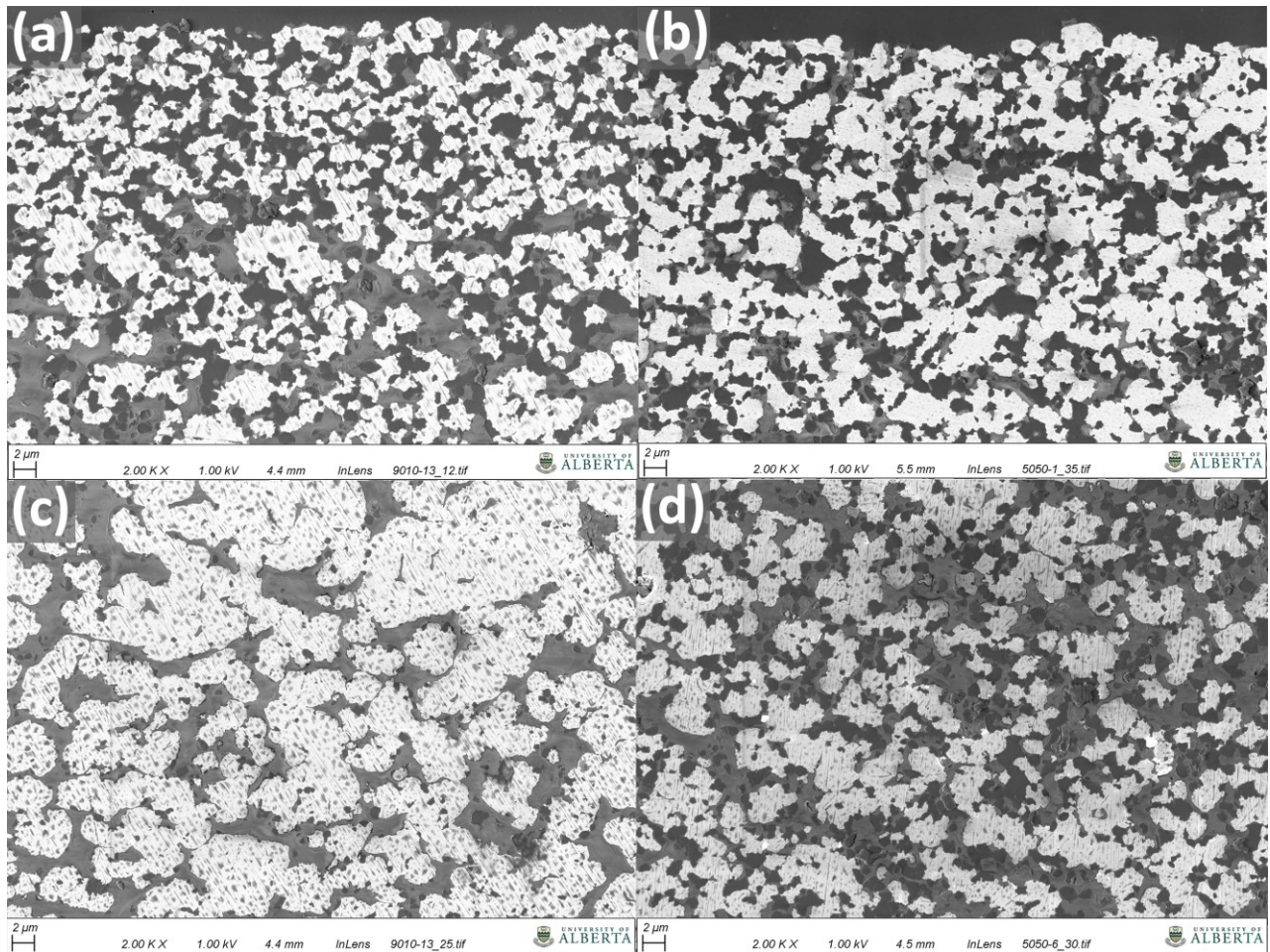


Figure B 1 SEM images of polished samples for (a) Ni82 functional layer and buffer layer (b) Ni50 functional layer and support (c) Ni82 support (d) Ni50 support. Color contrast shows different phases; YSZ: dark gray, Ni: white, pores: light gray.

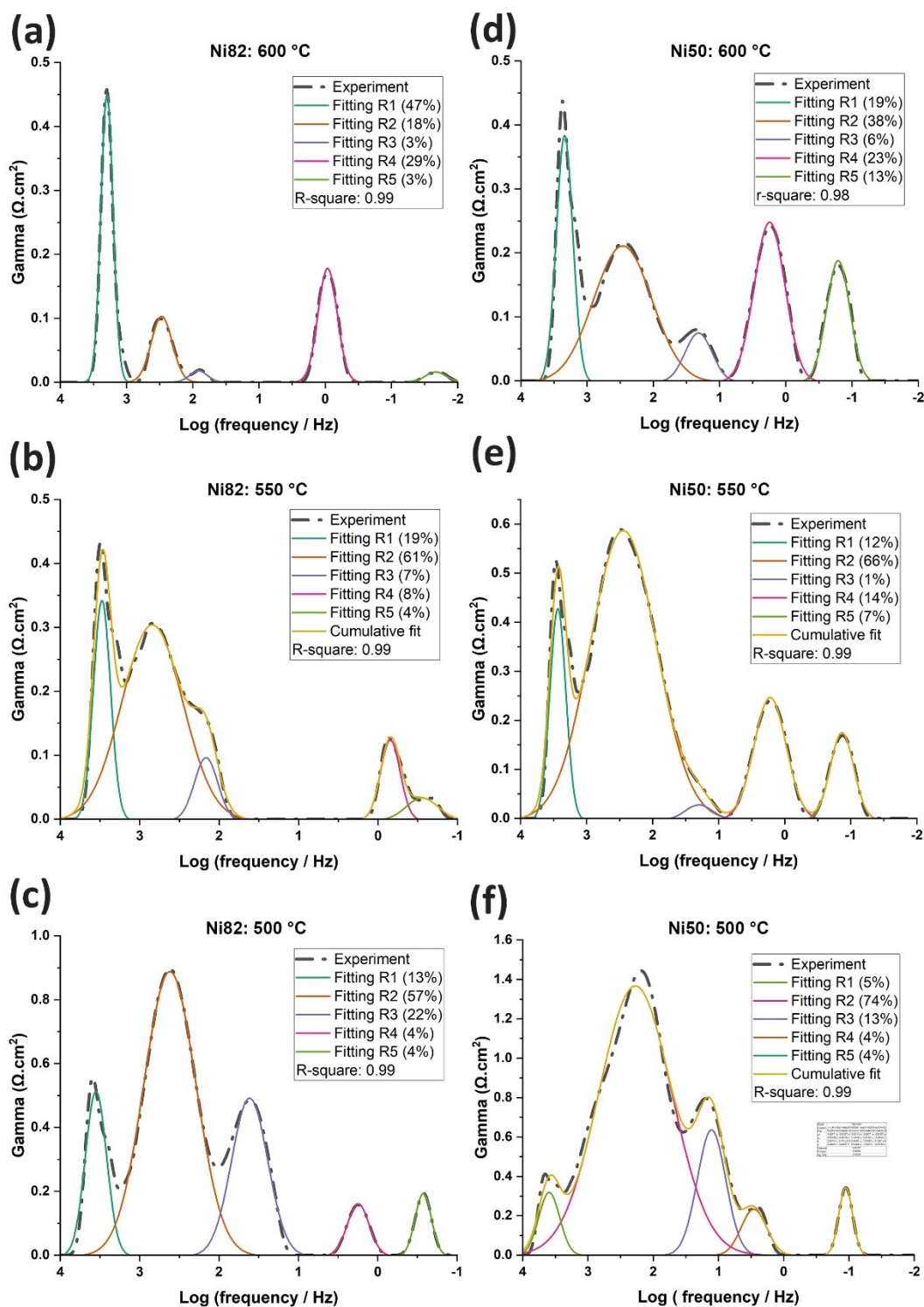


Figure B 2 Contribution of different resistances in the original DRT data extracted from EIS (experiment) at different temperatures for (a, b, c) Ni82 and (d, e, f) Ni50 cell. The values in the legends show the fraction of surface area under each peak to the total surface area under the DRT curves.

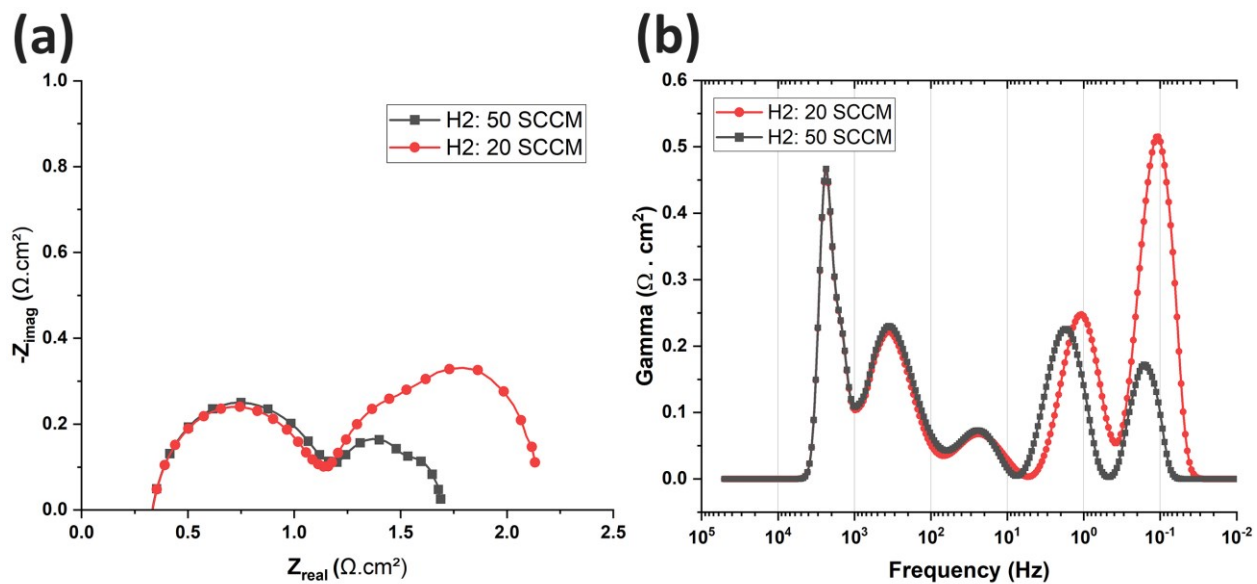


Figure B 3 (a) Nyquist plot of the Ni50 cell at 600 °C with two different fuel flow rates. (b) DRT data corresponding to the Nyquist plots.

Appendix C

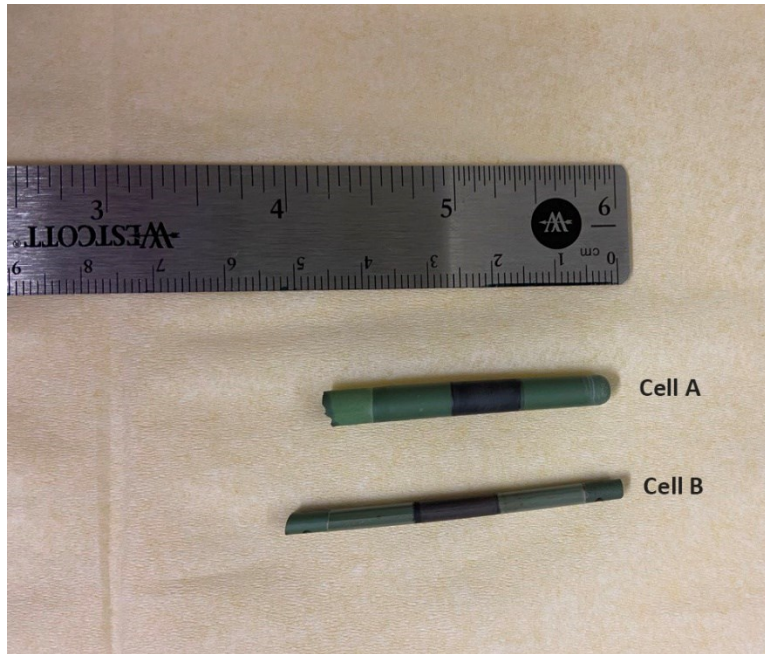


Figure C 1 Comparison of the shape and size of cell A and B used for the SOFC test.

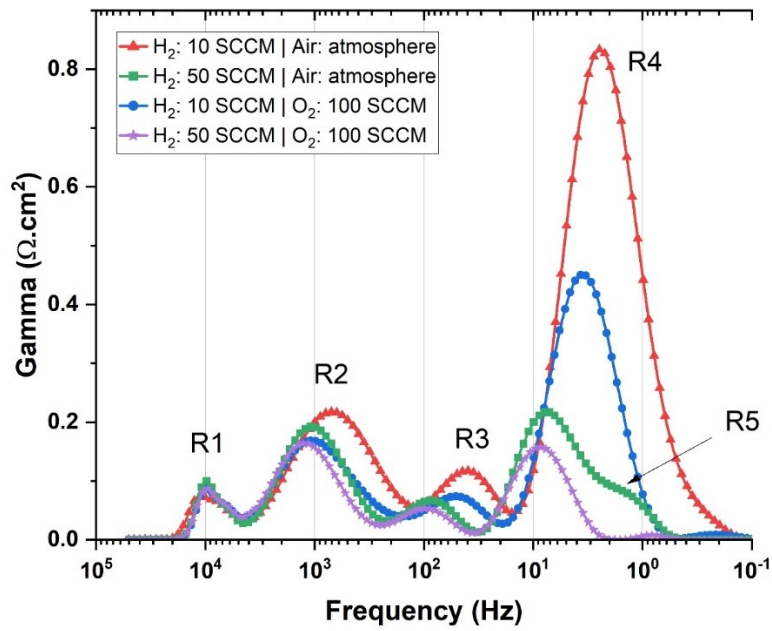


Figure C 2 DRT graphs for cell B with Pr_6O_{11} (PO) cathode at 650 °C for different cathode and anode gas compositions and varying flow rates.